Magnetooptical spectroscopy of magnetic multilayers: Theory and experiment (A review)

V. N. Antonov,* L. Uba, and S. Uba

Institute of Experimental Physics, University of Bialystok, Lipowa 41, PL-15-424 Bialystok, Poland

A. N. Yaresko and A. Ya. Perlov

Max-Planck-Institut for the Physics of Complex Systems, D-01187 Dresden, Germany

V. V. Nemoshkalenko

Institute of Metal Physics, 36 Vernadskii Str., 252142 Kiev, Ukraine

(Submitted December 8, 2000; revised February 3, 2001)
Fiz. Nizk. Temp. **27**, 579–626 (June 2001)

Experimental and theoretical results on the optical and magnetooptical (MO) spectral properties of a series of Co/Cu, Co/Pd, Co/Pt and Fe/Au multilayers are reviewed. Diagonal and off-diagonal components of the optical conductivity tensor have been determined in the photon energy range 0.8-5.5 eV from the polar and longitudinal Kerr rotation as well as ellipticity and ellipsometry measurements. The conductivity tensor has been evaluated on the basis of self-consistent spin-polarized relativistic linear muffin-tin orbital (LMTO) band-structure calculations within the local spin-density approximation. The role of the spin polarization and the spin–orbit interaction in the formation of the magnetooptical Kerr effect (MOKE) spectra as inferred from first-principles calculations is examined and discussed. The high sensitivity of the MO properties to the interface structure is studied by *ab initio* modeling of the effects of the interfacial alloying, substitutional disorder, and the roughness at the interfaces. It is shown that the MOKE spectra of the multilayered structures (MLS) calculated using the LMTO method reproduce the experimental spectra only moderately well if ideal MLS with sharp interfaces are assumed. It is shown that the MOKE spectra of the MLS can be adequately reproduced only by taking into account their real interface microstructure. The magnetooptical anisotropy (MOA) is studied both experimentally and theoretically for a series of Fe_n/Au_n superlattices prepared by molecular beam epitaxy with $n=1,2,3$ Fe and Au atomic planes of (001) orientation. The results of the LMTO calculations show that the microscopic origin of the large MOA is the interplay of the strong spin-orbit coupling on Au sites and the large exchange splitting on Fe sites via Aud–Fe d hybridization of the electronic states at the interfaces. The orientation anisotropy of the d orbital moment is calculated from first principles and analyzed on the basis of d orbital symmetry considerations. The relationship between the orbital moment anisotropy and the MOA is discussed. The reviewed results imply that the magnetooptical properties of multilayers with various compositions and structures can be quantitatively predicted from first-principles band-structure calculations. Such a possibility is important for basic research as well as applications.
[DOI: 10.1063/1.1382983]

1. INTRODUCTION

It was first discovered in 1845 by Faraday[1] that the polarization vector of linearly polarized light is rotated upon transmission through a sample that is exposed to a magnetic field parallel to the propagation direction of the light. About 30 years later, Kerr[2] observed that when linearly polarized light is reflected from a magnetic solid, its plane of polarization also becomes rotated by a small angle with respect to that of the incident light. This discovery has become known as the magnetooptical (MO) Kerr effect. Since then, many other magnetooptical effects, e.g., the Zeeman, Voigt, and Cotton-Mouton effects,[3] have been found. These effects all have in common that they are due to a different interaction of left and right circularly polarized light with a magnetic solid. The Kerr effect has now been known for more than a century, but it is only in recent times that it has become the subject of intensive investigations. The reason for this recent development is twofold: first, the Kerr effect gained considerable in interest due to modern data storage technology, because it can be used to ''read'' suitably stored magnetic information in an optical manner,[4] and second, the Kerr effect has rapidly developed into an appealing spectroscopic tool in materials research. The technological research on the Kerr effect was initially motivated by the search for good magnetooptical materials that could be used as information storage media. In the course of this research, the Kerr spectra of many ferromagnetic materials were investigated. Over the years the Kerr spectra of many ferromagnetic materials have been obtained. An overview of the experimental data col-

lected on the Kerr effect can be found in the review articles by Buschow,[5] Reim and Schoenes,[6] Schoenes,[7] Ebert,[8] and Antonov *et al.*[9]

The quantum-mechanical understanding of the Kerr effect began as early as 1932, when Hulme[10] proposed that the Kerr effect could be attributed to spin-orbit (SO) coupling (see also Kittel[11]). The symmetry between left and right circularly polarized light is broken due to the SO coupling in a magnetic solid. This leads to different refractive indices for the two kinds of circularly polarized light, so that linearly polarized incident light is reflected with elliptical polarization, and the major elliptical axis is rotated by the so-called Kerr angle from the original axis of linear polarization. The first systematic study of the frequency-dependent Kerr and Faraday effects was developed by Argyres,[12] and later Cooper presented a more general theory using some simplifying assumptions.[13] The very powerful linear response techniques of Kubo[14] gave general formulas for the conductivity tensor which are now widely used. A general theory of the frequency-dependent conductivity of ferromagnetic (FM) metals over a wide range of frequencies and temperatures was developed in 1968 by Kondorsky and Vediaev.[15]

The first *ab initio* calculation of MO properties was made by Callaway and co-workers in the mid-1970s.[16] They calculated the absorption parts of the conductivity tensor elements σ_{xx} and σ_{xy} for pure Fe and Ni and obtained rather good agreement with experiment. After these pioneering studies, there was a lull in MO calculations until MO effects were found to be important for magnetic recording and the computational resources had advanced. Different reliable numerical schemes for the calculation of optical matrix elements and the integration over the Brillouin zone have been implemented, giving essentially identical results.[17] Prototype studies have been performed using modern methods of band theory for Fe, Co, and Ni. Following the calculations for the elemental $3d$ ferromagnets, a number of groups have evaluated the MO spectra for more interesting compounds (see Refs. 8, 9, and references therein).

In recent years, artificial layered structures composed of magnetic transition metals separated by nonmagnetic metals have been studied intensively due to the fundamental research interest in these systems and also because of their potential for applications. Oscillatory interlayer exchange coupling,[18] giant magnetoresistance,[19] and the induced magnetic polarization effect in nonmagnetic layers (see, e.g., Ref. 20 and references therein) have become the most discussed phenomena in layered magnetic structures.

In particular, Co/Pt and Co/Pd multilayered structures (MLS) have attracted a lot of attention because these systems exhibit simultaneously a large magnetooptical Kerr rotation[21,22] and perpendicular anisotropy,[23] which in combination make these materials applicable for a new generation of storage devices.[24]

The aim of this paper is a review of recent achievements in both the experimental and theoretical investigations of the electronic structure, optical, and MO properties of transition-metal multilayered structures. We considered the most important from scientific and technological points of view: Co/Pt, Co/Pd, Co/Cu, and Fe/Au MLS. In these MLS, the nonmagnetic sites (Pt, Pd, Cu, and Au) exhibit an induced magnetic moment due to the hybridization with the transition-metal spin-polarized $3d$ states. The polarization is strong at Pt and Pd sites and weak at noble-metal sites due to the completely occupied d bands in the later case. Also of interest is how the spin-orbit interaction of nonmagnetic metal (increasing in the sequence Cu, Pd, Pt, Au) influences the MO response of the MLS. From the standpoint of applications a very important question is how the imperfection at the interface affects the physical properties of layered structures, including the MO properties.

The paper is organized as follows. In Sec. 2.1. the theoretical background of the *ab initio* calculations of the band structure and the optical conductivity tensor are reviewed. The experimental details are described in Sec. 2.2. Sections 3, 4, and 5 present the experimental and theoretical results for the MO properties of Co/Pd, Co/Pt, and Co/Cu MLS, respectively. Section 6 is devoted to the electronic structure and anisotropy of the MO properties in Fe/Au MLS. Finally, the results are summarized in Sec. 7.

2. EXPERIMENTAL AND COMPUTATIONAL DETAILS

2.1. Computational details

Phenomenologically, magnetooptical effects at optical frequencies are treated by means of a dielectric tensor. For the polar Kerr magnetization geometry and a crystal of at least threefold rotational symmetry, where both the symmetry axis and the magnetization direction are perpendicular to the sample surface and the z axis is chosen parallel to them, the dielectric tensor is composed of the diagonal components ε_{xx} and ε_{zz} and the off-diagonal component ε_{xy} in the form

$$\varepsilon = \begin{pmatrix} \varepsilon_{xx} & \varepsilon_{xy} & 0 \\ -\varepsilon_{xy} & \varepsilon_{xx} & 0 \\ 0 & 0 & \varepsilon s_{zz} \end{pmatrix}. \tag{1}$$

At normal light incidence the relation between the complex polar Kerr angle and the dielectric tensor components is given by[6]

$$\theta^{PK} + i\eta^{PK} = \frac{-\varepsilon_{xy}}{(\varepsilon_{xx}-1)\sqrt{\varepsilon_{xx}}}, \tag{2}$$

where θ^{PK} and η^{PK} are the polar Kerr rotation and the ellipticity, respectively.

Here and henceforth, the following definitions have been adopted. We choose the time dependence of the electric field as $e^{-i\omega t}$. Hence, all the complex quantities are expressed by their real and imaginary parts as follows: $\varepsilon_{\alpha\beta} = \varepsilon^{(1)}_{\alpha\beta} + i\varepsilon^{(2)}_{\alpha\beta}$, where $\alpha, \beta \equiv x, y, z$, $\varepsilon_{xx} = (n+ik)^2$, and n and k are the refractive index and extinction coefficient, respectively. The optical conductivity tensor $\sigma_{\alpha\beta} = \sigma^{(1)}_{\alpha\beta} + i\sigma^{(2)}_{\alpha\beta}$ is related to the dielectric tensor $\varepsilon_{\alpha\beta}$ through the equation

$$\varepsilon_{\alpha\beta}(\omega) = \delta_{\alpha\beta} + \frac{4\pi i}{\omega}\sigma_{\alpha\beta}(\omega). \tag{3}$$

For the longitudinal Kerr magnetization geometry, where the magnetization lies in the sample plane and the y axis is chosen parallel to both the magnetization direction and the plane of incidence, the dielectric tensor takes the form

$$\varepsilon = \begin{pmatrix} \varepsilon_{xx} & 0 & -\varepsilon_{xz} \\ 0 & \varepsilon_{xx} & 0 \\ \varepsilon_{xz} & 0 & \varepsilon_{zz} \end{pmatrix}. \tag{4}$$

The formula for the complex longitudinal Kerr angle as it has been derived from general formulas for the Kerr effect with arbitrary dielectric tensor[25] is given by

$$\theta_{s,p}^{LK} + i\,\eta_{s,p}^{LK} = -\frac{2\varepsilon_{xz}\sin\varphi\cos\varphi\sqrt{\varepsilon_{xx}}}{D} \tag{5}$$

with

$$D = (\sqrt{\varepsilon_{xx}(\varepsilon_{zz} - \sin^2\varphi)} + \sqrt{\varepsilon_{zz}(\varepsilon_{xx} - \sin^2\varphi)}) \times (\sqrt{\varepsilon_{xx} - \sin^2\varphi} \pm \cos\varphi)(\sqrt{\varepsilon_{xx}\varepsilon_{zz}}\cos\varphi \mp \sqrt{\varepsilon_{zz} - \sin^2\varphi}),$$

where φ is the angle of incidence of the light, and the upper and lower signs correspond to light of p and s polarizations, parallel and perpendicular to the plane of incidence, respectively.

In the case when the assumption $\varepsilon_{zz} \approx \varepsilon_{xx}$ is justified, formula (5) simplifies to[26]

$$\theta_{s,p}^{LK} + i\,\eta_{s,p}^{LK} = -\frac{\varepsilon_{xz}\sin\varphi(\sqrt{\varepsilon_{xx} - \sin^2\varphi} \pm \sin\varphi\tan\varphi)}{(\varepsilon_{xx} - 1)(\varepsilon_{xx} - \tan^2\varphi)\sqrt{\varepsilon_{xx} - \sin^2\varphi}}. \tag{6}$$

On straightforward symmetry considerations it can be shown that all MO phenomena are caused by the symmetry reduction, in comparison to the paramagnetic state, caused by magnetic ordering.[27] Concerning optical properties this symmetry reduction has consequences only when the SO coupling is also taken into consideration. To calculate MO properties one therefore has to take into account the magnetism and SO coupling at the same time when dealing with the electronic structure of the material considered. In the corresponding band structure calculations it is normally sufficient to treat the SO coupling in a perturbative way. A more rigorous scheme, however, is obtained by starting from the Dirac equation set up in the framework of relativistic spin density functional theory:[28]

$$[c\,\boldsymbol{\alpha}\cdot\mathbf{p} + \beta mc^2 + \mathbf{I}V + V_{sp}\beta\sigma_z]\psi_{n\mathbf{k}} = \epsilon_{n\mathbf{k}}\psi_{n\mathbf{k}} \tag{7}$$

with $V_{sp}(\mathbf{r})$ being the spin-polarized part of the exchange-correlation potential corresponding to the z quantization axis. All other parts of the potential are contained in $V(\mathbf{r})$. The 4×4 matrices α, β, and $\mathbf{I}$ are defined by

$$\alpha = \begin{pmatrix} 0 & \sigma \\ \sigma & 0 \end{pmatrix}, \quad \beta = \begin{pmatrix} \mathbf{1} & 0 \\ 0 & -\mathbf{1} \end{pmatrix}, \quad \mathbf{I} = \begin{pmatrix} \mathbf{1} & 0 \\ 0 & \mathbf{1} \end{pmatrix}, \tag{8}$$

where σ are the standard Pauli matrices, and $\mathbf{1}$ is the 2×2 unit matrix.

There are quite a few band structure methods available now that are based on the above Dirac equation.[29] In one of the schemes the basis functions are derived from the proper solution of the Dirac equation for the spin-dependent single-site potentials.[30,31] In another approach, the basis functions are obtained initially by solving the Dirac equation without the spin-dependent term[32,33] and then this term is taken into account in the variational step.[30,34] In spite of this approximation, the latter scheme gives results in close agreement with the former,[29] while being simpler to implement. We should also mention the widely used technique in which the SO coupling is added variationally[32] after the scalar relativistic magnetic Hamiltonian has been constructed. In this case, the Pauli equation with the SO coupling is solved instead of the Dirac equation. We should emphasize that all three techniques yield similar results.

The optical conductivity tensor or, equivalently, the dielectric tensor is the basic spectral quantity needed for evaluation of the Kerr effect.[7] The optical conductivity can be computed from the energy band structure by means of the Kubo–Greenwood linear-response expression:[14,16]

$$\sigma_{\alpha\beta}(\omega) = \frac{-ie^2}{m^2\hbar V_{uc}} \times \sum_{\mathbf{k}} \sum_{nn'} \frac{f(\epsilon_{n\mathbf{k}}) - f(\epsilon_{n'\mathbf{k}})}{\omega_{nn'}(\mathbf{k})} \frac{\Pi_{n'n}^{\alpha}(\mathbf{k})\Pi_{nn'}^{\beta}(\mathbf{k})}{\omega - \omega_{nn'}(\mathbf{k}) + i\gamma}, \tag{9}$$

where $f(\epsilon_{n\mathbf{k}})$ is the Fermi function, $\hbar\omega_{nn'}(\mathbf{k}) \equiv \epsilon_{n\mathbf{k}} - \epsilon_{n'\mathbf{k}}$ is the energy difference of the Kohn–Sham energies $\epsilon_{n\mathbf{k}}$, and γ is the lifetime parameter, which is included to describe the finite lifetime of excited Bloch electron states. The $\Pi_{nn'}^{\alpha}$ are the dipole optical transition matrix elements, which in a fully relativistic description are given by[35]

$$\Pi_{nn'}(\mathbf{k}) = m\langle\psi_{n\mathbf{k}}|c\,\alpha|\psi_{n'\mathbf{k}}\rangle \tag{10}$$

with $\psi_{n\mathbf{k}}$ being the four-component Bloch electron wave functions.

Equation (9) for the conductivity contains a double sum over all energy bands, which naturally separates into the so-called interband contribution, i.e., $n \neq n'$, and the intraband contribution, $n = n'$. The intraband contribution to the diagonal components of σ may be rewritten for zero temperature as

$$\sigma_{\alpha\alpha}(\omega) \equiv \frac{\omega_{p,\alpha}^2}{4\pi}\frac{i}{\omega + i\gamma_D}, \tag{11}$$

where $\omega_{p,\alpha}$ are the components of the plasma frequency, which are given by

$$\omega_{p,\alpha}^2 \equiv \frac{4\pi e^2}{m^2 V_{uc}} \sum_{n\mathbf{k}} \delta(\epsilon_{n\mathbf{k}} - E_F)|\Pi_{nn}^{\alpha}|^2, \tag{12}$$

E_F is the Fermi energy, and $\gamma_D = 1/\tau_D$, where τ_D is the phenomenological Drude electron relaxation time. The intraband relaxation time parameter γ_D may be different from the interband relaxation time parameter γ. The latter can be frequency dependent,[36] and, because excited states always have a finite lifetime, will be nonzero, whereas γ_D will approach zero for very pure materials. The contribution of intraband transitions to the off-diagonal conductivity is usually not considered. Also, the influence of local field effects on the MO properties has not been studied. We mention, lastly, that the Kramers–Kronig transformation was used to calculate the dispersive parts of the optical conductivity from the absorptive parts.

The electronic structure of the MLS was calculated self-consistently on the basis of the local spin density

approximation[37] to the density functional theory, using the fully relativistic spin-polarized LMTO method[32–34] in the atomic-sphere approximation, including the combined correction (ASA+CC).[32,38] Core-charge densities were recalculated at every iteration of the self-consistency loop. The spin polarization was included in the variational step.[30] The combined correction terms were also taken into account in the optical matrix element calculations.[35] The basis consisted of *s*, *p*, *d*, and *f* LMTOs. The **k**-space integrations were performed with the improved tetrahedron method.[39]

2.2. Experimental procedure

The polar Kerr rotation (θ_K) and ellipticity (η_K) spectra were measured with a MO spectrometer based on the polarization modulation technique[40] in the photon energy range 0.8–5.5 eV. Light from a super-quiet Xe arc lamp or D_2 lamp used in the UV region is focused by a condenser on the entrance slit of the monochromator (SPEX 500M), equipped with self-interchangeable gratings for measurements of different parts of the spectrum. The outcoming light beam is filtered by an appropriate filter to attenuate higher orders from the monochromator. After passing through the polarizer and photoelastic modulator (Hinds PEM-90 CaF_2) the light beam is focused by a quartz lens on the surface of the sample mounted on a sample holder with the temperature stabilized in the range 290–800 K inside the 1.8 T water-cooled electromagnets. The amplitude of the retardation of the light is periodically modulated at a frequency of 57 kHz by the modulator, oriented with its strain axis at 45° with respect to the polarizer axis. The angle of incidence of the light on the sample surface is set at 2 and 75 deg in the polar and longitudinal Kerr geometry, respectively. After reflection the light beam passes through the analyzer, oriented parallel or perpendicular to the modulator strain axis, and is detected by a low-noise photomultiplier in the energy range $1.4<h\nu<5.5$ eV and by a liquid-nitrogen-cooled Ge photodiode for $0.8<h\nu<1.4$ eV. The detector output signal from the current preamplifier is measured by lock-in amplifiers. The polar Kerr rotation and ellipticity, after appropriate calibration with the use of a driven Babinet–Soleil compensator, are derived from the ratio of total light intensity, corrected for zero offset with the use of a controlled light beam shutter, and the intensity of the first and second harmonics. The same setup is used to measure θ_K and η_K hysteresis loops at fixed light wavelength. The setup is fully automated and computer controlled via a data acquisition system (Keithley 500 A). The sensitivity of the Kerr spectrometer is of the order of 10^{-4} deg.

The optical properties—refractive index *n* and extinction coefficient *k*—have been measured by spectroscopic ellipsometry using the rotating analyzer method[41] in the spectral range 0.8–5.5 eV. The sample is mounted on a five-axis precision goniometer in a subset of the above described MO system. The ellipsometric angles Ψ and Δ were derived from the real-time digital harmonic analysis of the detected signal modulated by a rotating analyzer. The MgF_2 Rochon analyzer rotates with an angular frequency of 12 s^{-1} inside a rotary encoder with 4096 lines per revolution. The signal from the detectors is synchronously digitized at 20 μs intervals by the Keithley 500 A system and evaluated in real-time using the Hadamard transform. The angle of incidence was set at 67°, optimized as the averaged principal angle of incidence for the measured samples and the spectral range used. The accuracy of setting the angle of incidence is 0.005° and the average error in the determination of *n* and *k* values is of the order of 0.003.

TABLE I. The parameters of the Co/Pd MLS studied. The sample numbers are given, together with N_{layers}, the number of bilayers, and t_{Co} and t_{Pd}, the measured thicknesses of the Co and the Pd sublayers.[42]

No.	N_{layers}	t_{Co}, Å	t_{Pd}, Å
1	52	3.5	18.3
2	47	5.2	17.6
3	43	6.4	18.2
4	40	8.4	18.5
5	33	13.8	19.8
6	28	17.4	20.6

3. MAGNETO-OPTICAL PROPERTIES OF Co-Pd SYSTEMS

3.1. Co/Pd multilayers

A detailed experimental and theoretical study of the electronic structure and MO properties of Co/Pd MLS using MOKE spectroscopy and first-principles band-structure calculations was done in Ref. 42. The Co/Pd multilayers under consideration were prepared on water-cooled glass substrates using the dc magnetically enhanced face-to-face sputtering system described in Ref. 83. The chemical compositions of the films were determined by x-ray fluorescence analysis from the peak intensities of the characteristic fluorescence radiation. Structural studies were performed by conventional x-ray diffractometry. Formation of multilayer structures was confirmed by low angle x-ray diffraction, and the modulation period was deduced from the position of the Bragg peaks. The periods determined from the x-ray measurements agree with those evaluated from the fluorescence analysis. The films were found to be of fcc (111)-textured structure. The parameters of the samples studied are given in Table I.

3.1.1. Experimental results

The polar Kerr rotation (θ_K) and ellipticity (η_K) spectra of the Co/Pd MLS measured under saturation conditions are shown in Fig. 1a and 1b. For comparison, the spectra of a 2000 Å thick fcc Co film, multiplied by a factor of 0.7, are also plotted in Fig. 1. It can be seen that the MLS Kerr spectra never exceed in magnitude those of the fcc Co over the whole spectral range. The prominent features of the θ_K spectra are a broad negative peak at ~3 eV and a shoulder at ~4.3 eV, followed by a θ_K slope varying as a function of the Co layer thickness. The θ_K peak, centered at 1.5 eV, characteristic of fcc Co, is strongly reduced with decreasing MLS Co sublayer thickness, and the prominent minima at ~3 eV in θ_K and at ~5 eV in η_K diminish in amplitude. The shift of the zero-crossing of η_K up to ~3 eV with decrease of the amount of Co present is accompanied by the formation of a positive two-peak structure. Similar spectral features of the Co/Pd MLS, although within smaller spectral ranges and for other sublayer thicknesses, were observed in Refs. 22, 43, and 44. Inspection of the θ_K and η_K spectra of the MLS leads one to the conclusion that there is a MO contribution

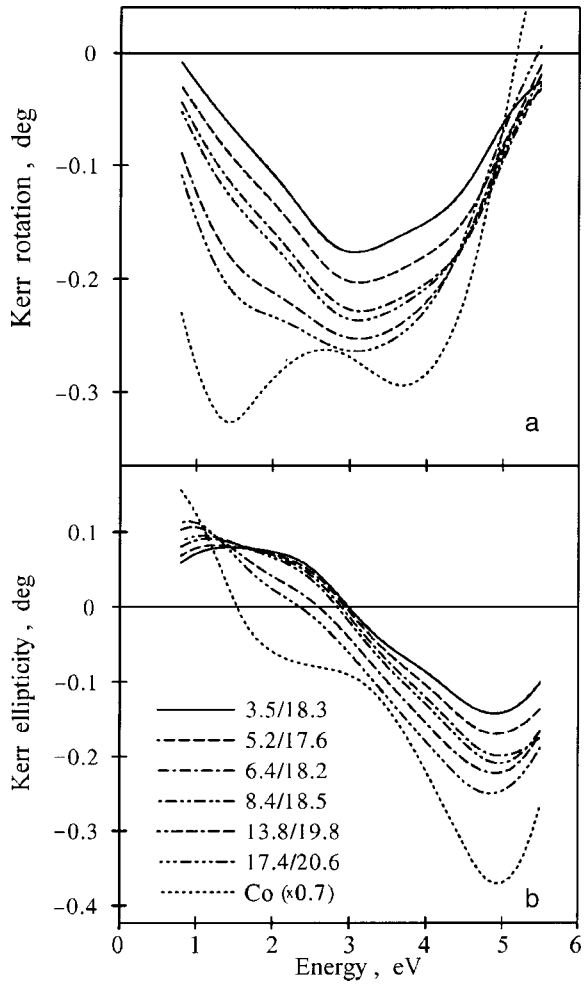

FIG. 1. Experimental polar Kerr rotation (a) and ellipticity (b) spectra of Co/Pd MLS and fcc Co film. The Co and Pd sublayer thicknesses are given in the keys in units of Å.[42]

independent of, or weakly dependent on, the cobalt sublayer thickness. These effects that are independent of the Co content may arise from Pd spin polarization induced by the proximity of Co layers and/or from the polarization caused by roughness and limited alloying at the Co-Pd interface.

To study the mechanism responsible for the MOKE in the Co/Pd MLS and to enable us to discuss the magnetooptical response of the films in terms of separate contributions of the Co and Pd sublattices, the data should, in principle, be analyzed using the off-diagonal optical conductivity tensor components σ_{xy}, which are directly related to the magnetooptical transitions between the spin-polarized electronic states. From the measured θ_K and η_K data and the diagonal tensor component σ_{xx}, the off-diagonal component σ_{xy} can be evaluated according to Eq. (2). The values of σ_{xx} for the fcc Co and Pd films and the Co/Pd MLS under consideration were obtained by an ellipsometric method for the range 0.8–5.5 eV. It was found that the σ_{xx} spectra of the multilayers are close to each other and do not exhibit fine structure, except for a small broad peak at about 4–5 eV.

For all of the Co/Pd MLS studied, it was found that the denominator in Eq. (2) evaluated from the optical data is a monotonic and structureless function over the whole energy range and depends weakly on the film composition. Consequently, all of the peaks in the polar Kerr rotation and ellipticity spectra originate from the corresponding features of the absorptive and dispersive parts of $\sigma_{xy}(\omega)$, respectively. The energy dependence of the denominator in equation (2) only changes the relative amplitudes of the UV and IR peaks of the spectra, without producing any additional spectral features. It can be concluded that in the Co/Pd MLS the MOKE is governed by the off-diagonal part of the optical conductivity tensor.

3.1.2. Multilayers with perfect interfaces

In an attempt to reproduce and to explain the experimental MOKE spectra, band-structure calculations of the MO properties of some model MLS were performed. As the influence of the structure of the Co-Pd interface on the MOKE spectra is the subject of this study, in the first step an idealized model with a sharp interface was adopted in the calculations. The numbers n of Co and m of Pd atomic planes in the model nCo/mPd MLS were chosen as close as possible to the experimentally measured ones. For all the MLS, an *abc* stacking sequence of close-packed Co and Pd planes was assumed. In Ref. 45 it was shown that for Co sublayers that are not very thick (less than 30 Å, with the Pd sublayer thickness being 12 Å), the in-plane lattice spacing in Co/Pd MLS is almost independent of the Co sublayer thickness and only ~2% less than the lattice spacing in fcc Pd. Therefore the lattice constant $a=2.694$ Å of the hexagonal lattice was chosen. The interplane spacings in the Co and Pd sublayers and at the interface were chosen to be equal and corresponding to the ideal c/a ratio ($c/a=q\sqrt{2/3}$, where $q=n+m$ is the number of close-packed atomic planes). The sphere radii of Co and Pd were both taken as equal to the average S_{WS} value of 1.49 Å.

The distributions of the spin magnetic moments in the Co and Pd atomic spheres derived from the band-structure calculations are given in Table II. For all the MLS studied, the dependence of the magnetic moments on the distance from the interface is the same. The Co magnetic moment is enhanced at the interface and already approaches the bulk

TABLE II. Calculated Co and Pd spin magnetic moments (μ_B/atom) in the Co/Pd MLS. The number after the chemical symbol denotes the number of corresponding atomic planes starting from the Co-Pd interface. For fcc Co with S_{WS} set at the same value as for the MLS, the value of 1.72μ_B/atom was obtained.[42]

MLS	Co2	Co1	Pd1	Pd2	Pd3
1Co/8Pd		1.94	0.26	0.12	0.04
2Co/7Pd		1.84	0.23	0.10	0.03
4Co/8Pd	1.72	1.83	0.23	0.11	0.04
6Co/9Pd	1.72	1.83	0.23	0.12	0.04
9Co/9Pd	1.72	1.83	0.23	0.12	0.04

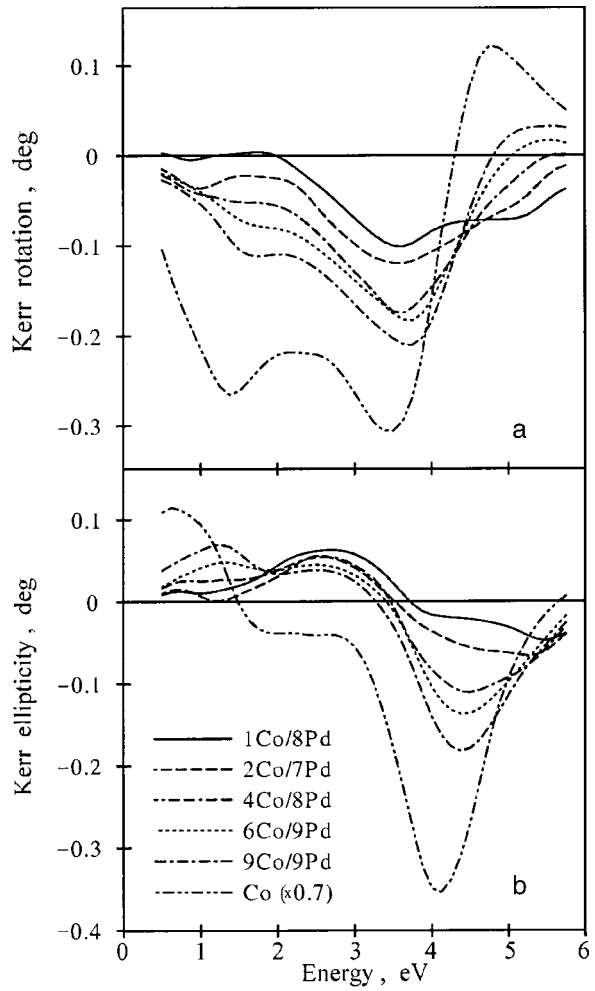

FIG. 2. Calculated polar Kerr rotation (a) and ellipticity (b) spectra for the model nCo/mPd MLS with sharp interfaces (n and m are the numbers of Co and Pd atomic planes, respectively). For comparison, spectra of fcc Co (calculated with the same value of S_{WS} as the MLS), multiplied by a factor of 0.7, are also shown.[42]

value of $1.72\mu_B$/atom in the second plane. The same value of the Co moment ($1.72\mu_B$/atom) was obtained from the calculations for fcc Co with the lattice constant expanded so that the value of S_{WS} was equal to that for the MLS. The value of the magnetic moment induced in Pd rapidly decreases with distance from the interface. In the MLS with a Pd sublayer consisting of more than six Pd atomic planes, the magnetic moments induced in the middle of the Pd sublayer are smaller than $0.015\mu_B$/atom and are not shown in Table II. The rapid decrease of the Pd magnetic moment with increase of the distance from the interface can be easily understood if one recalls that the moment is mainly due to Co $3d$–Pd $4d$ hybridization. A Pd atom even in only the second atomic plane from the interface has no Co atoms among even its second-nearest neighbors, and it interacts with the exchange-split Co $3d$ states only indirectly.

The calculated MOKE spectra of the Co/Pd MLS are shown in Fig. 2. For comparison, spectra of fcc Co (calculated with the same value of S_{WS} as the MLS), multiplied by a factor of 0.7, are also shown. From a comparison with the experimental spectra, it is seen that in the UV range the shoulder at $\sim$5 eV, which is a characteristic feature of the experimentally measured polar Kerr rotation spectra of the MLS, manifests itself only in the spectra of the 1Co/8Pd MLS and, to a lesser extent, those of the 2Co/7Pd MLS. For the MLS with larger numbers of Co atomic planes, the magnitude of the Kerr rotation spectra in the UV range increases with increase of the Co sublayer thickness, whereas the shape of the spectra changes only slightly. As can be seen in Fig. 2b, the features of the Kerr ellipticity spectra, corresponding to the peaks at 1.0 and 4.3 eV in the fcc Co spectrum, become more pronounced as the number of atomic planes of Co increases.

Such a dependence of the calculated MOKE spectra of the MLS on the Co sublayer thickness is explicable. As the magnetic moment induced in the Pd atoms located far from the interface is very small, one can expect these atoms to give only a small contribution to the off-diagonal optical conductivity. Consequently, if the model with a sharp interface is adopted, the MO properties of the MLS are determined by the Co sublayer and one, or perhaps two, adjacent Pd atomic planes. Also, from the calculated DOS curves and Co magnetic moments it follows that only the electronic states in the two Co atomic planes nearest to the interface are modified strongly by the hybridization with the Pd states. Hence, as the Co sublayer thickness increases, the MOKE spectra of the MLS should become closer to that of pure Co. This is exactly what can be seen in Fig. 2. As the number of Co atomic planes increases, the relative contribution of the interfacial layer to the spectra becomes smaller, and a shoulder appears in the spectra at 1.5 eV which is evidently related to the corresponding peak in the fcc Co spectrum.

A comparison with the experimental spectra of the MLS (Fig. 1) shows that the calculations reproduce only moderately well the main peculiarities of the MOKE spectra of the MLS and the tendencies in the modification of the MLS spectra with variation of the Co sublayer thickness, and the quantitative agreement is not satisfactory.

The calculated spectra are of smaller magnitude; the decrease of the magnitude for the MLS with a small number of Co atomic planes is larger than in the experiment. The feature at 1.5 eV in the calculated spectra of the MLS with a thin Co sublayer disappears completely, and the magnitude of the spectra goes almost to zero in this energy range. The loss of amplitude at this energy, although observed experimentally, is not so drastic. Also, the calculations predict a rapid decrease of the Kerr rotation amplitude of the shoulder at 5 eV with respect to that of the main minimum as the number of Co atomic planes increases, while the shoulder is observable in the experimental spectra.

It is worth recalling that the spectra of fcc Co shown in Fig. 2 were calculated with the enlarged lattice constant used for the model MLS and, consequently, they should not be compared directly to the experimental Co spectra (see Fig. 1). The position of the UV minimum in the polar Kerr rotation spectrum of Co, calculated using the experimental fcc Co lattice constant (i.e., for $S_{WS}=1.395$ Å), is shifted to higher energies by $\sim$1 eV (see Ref. 74). Thus, the shift of $\sim$0.7 eV in the energy position of the UV minimum observed in the experimental MLS spectra with respect to that for the fcc Co film is reproduced—although it is overestimated—by the calculations.

There are several possible sources of these discrepan-

cies. First of all, the peaks in the polar Kerr rotation spectra calculated for either fcc or hcp Co are shifted to higher energies with respect to the measured ones, and the magnitude of the minimum at 1.5 eV is too small. This discrepancy is apparently due to a failure of the LDA-based calculations to predict correctly the MOKE spectra of the ferromagnetic $3d$ metals; this failure has recently been extensively discussed in the literature.[74,85,86] A plausible cause for this lies in the approximate description of the exchange and correlation of rather localized $3d$ electrons. If the calculated magnitude of the IR peak of fcc Co were larger, it would bring the theoretical MOKE spectra of the MLS into closer agreement with the experimental ones for the energy range below 2 eV. In the UV range, however, a shift of the Co Kerr rotation peak to lower energies would hardly improve the agreement between the theory and experiment at all.

The shift of the calculated peak positions may also be caused by the difference between the experimental interatomic distances and those used in the calculations. Determination of the in-plane and interplane distances in an individual sublayer of the MLS or overlayered structures in an onerous task, and the experimental data available for Co/Pd MLS differ significantly.[34–36] To estimate the sizes of the possible effects of the interplane relaxation, test calculations using the unmodified in-plane interatomic distance but a smaller c/a ratio were performed for Co (with a hexagonal supercell) and 4Co/5Pd MLS. It was found that the theoretical MOKE spectra are rather insensitive to the interplane distance. A decrease of the c/a ratio by 5% results in a small increase in amplitude of the polar Kerr rotation spectra, but the peak positions remain unchanged. Thus, although a contraction of interplane distances in the Co sublayer has been derived from structural investigations,[46,47] it is unlikely to be responsible for the discrepancies between the theoretical and experimental MOKE spectra of the Co/Pd MLS. An in-plane relaxation in a thick Co sublayer might affect the calculated MOKE spectra strongly, but performing such a calculation is beyond the capability of our facilities. Moreover, there is no experimental evidence that relaxation really occurs in the MLS studied.

The idea of enhanced spin polarization in the Pd planes adjacent to the Co has also been considered. For some of the MLS studied, test calculations were performed in which an additional exchange splitting was introduced for one or two of the Pd atomic layers nearest to the interface. As a result of the additional spin polarization of the Pd atoms, the intensity of the calculated polar Kerr rotation spectra in the UV range increases. However, the strong positive rotation at low photon energies worsens the agreement with the experiment in this energy range.

It can be concluded that the main cause of the differences between the theory and experiment lies in the choice of a model with a sharp interface as a basis for the calculations. An intermixing at the interface, even within just one or two atomic layers, can appreciably change the shape and magnitude of the MOKE spectra of the MLS, especially those with small Co sublayer thicknesses. The next part of this Section is devoted to a quantitative study of this problem.

3.1.3. Multilayers with imperfect interfaces

From the discussion above, it follows that interfacial intermixing should be taken into account if one is to describe the MO properties of real Co/Pd MLS systems. A first improvement that takes us closer to describing ''real'' systems is that of considering an ordered compound at the interface. To examine the consequences of interfacial intermixing for Co/Pd MLS MOKE spectra and their relation to the chemical nature of the interface, a model of multilayer supercells with alloyed interfaces was considered. The study was performed with the use of the above-described formalism of *ab initio* band-structure calculations. As the LMTO method requires a crystal lattice with specified translational and point symmetry, special model supercells of the multilayered structures with alloyed interfaces and fcc (111) texture were constructed. In the [111] direction, for all model MLS an *abc* stacking sequence of close-packed atomic Co and Pd planes was assumed. As an interface between the neighboring Co and Pd layers, one or two Co-Pd mixed atomic planes were introduced. To satisfy the requirement of overall D_{3d}^3 lattice symmetry of the supercells and to minimize their volume, the unit cell was doubled in the basal plane. As a consequence, interfacial planes in these supercells can consist of mixed atomic planes composed of an ordered Co-Pd compound with 1:3 and 3:1 stoichiometry and threefold rotational symmetry. Three types of MLS with different interfacial atomic planes were considered. The structures of the nCo/A/mPd and nCo/B/mPd types contain Pd-rich Co_1Pd_3 (A) and Co-rich Co_3Pd_1 (B) ordered interfacial planar alloys, respectively. The structure nCo/C/mPd with $C=Co_3Pd_1/Co_1Pd_3$ has a two-layer interfacial ordered alloy composed of consecutive *B*- and *A*-type planes.

To understand the relationship between the interfacial structures and the MOKE spectra, a systematic study was performed for Co/Pd MLS with a period of six atomic layers. Calculations for larger supercells are extremely time consuming and were performed only for some selected cases. It was found that the calculations performed are sufficiently representative and illustrate the main trends in the modification of the MO spectra with interface imperfection. In all of the calculations, the same lattice constant as for the ideal model MLS was assumed.

The calculated polar Kerr rotation spectra for the Co/Pd MLS, where the Co and Pd layers are separated by three types of interfacial alloy layer (A, B, and C), are shown in Fig. 3a–c. For comparison, the spectrum of fcc Co calculated with the same value of S_{WS} and the spectra of ideal 1Co/5Pd, 2Co/4Pd, and 3Co/3Pd MLS are also included. The spectra calculated for the supercell structures in which the Pd layers are separated by alloy layers only are presented in Fig. 3a. The supercells 0Co/A/4Pd and 0Co/B/4Pd consist of a two-atomic-layer thickness of alloy, of either Co_1Pd_3 or Co_3Pd_1 composition, separated by a four-atomic-layer thickness of Pd spacer. The supercell 0Co/C/2Pd consists of repeated sequences of four alloy atomic planes, $Co_1Pd_3/Co_3Pd_1/Co_3Pd_1/Co_1Pd_3$, separated by two Pd atomic planes. These structures can be regarded as limiting cases, where Co atoms are present in alloy planes only.

As is seen from Fig. 3a, in the UV range the main features of the 0Co/A/4Pd spectrum are very similar in shape to

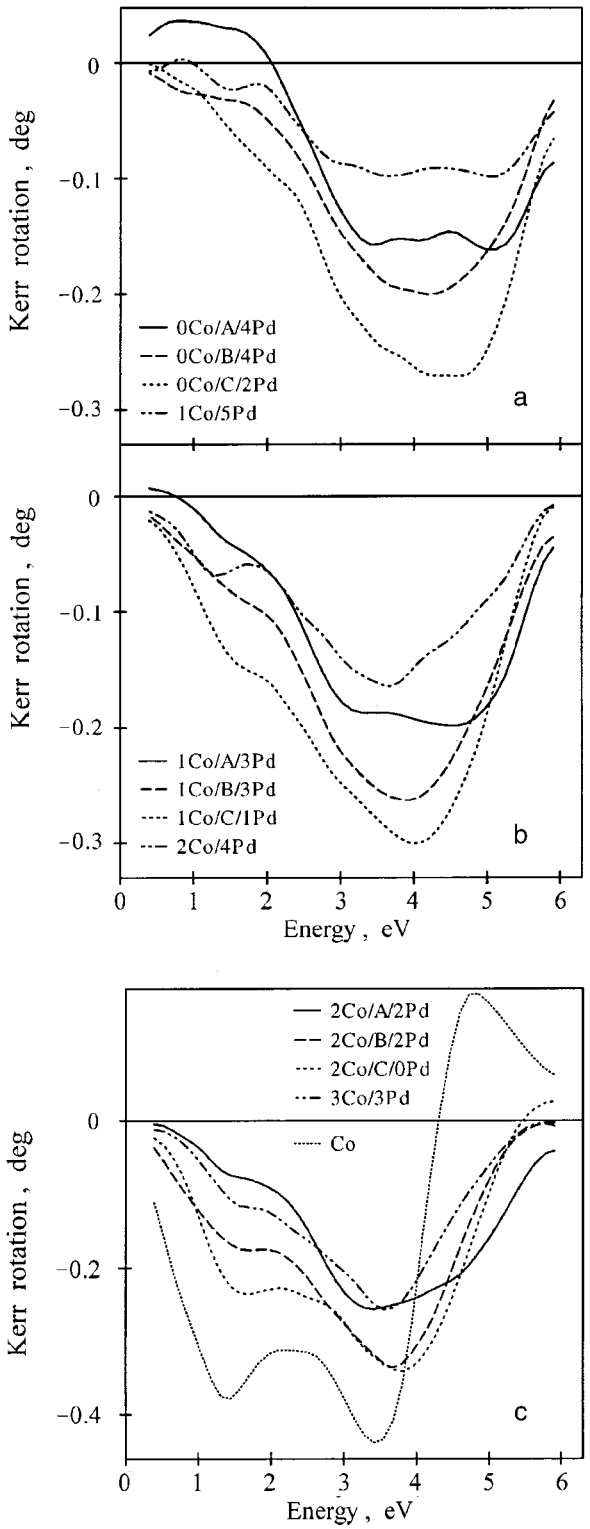

FIG. 3. Calculated polar Kerr rotation spectra for the model nCo/X/mPd multilayered structures with imperfect interfaces, n and m are the numbers of Co and Pd atomic planes, respectively. X=A, B, C denotes the interfacial planar ordered alloys Co_1Pd_3, Co_3Pd_1, and Co_3Pd_1/Co_1Pd_3, respectively. For a comparison, the corresponding MLS spectra for the ideal model nCo/mPd and the spectrum of fcc Co with the same value of S_{WS} as for the MLS are also shown.[42]

those of the 1Co/5Pd MLS with the sharp interface. It is interesting that the amplitude of the 0Co/A/4Pd spectrum is about 70% higher than the amplitude of the 1Co/5Pd spectrum, despite the higher Co content in the latter. However, in the energy range below ~2 eV positive rotation is observed for the 0Co/A/4Pd MLS. It should be noted that the overall shape of the 0Co/A/4Pd Kerr rotation spectrum is very close to that calculated for homogeneous diluted Co-Pd alloys.[48] Thus, the conclusions are that the Kerr rotation spectrum of the 0Co/A/4Pd structure is determined to a great extent by the MO properties of spin-polarized Pd. The spectrum of 0Co/B/4Pd, in which the interface region is formed by the Co-rich alloy, differs significantly from both the 0Co/A/4Pd and the 1Co/5Pd spectra. The two-peak UV structure transforms into a broad minimum centered at 4.2 eV, and in the IR region the rotation becomes negative. The structure with a *C*-type interfacial layer is particularly interesting, as it can be obtained from the ideal 2Co/4Pd multilayer structure simply by interchanging the positions of every fourth Co and Pd atom in the neighboring interfacial Co and Pd layers. As a result, Co-rich Co_3Pd_1 and Pd-rich Co_1Pd_3 planar alloy layers appear around the border. The composition of the 0Co/C/2Pd MLS corresponds to that of 2Co/4Pd; however, it should be pointed out that the change of the interface microstructure leads to very large changes in the shape and magnitude of the MO spectra, as can be seen from the comparison of the 0Co/C/2Pd and 2Co/4Pd Kerr rotation spectra in Figs. 3a and 3b, respectively.

The Kerr rotation spectra are modified appreciably upon addition of one (see Fig. 3b) or two (see Fig. 3c) Co atomic planes to an MLS with an imperfect interface. In the supercells, the Co and Pd planes are separated by *A*-, *B*-, and *C*-type interfacial layers. The essential points as regards the modification of the spectra can be summarized as follows:

i) The amplitude of the spectra increases as the amount of Co increases. In the IR spectral range, the characteristic features of the Co spectrum become more pronounced.

ii) For the supercells containing one planar alloy of Co_1Pd_3 composition treated as an interface region, the change of the relative amplitudes of the characteristic peaks in the UV region upon addition of two Co atomic planes is clearly visible.

iii) For the supercells containing as an interface region a single Co_3Pd_1 atomic plane or two Co_3Pd_1/Co_1Pd_3 atomic planes, the main effect of increasing the number of Co atomic planes is a shift of the UV peak position to lower energy. This effect is accompanied by a narrowing of the bandwidth.

iv) The amplitudes of the spectra in the energy range above 4 eV are up to 100% higher than those of the ideal 2Co/4Pd and 3Co/3Pd MLS.

From the band-structure calculation results it follows that the Co and Pd electronic states in the alloy interface layers are strongly modified by the hybridization. As the volume in which the hybridization occurs is significantly larger in a MLS with an imperfect interface, the contribution of these hybridized states to the MO spectra increases compared to that for a MLS with an ideal interface. Hence, the similarity between the nCo/A/mPd MLS spectra and the spectra of Pd-rich CoPd alloys[48] becomes closer, especially for the MLS with a small Co sublayer thickness. Another effect of interfacial alloy formation is stronger—compared to that for the ideal MLS—spin polarization of the whole Pd spacer. The averaged magnetic moment per Pd atom calculated for

the different structures approaches values up to 80% larger than those for the ideal MLS models. One can expect that as a result of the increased magnetic moment induced on the Pd atoms, they will make larger contributions to the MO spectra. This can be clearly seen in the energy range below 2 eV, where the Kerr rotation spectra are very sensitive to the Pd contribution. As was established earlier,[48,49] the interband magnetooptical transitions in spin-polarized Pd give a positive Kerr rotation in the IR energy range, whereas the transitions between the electronic states with a large degree of admixture of Co 3*d* states result in a negative contribution to the Kerr rotation in this range, even when the Co states are considerably modified by the hybridization with Pd states. As a result of the two compensating contributions, the amplitude of the Kerr rotation spectra of the MLS is suppressed in the IR energy range and the rotation becomes positive in the case of 0Co/A/4Pd MLS (see Fig. 3a). As the number of Co atomic planes increases, their relative contribution to the MOKE spectra becomes higher and the Kerr rotation in the IR range becomes negative, which brings the spectra closer to the fcc Co spectrum, as can be seen in Fig. 3. A peak appearing at 1.5 eV in the MLS spectra is evidently related to the corresponding peak in the fcc Co spectrum.

As is seen in Fig. 3a, in the UV spectral range the contribution to the MLS spectra coming from the interfacial alloy region and strongly polarized Pd atomic planes is also rather large, contrary to the case for the ideal model of the MLS, and controls the spectral shape in that energy range. The observed overall increase of the rotation amplitude along the sequence 0Co/A/4Pd, 0Co/B/4Pd, and 0Co/C/2Pd is related to an increase of the relative Co content in the structures, which changes from 8% in 0Co/A/4Pd up to 33% in 0Co/C/2Pd. If one or two Co atomic planes are included in the structures, the relative contribution of Co to the total Kerr spectra increases. Hence, the shape of the spectra becomes closer to that of the fcc Co spectra, and the enhancement of the Kerr rotation peak amplitude in the UV range can be seen in Fig. 3b, c. It is worth pointing out, however, that the MOKE spectra are not simple superpositions of the contributions arising from the constituent sublayers.

It was found that of all the model MLS considered, the models in which the interfacial alloy layer is a Pd-rich alloy reproduce better the main spectral features of the experimentally studied Co/Pd MLS and the tendencies in the modification of the spectra as the thickness of the Co sublayer increases. In Fig. 4, the MOKE spectra calculated for the ideal 2Co/7Pd MLS and the $2Co/(Co_1Pd_3)/5Pd$ model structure are directly compared to the experimental spectra of the 3.5 Å Co/18.3 Å Pd MLS with sublayer thicknesses closest to the model structure. It is clearly seen that, if the interfacial alloying is taken into account, the characteristic shape of the measured spectrum with the shoulder in the UV range is reproduced well by the calculations. Also, the amplitude of the calculated Kerr rotation is close to the experimentally studied one, unlike the case of the ideal model 2Co/7Pd MLS with the same period, for which the amplitude is 50% smaller. The enhancement of the calculated amplitude and better agreement with the experiment can be observed also for the Kerr ellipticity spectra.

To study the effect of total interlayer intermixing on the

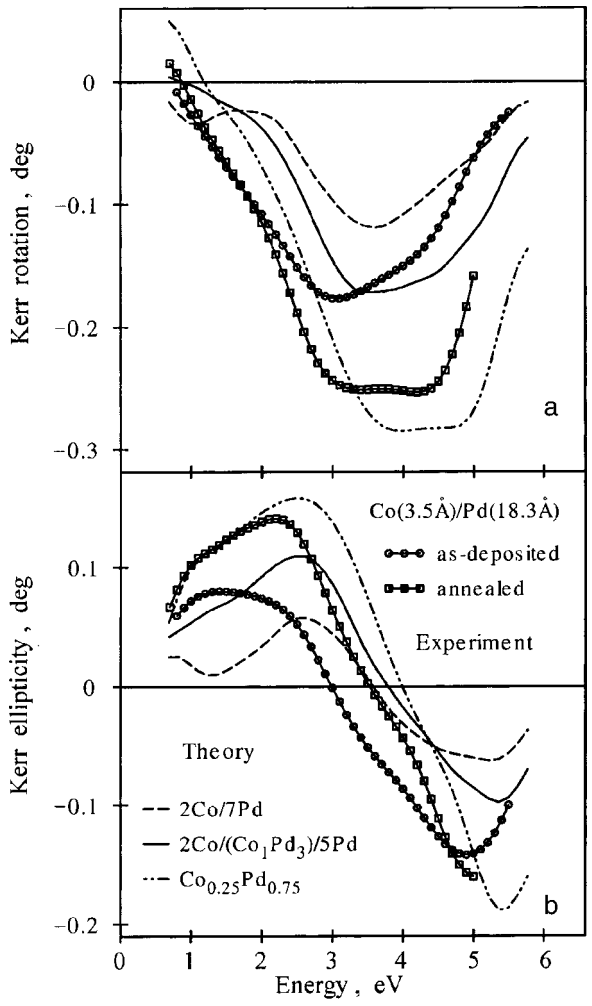

FIG. 4. Comparison of the measured and calculated polar Kerr rotation (a) and ellipticity (b) spectra of the as-deposited 3.5 Å Co/18.3 Å Pd MLS film and the model $2Co/(Co_1Pd_3)/5Pd$ as well as the ideal 2Co/7Pd MLS model. The spectra of the film annealed at 800 K and calculated for the model of fcc disordered $Co_{0.25}Pd_{0.75}$ alloy are included.[42]

MOKE spectra and as a final test of the assumed interface model, the 3.5 Å Co/18.3 Å Pd MLS film was annealed under high vacuum at 800 K for 5 h. At such high temperatures the diffusion processes are very intensive and the whole layered structure is uniformly homogenized, becoming a disordered fcc alloy film of effective composition $Co_{0.2}Pd_{0.8}$, as was controlled by our structural study. The huge changes of the MOKE spectra after annealing can be seen from Fig. 4. The Kerr rotation and ellipticity spectra amplitudes increase significantly, and the spectral shape become close to those observed for Co-Pd alloys of comparable composition.[48] The calculated MOKE spectra of disordered $Co_{0.25}Pd_{0.75}$ alloy taken from Ref. 48 are also included in Fig. 4 for comparison. As can be seen, the agreement of the calculated and measured Kerr rotation and ellipticity spectra of the alloyed structure is excellent (the systematic shifts of the spectra on the energy scale are of common nature for LDA-based calculations, as was discussed in Sec. 3.1.2.). Thus, on the basis of the results obtained for the Co/Pd MLS, the following conclusions have been reached:

i) the MLS studied have relatively sharp interfaces with a ''chemical thickness'' of the order of one atomic layer; and

ii) they can be well described by a model MLS structure with an ordered Pd-rich interfacial alloy.

In the real Co/Pd MLS the interface microstructure may be more complicated, and probably only partial chemical ordering occurs. As was inferred from the x-ray diffraction data, the Co/Pd MLS studied have well-defined layered structure. Nevertheless, some intermixing at the interface during the deposition of the samples is very probable. This effect leads, in turn, to higher induced spin polarization in a larger volume of Pd and makes the whole volume magnetooptically active. The results obtained allow us to explain the origin of the observed MOKE spectra of the MLS and to understand why the thickness of the so-called ''magnetic interface'' can be larger than that of the ''crystallographic'' one, as was recently reported for other Pd-based multilayered systems.[50] The conclusions are also consistent with the results derived from the phenomenological multireflection approach, not presented here, which indicate that the Pd spin polarization extends through a depth of the order of four Pd atomic layers.

In conclusion it should be pointed out that in the Co-Pd systems the MOKE is governed by the off-diagonal part of the optical conductivity tensor. It was found that the *ab initio* calculations performed for model Co/Pd MLS with sharp interfaces reproduced the main peculiarities of the experimental Co/Pd MOKE spectra only moderately well. It is shown that the main peculiarities and the tendencies in the modification of the MLS spectra with variation of the Co sublayer thickness are adequately reproduced when the alloying, even limited to one atomic plane, is taken into account. The MOKE spectra calculated for the model structures with ordered Co_1Pd_3 interfacial planes reproduce the measured spectra best. The results obtained demonstrate that interface microstructure plays a crucial role in the formation of the MOKE spectra of the Co/Pd layered structures.

3.2. Co_xPd_{1-x} alloys

In real MLS systems, chemical and structural disorder often occurs at the interface. These effects can be examined using model disordered alloys.

The description of the magnetooptical properties of a disordered system on a microscopic level and understanding of the effect of chemical order and crystal symmetry on these properties are of great importance. The most powerful approach to calculating the electronic structure of randomly disordered solids is the coherent potential approximation (CPA) in connection with the Korringa–Korr–Rostoker method of band structure calculation (KKR-CPA).[51] Within this formalism a quantitative description of such phenomena as magnetoresistance[52] and x-ray dichroism[53] has been obtained. In both cases the central quantity to be calculated is the optical conductivity tensor.[8] Unfortunately, techniques for dealing with that quantity for finite light frequencies in the optical regime have not yet been developed. For that reason the theoretical investigations of the optical and magnetooptical properties of disordered Co_xPd_{1-x} alloys in Ref. 48 was done using the supercell approximation. To test the theoretical approach, the MOKE spectra for a set of Co_xPd_{1-x} polycrystalline alloy films with $x=0.13$, 0.22, 0.31, and 0.44 have been also measured.

To investigate the influence of composition and local environment on the MO properties of disordered alloys, *ab initio* band-structure calculations for *ordered* Co-Pd alloys (Co_1Pd_{15}, Co_1Pd_{11}, Co_1Pd_7, Co_2Pd_{10}, Co_4Pd_{12}, Co_3Pd_9, Co_2Pd_6, Co_1Pd_3, and Co_1Pd_1) have been performed. This sequence corresponds to a variation of the Co content in the range of 6–50%. For Co_1Pd_1 and Co_1Pd_3 alloys the AuCu ($L1_0$) and $AuCu_3$ ($L1_2$) structures, respectively, were assumed. The supercells for all the other alloys except Co_1Pd_{11} consist of two or more adjacent fcc unit cells with Co and Pd atoms distributed over nonequivalent atomic positions according to the specific alloy composition. For the Co_1Pd_7 and Co_1Pd_{15} alloys both cubic and tetragonal supercells were constructed, whereas for the Co_1Pd_{11} alloy a hexagonal unit cell was used. The lattice constant for all the alloys has been chosen to correspond to the experimental data.[54]

As was mentioned above, the magnetooptical effects are determined by the dielectric tensor components $\varepsilon_{\alpha\beta}$. This tensor can be represented as a sum $\varepsilon_{\alpha\beta}=\varepsilon^s_{\alpha\beta}+\varepsilon^a_{\alpha\beta}$ of two parts which are symmetric (optical) and antisymmetric (magnetooptical) with respect to the magnetization direction. That is, the relations $\varepsilon^s_{\alpha\beta}(\mathbf{M})=\varepsilon^s_{\alpha\beta}(-\mathbf{M})$ and $\varepsilon^a_{\alpha\beta}(\mathbf{M})=-\varepsilon^s_{\alpha\beta}\times(-\mathbf{M})$ hold, where $\mathbf{M}$ denotes the magnetization vector. The antisymmetric part $\varepsilon^a_{\alpha\beta}$ can be expressed as $\varepsilon^a_{\alpha\beta}=ie_{\alpha\beta\gamma}g_\gamma$, where $e_{\alpha\beta\gamma}$ is the antisymmetric pseudo-tensor and g_γ is a component of the gyration vector $\mathbf{g}$.[55]

For most materials the relation $|\mathbf{g}|\ll\det\|\varepsilon^s_{\alpha\beta}\|$ holds and expressions for all nonreciprocal magnetooptical effects, measured usually as a difference quantity with respect to a reversal of the magnetization, can be decomposed into the product of the complex number $\mathbf{g}\hat{\mathbf{g}}$ and some function depending on the optical part of the dielectric tensor $\varepsilon^s_{\alpha\beta}$ as well as the light propagation and magnetization directions (see, e.g., Ref. 25).

It should be noted that although the optical part of the dielectric tensor may play a crucial role in the MO spectra formation, as, for example, in CeSb,[56] or may exhibit a noticeable anisotropy,[57] this is not the case for the Co-Pd compounds investigated here. It was found that in the energy range $0.5<h\nu<6$ eV the calculated components $\varepsilon^s_{\alpha\beta}$ are smooth and exhibit only a very weak dependence on both the chemical ordering and the alloy composition. Moreover, for the uniaxial model structures the optical anisotropy defined as $\delta_A=(\varepsilon_\perp-\varepsilon_\parallel)/\epsilon$ does not exceed 5%. Here we denoted $\epsilon=1/3(2\varepsilon^s_\perp+\varepsilon^s_\parallel)$, where $\varepsilon^s_\perp$ and $\varepsilon^s_\parallel$ stand for the main optical dielectric tensor components corresponding to the light polarization perpendicular and parallel to the n-fold symmetry axis (c) of the crystal. Thus, all features of the MO spectra of the Co-Pd compounds are determined by the function $g(\omega)$.

As was mentioned above, our calculations involved both cubic and uniaxial models. For the crystal with cubic symmetry the dependence of g on the magnetization direction $\hat{\mathbf{M}}$ is negligible,[84] whereas for uniaxial crystals it can be noticeable. Uspenskii *et al.*[58] have shown that, up to the second order the in spin-orbit coupling strength, this dependence can be expressed in terms of the gyration vectors $g_\parallel$ and $g_\perp$ calculated for the cases $\hat{\mathbf{M}}\|c$ and $\hat{\mathbf{M}}\perp c$, respectively:

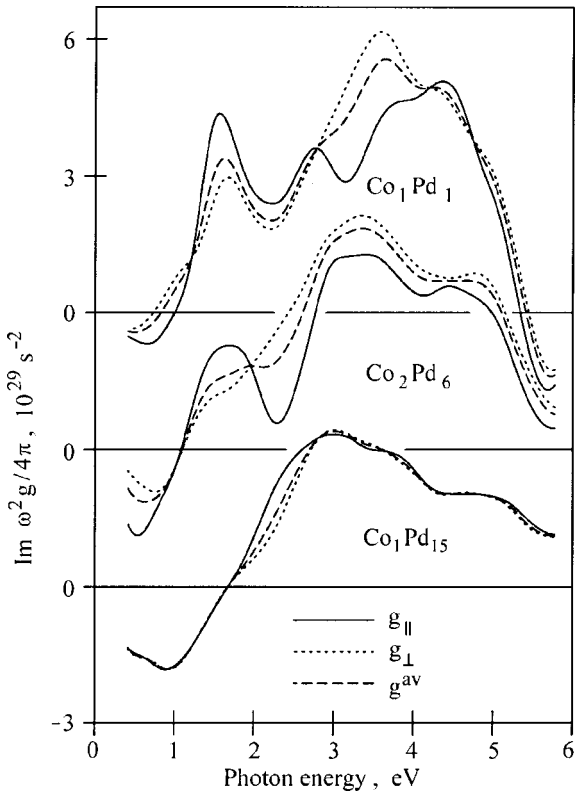

FIG. 5. Orientation dependence of the Im $\omega^2 g(\omega)$ spectra for the Co_1Pd_1, Co_2Pd_6 and Co_1Pd_{15}. All spectra were convoluted with a Lorentzian of width 0.5 eV.[48]

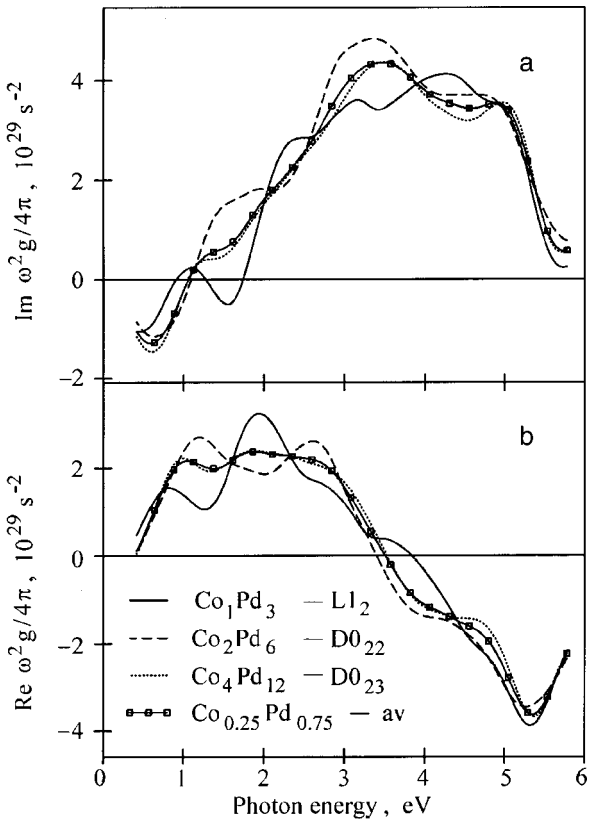

FIG. 6. Effect of the chemical order on the calculated $\omega^2 g(\omega)$ spectra of $Co_{0.25}Pd_{0.75}$ alloy.[48]

$$\mathbf{g}=\hat{\mathbf{M}}(g_{\parallel}\cos^2\theta+g_{\perp}\sin^2\theta)+\hat{\mathbf{n}}(g_{\parallel}-g_{\perp})\sin\theta\cos\theta, \tag{13}$$

where $\hat{\mathbf{n}}$ stands for the unit vector orthogonal to $\hat{\mathbf{M}}$ and lying in the same plane as $\hat{\mathbf{M}}$ and $\mathbf{c}$, and θ is the angle between the magnetization vector $\mathbf{M}$ and n-fold symmetry axis c.

Figure 5 presents the calculated $\mathrm{Im}\,\omega^2 g_{\parallel}(\omega)$ and $\mathrm{Im}\,\omega^2 g_{\perp}(\omega)$ spectra for a selected set of uniaxial crystals. One can see that for Co_1Pd_1 and Co_2Pd_6 the orientation dependence of the gyration vector is rather strong and manifests itself in changes of the relative magnitude and energy location of both the IR and UV maxima. The feature at 2.5 eV in the $g_{\parallel}(\omega)$ spectra disappears completely for $\mathbf{M}\perp c$. For the more diluted tetragonal Co_1Pd_7 alloy the orientation dependence of the $g(\omega)$ spectra was found to be relatively weak, and it practically disappears for Co_1Pd_{15} (see Fig. 5). The same tendencies were found also for the $\mathrm{Re}\,\omega^2 g(\omega)$ spectra.

To take into account the effects of random orientation of microcrystals in the alloys studied, we have to average Eq. (13) over different relative orientations of the crystal axes and magnetization direction, which gives

$$g^{\mathrm{av}}(\omega)=\frac{1}{3}[2g_{\perp}(\omega)+g_{\parallel}(\omega)]. \tag{14}$$

The main effect of the averaging (see Fig. 5) on the Co_1Pd_1 spectrum is a change of the band shape in the UV range as compared to the spectrum calculated with the magnetization directed along the c axis. The position of the main UV maximum shifts to lower energy and in Co_2Pd_6 the band becomes broader. In both alloys the structure at ~1.5 eV becomes less pronounced.

To study the dependence of the MO spectra on chemical ordering, let us consider the results for alloys with 1:3 stoichiometry. Calculations were done for the cubic $L1_2$ phase and for the tetragonal $D0_{22}$, $D0_{23}$, Co_3Pd_9, and second kind of Co_4Pd_{12} supercells. Tetragonal supercells Co_3Pd_9 and Co_4Pd_{12} consisting of one and two more central planes, respectively, as compared to the $D0_{22}$ structure were used. All the alloys have the same nominal composition of $Co_{0.25}Pd_{0.75}$ but differ in the symmetry and local environment of the Co and Pd sites. While all these structures have identical first neighbor coordination (each Co has 12Pd neighbors and each Pd has 8Pd+4Co neighbors), there are differences in the second atomic shell. For the $L1_2$, $D0_{22}$, and $D0_{23}$ cells each Co has 6Co, 4Co+2Pd, and 5Co+1Pd second neighbors with local site symmetry O_h, D_{4h}, and C_{4v}, respectively. The atomic coordination around Pd in the second shell consists of 6Pd for the $L1_2$ structure, while there are two inequivalent Pd sites for $D0_{22}$ (with 6Pd and 2Co+4Pd) and for $D0_{23}$ (with 6Pd and 1Co+5Pd). These three structures will be taken as basic because the other structures studied, like Co_3Pd_9 and Co_4Pd_{12}, are composed of various numbers of the above described nonequivalent Co and Pd sites.

In Fig. 6 the spectra of the imaginary (a) and real (b) parts of $\omega^2 g(\omega)$ are shown. For $Co_2Pd_6(D0_{22})$ and $Co_4Pd_{12}(D0_{23})$ alloys $\omega^2 g^{\mathrm{av}}(\omega)$ is presented. As a result of the change of the atomic arrangement and accompanied lowering of the symmetry of the local sites along the sequence

$L1_2-D0_{22}-D0_{23}$, the spectra become less structured and the peaks broaden, as can be seen, for example, by comparing the $\mathrm{Re}\,\omega^2 g(\omega)$ spectra in the spectral range up to 3 eV. This effect apparently arises from the fact that lowering of the local symmetry of atomic sites generally leads to the appearance of an increasing number of nonequivalent interband transitions, with their contributions to the MO spectra spread out over a wider energy range. It was found that the resulting $\omega^2 g^{\mathrm{av}}(\omega)$ spectra calculated for Co_3Pd_9 and Co_4Pd_{12} alloys can be well reproduced by averaging the basic $L1_2$, $D0_{22}$, and $D0_{23}$ spectra, weighted by the corresponding numbers of equivalent sites in these structures.

To estimate the $\omega^2 g^{\mathrm{av}}(\omega)$ spectrum of the disordered $Co_{0.25}Pd_{0.75}$ alloy it is necessary to adopt a procedure of averaging the spectra over possible atomic arrangements. Here the simplest assumption was made: that the basic cells appear with equal probabilities and that the contribution of each cell to the spectrum is proportional to its number of atomic sites. On this basis the averaged spectrum was obtained as the weighted average of the $L1_2$, $D0_{22}$, and $D0_{23}$ spectra with weights of 1, 2, and 4, respectively. As a result of the configuration averaging, the spectrum becomes less structured and is closet to the spectrum of the $D0_{23}$ structure (see Fig. 6). It can be concluded that for the alloys studied the local atomic arrangement and site symmetry control the MO properties.

To discuss the composition dependence of the MO properties of the alloys under consideration, we focus here on the polar Kerr rotation spectra, because they are the quantities measured directly in the experiment. If the optical anisotropy δ_A is small, the complex Kerr rotation angle, neglecting the second-order quantities (δ_A^2, $\delta_A g$, and g^2), has the form

$$\phi_K=\vartheta_K+i\,\eta_K=g/[\sqrt{\epsilon}(1-\epsilon)]. \tag{15}$$

Equation (15) is linear with respect to g and this allows us to use for the uniaxial systems g^{av} instead of g. To take into account finite-lifetime effects the calculated spectra were convoluted with a Lorentzian of width 1.0 eV. Calculated polar Kerr rotation and ellipticity spectra of Co-Pd alloys of different compositions are shown, together with experimentally measured ones, in Fig. 7. To take into account the decrease of Curie temperature for diluted alloys, all experimental spectra have been scaled with the factor $M_{4.2}/M_{300}$, where $M_{4.2}$ and M_{300} are the magnetization at 4.2 K and 300 K, respectively. Both experimental and theoretical data exhibit the same features. As the Co content diminishes, the magnitude of the rotation angle in the energy range 2.5–4.5 eV decreases. The shoulder at ~1.5 eV, clearly seen in the ϑ_K spectrum of Co_1Pd_1 alloy, disappears completely in diluted alloys, and the Kerr rotation changes sign below ~2 eV. In the UV range, the peak centered at 4 eV in Co_1Pd_1 transforms into a broad two-peak structure. Also, a shift of the Kerr ellipticity zero-crossing to higher energy with decrease of Co content is observed, as well as a diminishing of the amplitude at ~5 eV. However, the calculated peak positions of both the Kerr rotation and ellipticity are shifted slightly to higher energies with respect to the experimental ones. The discrepancy is apparently due to a drawback of the LDA-based calculations which has recently been discussed extensively in the literature.[74,82]

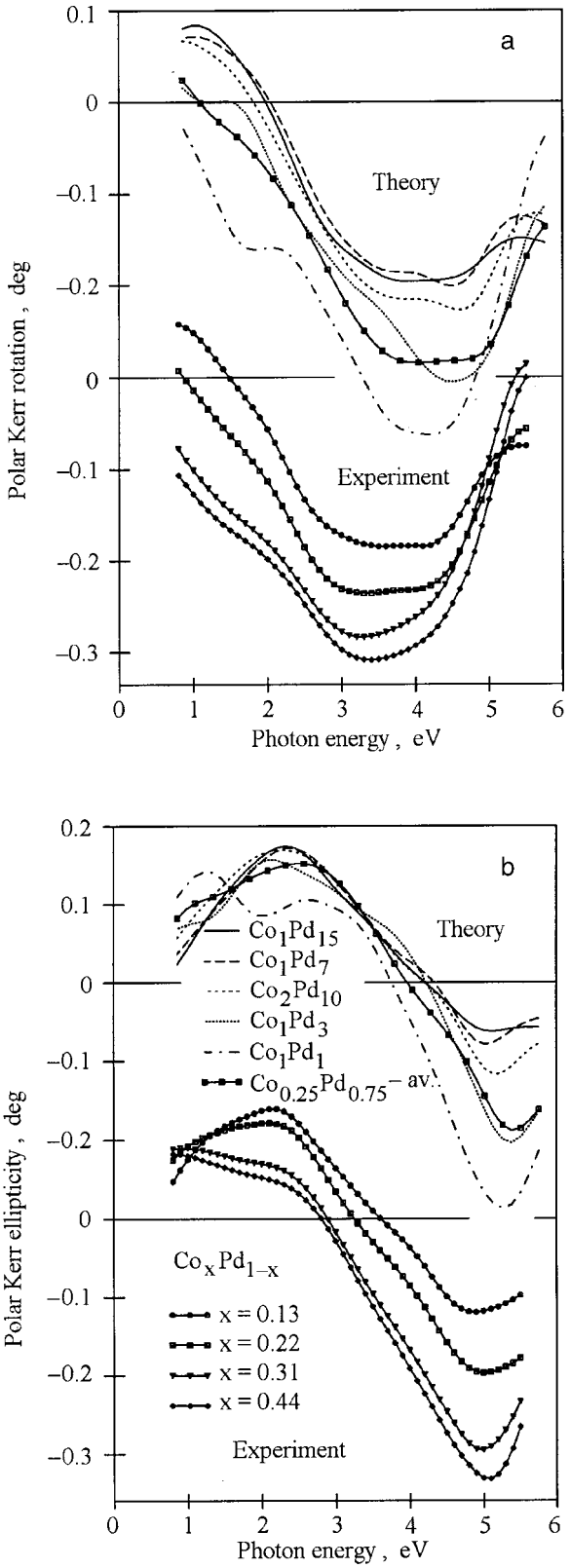

FIG. 7. Comparison of the calculated and experimental polar Kerr rotation (a) and ellipticity (b) spectra for different compositions of the Co-Pd alloys.[48]

It is interesting to note that the calculated MOKE spectra of Co_2Pd_{10}, Co_1Pd_7, Co_1Pd_{11}, and also Co_1Pd_{15} alloys are close to each other, although the Co content in the alloys decreases from 16.5% to as low as 6%. From this one can conclude that the MOKE spectra of diluted Co-Pd alloys are

determined to a great extent by the MO properties of spin-polarized Pd. This is in line with the relatively large average Pd magnetic moment obtained from the calculations (e.g., $0.24\mu_B$/atom for Co_1Pd_{15}), which depends weakly on Co content in the Co-Pd alloys.

It should be noted that the theoretical spectra shown in Fig. 7, except for the spectrum of $Co_{0.25}Pd_{0.75}$, have been obtained for one specific atomic arrangement. In Fig. 7 the theoretical spectrum for $Co_{0.25}Pd_{0.75}$, obtained as the weighted average of the spectra for $L1_2$, $D0_{22}$, and $D0_{23}$ structures according to the procedure described above, is presented. As a result of the averaging over different atomic configurations, the MOKE spectrum of $Co_{0.25}Pd_{0.75}$ becomes less structured, and the minimum in the polar Kerr rotation spectrum, centered at about 4.5 eV in the ordered $Co_1Pd_3-L1_2$, transforms into a broad structure like that observed in the measured spectrum of the disordered $Co_{0.22}Pd_{0.78}$ alloy film.

It can be concluded that the MOKE calculations in which the effects of random orientation of microcrystals and/or chemical disorder are taken into account reproduce well the experimental spectra of the Co-Pd disordered alloys and the dependence of the spectra on the composition. The optical part of the dielectric tensor of these compounds depends very weakly on both the alloy composition and chemical ordering and does not show noticeable anisotropy for the uniaxial crystals. Moreover, its frequency dependence is structureless, and all features in the magnetooptical spectra are determined by the gyrotropic part of the dielectric tensor, which exhibits a considerable orientation anisotropy increasing with the Co content.

4. MAGNETOOPTICAL PROPERTIES OF Co/Pt MULTILAYERS

4.1. Experimental results

A detailed experimental study of the MO properties of Co/Pt MLS using MOKE spectroscopy has been done in the Ref. 74 for the series of sputter-deposited MLS listed in Table III.

The measured polar Kerr rotation and ellipticity spectra of the Co/Pt MLS studied are shown in Fig. 8. All of the samples measured possess well-defined MOKE hysteresis curves with saturation characteristics, and all of the θ_K and η_K spectra were measured under saturation conditions. The Kerr rotation spectra display two well-known features. There is a prominent broad, negative peak in the UV region and a smaller one in the IR part. The IR peak, centered at 1.5 eV, is most prominent for a pure Co thick film,[59] and for MLS its amplitude continuously diminishes with decreasing MLS Co sublayer thickness. The UV peak varies slightly in energy position from 4.1 eV to 3.9 eV with increasing Co sublayer thickness. The amplitude of the UV peak exceeds that of the peak centered at 3.7 eV of the pure Co film and depends relatively weakly on the composition of the MLS studied.

TABLE III. The parameters of the Co/Pt MLS studied. No. is the sample number, N_{layers} is the number of bilayers, $t_{Co}(t_{Pt})$ is the measured thickness of the Co (Pt) sublayer.[74]

No.	N_{layers}	t_{Co}, Å	t_{Pt}, Å
1	50	4.6	13.6
2	47	5.8	15.2
3	43	6.9	12.5
4	40	9.0	14.4
5	33	18.9	14.3

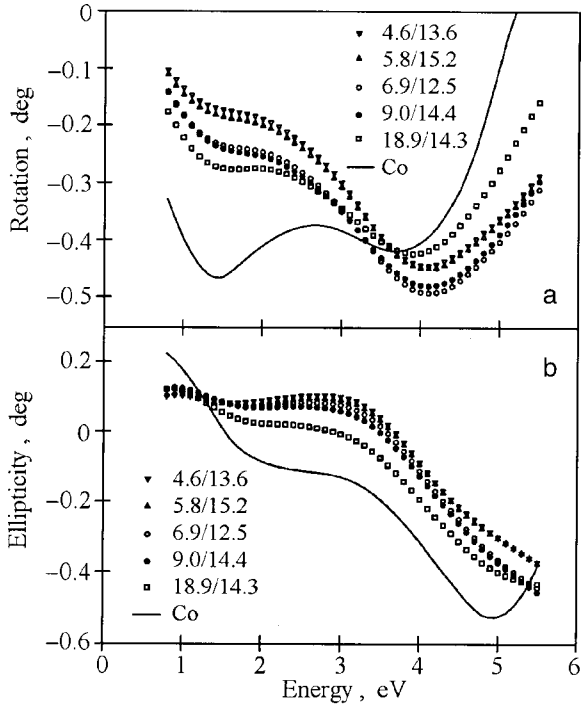

FIG. 8. Experimental polar Kerr rotation (a) and ellipticity (b) spectra of Co/Pt MLS and fcc Co film. Sublayer thicknesses marked in the pattern are given as $t_{Co}(Å)/t_{Pt}(Å)$.[74]

The characteristic feature in the Kerr ellipticity spectra is the shift of the zero-crossing from 1.5 eV in the pure Co film to 3.7 eV in MLS with decreasing Co sublayer thickness and the formation of a positive peak around 3 eV. The prominent minimum of the Kerr ellipticity centered at 4.9 eV observed in the Co film is presumably shifted in position to the photon energy region $\hbar\omega > 5.5$ eV, inaccessible in the present experiment.

The optical properties of the MLS, in the form of the spectral dependencies of the diagonal component of the effective optical conductivity tensor σ_{xx}, are shown for the real $\sigma_{xx}^{(1)}$ and imaginary part $\sigma_{xx}^{(2)}$ in Figs. 9a and 9b, respectively. For clarity the spectra of only three samples are shown in the pictures; the other MLS spectra lie in between them. As is seen from the results, generally there is little difference in the absorptive part of the optical conductivity $\sigma_{xx}^{(1)}$ for all MLS studied. The magnitudes of the spectra roughly scale with the thickness of Co sublayers. The corresponding spectra of thick Co and Pt films prepared by the same technique are shown for comparison. It can be observed that the $\sigma_{xx}^{(1)}(\omega)$ curves for the MLS do not lie between those for Co and Pt in the energy range 2–5.5 eV. Several reasons can be considered for this difference. A common problem in metal optics is the great sensitivity of the optical constants to the state of the sample surface.[60]

Another cause can be the fact that the optical properties of thick metal films are slightly different from the ones for

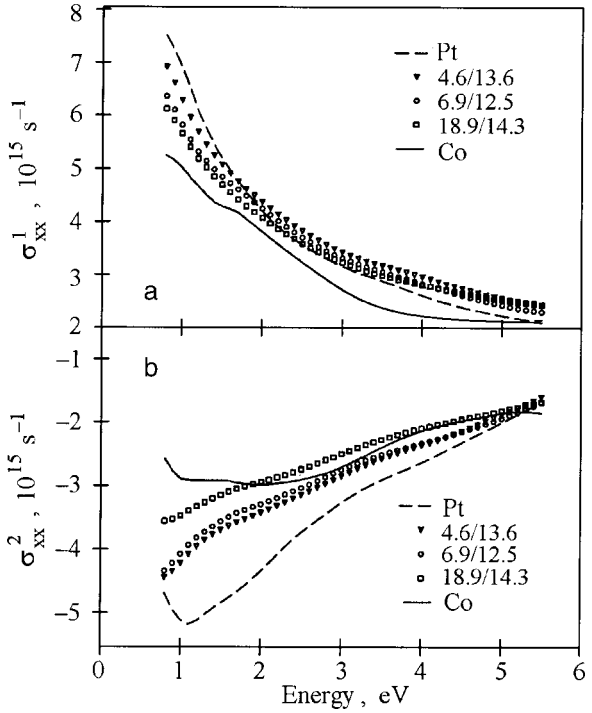

FIG. 9. The absorptive (a) and dispersive (b) parts of the diagonal components of the conductivity tensor for Co/Pt MLS and Co and Pt films, determined from the ellipsometric measurements.[74]

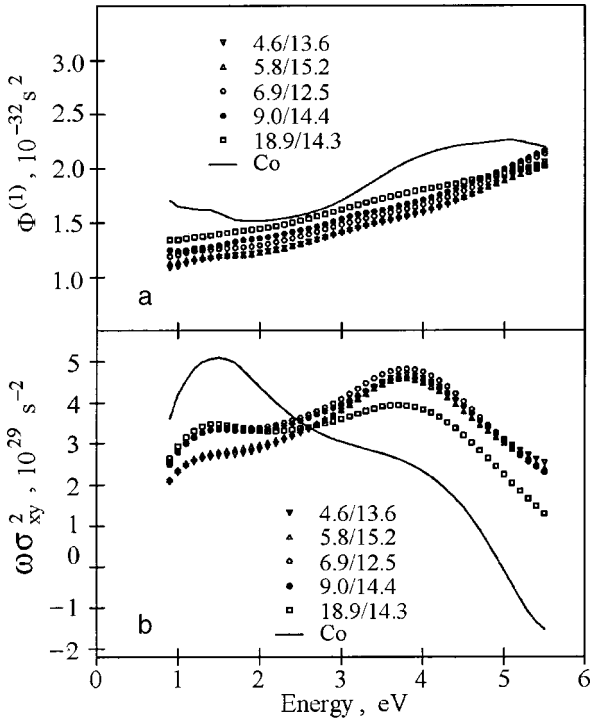

FIG. 10. The contribution to the Kerr rotation spectra from the diagonal part of the conductivity tensor (see text) (a) and the absorptive part of the off-diagonal component $\omega\sigma_{xy}^{(2)}$ (b), determined from the ellipsometric and the complex polar Kerr angle measurements for Co/Pt MLS and Co film.[74]

the MLS constituent sublayers.[61] In other words, for individual layer thicknesses of a few atomic monolayers the effective dielectric constants of the medium differ from the dielectric constants of the bulk or thick-film material. Besides, the response of an ultrathin medium to an electromagnetic wave is substantially influenced by the electronic interaction with adjacent layers.

The spectra of the dispersive part of the optical conductivity tensor $\sigma_{xx}^{(2)}$ are also weakly dependent on the MLS composition and lie in between the spectra for thick Co and Pt films.

To separate the contribution to the MOKE coming from the diagonal and off-diagonal conductivity tensor components the function $\Phi = 4\pi[\omega^2(\varepsilon_{xx}-1)\sqrt{\varepsilon_{xx}}]^{-1}$ has been evaluated from the optical measurements. The real part of the function $\Phi^{(1)}$ is shown in Fig. 10a. It has been found that for the compounds under consideration, the product of $\Phi^{(1)}$ and $\omega\sigma_{xy}^{(2)}$ gives the main contribution (>80%) to the polar Kerr rotation spectra. It should be noted that this function is nearly flat over the investigated spectral region for all the MLS studied and depends weakly on their composition. On the contrary, the shape and amplitude of the $\Phi^{(1)}$ spectrum change significantly in the case of the Co film. As a consequence, the absorptive part of the off-diagonal component of the conductivity tensor, $\omega\sigma_{xy}^{(2)}$, presented in Fig. 10b for the MLS studied, is in its overall form unexpectedly similar to that of the polar Kerr rotation, whereas for the case of pure Co the shape of the polar Kerr rotation and $\omega\sigma_{xy}^{(2)}$ differ significantly. Inspection of these curves shows that the presence of Pt leads to strong enhancement of $\omega\sigma_{xy}^{(2)}$ in the UV range. The measured enhancement of the polar Kerr rotation is much smaller because of the corresponding increase of the diagonal part of σ (see Fig. 10a).

Thus it can be concluded that the peak observed in the IR part of the Co/Pt MLS polar Kerr rotation spectra can be related mainly to the MO activity of Co. On the contrary, the peak observed in the UV region is for pure Co connected rather with the peculiarities in the diagonal part of the conductivity tensor, while for Co/Pt multilayers it is governed by the off-diagonal component of σ and originates from the Co-Pt interaction at the MLS interface.

The multilayer MOKE spectra measured are qualitatively similar to the spectra which have been published for Co/Pt MLS prepared by different techniques and for random fcc Co-Pt alloys[21,22,24,62–64] and all exhibit similar MOKE enhancement in the UV region.

4.2. Theoretical results and discussions

In order to reproduce the electronic structure of the interlayer interface, band-structure calculations of some model ordered Co-Pt alloys and MLS with various layer thicknesses were performed in Ref. 74. An *abcabc* stacking sequence of close-packed planes corresponding to the fcc-(111)-texture was assumed for all the MLS structures except for 1Co/1Pt for which the *ababab* stacking was also studied. No attempt has been made to optimize the interlayer spacing, which was taken to be corresponding to the ideal c/a ratio. Ordered $CoPt_3$ and the Co_3Pt alloys were calculated in the Cu_3Au crystal structure, while for the CoPt alloy the AuCu structure was used. For all the compounds the mean volume per atom was chosen to be equal to the average of the atomic volumes of pure fcc Pt and hcp Co, with the experimental lattice constants. The radii of the Co and Pt atomic spheres were chosen equal to 1.46 Å.

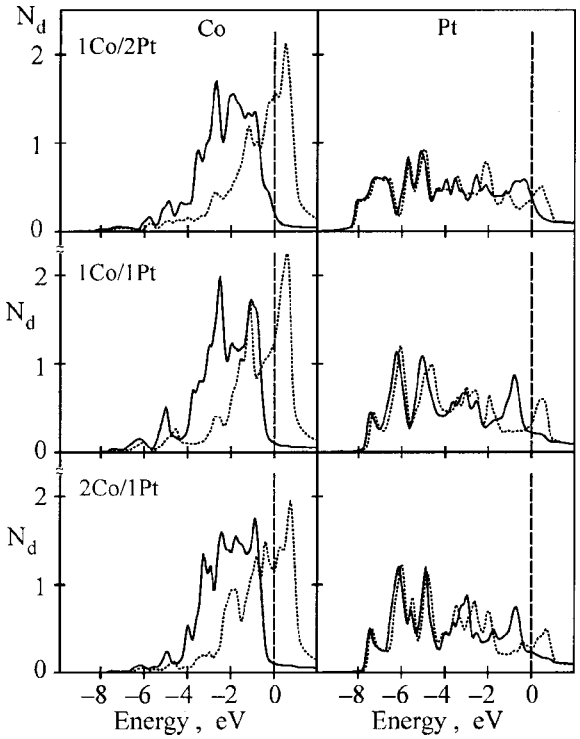

FIG. 11. Spin- and site-projected densities of d states [in units of states/(atom·spin·eV)] for Co and Pt in 1Co/1Pt, 2Co/1Pt, and 1Co/2Pt multilayers. Full and dotted lines correspond to majority and minority spin states, respectively; the dashed line marks the Fermi energy.[74]

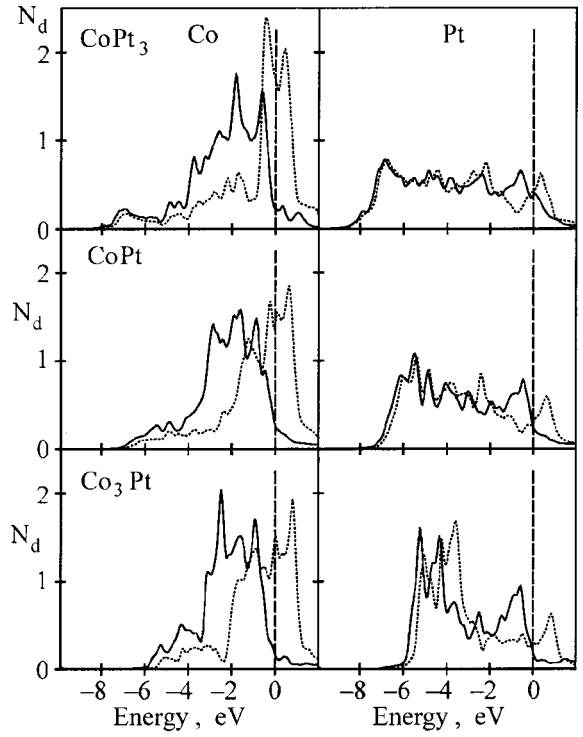

FIG. 12. Spin- and site-projected densities of d states (states/(atom·spin·eV)) for Co and Pt in Co_3Pt, CoPt, and $CoPt_3$ alloys. The solid and dotted lines correspond to majority and minority spin states, respectively.[74]

The characteristic feature of the electronic structure of Co-Pt multilayers and alloys is the strong hybridization of Co $3d$ and Pt $5d$ states, the later being much more delocalized. Figure 11 shows the spin- and site-projected densities of the electronic states (DOS) for Co and Pt site in 2Co/1Pt, 1Co/1Pt, and 1Co/2Pt multilayers. The valence band width in the MLS is mainly governed by Pt $d-d$ hybridization in the close-packed planes consisting of Pt atoms and varies moderately with an increase of the Pt sublayer thickness. The strong spin-orbit interaction in the Pt atomic sphere results in splitting of the $d_{3/2}$ and $d_{5/2}$ states, with the energy difference between their centers being $\sim$1.5 eV. Inside the Co atomic sphere the effect of the spin-orbit coupling is much weaker than the effect of the effective magnetic field. The centers of both Pt $d_{3/2}$ and $d_{5/2}$ states lie at lower energies than the centers of the corresponding Co states. As a result of the Co $d-$Pt d hybridization, the electronic states at the bottom of the valence band are formed mainly by Pt states, while the states in the vicinity of the Fermi level (E_F) have predominantly Co d character with an admixture of Pt d states. The hybridization with the exchange-split Co d states leads to a strong polarization of the Pt d states near E_F. The resulting difference in occupation numbers for Pt states with the opposite spin projections gives rise to a comparatively large spin magnetic moment at the Pt site.

In the case of the 4Co/2Pt, 2Co/4Pt, and 1Co/5Pt MLS the DOS curves for Co and Pt sites at the interface are similar to the curves shown in Fig. 11. The DOS projected to a site in the interior of the sublayer is close to that of the corresponding bulk metal.

Calculated spin- and site-projected DOS curves for ordered Co_3Pt, CoPt, and $CoPt_3$ alloys are shown in Fig. 12. As compared to the Co/Pt MLS, the electronic structure of the alloys depends much more strongly on the alloy composition. Variation in the relative positions of the Co and Pt d bands affects the Co $d-$Pt d hybridization. The valence band width is larger in the Pt-rich alloys because of the larger number of Pt nearest neighbors surrounding the Pt site.

The calculated spin m_s and orbital m_l magnetic moments of the Co-Pt multilayers and alloys are summarized in Table IV. Both the spin and orbital moments at the Co site in the MLS are bigger than in bulk hcp Co with the experimental

TABLE IV. Calculated spin m_s and orbital m_l magnetic moments of the Co-Pt multilayers and alloys. Values in parentheses correspond to the atoms in the layer below the interface. The magnetic moments of hcp Co with the experimental lattice constant $a=2.507$ Å are also given.[74]

	$m_s(\mu_B/\text{atom})$		$m_l(\mu_B/\text{atom})$	
System	Co	Pt	Co	Pt
hcp Co ($a=2.507$Å)	1.559		0.079	
hcp Co	1.716		0.130	
fcc Co	1.731		0.115	
2Co/1Pt	1.776	0.183	0.098	0.019
1Co/1Pt	1.752	0.255	0.089	0.028
1Co/2Pt	1.880	0.207	0.099	0.022
4Co/2Pt	1.810	0.192	0.103	0.018
	(1.738)		(0.104)	
2Co/4Pt	1.765	0.154	0.095	0.016
		(0.049)		(0.001)
1Co/5Pt	1.869	0.175	0.090	0.018
		(0.058)		(0.006)
Co_3Pt	1.735	0.339	0.087	0.083
CoPT	1.681	0.321	0.090	0.048
$CoPt_3$	1.607	0.199	0.027	0.035

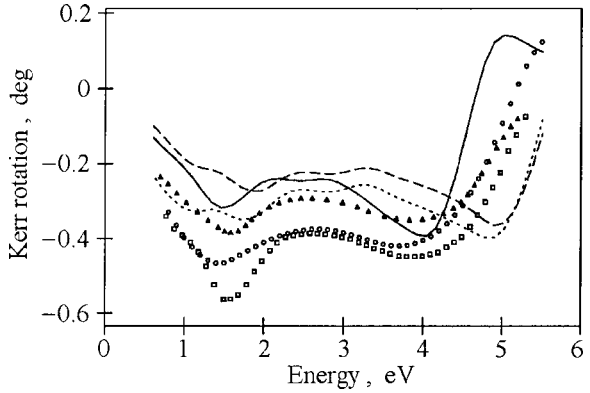

FIG. 13. Experimental and theoretical polar Kerr rotation spectra of Co.[74] The theoretical Kerr rotation spectra of fcc Co calculated using the experimental lattice constant and with the plasma frequency in the Drude term taken from the calculations (dashed curve), with $\hbar\omega_p = 5$ eV (dotted curve), and calculated using the same lattice constant as for the Co/Pt MLS (solid curve). Experimental spectra are shown by circles (present work), squares (Ref. 68), and triangles (Ref. 21).

lattice constant. Nevertheless, from a comparison with the values of m_s and m_l calculated for either hcp or fcc Co with the lattice constant used for the MLS it follows that the enhancement of the moments is mainly due to the lattice expansion. In contrast to the case of the MLS, the Co and Pt magnetic moments in the Co-Pt alloys decrease with increasing Pt content.

When studying the MO properties of the complex Co-Pt compounds it is natural to consider as a reference point the properties of pure Co.[65–67] The calculated energy dependence of the polar Kerr rotation angle of fcc Co with the lattice constant $a = 3.539$ Å corresponding to the experimental value for hcp Co is shown in Fig. 13 (dashed line). A comparison with the experimental data[21,68] shows that the calculations reproduce correctly the overall shape of the spectra but the UV peak is shifted by about 1 eV to higher energies. The discrepancy is similar to that observed in the theoretical Kerr rotation spectra of Ni[85,86] and is apparently due to a failure of the LSDA to describe correctly the width and the spin splitting of d bands in ferromagnetic $3d$ metals. Better agreement with the experiments is obtained for the Kerr rotation calculated with a larger lattice constant $a = 3.734$ Å, which is equal to the value chosen for all the model MLS studied (see the solid line in Fig. 13). The increase of the lattice constant results in a narrowing of the d band and, consequently, in an energy scaling of the calculated spectrum. The same tendency has been observed not only for pure Co but also for Co-Pt alloys and multilayers.

Although the lattice expansion removes the shift of the peaks, the calculated amplitude of the peak at 2 eV remains smaller than the experimental one. To elucidate the reason for the discrepancy in amplitudes, the dependence of the MOKE spectra on the intraband part of the conductivity tensor was examined.[74] It was found that in the case of pure Co the Kerr rotation is rather sensitive to the values of γ and ω_p^2 for energies up to 5 eV. Variation of the values changes the amplitude and the position of the UV peak as well as of the peak at 2 eV. The sensitive effect of the Drude term on the UV peak is due to the interband contribution to σ_{xx} being small in this energy range. Thus, although the absolute values of the intraband conductivity are small, its relative contribution is significant. The calculated plasma frequency of hcp Co with the experimental lattice constant was found to be 7.2 eV, while the experimental value for the hcp Co single crystal is ~5 eV.[57] Such a discrepancy is in agreement with the previous observation[69] that the calculated values of ω_p are, as a rule, 20–50% higher than the experimental values. The polar Kerr rotation calculated with $\hbar\omega_p = 5$ eV is shown by the dotted line in Fig. 13. The use of the smaller value of ω_p leads to a better agreement with the experiment. Nevertheless, it was not possible to achieve close agreement with experiment in the IR range by varying the Drude constants over reasonably wide limits. It has been found that for Co-Pt multilayers and alloys the dependence of the MOKE on the intraband contribution is much weaker, and in the following we use the calculated values of ω_p to evaluate the intraband conductivity.

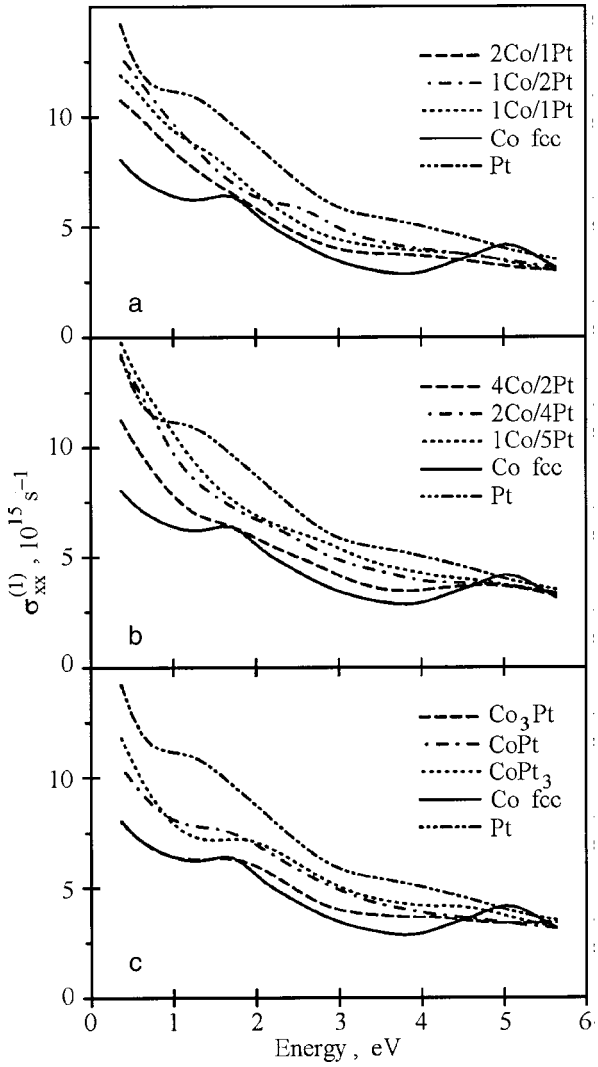

FIG. 14. Theoretical $\sigma_{xx}^{(1)}$ spectra of the Co-Pt multilayers (a, b) and alloys (c).[74]

Theoretical results for the absorptive part of the conductivity tensor $\sigma_{xx}^{(1)}$ for fcc Co, Pt, and some model Co-Pt multilayers and alloys are shown in Fig. 14. For energies higher than 1.5 eV the $\sigma_{xx}^{(1)}$ curves of the MLS and the alloys have similar energy dependence and fall within the range between

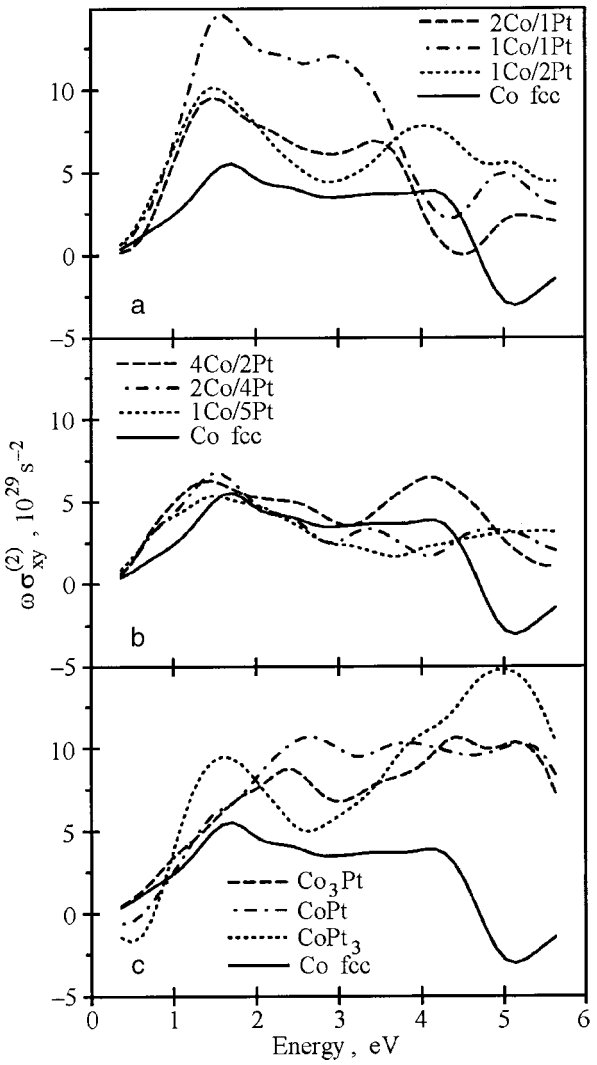

FIG. 15. Theoretical $\omega\sigma_{xy}^{(2)}$ spectra of the Co-Pt multilayers (a, b) and alloys (c).[74]

the $\sigma_{xx}^{(1)}$ curves of bulk Co and Pt, the conductivity of Co-rich MLS being closer to $\sigma_{xx}^{(1)}$ of Co.

The calculated dependence of $\sigma_{xx}^{(1)}$ on Co contents correlates well with the data obtained from the ellipsometric measurements of Co/Pt multilayers with different Co layer thickness. Although the calculations give $\sigma_{xx}^{(1)}$ of a higher amplitude than the experimental data, the theoretical results reproduce the changes of $\sigma_{xx}^{(1)}$ with the variation of the Co sublayer thickness. Of all the MLS considered, only $\sigma_{xx}^{(1)}$ of 4Co/2Pt has a subtle feature at ~5 eV corresponding to bulk Co. The fact that the σ_{xx} curves of the Co-Pt compounds of different composition and of different chemical ordering have similar shapes with no pronounced features suggests that, unlike the case of bulk Co, the two-peak structure of the polar Kerr rotation spectra of Co/Pt MLS comes from the energy dependence of the off-diagonal part of the conductivity tensor.

The results of the calculations of the absorptive part of $\omega\sigma_{xy}$ of Co-Pt MLS and alloys are shown in Fig. 15. The calculated $\omega\sigma_{xy}^{(2)}$ of pure fcc Co is shown for reference by the solid curve in all figures. All the compounds can be divided into three distinct groups according to differences between their $\omega\sigma_{xy}^{(2)}$ and that of pure Co. The first group consists of 2Co/1Pt, 1Co/1Pt, and 1Co/2Pt multilayers (Fig. 15a), which have no more than two consecutive planes of equivalent atoms. For these MLS the energy dependence of $\omega\sigma_{xy}^{(2)}$ varies strongly with MLS composition, with the absolute values of $\omega\sigma_{xy}^{(2)}$ being significantly larger compared to Co. In the case of 2Co/1Pt and 1Co/1Pt the curves have similar shape, but $\omega\sigma_{xy}^{(2)}$ of the latter is ~1.5 times greater. The position of the peak at ~1.5 eV is not altered compared to Co, while the feature at ~3.5 eV is shifted to lower energies by 1 eV, and an additional peak appears around 5.5 eV. There are two maxima in $\omega\sigma_{xy}^{(2)}$ of 1Co/2Pt, which lie at approximately the same energies as in Co, but their intensities are 2 times higher.

The situation is quite different in the case of multilayers with greater sublayer thickness (Fig. 15b). Some increase in $\omega\sigma_{xy}^{(2)}$ is observed only for 4Co/2Pt MLS, with the shape of the curve being similar to that of Co. The $\omega\sigma_{xy}^{(2)}$ curves of 2Co/4Pt and 1Co/5Pt lie very close to each other and are reduced compared to $\omega\sigma_{xy}^{(2)}$ of Co in the energy range of 2.5–4.5 eV. It should be noted that the last two MLS have Co and Pt sublayer thicknesses which are close to those of experimentally studied films.

Our results for 2Co/1Pt and 2Co/4Pt multilayers are somewhat different from those given in Ref. 70. The discrepancy is partially due to slightly different values of the structural parameters. Nevertheless, calculations performed with the same parameters as in Ref. 70 show that the difference between the two calculations disappears only when the combined corrections to the LMTO Hamiltonian and overlap matrices are not included. This is not surprising, because even with the current-density matrix elements computed accurately, the neglect of the combined-correction terms affects the calculated conductivity tensor via changes in band energies.

The calculated $\omega\sigma_{xy}^{(2)}$ curves for model alloys are shown in Fig. 15c. The common feature of all the spectra is a strong enhancement of $\omega\sigma_{xy}^{(2)}$ in the energy range 4–6 eV. Of the three curves, $\omega\sigma_{xy}^{(2)}$ for $CoPt_3$ is of a different shape, with two distinct maxima at ~1.5 eV and 5 eV, the amplitude of the latter being more than three times greater than the feature in the spectrum of Co at ~4.5 eV.

It has been shown[84,86] that in pure $3d$ metals the off-diagonal conductivity is proportional to the strength of the spin-orbit coupling. In transition metal compounds, however, the dependence of the MO properties on the spin-orbit coupling and effective magnetization of the constituent atoms is far more complicated.[71] To understand this better, model calculations were performed with the spin–orbit coupling set to zero on either the Co or the Pt site. It was found that "switching off" the spin–orbit coupling inside the Co atomic sphere affects the off-diagonal part of the conductivity tensor only slightly, while neglecting the spin-orbit interaction in the Pt sphere results in a strong decrease of $\omega\sigma_{xy}^{(2)}$. These results are in qualitative agreement with those obtained by the authors of Ref. 72, who also observed a strong dependence of $\omega\sigma_{xy}^{(2)}$ on the value of the spin-orbit coupling at the Pt site. We also investigated the effect of excluding the matrix elements of the effective magnetic field at the Co and Pt sites from the LMTO Hamiltonian. When the matrix elements on the Co sphere are zero, the off-diagonal part of the

conductivity decreases drastically. At the same time, ''switching off'' the effective magnetic field at the Pt site produces a negligible effect on the $\omega\sigma_{xy}^{(2)}$ spectra. Thus, a strong spin-orbit coupling at only one of the nonequivalent atomic sites and a large value of the effective magnetization at the other can be sufficient for alloys to manifest strong MO activity.

In addition, it has been found that the dominant contribution to the $\omega\sigma_{xy}^{(2)}$ spectra in the energy range of interest (1–6 eV) comes from transitions to unoccupied states lying in a rather narrow energy interval of ~1 eV just above the E_F. At the same time, these transitions give a relatively small contribution to the diagonal part of the optical conductivity. As has been mentioned above, the electronic states in the vicinity of the E_F are formed by strongly hybridized Co *d* and Pt *d* states.

It is worthwhile to note that in the case of transition-metal compounds, the wave functions of the initial and final states involved in an optical transition are delocalized. Consequently, it is difficult, if possible at all, to separate the contributions of any intra- or interatomic transitions to the MO spectra. The assumption that the enhanced MO effects in Co-Pt compounds are due to Co *d*–Pt *d* hybridization allows one to explain the relatively small (as compared to Co-Pt alloys) magnitude of the calculated $\omega\sigma_{xy}^{(2)}$ in 2Co/4Pt and 1Co/5Pt multilayers. In these MLS there are Pt layers consisting of atoms which have Co atoms among neither the first nor the second nearest neighbors, and the contribution of these layers to $\omega\sigma_{xy}^{(2)}$ is small. However, switching off the spin-orbit interaction for these atoms leads to a rather strong change in the spectrum. Neglecting the spin-orbit coupling for Pt atoms only at the Co-Pt interface leads to relatively pronounced changes, but the magnitude of $\omega\sigma_{xy}^{(2)}$ remains considerably higher than the magnitude of $\omega\sigma_{xy}^{(2)}$ calculated with the spin-orbit interaction at all Pt atoms set to zero.

Some calculated polar Kerr rotation spectra are shown in Fig. 16. From a comparison with the experimental MOKE spectra of the Co/Pt MLS shown in Fig. 8 it can be seen that the calculated spectra of MLS do not satisfactorily reproduce the experimental data. The magnitude of the calculated MOKE spectra of 2Co/4Pt and 1Co/5Pt MLS (Fig. 16a) in the energy range 3–5 eV is significantly smaller than that of pure Co, while an enhancement of the rotation angle of MLS versus pure Co is observed in the experiment. The enhancement is indeed found for Co/Pt MLS with smaller sublayer thickness (Fig. 16b), but in contrast to the experimental data the peak is shifted to lower energy with respect to its position in Co. Surprisingly, better agreement with the experimentally observed MOKE spectra is observed in the case of Co-Pt alloys (Fig. 16c). The calculated spectra reproduce fairly well both the increase of magnitude and the shift of the UV peak to higher energies.

The discrepancy between the experimental Kerr rotation spectra of Co/Pt MLS obtained in the present work and the calculated spectra of the model Co/Pt multilayers may be due to inadequacy of the adopted structure model of the MLS with the sharp interlayer interface. The observed energy dependence of the MOKE spectra of the MLS and their variation with the Co sublayer thickness may be explained by the

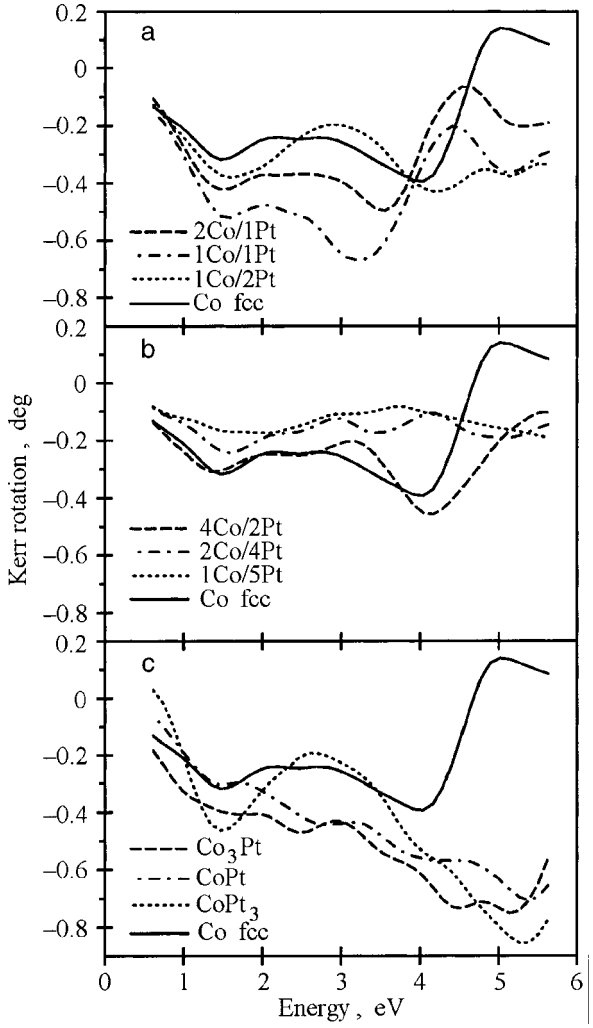

FIG. 16. Theoretical polar Kerr rotation spectra of the Co-Pt multilayers (a, b) and alloys (c).[74]

reasonable assumption that a Co-Pt alloy is formed at the interface.

It is interesting to compare the results of our calculations with the recently published polar Kerr rotation spectra of an artificial Co_3Pt alloy film.[73] X-ray diffraction data show that after annealing at 650 K the alloy consists of alternating sequence of close-packed Co and CoPt planes with an hcp-like stacking. Because of the well-defined order along the crystallographic *c* direction, the structure of the alloy is rather close to that of the model 1Co/1Pt multilayer. Nevertheless, because of the different compositions of the two compounds, the direct comparison of the experimental and calculated MOKE spectra should be made with care. The calculated MOKE spectra of 1Co/1Pt multilayers with *ababab* and *abcabc* layer sequences are shown in Fig. 17 together with the experimental spectra. Except in the IR range, the calculated spectra are similar, with slightly different amplitudes. Both theoretical spectra have a peak at ~3 eV which is clearly seen on the experimental curve. A 5-eV feature in the experimental spectrum is also reproduced by the calculations, but the corresponding peaks are shifted slightly to higher energies. The shift may be caused by the difference of the experimental and theoretical lattice constants. After annealing at 950 K the Co_3Pt alloy film has been

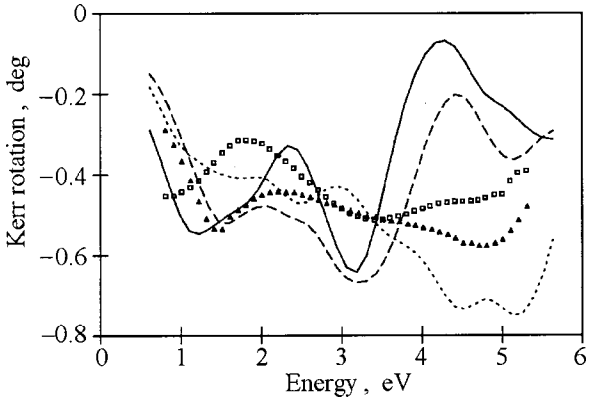

FIG. 17. Theoretical polar Kerr rotation spectra of 1Co/1Pt multilayers with *ababab* (solid line) and *abcabc* (dashed line) stacking. The calculated spectrum of Co_3Pt alloy is shown by the dotted line. Experimental spectra for ordered hexagonal Co_3Pt phase (squares) and chemically disordered fcc phase (triangles) are taken from Ref. 73.[74]

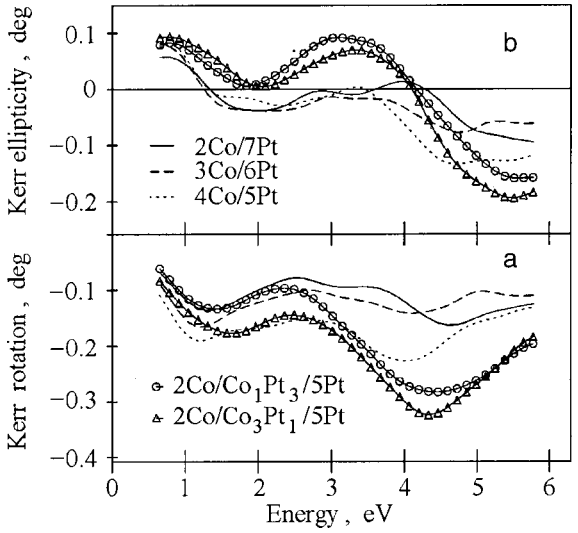

FIG. 18. Calculated polar Kerr rotation (a) and ellipticity (b) spectra for the model of Co/Pt multilayers with sharp interfaces (lines) and with single-layer interfacial alloys (symbols).[75]

shown to consist of a chemically disordered fcc phase. The modification of atomic arrangement and chemical short-range order causes significant changes of the observed MOKE spectra. The 3-eV peak disappears, while the amplitude of the spectra in the UV range increases and the 5-eV feature transforms into a peak. Similar changes are readily seen when comparing the calculated MOKE spectra of 1Co/1Pt multilayers with the calculated spectrum of the Co_3Pt alloy.

In conculsion it should be pointed out that the Kerr rotation of Co/Pt MLS is governed mainly by the off-diagonal part of the conductivity tensor. The infrared part of the spectrum originates from the MO activity of the Co layers themselves, and it scales with the Co content. On the other hand, the peak in the UV region is due to the hybridization of strongly spin-polarized Co *d* states with spin–orbit-split Pt *d* states, and its magnitude depends weakly on the MLS composition. It has been demonstrated that the chemical and structural ordering is accompanied by substantial electronic structure changes and result in a drastic MOKE spectra modification.

It should be noted that the *ab initio* description of the MOKE spectra for model Co/Pt multilayers performed under the assumption of a sharp, ideal interface is not adequate for the detailed explanation of the experimentally observed spectra. Simultaneously, in the case of model Co-Pt alloys the calculations properly reflect the main features of the spectra observed experimentally. Thus it can be concluded that in the real multilayer structures the limited interdiffusion region at the interface and its structure and chemical composition play a major role in the formation of the MO spectra of the Co/Pt MLS.

4.3. The effect of interfacial alloying on the magnetooptical spectra in Co/Pt multilayers

To examine the consequences of interfacial intermixing for Co/Pt MLS MOKE spectra and their relation to the chemical nature of the interface, special model supercells of the multilayered structures with alloyed interfaces and fcc (111) texture were constructed in Ref. 75. The same lattice constant and space group as for the idealized model were used in the calculations. As an interface between the neighboring Co and Pt layers, one or two Co-Pt mixed atomic planes were introduced. Three types of multilayered structures were considered: in the form of single-layer Pt-rich Co_1Pt_3 and Co-rich Co_3Pt_1 ordered interfacial planar alloys, and also in the form of a double alloy layer Co_3Pt_1/Co_1Pt_3 composed of consecutive single layers of different composition. The calculated spectra for Co/Pt MLS structures in which Co and Pt atomic planes are separated by a single interfacial alloy layer of different compositions are shown in Fig. 18. As can be seen, the presence of the interfacial alloy plane does not appreciably alter the spectra in the IR range, while significant enhancement of the Kerr rotation amplitude in the UV spectral range is clearly seen.

The enhancement of the Kerr rotation in the UV range brings the spectra into better agreement with experiment. However, the magnitudes of the calculated spectra are still significantly smaller than the experimental ones. In the ''real'' Co/Pt systems the intermixing probably extends to more than one atomic plane, with the composition changing gradually. Figure 19 presents the results of the calculations for the Co/Pt MLS model structure composed of double interfacial Co_3Pt_1/Co_1Pt_3 alloy atomic planes. From Figs. 18 and 19 it can be seen that in the IR region the amplitudes of the spectra depend weakly on the interfacial layer thickness and composition, whereas in the UV range the amplitudes increase by about 50% as compared to the spectra with a single interfacial alloy layer. Alloying at the Co/Pt MLS interfaces leads to an increase of the volume in which the strong $3d-5d$ hybridization occurs and, consequently, the contribution of these hybridized states to the MO spectra increases compared to the ideal MLS models. Another effect of interfacial alloy formation is stronger spin polarization of the whole Pt spacer. The averaged magnetic moment per Pt atom calculated for the structures with alloyed interface increases by up to 90% compared to that calculated for the ideal MLS model. It was found that the contribution to the MLS spectra coming from the interfacial alloy region and

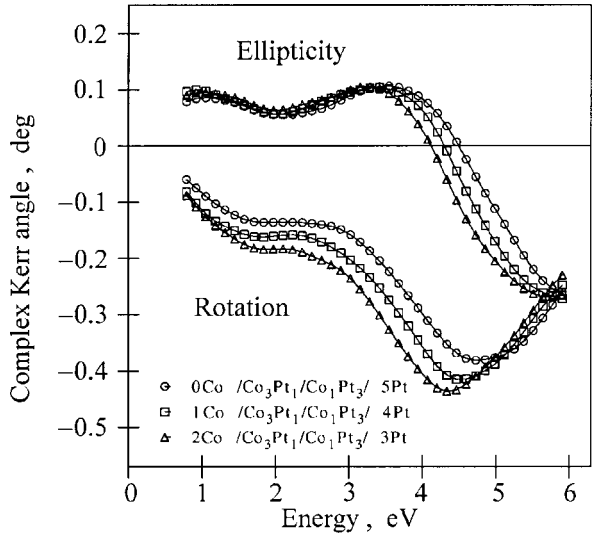

FIG. 19. Calculated polar Kerr rotation (a) and ellipticity (b) spectra for the model of Co/Pt multilayers with a two-layer interfacial alloy.[75]

polarized Pt atomic planes controls the shape and magnitude of the spectra in the UV energy range.

In conclusion, the results obtained clearly illustrate the crucial role of the interface structure on the magnetooptical spectra of the Co/Pt multilayers. It is shown that the main peculiarities and the tendencies in the modification of the MLS spectra with variation of the Co sublayer thickness are adequately reproduced when an alloying, limited to two atomic planes, is taken into account. The very good agreement between the calculated and measured MOKE spectra demonstrates the validity of the adopted model and approach.

5. MAGNETOOPTICAL PROPERTIES OF Co/Cu MULTILAYERS

In the pioneering study of Katayama *et al.*[76] it was shown that the Kerr rotation in Fe/Cu bilayers can be enhanced at the absorption edge energy of Cu. Since then, several investigations of MOKE spectra of Fe, Co/noble-metal bilayers and multilayers have been done.[77–81] The observed features of the MOKE spectra were interpreted as mainly related to the plasma edge in the noble metal and also to magnetooptically active transitions in the noble metal as a consequence of the spin polarization of the noble metal by the proximity of magnetic layers at the interface.

In Ref. 82 the complex MOKE spectra and optical properties—refractive index n and extinction coefficient k—were measured in a wide spectral range for a set of Co/Cu MLS structures. For the study the following set of Co/Cu MLS was prepared: 14.9 Å Co/10.1 Å Cu, 15.2 Å Co/15.2 Å Cu, 15.1 Å Co/21.7 Å Cu, and 22.3 Å Co/23.7 Å Cu, all with the same number of repetitions of the Co/Cu bilayer, equal to 40. The MLS were deposited by the face-to-face dc sputtering system described in Ref. 83. All of the samples were deposited on a water-cooled glass substrate. The argon pressure during the deposition was about 60 mPa, and the deposition rate was about 0.5 Å/s. The chemical composition of the films was determined by x-ray fluorescence analysis with an EDX system from the peak intensities

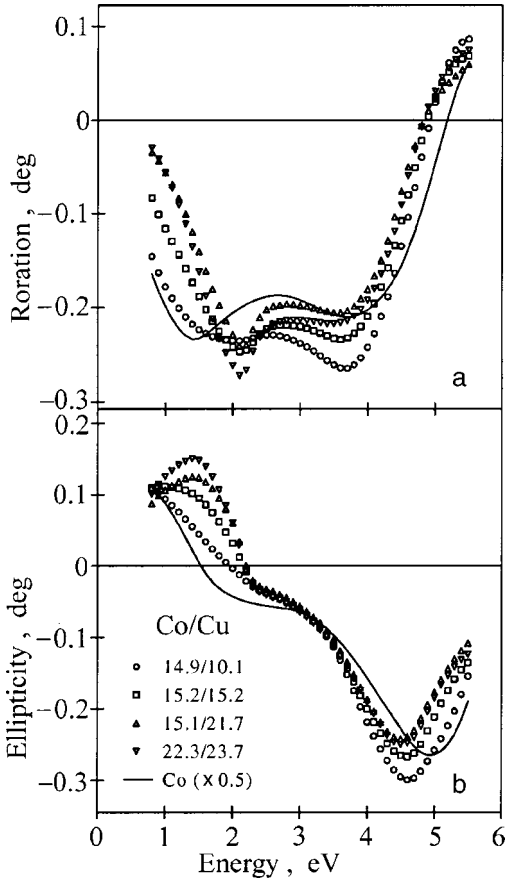

FIG. 20. Experimental polar Kerr rotation (a) and ellipticity (b) of Co/Cu MLS and thick fcc Co film (multiplied by a factor of 0.5). Co and Cu sublayer thicknesses are given in the legend in units of Å.[82]

of the characteristic fluorescence radiation. The crystal structure was examined by low- and high-angle x-ray diffraction (XRD) using Co-$K(\alpha)$ radiation. The layered structure was confirmed by low angle XRD. The modulation period was deduced from the position of the Bragg peaks. From the high-angle XRD a pronounced (111) texture was inferred.

Figure 20 shows the measured polar Kerr rotation θ_K and ellipticity η_K spectra of the Co/Cu MLS studied. The measured spectra of θ_K and η_K of a thick ($\sim$2000 Å) fcc Co film are included for comparison.

The essential points of the experimental MOKE results can be summarized as follows:

i) The θ_K spectra of the Co/Cu MLS exhibit a two-peak structure and are strongly reduced compared to the pure Co thick film.

ii) The broad negative θ_K peak appearing in the UV energy region has an amplitude which is approximately proportional to the Co content of the MLS. The energy position of this peak remains the same as for the Co thick film.

iii) The θ_K spectra in Co/Cu MLS exhibit a peak at $\hbar\omega \sim 2.1$ eV not observed in the pure Co film. The amplitude and width of this peak are directly connected with the Cu sublayer thickness. For the MLS with the thinnest Cu sublayer the peak transforms into a broad shallow minimum located between $\sim$1.5 eV and $\sim$2.1 eV, the former energy corresponding to the θ_K peak position of the Co thick film.

iv) As the amount of Co in the MLS decreases, the spectra generally scale down, while there is an increase in the

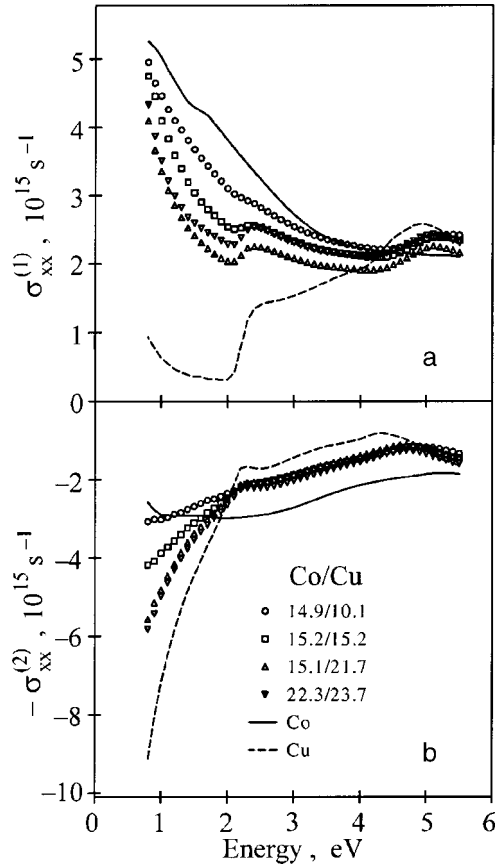

FIG. 21. The absorptive (a) and dispersive (b) parts of the conductivity tensor of Co/Cu MLS and thick fcc Co and Cu films determined from the ellipsometric measurements.[82]

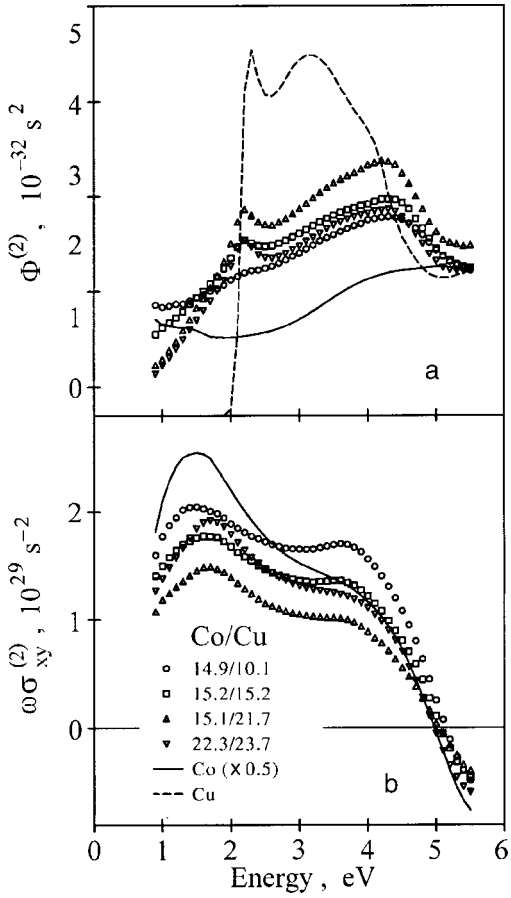

FIG. 22. The contribution to the Kerr rotation spectra from the diagonal part of the conductivity tensor (see text) (a) and the $\omega\sigma_{xy}^{(2)}$ of Co/Cu MLS and a thick fcc Co film, determined from the ellipsometric and the MOKE measurements (b).[82] The $\omega\sigma_{xy}^{(2)}$ of Co is multiplied by a factor of 0.5.

prominence of the θ_K peak located at the energy of ~2.1 eV.

v) At energies above ~2.1 eV the Kerr ellipticity spectra are very similar. The UV peak position shifts to lower energy compared to the Co thick film, and its amplitude scales with the amount of Co. In the energy range 0.8–2.1 eV a strong dependence of the spectra on the MLS composition is seen.

The measured optical properties of the MLS as well as of thick fcc Co and Cu films, prepared by the same technique, are shown in the form of the spectral dependencies of the absorptive ($\sigma_{xx}^{(1)}$) and dispersive ($\sigma_{xx}^{(2)}$) parts of the diagonal component of the optical conductivity tensor in Figs. 21a and 21b, respectively. The well-known prominent feature in the Cu optical conductivity tensor at energy ~2.1 eV, where there is a superposition of the Drude-like interband transitions and the interband transition edge, is clearly observed.

As can be seen from Fig. 21a, the $\sigma_{xx}^{(1)}$ spectra for the MLS studied lie between the spectra of pure Co and Cu films. These spectra have two features, a shoulder at an energy of ~2.1 eV and a broad maximum at about 5 eV. The feature at ~2.1 eV is related to the Cu plasma-edge resonance absorption, and its prominence increases with the Cu content. For all of the Co/Cu MLS studied the $\sigma_{xx}^{(1)}$ spectra have similar shape, and their magnitude in the IR range scales with the amount of Co. This can easily be understood by taking into account the weak absorption of Cu metal in this energy region.

The MOKE depends on the diagonal part of the optical conductivity through the denominator of Eq. (2). To separate the contribution to the MOKE coming from the diagonal and off-diagonal components of the optical conductivity tensor, the function $\mathbf{\Phi}(\omega)$ has been evaluated from the optical measurements:

$$\mathbf{\Phi}(\omega)=\mathbf{\Phi}^{(1)}(\omega)+i\mathbf{\Phi}^{(2)}(\omega)=\frac{1}{\omega\sigma_{xx}\sqrt{1+i(4\pi/\omega)\sigma_{xx}}}. \tag{16}$$

It has been found that for the compounds under consideration the imaginary part of the function multiplied by $\omega\sigma_{xy}^{(2)}$ gives the main contribution to the polar Kerr rotation spectra. (Here and below $\sigma_{xy}^{(2)}$ stands for the absorptive part of the off-diagonal conductivity component.) For the Co/Cu MLS the function $\mathbf{\Phi}^{(2)}(\omega)$ exhibits a two-peak structure (see Fig. 22a), a sharp peak at the same energy ~2.1 eV as in the Kerr rotation spectra and a broader one at an energy around 4.5 eV. Thus, it can be clearly seen that diagonal part of the optical conductivity tensor significantly influences the shape of the MOKE spectra.

Figure 22b shows the $\omega\sigma_{xy}^{(2)}$ spectra of the Co/Cu MLS. The shape of the curves for all MLS is qualitatively similar to the shape of the $\omega\sigma_{xy}^{(2)}$ determined for the Co thick film. Inspection of the curves shows that the magnitude of the $\omega\sigma_{xy}^{(2)}$ spectra in the UV spectral region scales with the amount of Co. However, this is not true for the IR spectral

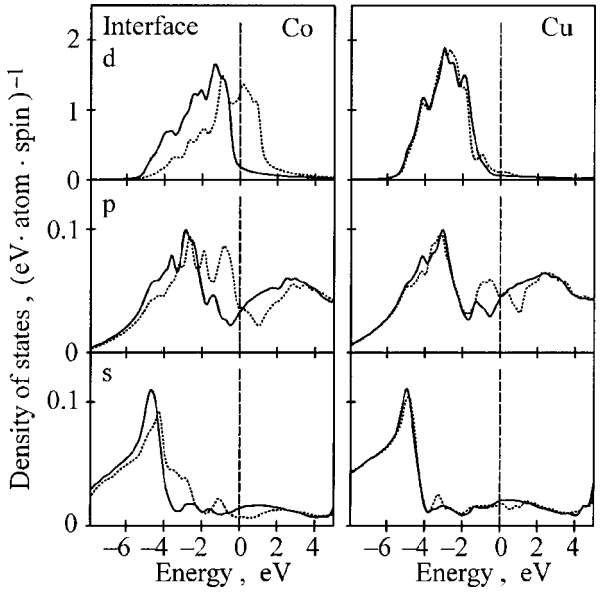

FIG. 23. Spin- and *l*-projected density of states at Co and Cu sites (states/(eV·atom·spin)) at the interface in 6Co/6Cu multilayer. The solid and dotted lines correspond to majority and minority spin states, respectively. The Fermi level is denoted by a vertical dashed line.[82]

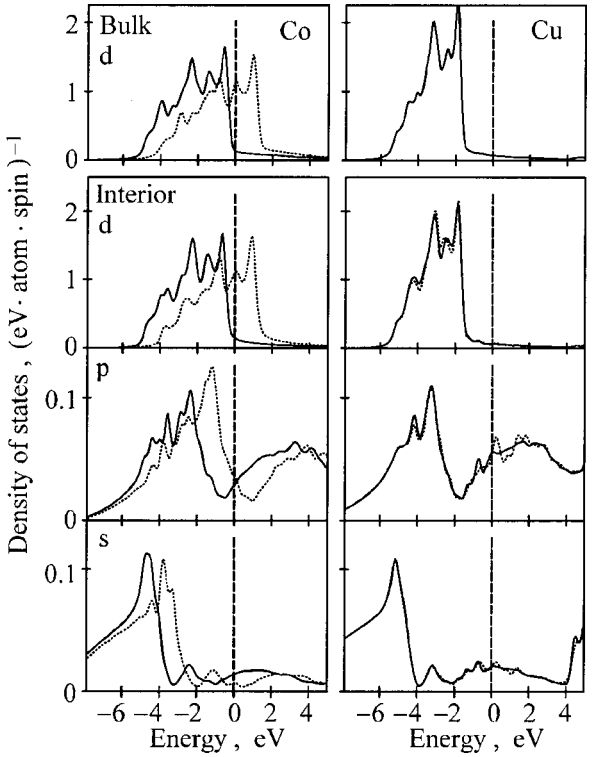

FIG. 24. Spin- and *l*-projected density of states at Co and Cu sites (states/(eV·atom·spin)) located in the middle of the corresponding sublayer in a 6Co/6Cu multilayer. The density of *d* states of bulk fcc Co and Cu is also shown. The solid and dotted lines correspond to majority and minority spin states, respectively. The Fermi level is denoted by a vertical dashed line.[82]

region: in particular, the position of the low energy peak shifts from that for the fcc Co film and depends on the MLS composition. The changes can be explained by a modification of the electronic states involved in the optical transitions due to the presence of the Co/Cu interface.

It can be concluded that the IR peak observed in the polar Kerr rotation spectra is mainly determined by the corresponding feature in the diagonal part of the conductivity tensor. The position of the θ_K peak observed in the UV spectral region coincides with the position of the peak in the $\omega\sigma_{xy}^{(2)}$ spectra, but its shape is to a great extent affected by the spectral form of σ_{xx}, just as in the case of pure Co.

To clarify the microscopic origin of the magnetooptical properties of the Co/Cu multilayers, we have performed self-consistent local-spin-density calculations of the electronic structure of some model Co/Cu structures by means of the spin-polarized fully relativistic (SPR) LMTO method.

Since the experimentally investigated MLS have pronounced fcc-(111) texture, in the *ab initio* calculations we constructed a number of nCo/mCu model MLS periodic along the [111] direction and consisting of close-packed n Co and m Cu planes with an *abc* stacking sequence. All the structures possess D_{3d}^3 symmetry. The lattice constant ($a = 3.574$ Å) was chosen as an average of those of the fcc Co and Cu metals. No attempt has been made to optimize the interlayer spacing, which was taken to be constant corresponding to the ideal c/a ratio.

The spin- and *l*-projected density of the electronic states for Co and Cu atoms in the representative 6Co/6Cu multilayer are shown in Fig. 23 for the sites at the interface and in Fig. 24 for the sites located in the middle of the appropriate sublayer. The densities of *d* states of bulk fcc Co and Cu are shown at the top of Fig. 24 for comparison. As could be anticipated, the density of Co and Cu *d* states of the interior atoms are similar to those of bulk metals. At the same time, the Co and Cu states at the interfacial sites are strongly hybridized. It is interesting to note that the Cu states at the interface are considerably spin-polarized due to the hybridization with Co states. It was found that the resulting Cu *sp* and *d* spin magnetic moments are of opposite sign and almost compensate each other.

To show the main trends in the formation of the optical and magnetooptical spectra of the Co/Cu MLS, the conductivity tensor of 2Co/4Cu, 3Co/3Cu, 6Co/6Cu, and 4Co/2Cu model multilayers was calculated. The calculated $\sigma_{xx}^{(1)}$ spectra are shown in Fig. 25a. All the spectra except that of Cu were broadened with a Lorentzian of width 1.2 eV to simulate the finite electron lifetime effects. For the Cu spectrum a Lorentzian of width 0.4 eV was used. To take into account the intraband contribution the phenomenological Drude term was also added to the diagonal components of σ. In accordance with the experimental data the curves lie very close to each other at energies higher than ~4 eV. In the visible and IR spectral regions a noticeable increase of the absorption with increasing Co content can be seen. An interesting feature of these spectra is the minimum at the energy $\hbar\omega \sim 1.5$ eV, which corresponds to a minimum of the interband absorption in pure Cu. From a comparison of $\sigma_{xx}^{(1)}$ for 3Co/3Cu and 6Co/6Cu it can be seen that this feature is enhanced as the number of adjacent Cu layers increases. An analysis of the partial density of states shows that such behavior of $\sigma_{xx}^{(1)}$ can be explained by the energy location of the Co and Cu *d* states (see Figs. 23 and 24). The dominant interband contribution to the $\sigma_{xx}^{(1)}$ spectra at photon energies lower than ~4 eV comes from transitions involving the Co and Cu *d* states. As in the pure Cu metal, the Cu *d* states in the MLS are

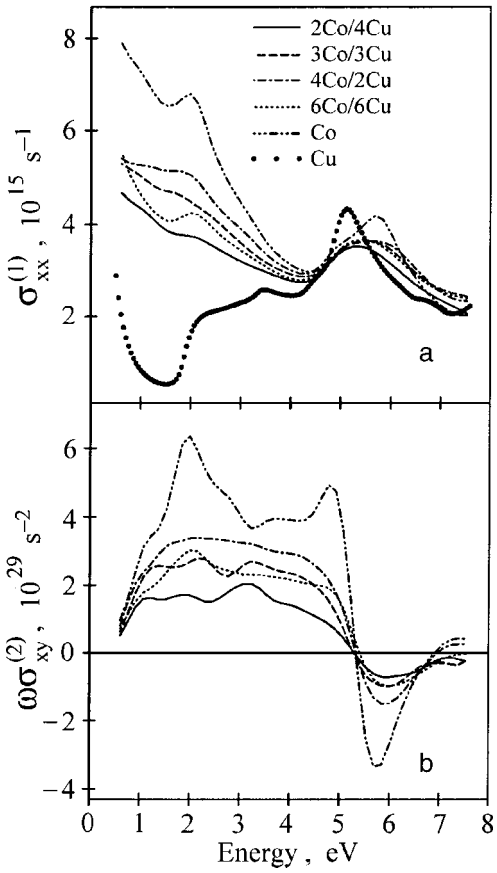

FIG. 25. Calculated $\sigma_{xx}^{(1)}$ (a) and $\omega\sigma_{xy}^{(2)}$ (b) spectra of the model Co/Cu multilayers.[82]

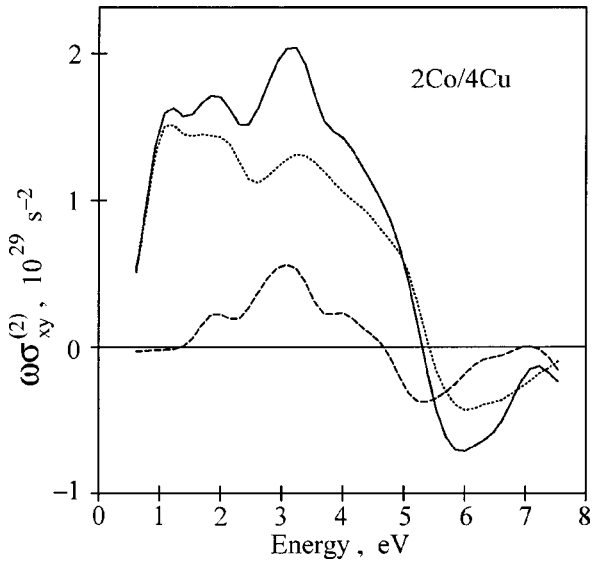

FIG. 26. The influence of the Co and Cu spin–orbit coupling strength on the theoretical $\omega\sigma_{xy}^{(2)}$ spectrum of 2Co/4Cu multilayer. The whole spectrum is shown by solid line. Dashed and dotted lines denote the spectra calculated with nonzero spin–orbit coupling strength at Co and Cu sites, respectively.[82]

located ~1.5 eV below the Fermi level and, consequently, give no contribution to $\sigma_{xx}^{(1)}$ at lower photon energies. On the contrary, optical transitions to/from the Co *d* states are possible at arbitrary energy, because the minority-spin Co *d* states are only partially filled. As a result of a superposition of the absorption in Co and Cu sublayers, the magnitude of the $\sigma_{xx}^{(1)}$ spectra of the Co/Cu MLS increases with the Co content at $\hbar\omega \leqslant 4$ eV. The peak in $\sigma_{xx}(\omega)$ at $\hbar\omega \sim 5.5$ eV is mainly due to transitions from the *s* states at the bottom of the valence band to the *p* states above the Fermi level. The densities of Co and Cu *s* states are rather similar, except for the spin splitting of the former. As a result, the peak becomes broader with increasing Co content in the MLS, its magnitude being almost unchanged.

Some calculated $\omega\sigma_{xy}^{(2)}$ spectra are shown in Fig. 25b. The magnitude of the spectra of the Co/Cu MLS is smaller than that of pure fcc Co, also shown in Fig. 25b, and approximately scales with the Co content. As compared to the $\omega\sigma_{xy}^{(2)}$ curve of Co, the spectra of the MLS have a less pronounced structure. For the model multilayers studied the peak centered at ~2 eV in the Co spectrum is observed most distinctly for the 6Co/6Cu structure, where the Co sublayer is sufficiently thick. It is remarkable that all the spectra cross zero at the same energy of about 5 eV. Considering the $\omega\sigma_{xy}^{(2)}$ spectra leads one to conclude that the dominant contribution is provided by optical transitions involving Co electronic states. The states are modified by the hybridization with Cu states at the interface, the hybridization effects being of greater importance for the MLS with smaller Co sublayer thickness.

Magnetooptical effects originate from a complicated interplay of the spin-orbit coupling and exchange splitting. As can be inferred from perturbation theory (see, e.g., Refs. 12 and 84), the $\sigma_{xy}^{(2)}$ spectrum can be expanded as a sum of contributions proportional to the spin-orbit coupling strength ξ_{tl} of the electronic states with angular momentum *l* at a site *t*. From the results of test calculations with $\xi_{tl}=0$ for all $l \neq 2$ it has been found that the MO properties of the Co/Cu multilayers are governed mainly by the spin-orbit coupling of *d* electrons. Then calculations were done with the value of ξ_{tl} nonzero only for either the Co *d* or Cu *d* states. The results of the calculations for a 2Co/4Cu multilayer are shown in Fig. 26. It can be seen that the Cu contribution is, in general, significantly smaller than the contribution from the Co sites. There are two inequivalent Cu atoms in the 2Co/4Cu multilayer, one of them being located at the Co/Cu interface and the another one in the interior of the Cu slab. From test calculations with ξ_{tl} set to zero for the interfacial Cu sites it has been found that the contribution from the interior Cu sites to the $\sigma_{xy}^{(2)}$ spectrum is negligible. The spin-obit coupling strengths for Co and Cu *d* states are, however, of the same order of magnitude. The relatively small effect of the Cu sites on the off-diagonal conductivity component can be explained by the fact that the exchange splitting at the Cu sites is much smaller than at the Co sites (see Figs. 23 and 24). Calculations were performed assuming zero exchange splitting at all Cu sites, and it was found that the effect of ''switching off'' the exchange splitting on the $\omega\sigma_{xy}^{(2)}$ of Co/Cu MLS is negligible. The results support the conclusion that the dominant role is played by the Co contribution to the MO properties of the Co/Cu MLS.

To investigate the dependence of the $\sigma_{\alpha\beta}$ on the local environment, calculations were performed for 2Co/4Cu MLS with *abc* and *ab* stacking sequences of the close-packed planes. In the both MLS the number of Co and Cu atoms

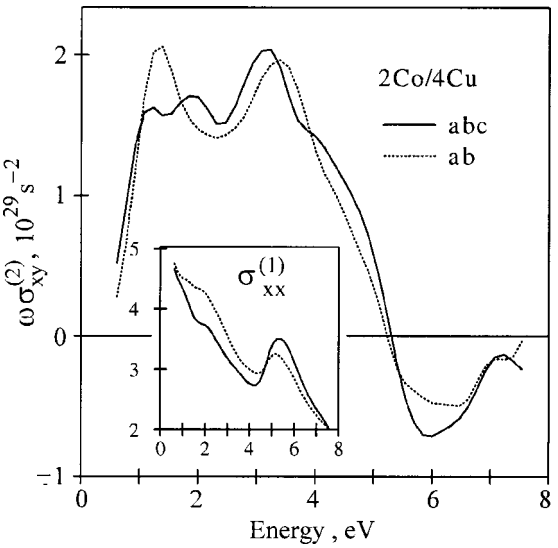

FIG. 27. Calculated $\omega\sigma_{xy}^{(2)}$ spectra of 2Co/4Cu multilayers with *abc* and *ab* stacking sequences. In the inset the corresponding $\sigma_{xx}^{(1)}$ spectra are shown.[82]

among both the first- and second-nearest neighbors around each site is the same, but the local symmetry is different. The calculated $\omega\sigma_{xy}^{(2)}$ spectra are shown in Fig. 27. Although the overall shape of the curves is similar, the fine structure is rather different. There are also differences in the corresponding $\sigma_{xx}^{(1)}$ curves shown in the inset in Fig. 27. It has been found that the joint density of states calculated for MLS with different kinds of stacking sequences are almost identical. Taking into account that the joint density of states is determined only by the band structure of a compound, one can conclude that the details of the short-range order affect the optical and MO spectra of the Co/Cu MLS mainly via the transition matrix elements.

Calculated polar Kerr rotation and elipticity spectra for the Co/Cu MLS are shown in Fig. 28. The spectra reproduce well the dependence of the magnitude of the UV peak on the Co content observed experimentally for the Co/Cu MLS studied. However, the calculated spectra are more structured. A well-defined peak at ~2 eV in the polar Kerr rotation, which is a characteristic feature of all the measured spectra, is distinctly present in the theoretical spectrum of the 6Co/6cu multilayer. A possible explanation is that due to the smaller Co and Cu sublayer thicknesses in the calculated model MLS as compared to the experimentally studied samples, the transitions to/from electronic states modified by the hybridization at the Co/Cu interfaces give a relatively large contribution to the MO spectra.

Accordingly to the experimental data, the low-energy peak in the $\omega\sigma_{xy}^{(2)}$ spectra of the Co film, like that of the Co/Cu MLS, is located below 2 eV. The feature in the $\sigma_{xx}^{(1)}$ curves which is related to the Cu plasma edge and manifests itself as a sharp peak in the Kerr rotation spectra is centered at 2.1 eV. On the other hand, the calculations predict that the peak in $\omega\sigma_{xy}^{(2)}$ of Co and the edge of interband transitions in Cu should lie at a similar energy position of approximately ~2 eV. The discrepancy may be due to the fact that the LSDA approximation is only moderately successful in the description of the energy band structure and MO properties of ferromagnetic $3d$ metals, especially Ni and Co.[74,85,86]

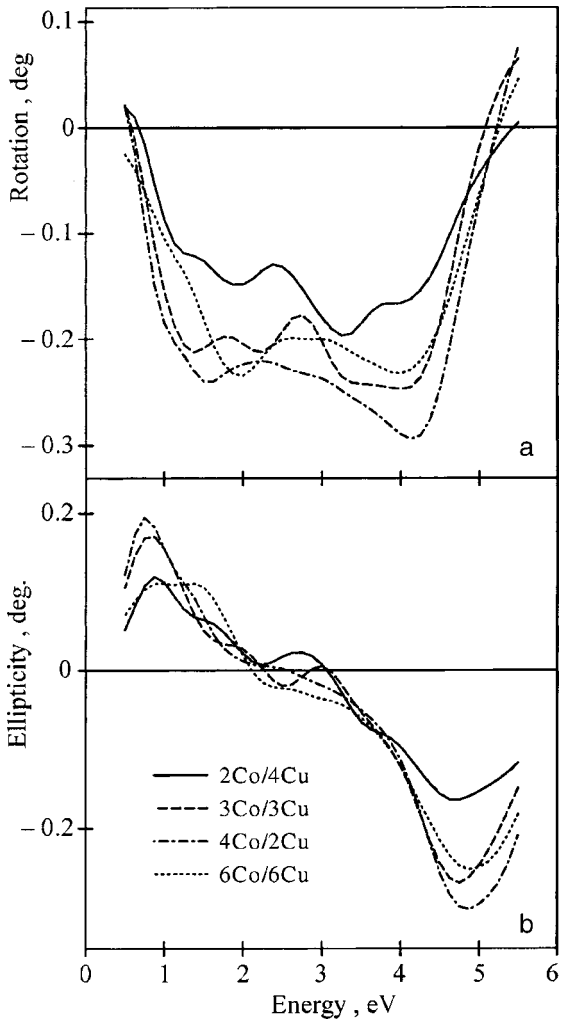

FIG. 28. Calculated polar Kerr rotation (a) and ellipticity (b) spectra of the model Co/Cu multilayers.[82]

Ab initio calculations of polar Kerr rotation and ellipticity spectra were performed for 6Co/3Cu, 6Co/6Cu, and 6Co/9Cu multilayers, assuming model multilayer structures with ideal interfaces. The calculated spectra are compared with the experimental ones in Fig. 29. Despite the idealized multilayer structures, good agreement between the theory and experiment is observed. Besides the overall similarity in the shape of the measured and calculated spectra, the calculations reproduce well the main trends in amplitudes of the spectra in different energy regions.

In conclusion it should be pointed out that from both the experimental and theoretical studies it follows that despite the spin polarization of the Cu d states due to the hybridization with the Co states at the MLS interface, the dominant contribution to the off-diagonal part of the optical conductivity tensor of the Co/Cu MLS comes from interband transitions involving Co electronic states. The feature observed at $\hbar\omega \sim 2.1$ eV in the spectra of the optical conductivity tensor component $\sigma_{xx}^{(1)}$ is related to the edge of interband transitions from Cu d states in the Cu sublayers and is responsible for the peak at 2.1 eV in the polar Kerr rotation spectra of the MLS studied. There are some discrepancies between the experimental and theoretical results mainly in the description of the Co-related peaks of the optical and MO spectra of the

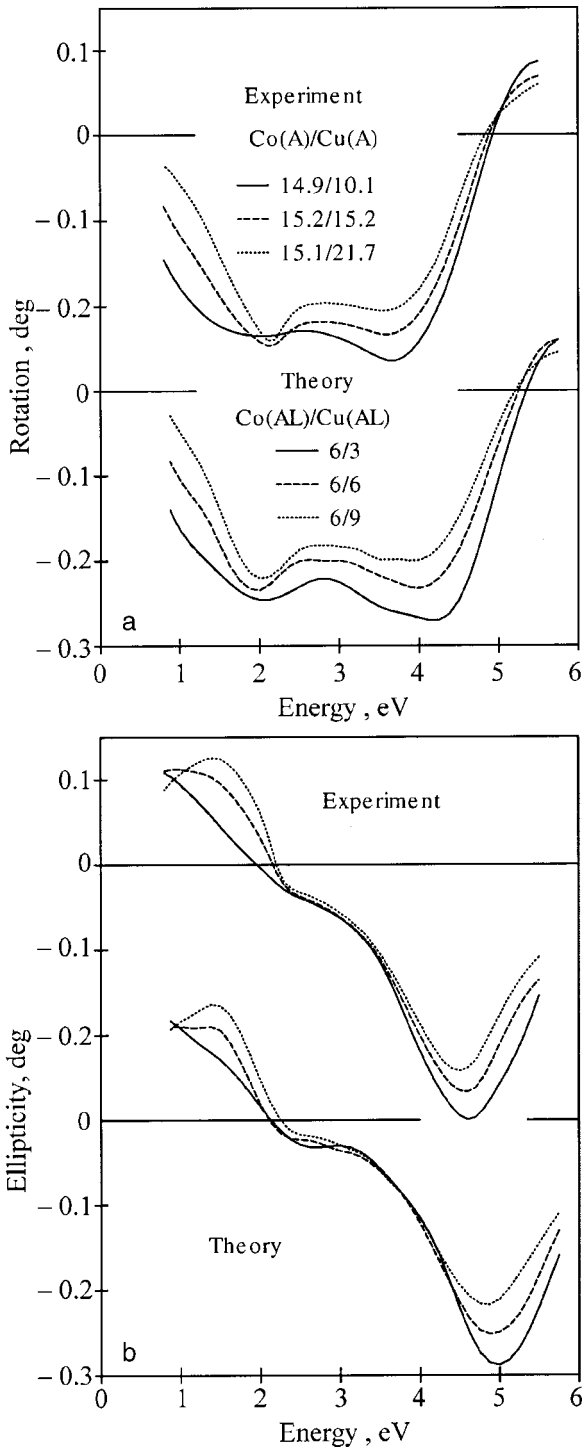

FIG. 29. The comparison of the polar Kerr rotation (a) and ellipticity (b) spectra measured for Co/Cu MLS films with the spectra calculated for the model nCo/mCu multilayers (the sublayer thicknesses are expressed in the key for the experimental films (in Å) and for the calculated structures (in atomic layers AL).[82]

Co/Cu MLS. Nevertheless, the *ab initio* calculations reproduce the main features of the spectra and provide an explanation of their microscopic origin.

6. MAGNETOOPTICAL ANISOTROPY IN Fe_n/Au_n SUPERLATTICES

Many important physical properties of magnetically ordered compounds depend on the relative orientation of the magnetization and the crystallographic axes, as the spin subsystem is coupled to the lattice by the spin-orbit (SO) interaction. The magnetocrystalline anisotropy (MCA), which is the energy that directs the magnetization along a certain crystallographic axis, is a ground-state property of a crystal. The magnetooptical anisotropy (MOA), defined as the dependence of the off-diagonal part of the optical conductivity tensor on the magnetization direction, arises as a result of electronic excitations and is due to the spin and orbital polarizations of initial and final states.

Although the MCA has been widely studied both experimentally[87] and theoretically[88–91] in a large number of materials, the investigations of the MOA are still restricted to a few cases only. Theoretical calculations have been performed for Co, FePt, CoPt,[92] CoPd,[48] and CrO_2.[58] Experimentally, however, the orientation dependence of the magnetooptical (MO) Kerr effect has been observed in only one magnetic system, hcp Co. In the equatorial Kerr effect Ganshina *et al.*,[93] and in the longitudinal Kerr effect (LKE) configuration Osgood *et al.*[94] have studied the dependence of the magnitude of the Kerr effect on the orientation of the magnetization with respect to the c axis, both lying in the basal plane of the hcp Co sample. For the polar Kerr effect (PKE) configuration with magnetization perpendicular to the sample plane, Weller *et al.*[68] observed an orientation dependence of the PKE by using two epitaxial hcp Co films with different, (0001) and $(11\bar{2}0)$, basal planes.

An extensive experimental and theoretical study of the observed large magnetooptical anisotropy was presented in Ref. 95 for a series of Fe_n/Au_n superlattices prepared by molecular beam epitaxy with $n=1$, 2, 3 of Fe and Au atomic planes of (001) orientation. The $(Fe_1/Au_1)\times 20$ and $(Fe_2/Au_2)\times 10$ and $(Fe_3/Au_3)\times 7$ MLS were grown by MBE under UHV conditions (base pressure during preparation below 5×10^{-10} mbar) on a 30 nm (001) Au buffer layer (preceded by a 4 nm Fe (001) seed layer), deposited on a MgO (001) cleaved substrates in a multi-stage process.[96] The whole structure was finally covered by a 5 nm Au cap layer. The Fe and Au monolayers were deposited alternately at 340 K at a rate of about 0.2 nm/min, as controlled by a quartz microbalance with an accuracy of $\pm 5\%$. Very uniform growth conditions are preserved for subsequent layers, resulting in a high epitaxial quality of the superlattices. For the growth mode and the resulting structure of the Fe/Au MLS an important role is played by the Au self-surfactant effect, which was observed when single Fe films were grown on the reconstructed (001)Au surface.[96,97] During the Fe growth, the Au surface segregation occurs by an atomic place exchange that leads to the formation of one Au monolayer on top of the growing Fe film. This process, particularly important for the growth of the Fe_1/Au_1 monatomic superlattices, is responsible for a deviation from a perfect layer structure, as was observed by Takanashi *et al.*[98] by XRD measurements. A conversion-electron Mössbauer spectroscopy (CEMS) analysis[99] clearly reveals that the $L1_0$ phase, characterized by a tetragonal distortion that is reflected in a large contribution of the quadrupole a interaction to the hyperfine pattern, is present in the $(Fe_1/Au_1)\times 20$ MLS. However, the amount of the $L1_0$ phase is only $\sim$30% of that expected for perfect layer growth. The vertical mass transport accompanying the

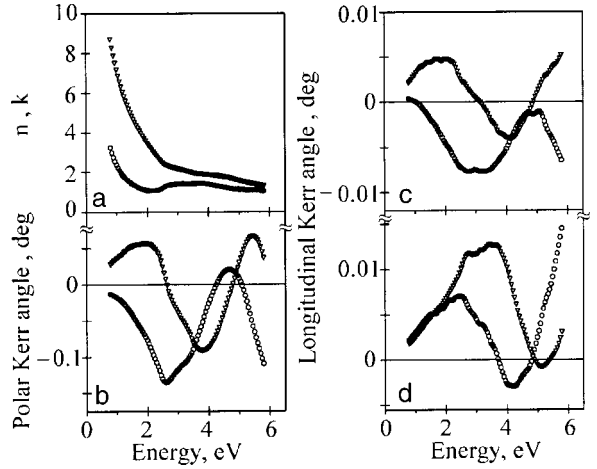

FIG. 30. Experimental results for Fe_1/Au_1 MLS: refractive index and extinction coefficient (a), polar Kerr rotation and ellipticity (b), longitudinal Kerr rotation and ellipticity for *s* (c) and *p* (d) light polarizations. In the panels the refractive index and rotation are depicted as circles, and the extinction coefficient and ellipticity as triangles.[95]

MLS growth leads to Fe aggregation, so that the resulting structure may be regarded as a mixture of a monolayer and bilayer (and to a less extent also trilayer) MLS. Nevertheless, it is enough to induce a strong perpendicular anisotropy, which forces the magnetization to the normal direction. The $L1_0$ phase disappears abruptly when the MLS modulation period is increased. For the $(Fe_2/Au_2)\times 10$ MLS, only traces of the component attributed to the tetragonally distorted phase can be found in the CEMS spectrum. The CEMS spectrum for the $(Fe_3/Au_3)\times 7$ sample resembles that measured for a single Fe trilayer film sandwiched between Au.[99]

6.1. Experimental results and data analysis

Most MO studies of the MLS employ polar magnetization geometry, PKE, and normal light incidence. The PKE configurations alone cannot be used, however, to study the MO orientation effects in a very rich family of magnetic layered structures. The reason is that the main structural anisotropy axis is perpendicular to the film surface, and no other basal planes exist. The only possibility is to use the polar and longitudinal (or equatorial) Kerr effect geometries simultaneously. This approach is more complicated, as additional data on the optical constants are required to extract the basic quantities—optical conductivity tensor components—underlying the MO spectra.

Figure 30 presents the complete set of experimentally obtained ellipsometric and magnetooptical spectra in both the polar and longitudinal magnetization geometry for the $Au(5\,nm)/(Fe_1/Au_1)\times 20/Au(30\,nm)/Fe(4\,nm)/MgO(001)$ sample. As is seen in Fig. 30a, the spectral dependence of the effective refractive index *n* and the extinction coefficient *k* of the sample exhibits an overall shape close to that of Au metal, with the well-known feature at the photon energy 2.5 eV, where there is a superposition of the Drude-like intraband transitions and the interband transition edge. Such a dependence can easily be understood by taking into account that the predominant parts of the sample are the Au overlayer and underlayer. The effective magnetooptical PKE rotation θ^{PK} and ellipticity η^{PK} spectra of the sample are shown in Fig. 30b. The essential points of the experimental θ^{PK} spectrum are the prominent negative peak centered at around 2.5 eV (i.e., in the Au plasma-edge spectral region), and a hump clearly visible near 3.2 eV. The θ^{PK} changes sign above 4 eV, and a positive peak at 4.7 eV is formed. The θ^{PK} enhancement at the plasma edge of Au (around 2.5 eV) is well explained by the classical optic multilayer model and is not related to the modification of the electronic structure of the intrinsic magnetic Fe_1/Au_1 multilayer. The corresponding η^{PK} spectrum changes sign at the energy of the plasma edge of Au and in the UV spectral region exhibits a two-peak structure with a negative peak at 3.8 eV and a positive one at 5.5 eV. The PKE spectra measured in the Fe_2/Au_2 and Fe_3/Au_3 superlattices (not shown) exhibit similar behavior to Fe_1/Au_1, with the peak structure in the UV spectral range shifted to higher energy. The main features and trends in the PKE spectra of Fe_n/Au_n superlattices modulated by integer atomic layers of Fe and Au are in agreement with those reported in Refs. 100 and 101. Similar characteristic structure in the PKE spectra in the UV spectral range (more distinct than in the multilayers) was observed in ultrathin Fe layers sandwiched by Au layers and was assigned to optical transitions involving quantum-well states.[102,103]

The corresponding complex LKE spectra measured in the longitudinal Kerr magnetization geometry at a 75° angle of incidence of the light are shown in Figs. 30c and 30d for *s* and *p* light polarizations, respectively. The measured θ^{LK} and η^{LK} appear one order of magnitude smaller than for the PKE. In the LKE spectra, the plasma edge of the Au overlayer and underlayer of the sample manifests itself as a peak or shoulder near 2.6 eV. As is seen in Figs. 30c and 3d, in the spectral region above 2.5 eV the θ^{LK} spectra are dominated by a peak at 3.2 and a minimum at around 5.0 eV for *s* polarization and a peak at 4.1 eV for *p* polarization. The corresponding features in the η^{LK} spectra are the peak centered at 4.1 for *s* polarization and the peaks at 3.4 eV and 5.1 eV for *p* polarization, respectively. The LKE spectra are consistent for the *s* and *p* light polarizations, and the optical functions *n* and *k* determined from the LKE data alone agree well with those measured directly by the ellipsometric method. It should be pointed out that one cannot expect direct correspondence between the shape of the spectra and the position of the energy peaks measured in polar and longitudinal geometry because the LKE spectra are strongly dependent on the angle of incidence of the light (particularly for the *p* polarization, when the angle of incidence approaches its principal value, equal to about 75° for the structures studied). Therefore, the direct comparison of the PKE and LKE spectra is not adequate, and appropriate treatment should be done by evaluation of the optical conductivity tensor components from the measured spectra. It is well known that the absorptive part of the tensor only, but not the Kerr rotation itself, is directly connected with the optical transitions between electronic states, their strengths and energy positions. Therefore, in the following, we will consider the energy dependence of the conductivity tensor components underlying the MO effects for the superlattices studied.

The effective optical conductivity tensor components, diagonal $\sigma_{xx}^{\rm eff}$ and off-diagonal $\omega\sigma_{xy}^{\rm eff}$, $\omega\sigma_{xz}^{\rm eff}$, were determined with the use of Eq. (3) from the measured optical and MO

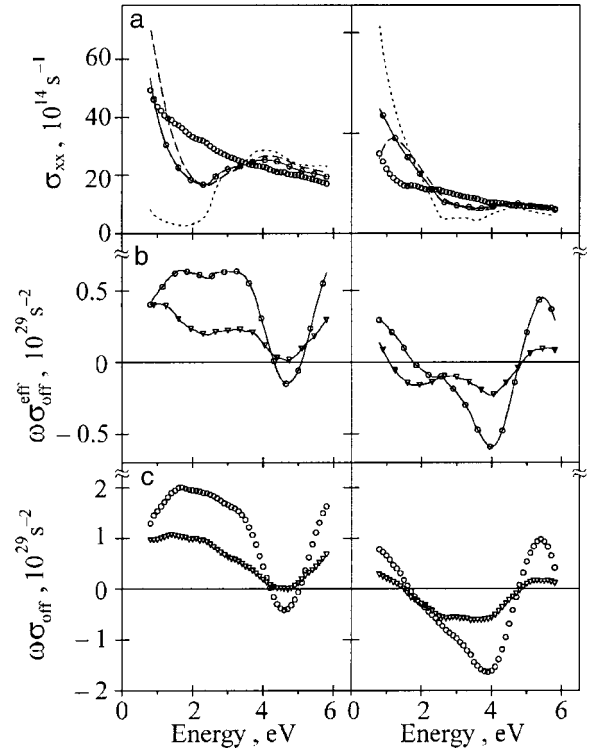

FIG. 31. Experimental absorptive (left panels) and dispersive (right panels) parts of the optical conductivity for the Fe_1/Au_1 sample. In the panels (a) the effective diagonal tensor components of the whole sample (solid lines with circles), the buffer sample (dashed lines), thick Au film (dotted lines), and the extracted (see text) component of the intrinsic Fe_1/Au_1 structure (circles) are shown. In the panels (b) the off-diagonal effective tensor components derived from the polar (solid lines with circles) and longitudinal (solid lines with triangles) Kerr effect are shown. In the panels (c) are the extracted off-diagonal tensor components of the intrinsic magnetic Fe_1/Au_1 structure derived from PKE (circles) and LKE (triangles).[95]

spectra according to Eq. (2) for the PKE and Eq. (6) for the LKE. The Fe_n/Au_n superlattices studied are two-dimensional structures and can exhibit optical anisotropy (i.e., the σ_{xx} and σ_{zz} tensor components can differ). Consequently, Eq. (5) for an optically anisotropic medium should be used instead of Eq. (6) to determine the off-diagonal tensor component. Unfortunately, in the case of thin *metallic* films or MLS direct ellipsometric measurements allow one to determine the $\sigma_{xx}^{\rm eff}$ tensor component only. As will be shown in the next Section, the errors caused by the using Eq. (6) for an optically isotropic medium to extract $\sigma_{xz}^{\rm eff}$ from LKE data are of little importance for the Fe_n/Au_n.

The results for the spectra of the effective complex optical conductivity $\sigma_{xx}^{\rm eff}$, $\omega\sigma_{xy}^{\rm eff}$, and $\omega\sigma_{xz}^{\rm eff}$ of the Au(5 nm)/$(Fe_1/Au_1)\times 20$/Au(30 nm)/Fe(4 nm)/MgO(001) sample are presented in Fig. 31a and 3b. In Fig. 31a the σ_{xx} spectra of a 100 nm thick fcc Au film deposited on GaAs(001) and of the buffer sample Au(30 nm)/Fe(4 nm)/MgO(001) used as the substrate for growing the Fe_n/Au_n superlattices are also included. As can be seen from Fig. 31a there is a significant difference between the effective $\sigma_{xx}^{\rm eff}$ spectra for the whole structure and the buffer sample as compared to that of the Au film in the spectral range below 2.5 eV. The rapid changes of the optical constants at the energy 2.5 eV caused by onset of Au interband transitions are clearly visible for all the samples. The characteristic features of the absorptive part of the $\omega\sigma_{xy}^{\rm eff}$ spectrum (Fig. 31b, solid lines with circles) of the whole structure are two broad peaks of comparable amplitude centered at around 1.6 and 3.3 eV and a negative minimum at 4.7 eV. The dispersive part of the $\omega\sigma_{xy}^{\rm eff}$ is dominated by a negative peak at 3.9 eV and a positive one at 5.3 eV. The complex $\omega\sigma_{xy}^{\rm eff}(\omega)$ functions (Fig. 31b, solid lines with triangles) evaluated independently from the LKE data measured for *s* and *p* light polarization are the same. As compared to the energy dependence of $\omega\sigma_{xy}^{\rm eff}(\omega)$, significant differences between the shape and the magnitude of the spectra are clearly visible. The IR peak position in the absorptive part of $\omega\sigma_{xz}^{\rm eff}$ shifts to lower energy, and the spectrum amplitude is much smaller.

The spectra of the conductivity tensor components discussed above represent the effective tensor components of the whole complex sample composed of the specific magnetic Fe_n/Au_n structure and the Au cap layer and underlayer film. To compare the theoretical *ab initio* calculations with the experiment and to discuss the origin of the magnetooptical and MOA effects of the magnetic superlattices, the tensor components for the intrinsic magnetic Fe_n/Au_n structure alone should be extracted from the experimental data. For this purpose we adopted the phenomenological matrix formalism based on the Maxwell theory, providing computer modeling of the MO response for a given structure (known as multi-reflection calculation).[104] The procedure assumes that the dielectric tensors of the constituent layers of the structure and their thicknesses are known. In our calculation, the thicknesses of the constituent layers determined from the technological data were used. To avoid possible uncertainties and to obtain the most precise results, the optical and magnetooptical response of the buffer underlying the Fe_n/Au_n structure, composed of Au(30 nm)/Fe(4 nm)/MgO(001), was directly measured with the use of a control sample and was subsequently used in the multi-reflection calculations. Finally, a two-layer system was considered, composed of the nonmagnetic Au cover layer and the magnetic $(Fe_n/Au_n)\times N$ superlattice on the Au(30 nm)/Fe(4 nm)/MgO(100) buffer substrate. In the procedure, the contribution of a single layer of given thickness is determined through its characteristic matrix, composed of the medium boundary and the medium propagation matrices.[104] The overall structure of the film is treated as a single layer with the parameters expressed in terms of those of individual sublayers.

The unknown tensor components of the intrinsic $(Fe_1/Au_1)\times N$ MLS structure were extracted by solving numerically the multi-reflection equations. The results for the Fe_1/Au_1 structure are shown in Fig. 31a for σ_{xx} (circles) and in Fig. 31c for $\omega\sigma_{xy}$ (circles) and $\omega\sigma_{xz}$ (triangles). The spectra represent the results after eliminating the MO contribution from the complex underlayer and Au overlayer. In the following discussion, the off-diagonal component $\omega\sigma_{xy}$ for the case of magnetization **M** parallel to the (001) direction will be denoted as $\omega\sigma_{\rm off}^{\parallel}$, whereas for $\omega\sigma_{xz}$ with the magnetization **M** perpendicular to the (001) direction we will use the notation $\omega\sigma_{\rm off}^{\perp}$. As compared to the effective tensor components, the feature related to the plasma edge of Au at 2.5 eV disappears for the $\omega\sigma_{\rm off}^{\parallel}$ and $\omega\sigma_{\rm off}^{\perp}$ spectra. The overall structure of the extracted off-diagonal tensor components of the magnetic superlattice alone is similar to that of the effec-

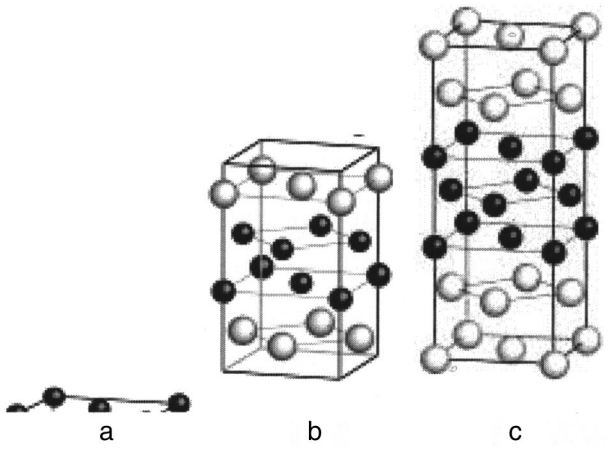

FIG. 32. The unit cells used for Fe_1/Au_1 ($L1_0$) (a), Fe_2/Au_2 (b), and Fe_3/Au_3 MLS (c). The black spheres are Fe atoms and the shaded ones are Au atoms.[95]

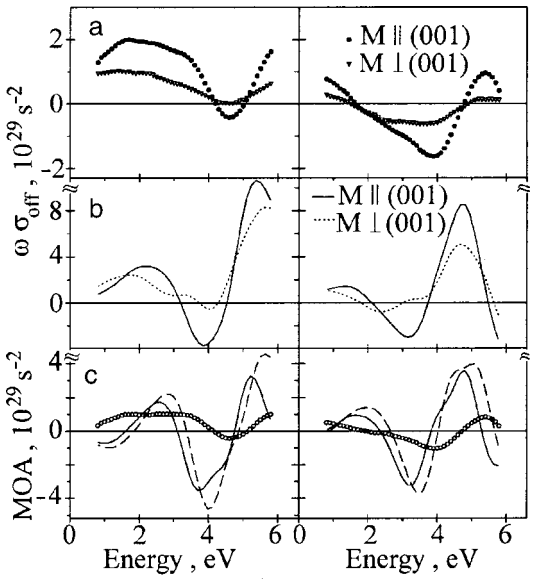

FIG. 33. Absorptive (left panels) and dispersive (right panels) parts of the off-diagonal conductivity tensor of Fe_1/Au_1 MLS; experimental results (a), LSDA calculated spectra for Fe_1/Au_1 MLS (b), the MO anisotropy spectra (c) (symbols represent experimental data, solid lines LSDA, and dashed lines LDA+U theory).[95]

tive ones, and the most significant changes in the spectra appear in the IR spectral range. The most important conclusion is that both the effective and the extracted off-diagonal tensor components of the magnetic superlattice exhibit large orientational anisotropy with respect to the magnetization direction.

6.2. Comparison of the experimental and theoretical spectra in Fe_n/Au_n MLS

The band structure calculations in Ref. 95 considered an Fe_1/Au_1 MLS system with one-by-one stacking of (001) planes whose structure can be regarded as $L1_0$-type (Fig. 32a). The lattice parameters used were chosen as follows. The in-plane atomic spacing was taken as an average between the Au and Fe bulk values ($a=4.066$ Å). The out-of-plane lattice spacing for the Fe_1/Au_1 MLS was taken from the recent work of Sato *et al.*[101] as 1.915 Å, which is slightly lower than the previously published value[98,105] used in our previous calculation.[106] The structures Fe_2/Au_2 and Fe_3/Au_3 are presented in Figs. 32b and 32c. There is no experimental knowledge about the three interlayer spacings, Au-Au, Au-Fe, and Fe-Fe, in these structures. The Au-Au spacing was taken the same as in fcc Au, 2.04 Å. For the Au-Fe spacing, the value 1.74 Å can be derived from the rigid sphere model as a mean between the fcc Au (2.04 Å) and bcc Fe (1.43 Å) bulk values. Similar values for the Au-Fe interlayer spacings have been obtained by total energy minimization using the LMTO *ab initio* calculations. Using the experimentally determined superlattice periods in Fe_2/Au_2 and Fe_3/Au_3 MLS structures published in Ref. 101 as constraints, a one-parameter minimization was performed. As a result, values of 1.76 Å and 1.74 Å for the Au-Fe interlayer spacing and corresponding values of 1.69 and 1.58 Å for the Fe-Fe interlayer spacing were obtained for the Fe_2/Au_2 and Fe_3/Au_3 MLS, respectively.

For a quantitative analysis of the magnetooptical anisotropy it is convenient to present the anisotropy as the difference between the off-diagonal conductivity tensor components $\omega\sigma^{\parallel}_{\rm off}-\omega\sigma^{\perp}_{\rm off}$, where the factor ω provides compatibility with the $\omega\sigma$ spectra themselves. In Fig. 33 the $\omega\sigma^{\parallel}_{\rm off}$ and $\omega\sigma^{\perp}_{\rm off}$ spectra of the MLS for the nominal Fe_1/Au_1 structure, extracted from the experimental PKE and LKE data as described in the previous Section, and the MOA are compared to the corresponding spectra calculated for the ideal Fe_1/Au_1 $L1_0$ structure.

Overall, both the spectral shape and the magnitude of the experimental optical conductivity spectra are qualitatively reproduced by the LSDA calculations. However, the positions of the calculated prominent peaks in the absorptive part of $\omega\sigma^{\parallel}_{\rm off}$ at 3.8 eV and 5.2 eV are shifted to lower energies as compared to the experiment. Also, the theoretical calculations predict a larger MOA in comparison with the experimental value in the nominal Fe_1/Au_1 structure. One of the possible reasons is that due to the inexact treatment of the electron exchange and correlations the LSDA underestimates the binding energy of *d* states and the threshold of interband transitions in noble metals as compared to photoemission and optical measurements.[107,108]

It seems quite likely that the use of a more appropriate approximation for the self-energy can give rise to a shift of the quasiparticle energy bands originating from the Au 5*d* states and, as a result, to a better agreement between the theory and the experiment. In Ref. 95 the LDA+U method[109] was adopted as a step beyond the LSDA in the treatment of the electronic correlations. As was discussed in Refs. 110 and 111, the LDA+U method can be considered as a rough approximation to both the self-interaction correction and to the self-energy of a system with strongly interacting electrons. Moreover, it has been found that the application of the LDA+U method to pure noble metals allows one to improve the calculated energy position of the threshold of the interband optical transitions and provides a better approach to the description of their MO spectra.[112] In the case of the Fe_1/Au_1 MLS a value $U_{\rm eff}=2.5$ eV was applied to Au 5*d* states.[95] This value of $U_{\rm eff}$, considered as a parameter of the model, was found to give the best agreement between the calculated and experimental optical conductivity for fcc Au.

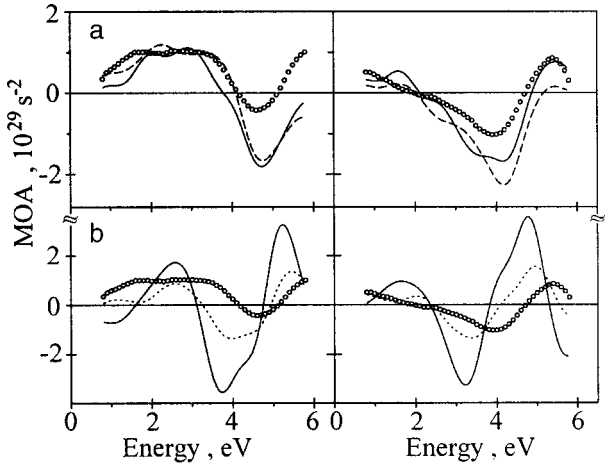

FIG. 34. Absorptive (left panels) and dispersive (right panels) part of the MOA measured for the Fe_1/Au_1 MLS (circles) compared with LSDA calculated spectra; MOA modeled with effective optical conductivity: $\omega\sigma_{\rm off} = x\omega\sigma_{\rm off}^{1/1} + (1-x)\omega\sigma_{\rm off}^{2/2}$ for $x=0.3$ (solid lines) and calculated for supercell containing 1/1 and 2/2 substructures (see Fig. 35) (dashed lines) (a); MOA calculated for perfect Fe_1/Au_1 structure (solid lines) and for the structure with the substitutional disorder (see Fig. 36) (dotted lines) (b).[95]

The use of the LDA+U approximation for Fe_1/Au_1 MLS does improve slightly the calculated energy position of the peaks of the off-diagonal optical conductivity for both orientations of the magnetization (not shown), but there is no improvement in the shape of the spectra. Comparing the MOA calculated within the LSDA and LDA+U methods (see Fig. 33c) to the experimental spectrum, one can conclude that the LDA+U approximation does not improve the description of the MOA in the nominal Fe_1/Au_1 structure.

Another and maybe even more important source of discrepancies is that the sample studied is not an ideal monoatomic Fe_1/Au_1 MLS of $L1_0$ structure but rather a mixture of mono- and bilayer structures. Having this in mind, we modeled the effective optical conductivity of the structure by a weighted average of the conductivities calculated for the Fe_1/Au_1 and Fe_2/Au_2 MLS: $\omega\sigma_{\rm off} = x\omega\sigma_{\rm off}^{1/1} + (1-x)\omega\sigma_{\rm off}^{2/2}$. The best agreement between the theory and the experiment, both in the MOA (Fig. 34a) and in the shape of the off-diagonal optical conductivity (not shown), was achieved with $x=0.3$. This value agrees well with the results of the CEMS analysis.[99]

In a more advanced approach, the interface roughness was studied by calculating the MO properties of the mixture of mono- and bilayers, distributed over the whole structure. The composed Fe/Au structure was modeled using a large supercell containing side-by-side Fe_1/Au_1 and Fe_2/Au_2 component structures spread over 3 and 7 lattice constants (see Fig. 35). This ratio of the areas was chosen in correspondence with the simple procedure described above, in which the resulting spectra were expressed as the sum of individual Fe_1/Au_1 and Fe_2/Au_2 contributions. The results of the *ab initio* calculations for the composed structure are shown in Fig. 34a, from which an even better overall agreement between the theory and experiment both in the shape and the amplitude of the MOA spectra is observed. As the opposite case to the structure composed of well-defined mono- and bi-layers, a series of modelings was performed for examination of the effect of substitutional disorder on the MO spectra and MOA. Although the solubility of Au in bulk bcc Fe at temperatures up to 400 K is negligible,[113] enhanced solubility of Au within the Fe layer up to 3% was observed for a 70 Å thick Fe film on Au(001).[114] Even up to one order greater substitutional disorder was reported for the Fe/Au(001) structures in the monolayer regime by Blum *et al.*[97] The incorporation of Au atoms in the Fe layers can be considered as an explanation (as discussed in Ref. 97) for the larger Fe-Au interlayer spacing observed experimentally in the Fe_1/Au_1 structure, as compared to the spacings derived under the assumption of rigid atomic spheres of bulk Fe and Au metals. The effect will lead to larger effective Fe-Fe and Fe-Au interlayer spacings in Fe_n/Au_n MLS. The particular model structure used in the calculations is presented in Fig. 36. The structure is composed of alternating atomic planes of Fe and Au in which one per nine atoms is interchanged by Au and Fe, respectively (an interlayer spacing of 1.915 Å was taken). It was found that the moderate substitutional disorder leads mainly to a scaling of the amplitudes of the calculated $\sigma_{\rm off}^{\parallel}$ and MOA spectra without significant changes of their shape. In Fig. 34b the MOA spectra calculated for the model structure (see Fig. 36) are shown. It is seen that an approximately twofold reduction of the MOA magnitude is observed when the level of the substitution is 11%.

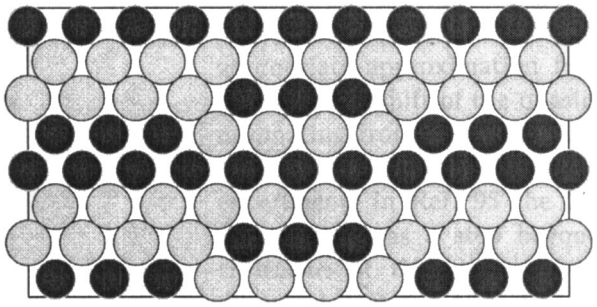

FIG. 35. Unit cell (doubled along *z* direction) of the Fe/Au structure composed of the 1/1 and 2/2 substructures (black spheres are Fe atoms and shaded ones are Au atoms).[95]

Figures 37 and 38 show the experimentally obtained $\omega\sigma_{\rm off}^{\parallel}$ and $\omega\sigma_{\rm off}^{\perp}$ spectra in the MLS of nominal Fe_2/Au_2 and Fe_3/Au_3 structures for two orientations of the magnetization: $\mathbf{M}\parallel(001)$ and $\mathbf{M}\perp(001)$, together with the MOA, in comparison with the corresponding spectra calculated for the ideal Fe_2/Au_2 and Fe_3/Au_3 structures. For Fe_2/Au_2 MLS, the overall shape of the theoretical spectra corresponds well to the experimental ones (Fig. 37b), and a better agreement of

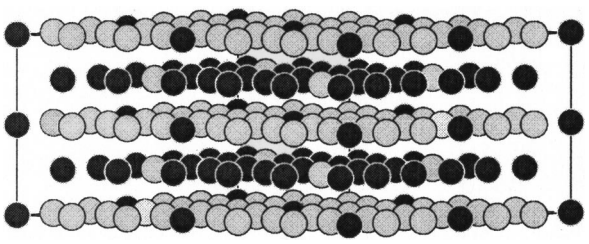

FIG. 36. Doubled $c(3/\sqrt{2}\times 3/\sqrt{2})$ unit cell used for modeling of alloying effect in the Fe/Au MLS (black spheres are Fe atoms and shaded ones are Au atoms).[95]

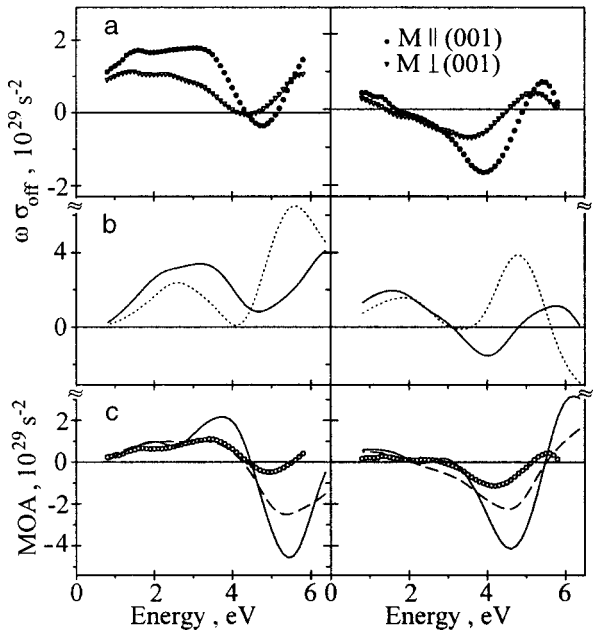

FIG. 37. Absorptive (left panels) and dispersive (right panels) parts of the off-diagonal conductivity tensor of Fe_2/Au_2 MLS; experimental results (a), LSDA calculated spectra (b). In the panels (c) the MOA spectra are shown (symbols represent experimental data, solid lines LSDA calculations for perfect Fe_2/Au_2 MLS, and dashed lines calculations for the structure with the substitutional disorder).[95]

the MOA as compared to the previously discussed case of the ideal Fe_1/Au_1 (see Fig. 33) is observed (Fig. 37c). The reason is that the ideal Fe_2/Au_2 MLS is a better approximation to the real experimental situation than was the case for the Fe_1/Au_1 MLS.[99] However, in the high-energy part of the spectra, above 4 eV, the $\omega\sigma_{\rm off}^{\parallel}$ and $\omega\sigma_{\rm off}^{\perp}$ and MOA amplitudes remain considerably higher than the ones obtained experimentally. To examine the origin of such a discrepancy, the influence of the substitutional disorder on the MOA was modeled in the case of the Fe_2/Au_2 MLS. In Fig. 37c the MOA spectra calculated for a Fe_2/Au_2 MLS model structure are shown. The model structure used in this case is similar to that considered for the case of Fe_1/Au_1 MLS (Fig. 36) with the same substitutional disorder level and is composed of double numbers of the Fe-rich and Au-rich atomic layers, with the experimental modulation period of 7.25 Å. It was found that the MOA magnitude for the Fe_2/Au_2 MLS in the high-energy part of the theoretical spectra is markedly reduced and is closest to the experimental values when the effect of the limited substitutional disorder at a level of the order of 10% is taken into account.

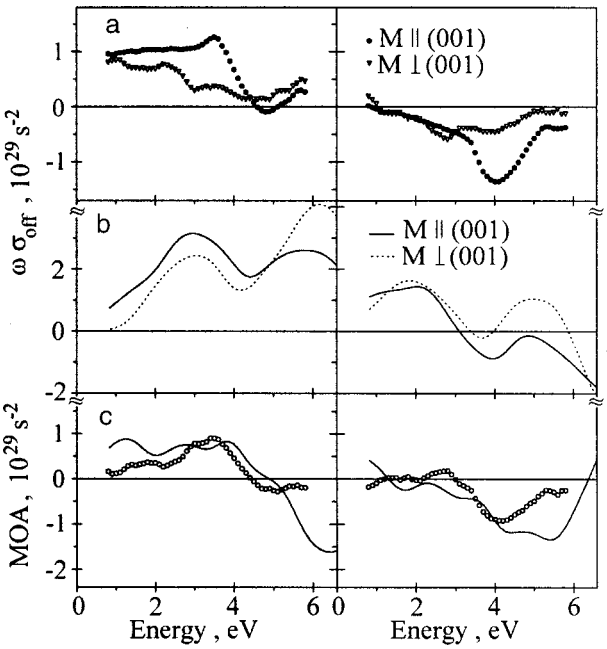

FIG. 38. Absorptive (left panels) and dispersive (right panels) parts of the off-diagonal conductivity tensor of Fe_3/Au_3 MLS; experimental results (a), LSDA calculated spectra (b). In the panels (c) the MOA spectra are shown (symbols represent experimental data, solid lines represent LSDA theory for perfect Fe_3/Au_3 MLS).[95]

The experimental and theoretical results for the Fe_3/Au_3 structure are presented in Fig. 38. The overall agreement between the calculated and observed $\omega\sigma_{\rm off}^{\parallel}$ and $\omega\sigma_{\rm off}^{\perp}$ spectra for the Fe_3/Au_3 structure is less satisfactory than for the Fe_2/Au_2 MLS. One of the possible reasons is that the real structure of the Fe_3/Au_3 superlattice is far from the ideal model considered. Nevertheless, both the theoretical and the experimental MOA spectra are of comparable magnitude. The modeling of the interfacial roughness effects and alloying for the Fe_3/Au_3 structure from first principles (much more complicated than for the simpler structures) is currently in progress.

Some conclusions can be drawn from the modeling performed: (i) The magnitude of the off-diagonal optical conductivity and MOA spectra is very sensitive to the actual structure at the interfaces, and thus MO spectroscopy can provide useful independent information about the Fe/Au MLS structures, complementary to that derived from CEMS measurements. (ii) In the modeling of the roughness effect, even using areas of the component structures as small as a few atomic spacings leads to a result qualitatively close to that obtained from a simple additive formula for the superposition of the spectra. (iii) The magnitude of the MOA decreases with increasing number of Fe and Au atomic layers of the superlattices. (iv) The limited substitutional disorder does not suppress the MOA effect in the Fe_n/Au_n MLS.

As was mentioned in Sec. 6.1, Fe_n/Au_n MLS can exhibit optical anisotropy, but the σ_{zz} component of the optical conductivity tensor is not directly available in the experiment. On the other hand, both σ_{xx} and σ_{zz} can be easily obtained from the calculations and allow us to verify numerically the correctness of using Eq. (6) instead of Eq. (5) to determine $\omega\sigma_{\rm off}^{\perp}$ from the experimental data. The absorptive parts of the diagonal components of the conductivity tensor calculated for ideal Fe_1/Au_1 and Fe_2/Au_2 structures are shown in Figs. 39a and 39c. The largest difference between the σ_{xx} and σ_{zz} spectra is observed for the Fe_1/Au_1 MLS below a photon energy of about 3.5 eV. For the Fe_2/Au_2 and also Fe_3/Au_3 (not shown in the figure) MLS the calculated optical anisotropy is significantly smaller. The theoretical conductivity tensor components were used to calculate the complex longitudinal Kerr angle according to the exact formula (5). Then the approximate $\omega\sigma_{\rm off}^{\perp}$ was derived from the calculated LKE angle using the formula (6) for an isotropic medium. The off-diagonal conductivity spectra recalculated in this way are compared to $\omega\sigma_{\rm off}^{\perp}$ obtained directly from the *ab initio* cal-

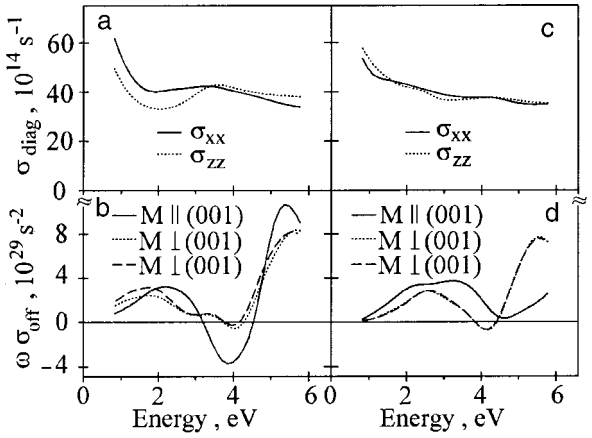

FIG. 39. LSDA calculated absorptive parts of the diagonal σ_{xx} and σ_{zz} (panels a and c) and off-diagonal $\omega\sigma^{\parallel}_{\text{off}}$ and $\omega\sigma^{\perp}_{\text{off}}$ (panels b and d) components of the optical conductivity tensor for Fe_1/Au_1 (left panels) and Fe_2/Au_2 (right panels) MLS. The *ab initio* calculated $\omega\sigma^{\perp}_{\text{off}}$ spectra are represented by dotted lines and the corrected ones by dashed lines (see text).[95]

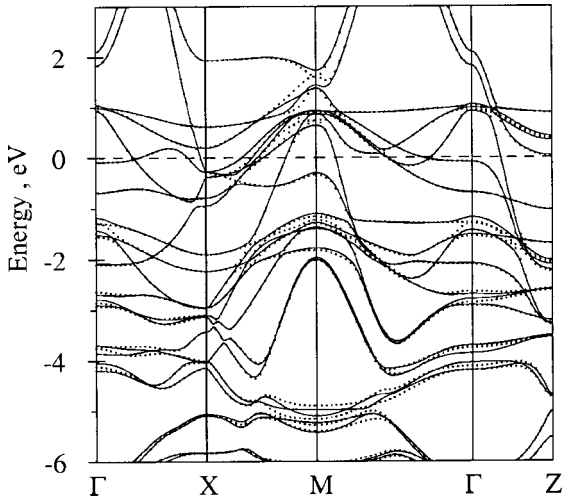

FIG. 41. LSDA energy band structure of the $L1_0$ ordered Fe_1/Au_1 MLS for two orientations of magnetization: $\mathbf{M}\parallel(001)$ (solid lines), and $\mathbf{M}\perp(001)$ (dotted lines).[95]

culations in Fig. 39b and 39d. A marked difference between the "exact" and "approximate" $\omega\sigma^{\perp}_{\text{off}}$ values is observed in the IR range for the Fe_1/Au_1 MLS only. It diminishes to a negligible value above this energy region and can be completely neglected in the whole energy range for the Fe_2/Au_2 and Fe_3/Au_3 structures. The possible errors caused by using Eq. (6) instead of Eq. (5) are then small and do not affect the conclusion that the large MOA is related to the anisotropy of the off-diagonal conductivity tensor components.

6.3. Microscopic origin of the magnetooptical and orbital moment anisotropy in Fe_n/Au_n MLS

To understand better the microscopic origin of the MOA, let us consider in detail the electronic structure of the Fe_1/Au_1 $L1_0$ MLS. Spin-projected densities of Fe and Au *d* states are shown in Fig. 40, and the calculated spin and orbital magnetic moments are summarized in Table I. Within the Au(Fe) monolayer, each atom is surrounded by four other Au(Fe) monolayer, each atom is surrounded by four other Au(Fe) atoms at a separation corresponding to the nearest-neighbor spacing in bulk Au(Fe). Because of the smaller number of the nearest neighbors of the same type, both the Fe and Au *d* states are much narrower than in the corresponding bulk metals. As a result, the majority spin Fe *d* states are fully occupied, which leads to a significant enhancement of Fe spin magnetic moment ($2.87\mu_B$) compared to the value of $2.2\mu_B$ for bulk Fe. This enhanced magnetization has been observed,[105] but the experimental value of $2.75\pm0.25\mu_B$ is somewhat smaller than the calculated one. Such a difference can be explained by the deviation of the sample structure from the ideal $L1_0$.

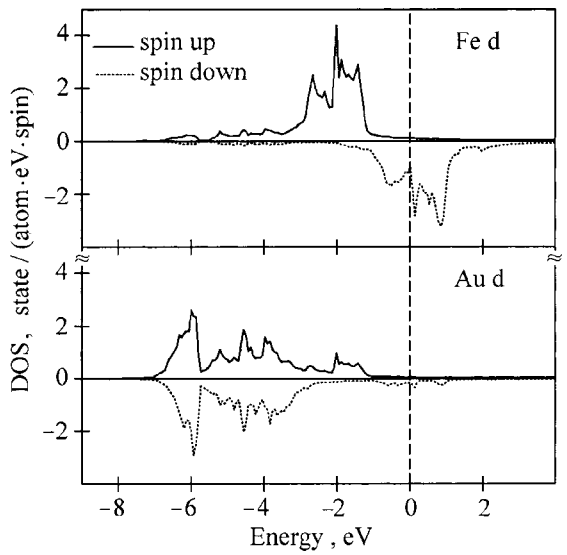

FIG. 40. LSDA spin-projected fully-relativistic partial DOS (in states/(atom-eV-spin)) of the $L1_0$ ordered Fe_1/Au_1 MLS.[95]

The energy bands in Fe_1/Au_1 MLS calculated for different magnetization directions are shown in Fig. 41. This comparison is useful as it helps to identify the states that are sensitive to the change of the magnetization direction and, consequently, can potentially give a contribution to the MOA, MCA, and the anisotropy of the orbital moment. In Fe_1/Au_1 MLS, for example, such states are the electronic states at about -4.0, -2.8, and -1.4 eV in the vicinity of the Γ point and those with energies -5.2, -1.5, and -0.5–1.8 eV located around the *M* symmetry point as well as along the Γ–*X*–*M*–Γ directions.

Comparing the values of the magnetic moments calculated for different magnetization directions, one can see from Table V that the Fe spin moments are almost independent of the magnetization direction. At the same time the anisotropy of the Fe orbital moment, which is determined mainly by the Fe *d* states, is quite large and is of the same order of magnitude as was experimentally observed in Co/Au MLS.[115] This behavior could be expected, as in the presence of the SO interaction the anisotropy of the orbital moment is of the order of ξ/Δ, where ξ is the SO coupling strength and Δ is the crystal field splitting, while the anisotropy of the spin moment is proportional to $(\xi/\Delta)^2$ (Ref. 116). As the Au *d* states are fully occupied, the spin and orbital moments at the Au site are small and depend weakly on the magnetization direction.

To understand better the anisotropic behavior of the Fe

TABLE V. Calculated spin M_S and orbital M_L magnetic moments (in μ_B) of Fe_1/Au_1 versus magnetization direction.[95]

		$\mathbf{M}\parallel$ [001]		$\mathbf{M}\perp$ [001]	
Atom	State	M_S	M_L	M_S	M_L
	s	0.0097	0.0000	0.0098	0.0000
	p	−0.0033	−0.0006	−0.0030	0.0005
Fe	*d*	2.8593	0.0920	2.8612	0.0587
	f	0.0019	−0.0008	0.0019	−0.0010
	total	2.8676	0.0906	2.8698	0.0582
	s	−0.0346	0.0000	−0.0345	0.0000
	p	−0.0567	0.0035	−0.0566	0.0058
Au	*d*	0.1085	0.0293	0.1098	0.0300
	f	0.0100	−0.0014	0.0100	−0.0016
	total	0.0272	0.0315	0.0287	0.0342

and Au orbital magnetic moments, let us introduce a site-dependent function $dm_l(E)$ given by

$$dm_{tl}(E)=\sum_{n\mathbf{k}}\langle\Psi_{tl}^{n\mathbf{k}}|\hat{l}_z|\Psi_{tl}^{n\mathbf{k}}\rangle\,\delta(E-E_{n\mathbf{k}}), \tag{17}$$

where $\hat{l}_z$ is the z projection of the angular momentum operator, $E_{n\mathbf{k}}$ and $\Psi_{tl}^{n\mathbf{k}}$ are the energy of the nth band and the part of the corresponding LMTO wave function formed by the states with angular momentum l inside the atomic sphere centered at the site t, respectively (see Ref. 95). In analogy to the l-projected density of states, $dm_{tl}(E)$ can be referred to as the site- and l-projected density of the expectation value of $\hat{l}_z$. This quantity has purely relativistic origins, and when the SO interaction is equal to zero one has $dm_{tl}(E)\equiv 0$. As Van Vleck[117] showed for a free ion, the absence of orbital degeneracy is a sufficient condition for the quenching of the orbital moment, which means that the first-order contribution should vanish: $\langle\Psi_{\mathbf{k}}|\hat{l}_z|\Psi_{\mathbf{k}}\rangle=0$. Thus $dm_{tl}(E)$ can be considered as a measure of the unquenching of the orbital moment due to the SO interaction.

Furthermore, just as the number of states is defined as the integral of the DOS, we can define the integral of $dm_{tl}(E)$ as

$$m_{tl}(E)=\int_{E_b}^{E} dm_{tl}(E)dE, \tag{18}$$

where E_b is the bottom of the valence band. Then the orbital moment m_l at the site t is given by

$$m_l\equiv m_{tl}(E_F) \tag{19}$$

(here and henceforth we will drop the index t for simplicity).

Both $dm_l(E)$ and $m_l(E)$ are defined in a local coordinate system chosen in such a way that the z axis is directed along the magnetization and, consequently, they depend on the relative orientation of the magnetization with respect to the crystallographic axes. In the case of Fe_n/Au_n MLS we will use the notations $m_l^{\parallel}(E)$ and $m_l^{\perp}(E)$ for $m_l(E)$ calculated with $\mathbf{M}\parallel(001)$ and $\mathbf{M}\perp(001)$, respectively. The difference of these two functions

$$\Delta m_l(E)=m_l^{\parallel}(E)-m_l^{\perp}(E) \tag{20}$$

can provide useful information on the orientation dependence of the orbital moment. Figure 42 shows the functions $dm_l(E)$, $m_l(E)$, and $\Delta m_l(E)$ calculated for Fe and Au sites in Fe_1/Au_1 MLS. Here and in the rest of the paper we will only consider the contribution from the d orbitals to the m_l related functions. All three functions show strong energy dependence. The variations of the functions at Au and Fe sites are comparable, but the Au d orbital moment $m_l(E_F)$ is significantly smaller, as the Au d states are almost fully occupied (see Fig. 40). The anisotropy of the Au orbital moment $\Delta m_l(E)$ vanishes at E_F. At about -1.2 eV the Fe $d_\uparrow$ states are already occupied, while the $d_\downarrow$ states are still almost empty (Fig. 40), and, as a result, both $m_l(E)$ and $\Delta m_l(E)$ are zero at this energy. At the Fermi energy, however, strong anisotropy of Fe d orbital moment was observed.

To better understand such behavior, let us analyze the orbital character of the partial density of Fe d states in the vicinity of the Fermi level (Fig. 43). It should be recalled that the only nonzero matrix elements of the $\hat{l}_z$ operator calcu-

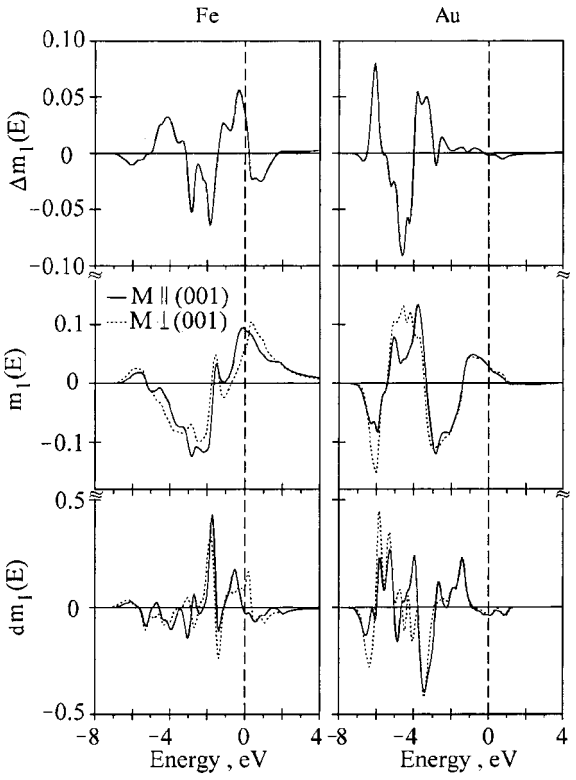

FIG. 42. The $dm_l(E)$ and $m_l(E)$ for two orientations of magnetization together with $\Delta m_l(E)$ for the $L1_0$ ordered Fe_1/Au_1 MLS (see text).[95]

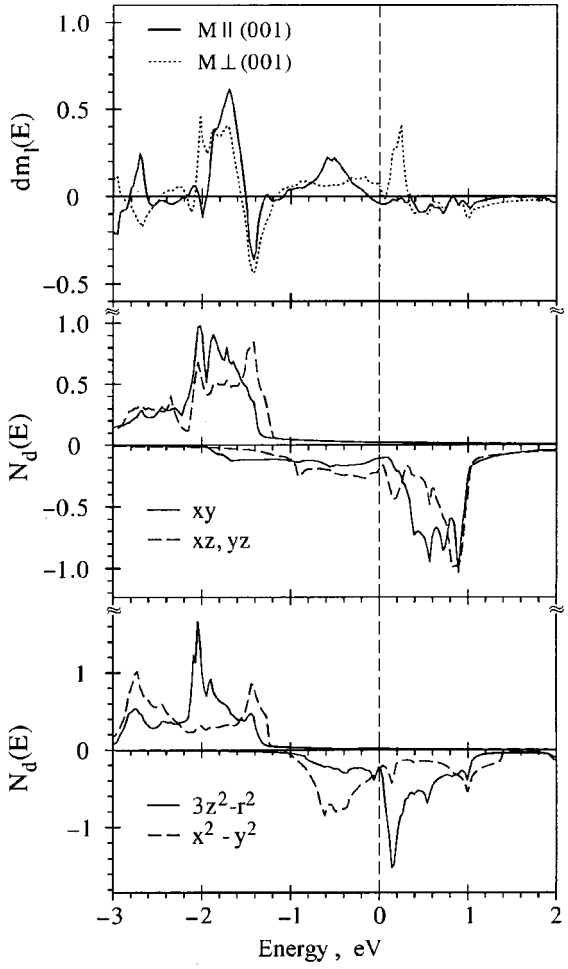

FIG. 43. The d orbitals projected $dm_l(E)$ on Fe site for two orientations of magnetization and d-partial density of states (in states/(atom · eV · spin)) for the $L1_0$ ordered Fe_1/Au_1 MLS.[95]

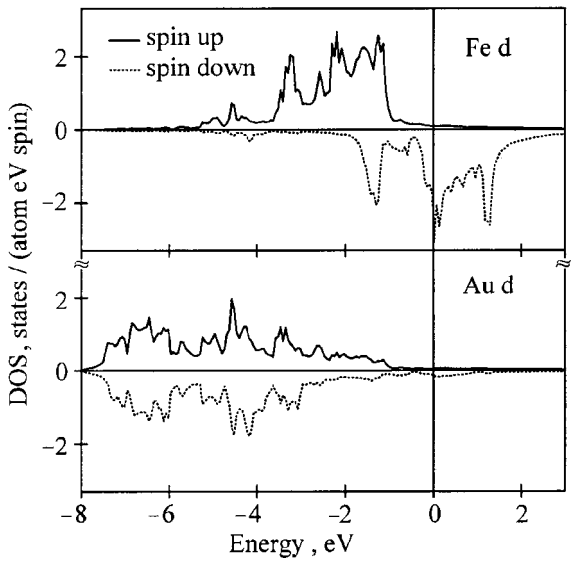

FIG. 44. LSDA spin-projected fully-relativistic partial DOS (in states/(atom · eV · spin)) of the Fe_2/Au_2 MLS.[95]

lated between real harmonics with $l=2$ are $|\langle d_{x^2-y^2}|\hat{l}_z|d_{xy}\rangle|=2$ and $|\langle d_{xz}|\hat{l}_z|d_{yz}\rangle|=1$. Hence, the largest contribution to $m_l(E)$ can be expected from the $d_{x^2-y^2}$ and d_{xy} orbitals. Also, it should be pointed out that, in contrast to the case of transition metal films considered in Ref. 90, in which the on-site SO interaction is the only source of unquenching of the orbital moment, in a compound consisting of $3d$ metal atoms, with a large magnetization and a relatively weak SO coupling, and $5d$ atoms, for which the SO coupling is strong, the unquenching of the $3d$ orbital moment can be caused to a great extent by the $3d-5d$ hybridization. In the particular case of Fe_1/Au_1 MLS there is a peak at -0.5 eV in the density of Fe $d_{x^2-y^2}$ states (Fig. 43), which hybridize rather strongly with Au d states. The density of d_{xy} states is constant in this energy interval and, as a consequence, the $dm_l(E)$ has a maximum at this energy for $\mathbf{M}\|(001)$. The states that form the peak of the DOS just above the Fermi level are predominantly of $d_{3z^2-r^2}$ character, and they do not contribute to $dm_l(E)$. When the magnetization direction changes from $\mathbf{M}\|(001)$ to $\mathbf{M}\perp(001)$ the local coordinate system in which $dm_l(E)$ is calculated should also be changed accordingly. In the new coordinate system the $d_{3z^2-r^2}$ orbital transforms into a linear combination of the $d_{3z^2-r^2}$ and $d_{x^2-y^2}$ orbitals, and a sharp peak of $dm_l^{\perp}(E)$ appears above the Fermi level and follows the shape of the corresponding peak of the density of $d_{3z^2-r^2}$ states. At the same time, the $d_{x^2-y^2}$ orbital, which plays the crucial role in the formation of the peak of $dm_l^{\|}(E)$ at -0.5 eV, transforms into $\sqrt{3}/2\ d_{3z^2-r^2}+1/2\ d_{x^2-y^2}$, and, as a result of the reduced contribution of the $d_{x^2-y^2}$ orbital to the wave function, $dm_l^{\perp}(E)$ is suppressed below the Fermi level. These simple considerations allow one to explain the strong dependence of the Fe orbital moment on the magnetization direction in the Fe_1/Au_1 MLS.

Spin-projected densities of Fe and Au d states for Fe_2/Au_2 MLS are shown in Fig. 44, and the calculated spin and orbital magnetic moments are given in Table VI. As compared to the results for Fe_1/Au_1 MLS, the change in the local environment and the increase of the number of Fe nearest neighbors around the Fe sites result in broadening of the d bands and a decrease of the calculated Fe spin magnetic moment to 2.79 μ_B. As opposed to the Fe_1/Au_1 MLS, where we observed strong anisotropy of the Fe d orbital moment, the Fe_2/Au_2 MLS exhibits very small anisotropy of the orbital magnetic moment (Table VI and Fig. 45). In Fig. 45 the functions $dm_l(E)$, $m_l(E)$, and $\Delta m_l(E)$ calculated for Fe and Au sites in Fe_2/Au_2 MLS are shown. Although all the three functions show strong energy dependence as in the case of Fe_1/Au_1, negligible anisotropy of the Fe d orbital moment is observed at the Fermi energy. The explanation can be found in Fig. 46. In the case of Fe_2/Au_2 MLS there also are two peaks in the partial density of Fe d states below and above the Fermi level, but in contrast to the Fe_1/Au_1 MLS they have the same $d_{x^2-y^2}$ character (Fig. 46) with a strong admixture of $d_{3z^2-r^2}$. Moreover, the partial weights of $d_{x^2-y^2}$ and $d_{3z^2-r^2}$ states at the Fermi level are such that $m_l(E_F)$ changes only slightly upon a change of the magnetization direction from $M\|(001)$ to $M\perp(001)$, and the anisotropy of the Fe orbital moment $\Delta m_l(E_F)$ is very small (see the inset in Fig. 45).

The dependence of the MOA on the SO coupling and hybridization strengths is very complicated (see, e.g., Ref. 118) and does not allow one to introduce a simple model consideration as in the case of the MC anisotropy.[89,90] While

TABLE VI. Calculated spin M_S and orbital M_L magnetic moments (in μ_B) of Fe_2/Au_2 versus magnetization direction.[95]

Atom	State	**M**∥ [001]		**M**⊥ [001]	
		M_S	M_L	M_S	M_L
Fe	*s*	−0.0045	0.0000	−0.0044	0.0000
	p	−0.0192	0.0001	−0.0191	−0.0005
	d	2.8056	0.0835	2.8064	0.0934
	f	0.0084	−0.0013	0.0084	−0.0015
	total	2.7902	0.0824	2.7912	0.0914
Au	*s*	−0.0260	0.0000	−0.0259	0.0000
	p	−0.0200	0.0026	−0.0200	0.0036
	d	0.0778	0.0155	0.0770	0.0182
	f	0.0059	−0.0009	0.0059	−0.0012
	total	0.0377	0.0172	0.0370	0.0206

the anisotropic band splitting can be directly related to the MCA, the situation with MOA is more complex, as the eigenvalues and wave functions of both the initial and final states enter the expression for the matrix elements. Therefore, the only way to obtain a realistic description of the MOA is to perform numerical calculations. The optical conductivity can be expressed as a sum of additive contributions coming from interband transitions with the initial and/or final states lying in different nonoverlapping energy intervals. In the case of Fe_1/Au_1, the Fe $d_\uparrow$ and Fe $d_\downarrow$ states are well separated in energy but overlap with the Au *d* states in a wide energy interval (see Fig. 40). Even less distinct separation in the energy position of the initial Fe and Au *d* states is observed in the case of the Fe_2/Au_2 MLS (see Fig. 44). It seems to be more informative to examine the dependence of the MOA on the site-dependent optical transition matrix elements. The calculations have been performed in the way described in Ref. 119, where, within an atomic sphere about either one of the atomic positions, the optical transition matrix elements were set to zero. In this way, the optical conductivity spectra and MOA can be analyzed in terms of the contributions arising from the transitions on the particular sites. The decomposition of the MOA into the contributions from interband transitions on the Fe and Au sites in Fe_1/Au_1

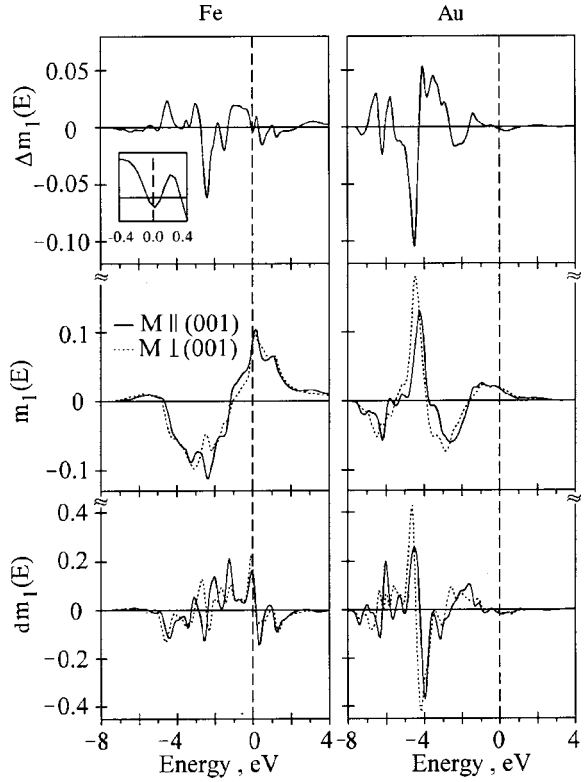

FIG. 45. The $dm_l(E)$ and $m_l(E)$ for two orientations of magnetization together with $\Delta m_l(E)$ for the Fe_2/Au_2 MLS.[95]

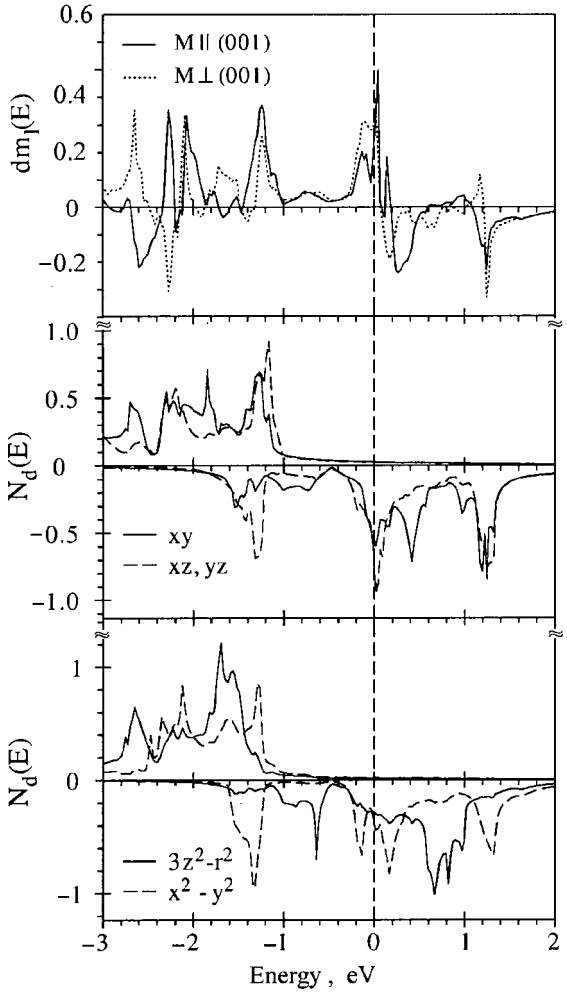

FIG. 46. The $dm_l(E)$ on Fe site for two orientations of magnetization and *d*-partial density of states (in states/(atom · eV · spin)) for the Fe_2/Au_2 MLS.[95]

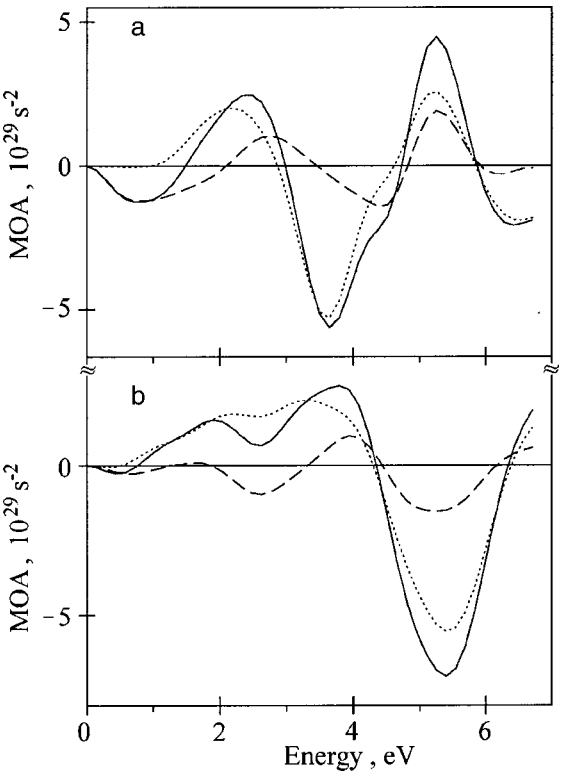

FIG. 47. Decomposition of the calculated MOA spectra (solid lines) into the contributions coming from all interband transitions on Fe (dashed lines) and Au (dotted lines) sites in Fe_1/Au_1 (a) and Fe_2/Au_2 (b) MLS.[95]

MLS is shown in Fig. 47a. As can be seen, the magnitude of the MO anisotropy spectrum is determined by both the Au and Fe sites, depending on the spectral region. Only in the 0 to ~1 eV energy interval can the MOA be connected exclusively with the transition on the Fe site. The interband transitions on the Au site are mainly responsible for the MOA spectra in the ~1 to ~5 eV energy interval. The transitions occur between the Au $d_\downarrow$ states located at energies $E \leqslant 1$ eV below the Fermi level and the hybridized states of p and f characters lying in the energy range up to 2 eV above the Fermi level. The enhanced density of these final states arises due to the strong hybridization with Fe $d_\downarrow$ states in the energy interval. In particular, the peak at 3.7 eV in the MOA spectra is completely determined by these transitions. The peak at 5.3 eV is equally due to both the Fe and Au related transitions. The results of the analysis for Fe_2/Au_2 MLS is shown in Fig. 47b. As in the case of Fe_1/Au_1 MLS, the transitions on both the Fe and Au sites determine the resulting MOA spectra in the Fe_2/Au_2 MLS; however, the main contribution arises from transitions on the Au site in the whole spectral range. We have verified that the prominent peak in the Fe_2/Au_2 MOA spectra at 5.5 eV is mostly determined by Au d-related transitions to the final states extending up to ~4 eV above the Fermi level.

Two major effects lead to the appearance of the MOA when the magnetization direction is changed: (i) the change of the band energies (Fig. 41) and (ii) the change of the orbital character of the wave functions. To determine which of the effects dominates we performed two model calculations. In the first one, the spectra were obtained using the as-calculated band energies, while the corresponding momentum matrix elements at every **k** point were averaged over the magnetization directions. The calculated MOA is zero in this case, whereas the MOA obtained from the second calculation, in which—vice versa—the averaged band energies and as-calculated matrix elements were used, is in very good agreement with the results of the *ab initio* calculation. It clearly demonstrates that the main effect of MOA comes from the change of the orbital character of the wave functions due to rotation of the magnetization axis. This is exactly the origin of the anisotropy of the orbital moment also, as discussed before. Although the common origin of both anisotropies is the spin–orbit interaction, the relationship between the orbital moment anisotropy and the MOA is not simple. While the orbital moment anisotropy is determined by the integral property of the occupied states [Eqs. (17)–(20)], the magnetooptical anisotropy is related to the energy-dependent quantity given by the convolution of all the initial occupied and final unoccupied states within the given energy difference [Eq. (9)].

The dependence of the MOA on the exchange splitting and the SO interaction was examined in the same way as in Refs. 74 and 119. It was found that the SO coupling of Au is equally responsible for the large MOA as the exchange splitting of Fe. If we set the SO coupling on Fe to zero, the off-diagonal optical conductivity is changed in the whole energy interval by a negative shift similar for both magnetization directions (Figs. 48a and 48b). Thus the contribution of the SO coupling on the Fe site to the conductivity is significant but almost isotropic. As a result, the MO anisotropy is practically independent of the SO coupling strength on the Fe site (Fig. 48c). On the other hand, putting the SO coupling on the Au site to zero affects the off-diagonal optical conductivities strongly, leading to a strong suppression of the MOA. As in the case of the Fe_1/Au_1 MLS, setting the SO coupling on Fe to zero in the Fe_2/Au_2 MLS changes the MO anisotropy to a lesser extent than the off-diagonal optical conductivity (not shown). However, putting the SO coupling on the Au site to zero affects strongly both the off-diagonal optical conductivity and the MOA. Thus the SO coupling of Au is mainly responsible for the large MO anisotropy in the Fe/Au MLS.

7. SUMMARY

The investigation of the optical and magnetooptical properties of Co/Pd, Co/Pt, Co/Cu, and Fe/Au multilayers both experimentally and theoretically from first principles has been reviewed.

A detailed comparative experimental and theoretical study of the electronic structure and the magnetooptical properties of Co/Pd multilayers shows that in these systems the MOKE is governed by the off-diagonal part of the optical conductivity tensor. *Ab initio* calculations performed for model Co/Pd MLS with sharp interfaces reproduced the main features of the experimental Co/Pd MOKE spectra only moderately well. The Co/Pd MLS with the interface microstructure modeled by ordered planar alloys of different compositions were examined. The MOKE spectra calculated from first principles for these MLS differ considerably from those obtained for the models with sharp interfaces. It is shown that the main features and the tendencies in the modi-

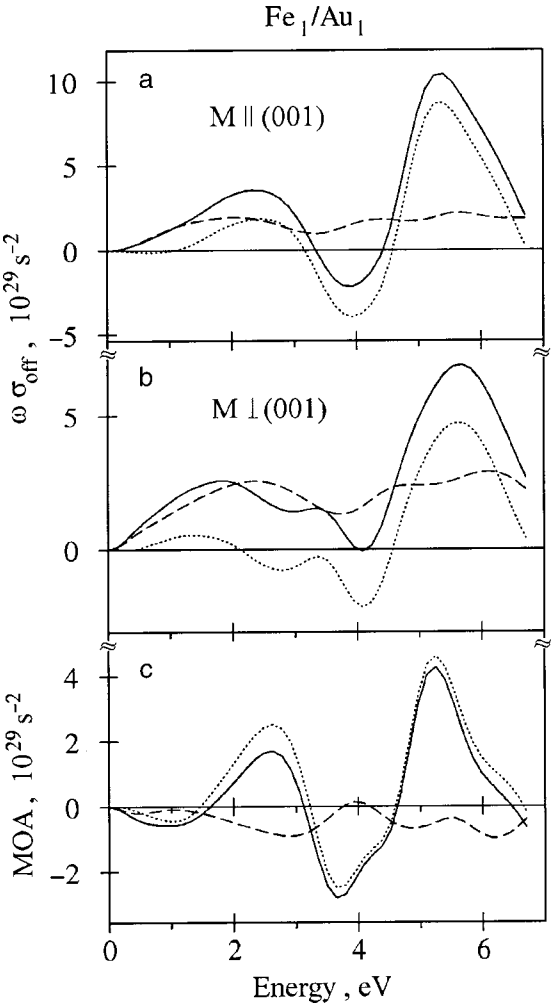

FIG. 48. Calculated absorptive off-diagonal part of the optical conductivity (a, b) and MO anisotropy (c) in the Fe_1/Au_1 MLS (solid lines) together with the results of the calculations for the SO coupling set to zero on Au site (dashed lines) and Fe site (dotted lines).[95]

fication of the MLS spectra with variation of the Co sublayer thickness are adequately reproduced when the alloying, even limited to one atomic plane, is taken into account. The MOKE spectra calculated for the model structures with ordered Co_1Pd_3 interfacial planes, reproduce the measured spectra best. The results obtained demonstrate that interface microstructure plays a crucial role in the formation of the MOKE spectra of the Co/Pd layered structures.

The Kerr rotation of Co/Pt MLS is governed mainly by the off-diagonal part of the conductivity tensor. The infrared part of the spectrum originates from the MO activity of the Co layers themselves and scales with the CO content. On the other hand, the peak in the UV region is due to the hybridization of strongly spin-polarized Co *d* states with spin–orbit-split Pt *d* states, and its magnitude depends weakly on the MLS composition. It has been demonstrated that the chemical and structural ordering is accompanied by substantial electronic structure changes and results in a drastic modification of the MOKE spectra. The *ab initio* description of the MOKE spectra for model Co/Pt multilayers performed under the assumption of a sharp, ideal interface is not adequate for the detailed explanation of the experimentally observed spectra. The modeding of multilayers with alloyed interfaces clearly illustrates the crucial role of the interface structure on the magnetooptical spectra of the Co/Pt MLS. It is shown that the main peculiarities and the tendencies in the modification of the MLS spectra with the variation of the Co sublayer thickness are adequately reproduced when the alloying, limited to two atomic planes, is taken into account. Very good agreement between the calculated and measured MOKE spectra demonstrates the validity of the adopted model and approach.

It was shown that although the dominant contribution to the off-diagonal part of the optical conductivity tensor of the Co/Cu MLS comes from the interband transitions involving Co electronic states, the interband transitions from Cu *d* states in the Cu sublayers play an important role. The Cu states at the interface are spin-polarized due to hybridization with Co states. The feature observed at $\hbar\omega \sim 2.1$ eV in the spectra of the optical conductivity tensor component $\sigma_{xx}^{(1)}$ is related to the edge of interband transitions from Cu *d* states in the Cu sublayers and is responsible for the peak at 2.1 eV in the polar Kerr rotation spectra of the Co/Cu MLS. The *ab initio* calculations reproduce the main features of the Co/Cu MLS spectra and provide an explanation of their microscopic origin.

A large orientation dependence of the magnetooptical response was experimentally observed in the Fe_n/Au_n multilayer structures. It was found that the magnitude of the magnetooptical anisotropy is very sensitive to the actual atomic structure of the superlattice and decreases as the number of atomic layers of the same type increases. In the case of the Fe_1/Au_1 MLS the calculations describe the measured spectra well only after taking into account the real structure of the MLS, namely, the mixture of mono- and bilayer structures. It can be verified that limited substitutional disorder at the interfaces leads to a decrease of the MO anisotropy.

The orientation anisotropy of the *d* orbital moment calculated from first principles shows that as the Au *d* states are almost completely occupied, the spin and orbital moments at the Au site are small and depend weakly on the magnetization direction in the Fe_1/Au_1. At the same time, the anisotropy of the Fe orbital moment, which is determined mainly by the Fe *d* states, is quite large. Two strong maxima in the Fe *d* partial density of states arise in the vicinity of the Fermi level of the Fe_1/Au_1 MLS, which are predominantly of $d_{x^2-y^2}$ character below the Fermi level and of $d_{3z^2-r^2}$ character just above the Fermi level. Such an orbital character of the partial density of states leads to strong anisotropy of the Fe *d* orbital moment in the Fe_1/Au_1 MLS. In the case of the Fe_2/Au_2 MLS there are two strong maxima in the Fe *d* partial density of states, both being of predominantly of $d_{x^2-y^2}$ character. As a result, a change of the magnetization direction leads to an almost isotropic Fe *d* orbital moment in the Fe_2/Au_2 MLS.

The interplay of the strong SO interaction on the Au sites and the large exchange splitting on the Fe sites through Au *d*–Fe *d* hybridization is responsible for the large MOA and the anisotropy of the Fe *d* orbital moment. The main effect of the MO anisotropy arises from the changing of the orbital character of the wave functions due to the change of the magnetization direction.

The results obtained imply that the magnetooptical prop-

erties of multilayers with various compositions and structures can be quantitatively predicted from first principles band-structure calculations. Such a possibility is important for basic research as well as applications.

*E-mail: anton@imp.kiev.ua

[1]M. Faraday, Philos. Trans. R. Soc. London **136**, 1 (1846).
[2]J. Kerr, Philos. Mag. **3**, 321 (1877).
[3]M. J. Freiser, IEEE Trans. Magn. **4**, 1 (1968).
[4]C. D. Mee and E. D. Daniel, *Magnetic Recording*, McGraw-Hill, New York (1987); M. Mansuripur, *The Physical Principles of Magneto-Optical Recording*, University Press, Cambridge (1995).
[5]K. H. J. Buschow, in *Ferromagnetic Materials*, edited by E. P. Wohlfarth and K. H. J. Buschow, North-Holland, Amsterdam (1988), Vol. 4, p. 588.
[6]W. Reim and J. Schoenes, in *Ferromagnetic Materials*, edited by E. P. Wohlfarth and K. H. J. Buschow, North-Holland, Amsterdam (1990), Vol. 5, p. 133.
[7]J. Schoenes, in *Materials Science and Technology, Electronic and Magnetic Properties of Metals and Ceramics*, edited by K. H. J. Buschow, R. W. Cahn, P. Haasen and E. J. Kramer, Verlag Chemie, Weinheim (1992), Vol. 3A, p. 147.
[8]H. Ebert, Rev. Prog. Phys. **59**, 1665 (1996).
[9]V. N. Antonov, A. N. Yaresko, A. Ya. Perlov, V. V. Nemoshkalenko, P. M. Oppeneer, and H. Eschrig, Fiz. Nizk. Temp. **25**, 387 (1999) [Low Temp. Phys. **25**, 527 (1999)].
[10]H. R. Hulme, Proc. R. Soc. London, Ser. A **135**, 237 (1932).
[11]C. Kittel, Phys. Rev. A **83**, A208 (1951).
[12]P. N. Argyres, Phys. Rev. **97**, 334 (1955).
[13]B. R. Cooper, Phys. Rev. A **139**, A1504 (1965).
[14]R. Kubo, J. Phys. Soc. Jpn. **12**, 570 (1957).
[15]A. E. Kondorsky and A. V. Vediaev, J. Appl. Phys. **39**, 559 (1968).
[16]C. S. Wang and J. Callaway, Phys. Rev. B **9**, 4897 (1974); M. Singh, C. S. Wang, and J. Callaway, *ibid.* **11**, 287 (1975).
[17]G. H. O. Daalderop, F. M. Mueller, R. C. Albers, and A. M. Boring, J. Magn. Magn. Mater. **74**, 211 (1988); H. Ebert, P. Strange, and B. L. Gyorffy, J. Phys. **49**, 31 (1988); Yu. Uspenskil and S. V. Halilov, Sov. Phys. JETP **68**, 588 (1989).
[18]S. S. P. Parkin, N. More, and K. P. Roche, Phys. Rev. Lett. **64**, 2304 (1990).
[19]M. N. Baibich, J. M. Broto, A. Fert, F. Nguyen Van Dau, F. Petroff, P. Etienne, G. Creuzet, A. Friederich, and J. Chazelas, Phys. Rev. Lett. **61**, 2472 (1988).
[20]M. G. Samant, J. Stöhr, S. S. S. Parkin, G. A. Held, B. D. Hermsmeier, F. Herman, M. van Schilfgaarde, L.-C. Duda, D. C. Mancini, N. Wassdahl, and R. Nakajima, Phys. Rev. Lett. **72**, 1112 (1994).
[21]W. B. Zeper, F. J. A. M. Greidanus, P. F. García, and C. R. Fincher, J. Appl. Phys. **65**, 4971 (1989).
[22]D. Weller, W. Reim, K. Spörl, and H. Brändle, J. Magn. Magn. Mater. **93**, 183 (1991).
[23]C.-J. Lin, G. L. Gorman, C. H. Lee, R. F. C. Farrow, E. E. Marinero, H. V. Do, H. Notarys, and C. J. Chien, J. Magn. Magn. Mater. **93**, 194 (1991).
[24]K. Sato, H. Ikekame, Y. Tosaka, K. Tsuzukiyama, Y. Togami, and M. Fujisawa, J. Magn. Magn. Mater. **126**, 572 (1993).
[25]S. Visnovsky, Czech. J. Phys., Sect. B **34**, 969 (1984).
[26]G. Metzger, P. Pluvinage, and R. Torguet, Ann. Phys. (Paris) **10**, 5 (1965).
[27]W. H. Kleiner, Phys. Rev. **142**, 318 (1966).
[28]A. H. MacDonald and S. H. Vosko, J. Phys. C: Solid State Phys. **12**, 2977 (1979).
[29]H. Ebert, H. Freyer, A. Vernes, and G.-Y. Guo, Phys. Rev. B **53**, 7721 (1996).
[30]H. Ebert, Phys. Rev. B **38**, 9390 (1988).
[31]I. V. Solovyev, A. B. Shik, V. P. Antropov, A. I. Liechtenstein, V. A. Gubanov, and O. K. Andersen, Fiz. Tverd. Tela (Leningrad) **31**, 13 (1989) [Sov. Phys. Solid State **31**, 1285 (1989)].
[32]O. K. Andersen, Phys. Rev. B **12**, 3060 (1975).
[33]V. V. Nemoshkalenko, A. E. Krasovskii, V. N. Antonov, Vl. N. Antonov, U. Fleck, H. Wonn, and P. Ziesche, Phys. Status Solidi B **120**, 283 (1983).
[34]V. N. Antonov, A. Ya. Perlov, A. P. Shpak, and A. N. Yaresko, J. Magn. Magn. Mater. **146**, 205 (1995).
[35]V. N. Antonov, A. I. Bagljuk, A. Ya. Perlov, V. V. Nemoshkalenko, Vl. N. Antonov, O. K. Andersen, and O. Jepsen, Fiz. Nizk. Temp. **19**, 689 (1993) [Low Temp. Phys. **19**, 494 (1993)].
[36]A. Santoni and F. J. Himpsel, Phys. Rev. B **43**, 1305 (1991).
[37]U. von Barth and L. A. Hedin, J. Phys. C **5**, 1629 (1972).
[38]V. V. Nemoshkalenko and V. N. Antonov, *Computational Methods in Solid State Physics* [Gordon and Breach, London (1998)].
[39]P. E. Blöchl, O. Jepsen, and O. K. Andersen, Phys. Rev. B **49**, 16223 (1994).
[40]K. Sato, Jpn. J. Appl. Phys. **20**, 2403 (1981).
[41]D. E. Aspnes and A. A. Studna, Appl. Opt. **14**, 220 (1975).
[42]S. Uba, L. Uba, A. N. Yaresko, A. Ya. Perlov, V. N. Antonov, and R. Gontarz, J. Phys.: Condens. Matter **10**, 3769 (1998).
[43]K. Sato, H. Ikekame, Y. Tosaka, and S.-C. Shin, J. Magn. Magn. Mater. **126**, 553 (1993).
[44]S. Uba, L. Uba, and R. Gontarz, IEEE Trans. Magn. **30**, 806 (1994).
[45]M. Nawate, T. Takeuchi, Y. Tamura, and S. Honda, in *Proceedings of the International Conference on Magnetism, Warsaw, 1994*, S. Krompiewski, A. Szajek, and J. Morkowski (Eds.), Poznan, Osrodek Wydawnictw Naukowych (1994), p. 517.
[46]S. K. Kim, Y. M. Koo, V. A. Chernov, and H. Padmore, Phys. Rev. B **53**, 11114 (1996).
[47]H. Giordano, A. Atrei, M. Torrini, U. Bardi, M. Gleeson, and C. Barnes, Phys. Rev. B **54**, 11762 (1996).
[48]S. Uba, A. N. Yaresko, L. Uba, A. Ya. Perlov, V. N. Antonov, R. Gontarz, and H. Ebert, Phys. Rev. B **57**, 1534 (1998).
[49]W. Reim, H. Brändle, D. Weller, and J. Schoenes, J. Magn. Magn. Mater. **93**, 220 (1991).
[50]J. Vogel, A. Fontaine, V. Cros, F. Petroff, J.-P. Kappler, G. Krill, A. Rogalev, and J. Goulon, Phys. Rev. B **55**, 3663 (1997).
[51]A. B. Shick, V. Drchal, J. Kurdnovský, and P. Weinberger, Phys. Rev. B **54**, 1610 (1996); H. Ebert, B. Drittler, and H. Akai, J. Magn. Magn. Mater. **104–107**, 733 (1992).
[52]J. Banhart and H. Ebert, Europhys. Lett. **32**, 517 (1995).
[53]H. Ebert, Jpn. J. Appl. Phys. Suppl. **32**, Suppl. 32–2 (1993); H. Ebert and H. Akai, Mater. Res. Soc. Symp. Proc. **253**, 329 (1992).
[54]R. M. Bozorth, P. A. Wolff, D. D. Davis, V. B. Compton, and J. H. Wernick, Phys. Rev. **122**, 1157 (1961).
[55]L. D. Landau and E. M. Lifshitz, *Electrodynamics of Continuous Media* [Pergamon, New York (1960)].
[56]A. N. Yaresko, P. M. Oppeneer, A. Ya. Perlov, V. N. Antonov, T. Kraft, and H. Eschrig, Europhys. Lett. **36**, 551 (1996).
[57]M. M. Kirillova, G. A. Bolotin, and L. V. Nomerovannaja, Opt. Spectrosc. **49**, 742 (1980).
[58]Yu. A. Uspenskii, E. T. Kulatov, and S. V. Halilov, Phys. Rev. B **54**, 474 (1996); G. Y. Guo and H. Ebert, *ibid.* **50**, 10377 (1994).
[59]The MOKE spectrum of the Co film presently studied differs from the previously published [S. Uba, L. Uba, R. Gontarz, V. N. Antonov, A. Ya. Perlov, and A. N. Yaresko, *J. Magn. Magn. Mater.* **140–144**, 575 (1995)] due to the smaller film thickness of the later and known dependences of MOKE on the film microstructure, see, e.g., T. Suzuki, D. Weller, C.-A. Chang, R. Savoy, T. Huang, B. A. Gurney, and V. Speriosu, Appl. Phys. Let. **64**, 2736 (1994).
[60]D. E. Aspnes, in *Handbook of Optical Constants of Solids*, edited by E. D. Palik, Academic, Orlando, FL (1985).
[61]S. Logothetidis, S. Boultadakis, N. K. Flevaris, and D. Fuchs, J. Magn. Magn. Mater. **93**, 444 (1991).
[62]H. Brändle, D. Weller, J. C. Scott, S. S. P. Parkin, and C.-J. Lin, IEEE Trans. Magn. **28**, 2967 (1992).
[63]K. Sato, H. Hongu, H. Ikekame, J. Watanabe, K. Tsuzukiyama, Y. Togami, M. Fujisawa, and T. Fukazawa, Jpn. J. Appl. Phys. **31**, 3603 (1992).
[64]S. Visnovsky, M. Nyvlt, V. Parizek, P. Kielar, V. Prosser, and R. Krishnan, IEEE Trans. Magn. **29**, 3390 (1993).
[65]V. N. Antonov, A. Ya. Perlov, A. P. Shpak, and A. N. Yaresko, J. Magn. Magn. Mater. **146**, 205 (1995).
[66]P. M. Oppeneer, T. Kraft, and H. Eschrig, Phys. Rev. B **52**, 3577 (1995).
[67]G. Y. Guo and H. Ebert, Phys. Rev. B **50**, 10377 (1994).
[68]D. Weller, G. R. Harp, R. F. C. Farrow, A. Cebollada, and J. Sticht, Phys. Rev. Lett. **72**, 2097 (1994).
[69]S. N. Rashkeev, Yu. A. Uspenskii, and I. I. Mazin, Zh. Éksp. Teor. Fiz. **88**, 1687 (1985) [Sov. Phys. JETP **61**, 1004 (1985)].
[70]G. Y. Guo and H. Ebert, Phys. Rev. B **51**, 12633 (1995).
[71]P. M. Oppeneer, V. N. Antonov, T. Kraft, H. Eschrig, A. N. Yaresko, and A. Ya. Perlov, Solid State Commun. **94**, 255 (1995).
[72]D. Weller, J. Sticht, G. R. Harp, R. F. C. Farrow, R. F. Marks, and H. Brändle, Mater. Res. Soc. Symp. Proc. **313**, 501 (1993).

[73]G. R. Harp, D. Weller, T. A. Rabedeau, R. F. C. Farrow, and M. F. Toney, Phys. Rev. Lett. **71**, 2493 (1993).
[74]S. Uba, L. Uba, A. N. Yaresko, A. Ya. Perlov, V. N. Antonov, and R. Gontarz, Phys. Rev. B **53**, 6526 (1996).
[75]L. Uba, S. Uba, A. N. Yaresko, A. Ya. Perlov, V. N. Antonov, and R. Gontarz, J. Magn. Magn. Mater. **193**, 159 (1999).
[76]T. Katayama, Y. Suzuki, H. Awano, Y. Nishihara, and N. Koshizuka, Phys. Rev. Lett. **60**, 1426 (1988).
[77]Y. B. Xu, Q. Y. Jin, Y. Zhai, M. Lu, Y. Z. Miao, Q. S. Bie, and H. R. Zhai, J. Appl. Phys. **74**, 3470 (1993).
[78]M. Sakurai and T. Shinjo, J. Appl. Phys. **74**, 6840 (1993).
[79]Y. B. Xu, Q. Y. Jin, Y. Zhai, Y. Z. Miao, M. Lu, and H. R. Zhai, J. Magn. Magn. Mater. **126**, 541 (1993).
[80]Y. B. Xu, M. Lu, Q. S. Bie, Y. Zhai, Q. Y. Jin, X. B. Zhu, and H. R. Zhai, J. Magn. Magn. Mater. **140–144**, 581 (1995).
[81]S. Visnovsky, M. Nyvlt, V. Prosser, J. Ferre, G. Penissard, D. Renard, and G. Sczigel, J. Magn. Magn. Mater. **128**, 179 (1993).
[82]S. Uba, L. Uba, A. Ya. Perlov, A. N. Yaresko, V. N. Antonov, and R. Gontarz, J. Phys.: Condens. Matter **9**, 447 (1997).
[83]R. Gontarz and T. Lucinski, J. Magn. Magn. Mater. **101**, 253 (1991).
[84]Yu. A. Uspenskii and S. V. Khalilov, Zh. Eksp. Teor. Fiz. **95**, 1022 (1989) [Sov. Phys. JETP **68**, 588 (1989)].
[85]P. M. Oppeneer, T. Maurer, J. Sticht, and J. Kübler, Phys. Rev. B **45**, 10924 (1992).
[86]P. M. Oppeneer, J. Sticht, T. Maurer, and J. Kübler, Z. Phys. B: Condens. Matter **88**, 309 (1992).
[87]*Ultrathin Magnetic Structures*, edited by J. A. C. Bland and B. Heinrich, Springer-Verlag, Berlin (1994), Vols. I and II.
[88]H. Brooks, Phys. Rev. **58**, 909 (1940); G. C. Fletcher, Proc. Phys. Soc., London, Sect. A **67**, 505 (1954); N. Mori, J. Phys. Soc. Jpn. **27**, 307 (1969); E. I. Kondorskii and E. Staube, Zh. Éksp. Teor. Fiz. **63**, 356 (1972) [Sov. Phys. JETP **36**, 188 (1973)]; J. G. Gay and R. Richter, Phys. Rev. Lett. **56**, 2728 (1986); J. G. Gay and R. Richter, J. Appl. Phys. **61**, 3362 (1987).
[89]P. Bruno, Phys. Rev. B **39**, 865 (1989).
[90]G. van der Laan, J. Phys.: Condens. Matter **10**, 3239 (1998).
[91]J. Trygg, B. Johansson, O. Eriksson, and J. M. Wills, Phys. Rev. Lett. **75**, 2871 (1995); S. V. Halilov, A. Ya. Perlov, P. M. Oppeneer, A. N. Yaresko, and V. N. Antonov, Phys. Rev. B **57**, 9557 (1998).
[92]P. M. Oppeneer and V. N. Antonov, in *Spin-Orbit Influenced Spectroscopies of Magnetic Solids*, edited by H. Ebert and G. Schütz, Springer, Berlin (1996), p. 29.
[93]E. A. Ganshina, G. S. Krinchik, L. S. Mironova, and A. S. Tablin, Zh. Éksp. Teor. Fiz. **78**, 733 (1980) [Sov. Phys. JETP **51**, 369 (1980)].
[94]R. M. Osgood III, K. T. Riggs, A. E. Johnson, J. E. Mattson, C. H. Sowers, and S. D. Bader, Phys. Rev. B **56**, 2627 (1997).
[95]L. Uba, S. Uba, V. N. Antonov, A. N. Yaresko, T. Slezak, and J. Korecki, Phys. Rev. B **62**, 13731 (2000).
[96]N. Spiridis and J. Korecki, Appl. Surf. Sci. **141**, 313 (1999).
[97]V. Blum, Ch. Rath, S. Müller, L. Hammer, K. Heinz, J. M. García, J. E. Ortega, J. E. Prieto, O. S. Hernán, J. M. Gallego, A. L. Vázquez de Parga, and R. Miranda, Phys. Rev. B **59**, 15966 (1999).
[98]K. Takanashi, S. Mitani, M. Sano, H. Fujimori, H. Nakajima, and A. Osawa, Appl. Phys. Lett. **67**, 1016 (1995); S. Mitani, K. Takanashi, H. Nakajima, K. Sato, R. Schreiber, P. Grünberg, and H. Fujimori, J. Magn. Magn. Mater. **156**, 7 (1996).
[99]T. Slezak, W. Karas, M. Kubik, M. Mohsen, M. Przybylski, N. Spiridis, and J. Korecki, Hyperfine Interact. C **3**, 409 (1998); J. Korecki, M. Kubik, N. Spiridis, and T. Slezak, Acta Phys. Pol. A **97**, 129 (2000).
[100]K. Takanashi, S. Mitani, H. Fujimori, M. Sato, and Y. Suzuki, J. Magn. Magn. Mater. **177–181**, 1199 (1998).
[101]K. Sato, E. Takeda, M. Akita, M. Yamaguchi, K. Takanashi, S. Mitani, H. Fujimori, and Y. Suzuki, J. Appl. Phys. **86**, 4985 (1999).
[102]Y. Suzuki, T. Katayama, S. Yoshida, K. Tanaka, and K. Sato, Phys. Rev. Lett. **68**, 3355 (1992); W. Geerts, Y. Suzuki, T. Katayama, K. Tanaka, K. Ando, and S. Yoshida, Phys. Rev. B **50**, 12581 (1994).
[103]Y. Suzuki, T. Katayama, P. Bruno, S. Yuasa, and E. Tamura, Phys. Rev. Lett. **80**, 5200 (1998).
[104]J. Zak, E. R. Moog, C. Liu, and S. D. Bader, J. Magn. Magn. Mater. **89**, 107 (1990); J. Zak, E. R. Moog, C. Liu, and S. D. Bader, Phys. Rev. B **43**, 6423 (1991).
[105]K. Takanashi, S. Mitani, K. Himi, and H. Fujimori, Appl. Phys. Lett. **72**, 737 (1998).
[106]L. Uba, S. Uba, V. N. Antonov, A. N. Yaresko, A. Ya. Perlov, T. Slezak, and J. Korecki, Solid State Commun. **114**, 441 (2000).
[107]K. A. Mills, R. F. Davis, S. D. Kevan, G. Thornton, and D. A. Shirley, Phys. Rev. B **22**, 581 (1980).
[108]E. E. Krasovskii, A. N. Yaresko, and V. N. Antonov, J. Electr. Spectros. **68**, 157 (1994).
[109]V. I. Anisimov, J. Zaanen, and O. K. Andersen, Phys. Rev. B **44**, 943 (1991).
[110]V. I. Anisimov, F. Aryasetiawan, and A. I. Liechtenstein, J. Phys.: Condens. Matter **9**, 767 (1997).
[111]V. N. Antonov, A. N. Yaresko, A. Ya. Perlov, P. Thalmeier, P. Fulde, P. M. Oppeneer, and H. Eschrig, Phys. Rev. B **58**, 9752 (1998).
[112]L. Uba, S. Uba, A. N. Yaresko, and V. N. Antonov (unpublished)
[113]H. Okamoto, T. B. Massalski, L. J. Swartzendruber, and P. A. Beck, Bull. Alloy Phase Diagrams **5**, (6) (1984).
[114]C. J. Pastor, C. Limones, J. J. Hinarejos, J. M. García, R. Miranda, J. Gómez-Goni, J. E. Ortega, and H. D. Abruna, Surf. Sci. **364**, L505 (1996).
[115]D. Weller, J. Stöhr, R. Nakajima, A. Carl, M. G. Samant, C. Chappert, R. Megy, P. Beauvillain, P. Veillet, and G. A. Held, Phys. Rev. Lett. **75**, 3752 (1995).
[116]J. Stöhr and H. König, Phys. Rev. Lett. **75**, 3748 (1995).
[117]J. H. van Vleck, *Electric and Magnetic Susceptibilities* [Oxford University Press, Oxford (1932)].
[118]H. S. Bennet and E. A. Stern, Phys. Rev. **137**, A448 (1965).
[119]P. M. Oppeneer, V. N. Antonov, T. Kraf, H. Eschrig, A. N. Yaresko, and A. Ya. Perlov, J. Phys.: Condens. Matter **8**, 5769 (1996).

This article was published in English in the original Russian journal. Reproduced here with stylistic changes by AIP.

QUANTUM LIQUIDS AND QUANTUM CRYSTALS

Cyclotron resonance of a two-dimensional Wigner solid

Yu. P. Monarkha*

B. Verkin Institute for Low Temperature Physics and Engineering of the National Academy of Sciences of Ukraine, 47 Lenin Ave., 61103 Kharkov, Ukraine

(Submitted January 15, 2001; revised February 12, 2001)
Fiz. Nizk. Temp. **27**, 627–633 (June 2001)

Cyclotron resonance absorption from a two-dimensional electron solid formed on a free surface of liquid helium is analyzed by means of the memory function formalism. The presence of the low-frequency phonon mode of the Wigner solid in a strong magnetic field is shown to broaden significantly the electron dynamical structure factor (DSF) as a function of frequency, strengthening the contribution from multiphonon emission terms of the high-frequency mode. Thus in most cases the linewidth is formed by nonlinear terms of the DSF expansion in the cyclotron motion factor $\exp(-i\omega_c t)$ rather than by the linear terms analyzed previously. The inclusion of all these multiphonon terms changes the sign of the many-electron effect and agrees well with available experimental data, eliminating the discrepancy between theory and experiment. © *2001 American Institute of Physics.* [DOI: 10.1063/1.1382984]

1. INTRODUCTION

Coulomb forces can strongly affect the properties of a two-dimensional (2D) electron system. An extreme example of this kind is the Wigner solid transition. The Wigner solid (WS) of a 2D nondegenerate electron gas was first observed in a sheet of electrons formed on a free surface of liquid helium.[1,2] The long-range order of a finite 2D electron system was detected by a resonance coupling of the electron lattice with capillary wave quanta (ripplons).

Significant research has been performed on using the cyclotron resonance (CR) as a probe of the many-electron effects and the WS phase. A strong narrowing of the CR linewidth was observed in semiconductor degenerate 2D electron systems[3,4] for small filling factors. It should be noted that in degenerate systems, the influence of Coulombic effects increases with decreasing electron density n_S. A detailed experimental study of CR absorption from surface electrons (SEs) on liquid helium was reported in Refs. 5 and 6, though by that time the many-electron theory was insufficiently developed to explain these data. For SEs on liquid helium the Fermi energy is very small $\varepsilon_F \ll T$, and increasing the electron density introduces many-electron effects. Some data of Refs. 5 and 6 had shown a decrease of the CR linewidth with increase of the holding electric field $E_\perp$, which was maintained under the saturation condition: $E_\perp = 2\pi e n_S$. However, at low temperatures, the holding electric field acts also as an electron-ripplon coupling parameter directly affecting the CR linewidth.

A CR theory of a 2D electron crystal was introduced in Ref. 7. According to it, the CR linewidth is due to decay of the long-wavelength ($k \to 0$) high-frequency phonon $\Omega_{+,k} \simeq \omega_c$ into a short-wavelength phonon of the same branch, accompanied by the creation and annihilation of a great number of low-frequency phonons $\Omega_{-,k} \simeq \omega_{l,k}\omega_{t,k}/\omega_c \ll T/\hbar$ [here $\omega_{p,k}$ is the spectrum of longitudinal ($p=l$) and transverse ($p=t$) phonons in the absence of the magnetic field, and ω_c is the cyclotron frequency]. The WS theory[7] was confined to analysis of the linear terms of the conductivity expansion in the cyclotron motion factor $\exp(-i\omega_c t)$, which is similar to considering only one-phonon terms in the dynamical structure factor (DSF) of a solid. This approximation resulted in a remarkable conclusion: the CR linewidth γ_{CR} decreases with electron density as $\gamma_{CR} \propto n_s^{-3/4}$ (Ref. 7). This result was used to explain the narrowing of the CR absorption line reported earlier.[5,6] A similar result was found by the path-integral method.[8]

A direct check of the theory[7] performed for SEs at low temperatures ($T = 0.062$ K) and relatively weak magnetic fields ($B \approx 0.071$ T, $\hbar\omega_c/T \approx 1.55$) has strikingly shown an opposite density dependence: the linewidth increases with electron density approximately as $\gamma_{CR} \propto n_S$ (Ref. 9). In this experiment, the electron density was varied independently of the holding electric field. For a liquid state of the electron system the explanation of this conflict between experiment and theory was found in Refs. 10 and 11: the ultrafast motion of electron orbit centers in a fluctuational many-electron field $\mathbf{E}_f$ stimulates electron scattering between different Landau levels, causing an increase of the CR linewidth. This picture describes nicely the CR absorption from SEs on liquid helium interacting with helium vapor atoms. Still, it is of interest to find out how this concept changes for the WS state, and what revision of the WS theory should be introduced.

In this paper, to describe the CR of the WS we employ the memory function formalism,[12,13] which allows one to find a relation between the CR linewidth and the DSF $S(q,\omega)$ of the electron solid. The present analysis of the DSF of a Wigner solid in a high magnetic field shows that for strong Coulomb forces the nonlinear terms of the expansion in the cyclotron motion factor $\exp(-i\omega_c t)$ cannot be disregarded. In other words, multi-high-frequency-phonon terms

crucially affect the CR linewidth if $\Gamma_C \equiv \sqrt{2} eE_f l > \hbar\omega_c$ (here $l=\sqrt{\hbar c/eB}$ is the magnetic length). The strong broadening Γ_C of the DSF $S(q,\omega)$ caused by the low-frequency mode $\Omega_{-,k}$ makes it possible to emit many high-frequency phonons $\Sigma\Omega_{+,k} \simeq N\omega_c$, a process which is equivalent to the electron scattering on higher Landau levels introduced for the electron-liquid CR theory.[10] When all of the nonlinear terms $\exp(-i\omega_c tN)$ are taken into account, the DSF of a Wigner solid is found to be similar to the DSF of a highly correlated electron liquid, reported in Ref. 11. The result of evaluation of the CR linewidth induced by the electron-ripplon scattering agrees well with experimental data of Refs. 5, 6, and 9, eliminating the conflict between theory and experiment.

2. BASIC RELATIONS

The memory function formalism[12,13] establishes a general relation between the electron conductivity σ and the memory function or the relaxation kernel $M(\omega)$. The effective collision frequency can be introduced as $\nu_{\rm eff} = {\rm Im}[M(\omega)]$. Searching for the CR linewidth, we disregard ${\rm Re}[M(\omega)]$ or consider that it is included somehow in the definition of the resonance frequency. In this case, we have

$$\sigma_{xx} \pm i\sigma_{xy} = \frac{ie^2 n_s}{m[\omega \mp \omega_c + i\nu_{\rm eff}(\omega)]}. \tag{1}$$

In the conventional procedure,[12] $M(\omega)$ is expressed in terms of the force–force Green's function. For ${\rm Im}[M(\omega)]$ the final equation can be simplified significantly by employing general properties of the Green's function,

$$\nu_{\rm eff}(\omega) = -\frac{[1-\exp(-\hbar\omega/T)]m}{2e^2 n_s \hbar^3 \omega S_A} \times \int_{-\infty}^{\infty} \langle F_x(t) F_x \rangle \exp(i\omega t)\, dt, \tag{2}$$

where S_A is the surface area, $F_\beta = i[J_\beta, H_{\rm int}]$ is the force acting on electrons (with a factor e/m), determined by the interaction Hamiltonian $H_{\rm int}$ and current density $\mathbf{J} = -\sum_S e\mathbf{v}_s$.

Ripplons represent a sort of 2D phonons with the capillary spectrum $\omega_q = \sqrt{\alpha/\rho}\, q^{3/2}$ (here α is the surface tension and ρ is the density of liquid helium). On introducing a 2D electron density operator $n_{\mathbf{q}} = \sum_s \exp(-i\mathbf{q}\cdot\mathbf{r}_s)$ and the interaction Hamiltonian

$$H_{\rm int} = \frac{1}{\sqrt{S_A}} \sum_{\mathbf{q}} U_q n_{-\mathbf{q}} (b_{\mathbf{q}} + b^+_{-\mathbf{q}}), \qquad U_q = V_q \sqrt{\hbar q/2\rho\omega_q}, \tag{3}$$

the force operator can be found as[14]

$$F_\beta = -\frac{i\hbar e}{m\sqrt{S_A}} \sum_{\mathbf{q}} q_\beta U_q n_{-\mathbf{q}} (b_{\mathbf{q}} + b^+_{-\mathbf{q}}). \tag{4}$$

Here $b_{\mathbf{q}}$ is the ripplon annihilation operator.

The particular form of the electron-ripplon coupling V_q is taken from Ref. 15:

$$V_q = eE_\perp + \frac{\Lambda q^2}{2} w\left(\frac{q^2}{4\gamma_\perp^2}\right), \tag{5}$$

where

$$w(x) = -\frac{1}{1-x} + \frac{1}{(1-x)^{3/2}} \ln\left(\frac{1+\sqrt{1-x}}{\sqrt{x}}\right), \tag{6}$$

$\gamma_\perp^{-1}$ is the localization length of the electron wave function in the perpendicular direction, $\Lambda = e^2(\varepsilon-1)/[4(\varepsilon+1)]$, and ε is the dielectric constant of liquid helium.

Equations (2) and (4) allow one to express the CR linewidth function $\gamma_{CR}(\omega) = 2\nu_{\rm eff}(\omega)$ in terms of the equilibrium electron DSF

$$\gamma_{CR}(\omega) = \frac{[1-\exp(-\hbar\omega/T)]}{2\hbar\omega m S_A} \sum_{\mathbf{q}} q^2 V_q^2 \frac{\hbar q}{2\rho\omega_q} \times [(N_q+1)S(q,\omega-\omega_q) + N_q S(q,\omega+\omega_q)]. \tag{7}$$

Here N_q is the ripplon distribution function. We use the conventional definition of the electron DSF:

$$S(q,\omega) = N_e^{-1} \int \exp(i\omega t) \langle n_{\mathbf{q}}(t) n_{-\mathbf{q}} \rangle dt,$$

Where N_e is the number of electrons. Equation (7) can be applied to either state of the electron system: liquid or solid. In most cases, the resonance frequency ω is much higher than the typical ripplon frequency ω_q, and the latter can be disregarded in the argument of the electron DSF.

3. WIGNER SOLID DYNAMICAL STRUCTURE FACTOR

According to the previous Section, the determination of the CR line shape of a 2D electron system is reduced to evaluation of its equilibrium DSF. The important thing is that the Wigner solid consists of charged particles, and its dynamics is crucially affected by a strong normal magnetic field B. The magnetic field mixes the longitudinal and transverse phonon modes. According to,[16] the excitation spectrum of the WS $\Omega_{p,k}$ (here $p=+,-$) is determined by the equation

$$2\Omega_{\pm,k}^2 = \omega_{l,k}^2 + \omega_{t,k}^2 + \omega_c^2 \pm \sqrt{(\omega_{l,k}^2 + \omega_{t,k}^2 + \omega_c^2)^2 - 4\omega_{l,k}^2 \omega_{t,k}^2}. \tag{8}$$

For high cyclotron frequencies we disregard the presence of surface dimples beneath each electron. In the limiting case $\omega_c \gg \omega_{l,k}$, the spectrum of the low-frequency mode decreases steadily with B as $\Omega_{-,k} \simeq \omega_{l,k}\omega_{t,k}/\omega_c \propto 1/B$, while the spectrum of the high-frequency mode $\Omega_{+,k}$ approaches $\omega_c \propto B$.

Although the electron displacement operator is also affected by the magnetic field, its general form can still be written in a conventional way:

$$\mathbf{u}_n = \sum_{p,\mathbf{k}} \left[\frac{\hbar}{2N_e m \Omega_{p,k}}\right]^{1/2} [\mathbf{E}_{p,\mathbf{k}} a_{p,\mathbf{k}} \exp(i\mathbf{k}\mathbf{r}_{\mathbf{n}}) + {\rm h.c.}]. \tag{9}$$

In the presence of the magnetic field, the polarization vectors of the WS phonons $\mathbf{E}_{p,\mathbf{k}}$ are no longer orthonormalized:[17]

$$\mathbf{E}_{-,\mathbf{k}}=\sin(\lambda)\mathbf{e}_{l,\mathbf{k}}+i\cos(\lambda)\frac{\Omega_{-,k}}{\omega_{t,k}}\mathbf{e}_{t,\mathbf{k}},$$

$$\mathbf{E}_{+,\mathbf{k}}=\cos(\lambda)\mathbf{e}_{l,\mathbf{k}}-i\sin(\lambda)\frac{\Omega_{+,k}}{\omega_{t,k}}\mathbf{e}_{t,\mathbf{k}}, \tag{10}$$

where $\mathbf{e}_{l,\mathbf{k}}$ and $e_{t,k}$ are the usual polarization vectors in the absence of the magnetic field, and

$$\sin^2(\lambda)=\frac{\omega_{t,k}^2-\Omega_{-,k}^2}{\Omega_{+,k}^2-\Omega_{-,k}^2}. \tag{11}$$

It is easy to prove that $|\mathbf{E}_{+,\mathbf{k}}|^2+|\mathbf{E}_{-,\mathbf{k}}|^2=2$. In the strong magnetic field limit, $|\mathbf{E}_{-,\mathbf{k}}|^2\simeq(\omega_{l,k}^2+\omega_{t,k}^2)/\omega_c^2\to 0$, while $|\mathbf{E}_{+,\mathbf{k}}|^2\simeq 2$.

Following the procedure developed for the neutron scattering theory,[18] the Wigner solid DSF can be written as

$$S(q,\omega)=\sum_{\mathbf{n}}\exp(-i\mathbf{q}\mathbf{r}_{\mathbf{n}})\int_{-\infty}^{\infty}\exp\Bigg\{i\omega t+2q^2\times\sum_{p=+,-}[W_p(\mathbf{n},t)-W_p(0,0)]\Bigg\}dt, \tag{12}$$

where

$$W_p(\mathbf{n},t)=\frac{\hbar}{8N_e m}\sum_{\mathbf{k}}\frac{|\mathbf{E}_{p,\mathbf{k}}|^2}{\Omega_{p,k}}\{(n_{p,k}+1)e^{i(\mathbf{k}\mathbf{r}_{\mathbf{n}}-\Omega_{p,k}t)}+n_{p,k}e^{-i(\mathbf{k}\mathbf{r}_{\mathbf{n}}-\Omega_{p,k}t)}\}, \tag{13}$$

$n_{p,k}$ is the WS phonon distribution function. Usually, the expansion of $W_p(\mathbf{n},t)$ in $\Omega_{p,k}t$ is justified only for high temperature range $T>\theta_D$, where θ_D is the WS Debye temperature. In this case, the Debye–Waller function $2q^2W_p(0,0)\gg 1$ and the main contribution into the integral of Eq. (12) comes from the region near $t=0$.

Another approximation is usually used for low temperatures, when $2q^2W(\mathbf{n},t)$ is small. In this case, the exponential of Eq. (12) is expanded in $2q^2W(\mathbf{n},t)$, giving an elastic term, one-phonon terms, and multi-phonon terms.

In Ref. 7 it was reasonably noted that for strong magnetic fields the frequency $\Omega_{-,k}$ is low, and one can expand the displacement correlators in $\Omega_{-,k}t$ even for temperatures $T\ll\theta_D$. Additionally, it was shown that one can use the incoherent approximation. Taking this approach, we find

$$2q^2[W_-(0,t)-W_-(0,0)]\simeq -x_q\frac{\Gamma_C^2}{4\hbar^2}\left(t^2+\frac{it\hbar}{T}\right),$$

$$\Gamma_C^2=\frac{\hbar\omega_c}{N_e}\sum_{\mathbf{k}}|\mathbf{E}_{-,\mathbf{k}}|^2\hbar\Omega_{-,k}(2n_{-,k}+1), \tag{14}$$

where $x_q=q^2l^2/2$ is a dimensionless parameter. At $\omega_c\gg\omega_{l,k}$, we have $\Gamma_C=\sqrt{2}eE_f^{(0)}l$, with

$$eE_f^{(0)}=\sqrt{(mT/N_e)\sum_{\mathbf{k}}(\omega_{l,k}^2+\omega_{t,k}^2)}. \tag{15}$$

The quantity $E_f^{(0)}$ is a measure of the average fluctuational electric field acting on an electron. The most important physics comes from the first term of Eq. (14), proportional to t^2. It is because of this term, which affects the time integral of Eq. (12), that the conventional energy-conservation δ function is replaced by a heavily broadened Gaussian function.

For the high-frequency mode one can assume $n_{+,k}\ll 1$ and $|\mathbf{E}_{+,\mathbf{k}}|^2\simeq 2$, which gives

$$2q^2W_+(0,t)\simeq\frac{x_q}{N_e}\sum_k\frac{\omega_c}{\Omega_{+,k}}\exp(-i\Omega_{+,k}t), \tag{16}$$

and $2q^2W_+(0,0)\simeq x_q$, where $\Omega_{+,k}\simeq\omega_c$. Therefore, we can keep the high-frequency Debye–Waller factor $\exp(-x_q)$ as it is and expand the DSF in $2q^2W_+(0,t)$, a procedure which is similar to the conventional low-temperature expansion. Thus, we have multiphonon emission terms for the high-frequency mode. Usually, the scattering events described by terms proportional to $\exp(-iN\omega_c t)$ are forbidden at low temperatures $T\ll\hbar\omega_c$ (except for the term with $N=1$), since a ripplon or a vapor atom does not have enough energy in the laboratory frame for such emission. In our case, the multiphonon emission of high-frequency phonons is possible because of the strong broadening introduced by the low-frequency mode [Eq. (14)]. Such emission is accompanied by the creation and annihilation of a great number of low-frequency phonons.

A straightforward evaluation of all terms of the expansion in $2q^2W_+(0,t)$ gives the following result:

$$S(q,\omega)=\frac{2\sqrt{\pi}\hbar}{\Gamma_C}\sum_{N=0}^{\infty}\frac{x_q^{N-1/2}}{N!}\times\exp\left[-x_q-\frac{\hbar^2(\omega-N\omega_c)^2}{x_q\Gamma_C^2}\right]. \tag{17}$$

We have disregarded the small frequency shift caused by the second term of Eq. (14). Contrary to Ref. 7, here the WS DSF involves many quanta of cyclotron motion ($N\omega_c$). Surprisingly, Eq. (17) evaluated for the electron solid state coincides with the DSF of a highly correlated electron liquid[11] in which the electron motion is affected by the quasi-uniform fluctuational electric field E_f, distributed as a Gaussian with $\sqrt{\langle E_f^2\rangle}=E_f^{(0)}$, and the collision broadening of Landau levels Γ_N is disregarded ($\Gamma_C\gg\Gamma_N$). The quantity Γ_C can be called the Coulomb broadening of the electron DSF, but it has no relation with the Landau level broadening. Moreover, according to Refs. 10 and 11, the quasi-uniform fluctuational electric field reduces the collision broadening of Landau levels. The result of Eq. (17) explains the experimental observation reported in Ref. 9 that the WS transition does not affect the CR linewidth.

The first term ($N=0$) of Eq. (17) describes the DC magnetoconductivity of the WS. In the extreme limit $\Gamma_C\gg\Gamma_N$ the electron DSF $S(q,0)\propto 1/\Gamma_C\propto n_s^{-3/4}$, which decreases the effective collision frequency and σ_{xx}.

When the fluctuational field is weak ($\Gamma_C\ll\hbar\omega_c$), the CR linewidth is determined by the term with $N=1$. The frequency dependence of $\gamma_{CR}(\omega)$ affects the CR line shape. As a result, the CR absorption approaches the Lorentzian shape only in the limit $\Gamma_C\gg\gamma_{CR}(\omega_c)$ where $\gamma_{CR}(\omega)\simeq$const. In spite of the frequency dependence of the parameter γ_{CR}, the linewidth of the absorption curve at a half-height is very close to $\gamma_{CR}(\omega_c)$. Increasing the fluctuational field $E_f^{(0)}$ makes nonlinear terms ($N\neq 1$) important, changing significantly the density dependence of the linewidth.

4. RESULTS AND DISCUSSIONS

Employing the Wigner solid DSF found above, we can write the CR linewidth $\gamma_{CR}(\omega_c)$ as

$$\gamma_{CR}(\omega_c)=\frac{(eE_\perp)^2[1-\exp(-\hbar\omega/T)]T}{2\sqrt{\pi}\hbar\alpha\Gamma_C}\times\sum_{N=0}^{\infty}\frac{1}{N!}F_N(\hbar\omega_c|N-1|/\Gamma_C), \tag{18}$$

where

$$F_N(\eta)=\int_0^\infty x^{N-1/2}V_S^2(x)\exp(-x-\eta^2/x)dx,$$

$$V_S(x)=1+\frac{\Lambda x}{eE_\perp l^2}w\left(\frac{x}{2\gamma^2 l^2}\right), \tag{19}$$

and the coupling function $w(x)$ is defined in Eq. (6). For small broadening of the WS DSF ($\Gamma_C \ll \hbar\omega_c$), the main contribution to Eq. (18) is given by the term with $N=1$. Since $F_1(0)$ does not depend directly on the electron density n_s, the CR linewidth determined by this term decreases with electron density $\gamma_{CR}(\omega_c)\propto 1/\Gamma_C$, in accordance with Ref. 7.

For strong Coulomb broadening of the DSF ($\Gamma_C \sim \hbar\omega_c$), terms with $N\neq 1$ play an important role, changing the sign of the many-electron effect on the CR linewidth: the decrease of the CR linewidth is turned into an increase. Therefore, the same Coulombic effect (broadening of the electron DSF) leads to the successive narrowing and broadening of the CR linewidth.

Under conditions of the experiment of Ref. 9, the Debye frequency of WS phonons $\omega_D \gtrsim \omega_c$ and therefore the requirement $\omega_{l,k}<\omega_c$ is met only for the long-wavelength part of the phonon spectrum. According to Eq. (14), in this regime $\Gamma_C \gtrsim \hbar\omega_c$ and the terms of Eq. (18) with $N\gg 1$ should be dominant. In evaluating Eq. (18) numerically we use $E_f^{(0)}$ found by Monte Carlo simulations[19] for a broad range of the Coulomb coupling parameter $e^2\sqrt{\pi n_s}/T$. The full linewidth of the CR calculated according to Eq. (18) is shown in Fig. 1. As the electron density n_s is varied, the holding field is fixed at $E_\perp=275$ V/cm. It is clear that the contribution from the linear term (the approximation of Ref. 7—dashed curve) cannot explain the experimental data. On the other hand, the contribution from all terms (solid curve) behaves in good accordance with the data. The deviations of the experimental data at high densities from the proposed model are assumed to be caused by the substantial increase of the WS Debye frequency $\omega_D>\omega_c$ and $\Omega_{+,k}$ for the short-wavelength part of the phonon spectrum.

It is interesting to compare the new WS theory with the old linewidth versus $E_\perp$ data of Refs. 5 and 6, where the electron density n_s was varied according to the saturation condition $E_\perp=2\pi e n_s$. For comparably high temperatures ($T=0.72$ K), in addition to the electron–ripplon scattering, we take into account the electron interaction with vapor atoms. The half-width data and the corresponding theoretical curves are shown in Fig. 2. The theoretical curve, including all nonlinear terms $\exp(iN\omega_c t)$ (solid curve), describes the data nicely. For the low-temperature regime of Fig. 3 ($T=0.4$ K) the interaction with vapor atoms can be disregarded.

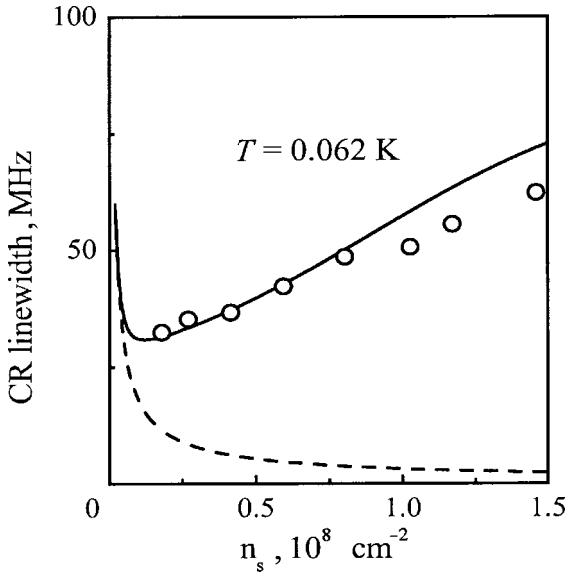

FIG. 1. CR linewidth versus n_s: data from Ref. 9 (circles), WS theory [Eq. (18)] (solid curve), approximation of Ref. 7 (dashed curve).

Both figures (2 and 3) show that the contribution from terms with $N>1$ is crucial for strong holding fields (high electron densities). The holding field dependence of the electron-ripplon coupling V_q is not strong enough to explain the sharp increase of the linewidth data, taking into account the only linear term with $N=1$ (dashed curves). The inclusion of many cyclotron motion quanta $N\omega_c (N\gg 1)$ makes the WS theory (solid curves) close to the data and the half-width behavior similar to that of the semi-classical half-width (dotted curves).

It is instructive to note that exciting many high-frequency phonons with energy $\Sigma\hbar\Omega_{+,k}>N\hbar\omega_c$ in a single scattering event involving a ripplon or a vapor atom is a pure many-electron effect, since at low temperatures $T<\hbar\Omega_c$ neither a scatterer nor an electron have enough energy for this excitation. In a liquid state of the electron system, it is a

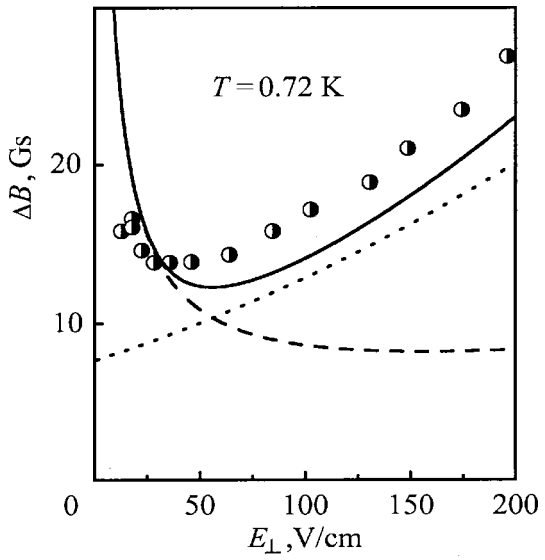

FIG. 2. CR half-width ΔB versus the holding electric field ($E_\perp=2\pi e n_s$): data from Ref. 5 (circles), WS theory [Eq. (18)] (solid curve), approximation of Ref. 7 (dashed curve), semi-classical theory (dotted curve).

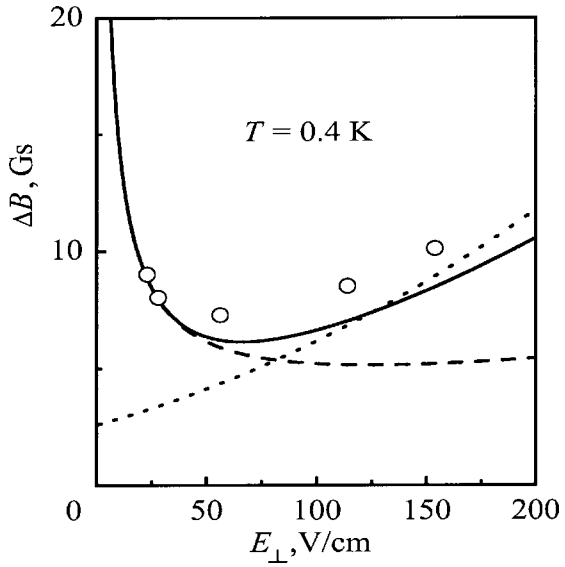

FIG. 3. Low temperature CR half-width data and theory. The notation is the same as in Fig. 2.

quasi-uniform electric field E_f created by many other electrons that makes the electron scattering inelastic in the frame moving along with an electron orbit center. In this frame, a heavy helium vapor atom moving with the velocity $-\mathbf{u}_f$ (here $\mathbf{u}_f$ is the electron-orbit drift velocity induced by E_f) has enough kinetic energy, and electron scattering on higher Landau levels becomes possible if the energy exchange in the moving frame $\hbar\mathbf{q}\cdot\mathbf{u}_f \sim eE_f l$ is larger than the level spacing $\hbar\omega_c$.

In the WS theory, it is the inclusion of a great number of low-frequency WS phonons ($\Omega_{-,k} \ll T/\hbar$) with the distribution function $n_{-,k} \simeq T/\hbar\Omega_{-,k} \gg 1$ that makes possible the emission of many high frequency phonons. One can find the proper multiphonon terms with conventional δ functions by expanding the exponential of Eq. (12) in both $2q^2W_-(\mathbf{n},t)$ and $2q^2W_+(\mathbf{n},t)$. The explanations given just above describe a complicated phenomenon, involving not only many electrons but also a great number of WS excitations, in terms of simple scattering events. Still, the quantity in Eq. (17) represents a DSF of an electron crystal which does not depend on the interaction with scatterers.

5. CONCLUSIONS

Establishing a relation between the effective collision frequency and the electron dynamical structure factor, the conductivity theory of the Wigner solid presented here takes advantage of methods developed for the theory of thermal neutron scattering. The important point is that a 2D electron system represents a moving target whose DSF is analyzed, while scatterers (ripplons and vapor atoms) play the role of thermal particle fluxes, since their properties are well known.

The existence of strongly separated phonon modes of the electron crystal in a high magnetic field [$\Omega_{-,k} \ll T/\hbar$ and $\Omega_{+,k} > \omega_c \gg T/\hbar$] allows one to combine the conventional high-temperature approximation for the solid DSF (applied to the low-frequency mode only) and an exact evaluation of the contribution from the high-frequency mode. The low-frequency mode is shown to affect crucially the result that comes out for the high-frequency mode, causing a strong broadening of the DSF and strengthening the contribution from multiphonon terms.

We have shown that under the conditions of the CR experiments with SEs conducted up until the present[5,6,9] the many-electron effect is very strong, and the multiphonon emission terms of the high-frequency mode disregarded previously can dominate the usual one-phonon term. The inclusion of all these terms leads to a DSF of the Wigner solid which practically coincides with the DSF of a 2D electron liquid whose properties are affected by a quasi-uniform fluctuational electric field E_f of the proper strength.[11] The CR linewidth calculated for the electron-ripplon scattering regime agrees well with the data of Refs. 5, 6, and 9, eliminating the discrepancy between theory and experiment reported in Ref. 9.

A part of this work was supported by the Grant INTAS-97-1643.

*E-mail: monarkha@ilt.kharkov.ua

[1] C. C. Grimes and G. Adams, Phys. Rev. Lett. **42**, 795 (1979).
[2] D. S. Fisher, B. I. Halperin, and P. M. Platzman, Phys. Rev. Lett. **42**, 798 (1979).
[3] B. A. Wilson, S. J. Allen, Jr., and D. C. Tsui, Phys. Rev. Lett. **44**, 479 (1980); B. A. Wilson, S. J. Allen, Jr., and D. C. Tsui, Phys. Rev. B **24**, 5887 (1981).
[4] Z. Schlesinger, W. I. Wang, and A. H. MacDonald, Phys. Rev. Lett. **58**, 73 (1987).
[5] V. S. Edel'man, Zh. Éksp. Teor. Fiz. **77**, 673 (1979) [Sov. Phys. JETP **50**, 338 (1979)].
[6] V. S. Edel'man, Usp. Fiz. Nauk **130**, 675 (1980) [Sov. Phys. Usp. **23**, 227 (1980)].
[7] M. I. Dykman, J. Phys. C **15**, 7397 (1982).
[8] M. Saitoh, J. Phys. Soc. Jpn. **56**, 706 (1987).
[9] L. Wilen and R. Giannetta, Phys. Rev. Lett. **60**, 231 (1988).
[10] E. Teske, Yu. P. Monarkha, M. Seck, and P. Wyder, Phys. Rev. Lett. **82**, 2772 (1999).
[11] Yu. P. Monarkha, E. Teske, and P. Wyder, Phys. Rev. B **62**, 2593 (2000).
[12] W. Gotze and J. Hajdu, J. Phys. C **11**, 3993 (1978).
[13] Y. Shiwa and A. Isihara, J. Phys. C **16**, 4853 (1983).
[14] Yu. P. Monarkha and K. Kono (submitted for publication).
[15] Yu. P. Monarkha, in *Two-Dimensional Electron Systems on Helium and Other Cryogenic Substrates*, edited by E. Y. Andrei [Kluver Academic Publishers, Dordrecht, Boston, London (1997)].
[16] A. V. Chaplik, Zh. Éksp. Teor. Fiz. **62**, 746 (1972) [Sov. Phys. JETP **35**, 395 (1972)].
[17] Yu. P. Monarkha and S. S. Sokolov, Fiz. Nizk. Temp. **8**, 350 (1982) [Sov. J. Low Temp. Phys. **8**, 173 (1982)].
[18] W. Marshall and S. W. Lovesey, *Theory of Thermal Neutron Scattering* (Oxford, Clarendon Press, 1971).
[19] C. Fang-Yen, M. I. Dykman, and M. J. Lea, Phys. Rev. B **55**, 16272 (1997).

This article was published in English in the original Russian journal. Reproduced here with stylistic changes by AIP.

SUPERCONDUCTIVITY, INCLUDING HIGH-TEMPERATURE SUPERCONDUCTIVITY

Spin and superconducting fluctuations in the copper–oxygen planes of a quasi-two-dimensional high-temperature superconductor

G. G. Sergeeva* and V. Yu. Gonchar

Kharkov Physics and Technology Institute National Research Center, ul. Akademichaskaya 1, 61108 Kharkov, Ukraine

A. V. Voitsenya

V. N. Karazin Kharkov National University, pl. Svobody, 61007 Kharkov, Ukraine

(Submitted September 7, 2000; revised January 10, 2001)
Fiz. Nizk. Temp. **27**, 634–641 (June 2001)

The features of the two-dimensional superconducting and spin fluctuations in the copper–oxygen planes of quasi-two-dimensional high-T_c superconductors at $T<T^*$, where T^* is the charge ordering temperature, are studied in the two-dimensional (2D) XY model of Berezinskiĭ, Kosterlitz, and Thouless. It is shown that the coexistence of three phases (metallic, almost insulating, and superconducting) in the copper–oxygen planes, with an independent distribution in each plane, enhances the semiconductor character of the charge transport along the $\hat{\mathbf{c}}$ axis and leads to two channels of charge tunneling with different temperature dependence of the tunneling probability $t_c(T)$. The expressions obtained for the temperature dependence of the resistivity $\rho_c(T)$ can be used to determine the temperature of the 2D XY ordering of the copper spins in the insulating stripes and the dimensionality of the superconducting transition from the results of measurements. © *2001 American Institute of Physics.* [DOI: 10.1063/1.1382988]

1. INTRODUCTION

It is known that the superconducting transition temperature T_c in layered high-T_c superconductors (HTSCs) depends substantially on the degree of doping δ and reaches a maximum at an optimal value $\delta\sim\delta_c$. Compounds with $\delta<\delta_c$, such as $YBa_2Cu_3O_\delta$ with $\delta<6.7$, $La_{2-\delta}Sr_\delta CuO_4$ with $\delta<0.2$, and the superconducting phases Bi2212 and Tl2212 for all values of δ are examples of quasi-2D HTSCs. A peculiarity of these materials is that they have a weak interaction between planes and strong anisotropy of the resistivity, ρ_c along the $\hat{\mathbf{c}}$ axis and ρ_{ab} in the CuO_2 plane: from $\rho_c/\rho_{ab}\sim10^5$ for Bi2212 to $\rho_c/\rho_{ab}\sim10^3$ for $YBa_2Cu_3O_{6.7}$ and $La_{2-\delta}Sr_\delta CuO_4$. The strong, δ-dependent anisotropy of these compounds leads to substantially anisotropic changes in the spectral density of the current carriers for $T_c(\delta)<T<T^*(\delta)$, i.e., it gives rise to features near the Fermi energy and the related state known as the pseudogap.[1] The temperature $T^*(\delta)$ at which the pseudogap appears is also called the charge-ordering temperature: at $T\leqslant T^*$ insulating and metallic stripes are formed in a process which is the dynamic analog of phase separation.

For $T_c<T\leqslant T^*$ quasi-2D HTSCs exhibit some unusual effects for the normal state of HTSCs, such as 2D fluctuations of the short-range antiferromagnetic order parameter in the insulating stripes, semiconductor behavior of $\rho_c(T)$, and 2D–3D dimensional crossover of the superconducting fluctuations. The 2D vortices and 2D superconducting fluctuations are observed in an unusually large temperature interval: 97–178 K for yttrium HTSCs[2] and 84–245 K for Bi2212.[3] This suggests that the superconducting transition is due to a Berezinskiĭ–Kosterlitz–Thouless (BKT) transition,[4–6] i.e., to a process of 2D XY ordering of the copper spins in the CuO_2 planes at a temperature $T_{BKT}<T_{c0}$, where $T_{c0}\leqslant T^*$ is the temperature of the 2D superconducting transition in mean field theory. In spite of the fact that the 2D superconducting fluctuations and the signs indicative of a BKT transition have been observed in the majority of quasi-2D HTSCs (see the review[7] and the references cited therein), it has remained unclear whether such a transition will occur in bulk HTSCs when the interactions along the $\hat{\mathbf{c}}$ are taken into account.[8]

The cause of the change in character of the temperature dependence of $\rho_c(T)$ in quasi-2D HTSCs from metallic to semiconductor behavior has not been established. The main difficulty is apparently that in the temperature region where ρ_c exceeds the Mott–Ioffe–Regel limit $\rho_M\sim10^{-2}\,\Omega\cdot$cm a quasi-2D HTSC can no longer be treated as an anisotripic 3D metal.[9] Then it becomes problematic to describe the normal state of the CuO_2 plane, which on a mesoscopic level is substantially inhomogeneous for $T_c<T\leqslant T^*$: in addition to the insulating and metallic stripes, for $T\leqslant T_{c0}$ superconducting regions also arise in the plane.[10–12] Several models have been proposed to explain the resistivity anomalies of the quasi-2D HTSCs (see Sec. II, 2a of Ref. 7); these include the interlayer tunneling (ILT) model[13–15] and theoretical models of the ground state for the CuO_2 plane which go beyond the framework of the ordinary Fermi liquid.[11,12] In the ILT model there have been interesting attempts to link the incoherent character of the charge transport along the $\hat{\mathbf{c}}$ axis to features of the charge dynamics in the CuO_2 plane[16] and also the interesting hypothesis that the resistivity anomalies of

quasi-2D HTSCs are of a fluctuational nature.[17–20] Using this hypothesis, it was shown that taking into account the strong 2D superconducting fluctuations for $T_c<T<T^*$ leads to an excess conductivity in the CuO_2 plane[18] and to semiconductor temperature dependence of the resistivity $\rho_c(T)$.[19]

To elucidate the relationship between the superconducting and BKT transitions in quasi-2D HTSCs, in this paper the fluctuational model of interlayer tunneling[19] is used to find the temperature dependence of the resistivity $\rho_c(T)$ for $T_c<T<T^*$. A comparison of the expression obtained below (Eq. 4) with the measured $\rho_c(T)$ for Bi2212 single crystals[21] has made it possible to determine, without the use of fitting parameters, the temperature $T_{BKT}(\delta)$ of the 2D XY ordering of the copper spins in the insulating stripes and the dimensionality of the superconducting transition. To illustrate how the different regimes of magnetic behavior of the spins of copper and holes in the CuO_2 plane of quasi-2D HTSCs depend on the oxygen concentration, we construct a magnetic phase diagram in which, in addition to the phases observed previously,[22] we note phases of 2D XY ordering of the copper spins in the CuO_2 plane and in the insulating stripes.

2. 2D FLUCTUATIONS IN "STRIPED" CuO_2 PLANES

The strong antiferromagnetic (AFM) fluctuations in quasi-2D HTSCs, despite the substantial difference of the exchange constants of the in-plane J_0 and interplane J_1 interactions ($J_0/J_1>10^3$), prevent the 2D Heisenberg ordering of the spins. For $T<T^*$ the CuO_2 planes can be called "striped"—a structure is established which consists of stripes of insulating and metallic phases with a stripe width dependent on the hole concentration in the plane. Although destruction of the AFM order in the system of copper spins of an individual insulating stripe does not occur, the short-range order for the copper spins of each stripe is established independently,[10] and in the absence of magnetic field the sample remains unmagnetized. Thus the "striped" plane in the normal state is an unusual 2D object with regions of spin and charge nonuniformity (of mesoscopic dimensions). For such a plane one can speak of fluctuations of the short-range AFM ordering and of the "two-dimensional" charge of the quasiparticles. The value of the "two-dimensional" charge is proportional to the 3D interaction constant divided by the distance between planes.[23] The ground state of such a mesoscopically inhomogeneous plane goes beyond the framework of the usual Fermi liquid theory, and this topic is currently of great interest[11,12] and requires a separate discussion.

It can be assumed that in the "striped" plane at $T\sim T_{c0}<T^*$ the exchange of 2D spin excitations with wave vector equal to the AFM vector $Q=(\pi,\pi)$ leads to pairing of the 2D charges. As was noted in Ref. 24, only excitations with such a wave vector will leave a quasiparticle on the Fermi surface after interacting with it. The spin-fluctuation mechanism of pairing, which has been discussed for almost ten years now,[25] gives rise to fluctuational superconducting regions[10] in the "striped" planes in quasi-2D HTSCs at $T<T_{c0}$; the size of these regions is limited on from above by the correlation length of the 2D AFM fluctuations and from below by the correlation length of the superconducting fluctuations. With allowance for dimensional scaling there exists a maximum value $T_{cl}<T_{c0}$ and a minimum value T_{cm} of the transition temperature; these are determined by the averaged values of the exchange interaction constants of the copper spins in insulating regions of the maximum and minimum sizes, respectively.

Thus for $T_{cm}<T<T_{cl}$ the "striped" planes have coexisting regions of metallic, almost insulating, and superconducting phases.[10,19] Further lowering of the temperature is accompanied by the excitation of fluctuations in the superconducting regions; these relations are described by the BKT 2D XY model[4–6] (2D vortices, antivortices, and paired vortices) with an exponential temperature dependence of the correlations for $T_{cm}>T>T_{BKT}$ and with a power-law dependence for $T<T_{BKT}$.

3. ANALYSIS OF THE TEMPERATURE DEPENDENCE OF THE RESISTIVITY $\rho_c(T)$

At temperatures such that $\rho_{ab}\rho_c>\rho_M^2$, a quasi-2D HTSC can no longer be treated as an anisotropic 3D metal.[9] The charge transport along the $\hat{\mathbf{c}}$ axis takes place by a process of tunneling through a nonconducting barrier, and the quantity ρ_c/ρ_M is proportional to N/N_0t_c, the ratio of the density of states N in the sample to the fraction of the states N_0 in the CuO_2 plane which, with probability t_c, have overcome the barrier.[14,17–21] Thus, to within a constant factor, the temperature dependence $\rho_c(T)$ is given by the expression

$$\rho_c(T)\approx\frac{\rho_M N}{N_0 t_c}. \tag{1}$$

The lack of success met in attempts to explain the semiconductor behavior of $\rho_c(T)$ in quasi-2D HTSCs by a decrease of the density of states N_0 due to superconducting fluctuation effects in the CuO_2 plane[17,18] has motivated studies of the temperature dependence of the tunneling probability $t_c(T)\sim\gamma^{-2}$ (γ is the degree of anisotropy of the HTSC):[19–21]

$$t_c(T)\approx\left[\frac{\xi_c(T)}{\xi_{ab}(T)}\right]^2, \tag{2}$$

where $\xi_{ab}(T)$ and $\xi_c(T)$ are the correlation lengths in the CuO_2 plane and along the $\hat{\mathbf{c}}$ axis. In a 3D superconductor the temperature dependence of $\xi_{ab}(T)$ and $\xi_c(T)$ is the same, and the tunneling probability t_c and the degree of anisotropy are therefore independent of temperature. We shall show below that in quasi-2D HTSCs the coexistence of three phases in "striped" planes, with an independent distribution in each plane, enhances the semiconductor character of the charge transport along the $\hat{\mathbf{c}}$ and leads to several channels for the tunneling of charge, with different temperature dependences of the probability $t_c(T)$.

As we see from Eq. (1), the main contribution to the resistivity $\rho_c(T)$ is from the tunneling channels with the smallest values of $t_c(T)$. In quasi-2D HTSCs at $T_c<T<T_{cl}$ the two-dimensionality of the superconducting fluctuations (up to temperatures of $\sim 200\,\mathrm{K}$)[2,3] leads to a situation where $\xi_c(T)\sim$const while the correlation length $\xi_{ab}(T)$ is temperature-dependent, i.e., to a temperature-dependent probability $t_c(T)$ [Eq. (2)]. In a study of 2D fluctuation effects for $\xi_{ab}(T)$ one can use the results obtained by Halperin and Nelson[26] for superconducting films with a superconducting transition temperature equal to T_{BKT}. In the temperature

region $T_{cm}<T<T_{cl}$ the temperature dependence of the correlation length $\xi_{ab}(T)=\xi_{ab}(T/T_{BKT}-1)^{-1/2}$ is determined by the Landau–Ginzburg formula, and the tunneling probability decreases with decreasing temperature:

$$t_c(T)\sim\frac{\xi_c^2}{\xi_{ab}^2}\left(\frac{T}{T_{BKT}}-1\right), \tag{3}$$

where ξ_{ab} and ξ_c are the values of the correlation lengths at $T=T_{BKT}$. It follows from Eqs. (1) and (3) that in this temperature region the resistivity $\rho_c(T)$ increases with decreasing temperature:

$$\rho_c(T)=k(T-T_{BKT})^{-1}, \tag{4}$$

where

$$k=T_{BKT}\frac{\rho_M\xi_{ab}^2}{N_0\xi_c^2}N. \tag{5}$$

At lower temperatures $T_{BKT}<T<T_{cm}$, when vortex fluctuations are described by the BKT 2D XY model,[4–6,26]

$$\xi_{ab}(T)\sim\xi_{ab}\left[\frac{T_{BKT}}{4b(T_{cm}-T_{BKT})}\right]^{1/2}\exp\left[\frac{T_{cm}-T_{BKT}}{T-T_{BKT}}\right]^{1/2}, \tag{6}$$

a second channel of tunneling opens up, which has an exponential temperature dependence of the tunneling probability $t_c(T)$ and carries the main contribution to the resistivity in this temperature interval:

$$\rho_c(T)=k_1\exp\left[4b\frac{T_{cm}-T_{BKT}}{T-T_{BKT}}\right]^{1/2}, \tag{7}$$

where

$$k_1=\frac{\rho_M\xi_{ab}^2}{N_0\xi_c^2}\frac{NT_{BKT}}{4b(T_{cm}-T_{BKT})}. \tag{8}$$

Here b is a constant.[26]

Expressions (4) and (7) allow us to determine T_{cm}, T_{cl}, and T_{BKT} from measurements of $\rho_c(T)$. Choosing a pair of points T_i, T_j in the interval $T_{cl}>T_{i,j}>T_{cm}$, we can determine the temperature T_{BKT} from (4) without adjustable parameters:

$$T_{BKT}=\frac{\rho_iT_i-\rho_jT_j}{\rho_i-\rho_j}, \tag{9}$$

where $\rho_i=\rho(T_i)$ and $\rho_j=\rho(T_j)$. For calculating T_{BKT} from Eq. (9) we used the results of measurements of $\rho_c(T)$ for Bi2212 single crystals[21] with different oxygen concentrations δ (Fig. 1). Pairs of points T_i, T_j on the $\rho_c(T)$ curve were chosen in a temperature interval starting 15–20 K above the temperature T_c^0 at which the semiconductor behavior of the resistivity stops. The results obtained after averaging the values of T_{BKT} for four pairs T_i, T_j are given in Table I.

The solid curve on the $\rho_c(T)$ plot in Fig. 1 indicates the regions in which the results of the measurements are described by expression (4) with a single value of the fitting parameter k. This makes it possible to estimate the values of the temperatures T_{cm} and T_{cl}. As we see from Fig. 1, $T_{cm}\simeq 96$ K and is almost independent of the oxygen concentration. The value of T_{cl} (given in Table I) and, hence, the value of the fluctuation interval $T_{cl}-T_{cm}$ depend substantially on

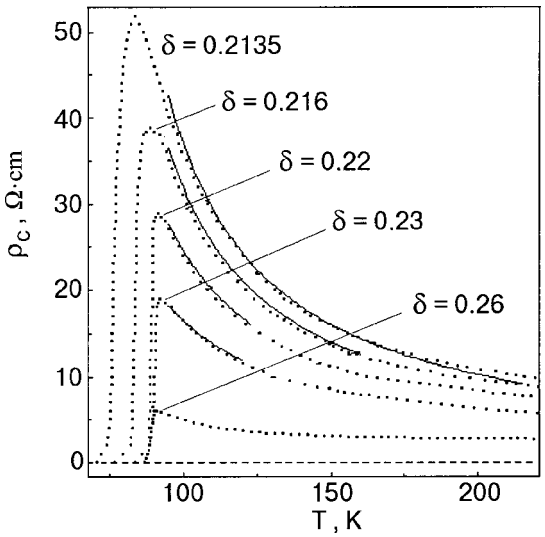

FIG. 1. Temperature dependence of the resistivity ρ_c of Bi2212 single crystals with different oxygen concentrations. The points are the measurements of Ref. 21, the curves show the dependence $\rho_c(T)=k(T-T_{BKT})^{-1}$ (Eq. (4)) for a single value of the adjustable parameter k, which for $\delta=0.2135$, 0.216, 0.22, and 0.23 had the values $k=1418$, 1253, 1075, and 859.2, respectively.

δ. The reason for this dependence is clear: T_{cl} depends on the number of dangling bonds between the spins of the copper atoms in the insulating stripe, which is determined by the stripe width $\sim\delta^{-1/2}$. The smaller the value of δ, the wider are these stripes and the larger is the value of the exchange constant, i.e., T_{cl} and $T_{cl}-T_{cm}$ increase with decreasing δ: $T_{cl}-T_{cm}$ changes from 24 K for $\delta=0.23$ to 120 K for $\delta=0.2135$.

Figure 1 shows the results of measurements of $T_c(\delta)$ and calculation of the averaged values $T_{BKT}(\delta)$ for Bi2212 single crystals.[17] As we see from Fig. 1 and Table I,

$$\log T_{BKT}(\delta)\simeq 6(0.5-\delta), \tag{10}$$

and so the temperature T_{BKT} and, hence, the degree of anisotropy of the samples increase with decreasing δ.

Taking the logarithm of expression (7) and finding the difference $\ln\rho_i-\ln\rho_j$, we obtain the expression

$$4b(T_{cm}-T_{BKT})=\frac{(\ln\rho_i/\rho_j)^2(T_i-T_{BKT})(T_j-T_{BKT})}{|(T_i-T_{BKT})^{1/2}-(T_j-T_{BKT})^{1/2}|^2}, \tag{11}$$

from which, for known T_{cm}, T_{cl}, and T_{BKT}, we can determine the constant b. Calculations of b for the curve with $\delta=0.2135$ give the reasonable value $b=0.42$.

As we see from Fig. 1, the values of T_c^0 for samples with different degrees of doping are close to the superconducting transition temperature of an ideally doped sample, $T_c\sim 88$ K.

TABLE I.

δ	T_{BKT}, K	T_{cl}, K
0.2135	61.72	215
0.2160	60.62	160
0.2200	56.20	123
0.2300	47.92	120
0.2600	32.78	

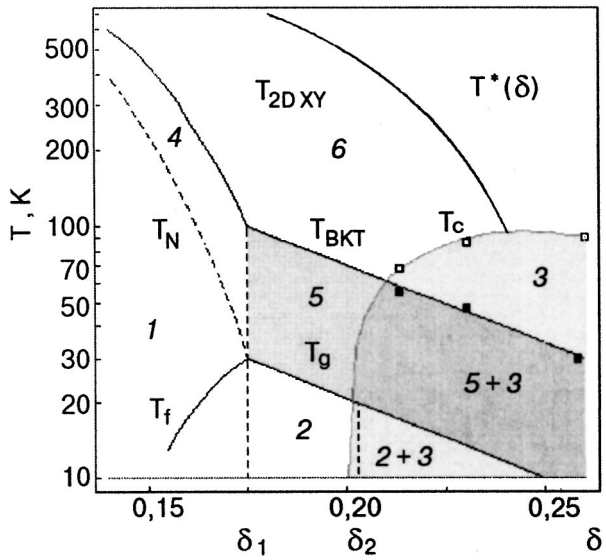

FIG. 2. Magnetic phase diagram as a function of the oxygen concentration δ for Bi2212 single crystals: *1*—3D AFM state with ordering of the copper spins, $T_N(\delta)$, and ''freezing'' of the hole spins, $T_f(\delta)$; *2*—cluster spin glass state for $\delta \geqslant \delta_1$, $T \leqslant T_g(\delta)$; *3*—region of the superconducting state (light shading), $T_c(\delta)$ (□—the results of measurements[21]); *2+3*—coexistence region; *4*—2D *XY* ordering of the copper spins in the CuO_2 planes, $T_{2DXY}(\delta)$; *5*—2D *XY* ordering of the copper spins in the insulating stripes for $\delta \geqslant \delta_1$, $T \leqslant T_{BKT}(\delta)$ (■—the results of calculations, see Table I); *5+3*—the coexistence region of these states for $\delta \geqslant \delta_2$; *6*—normal state with charge ordering in the CuO_2 planes.

Thus the second tunneling channel, which leads to exponential growth of the resistivity $\rho_c(T)$ [Eq. (7)] with decreasing temperature, gives a contribution in a relatively small temperature interval $T_{cm} - T_c^0 \sim 8$ K, which is nearly independent of the oxygen concentration.

It has been established experimentally that in the superconducting state for $T \leqslant T_c$ the tunneling probability no longer depends on temperature.[27] This allows us, as in Ref. 18, to define the temperature T_c^0 at which the semiconductor trend of $\rho_c(T)$ abruptly stops, as the temperature of the dimensional crossover from 2D to 3D superconducting fluctuations. A comparison of Table I and Fig. 1 shows that $T_{BKT} < T_c$, i.e., taking into account the 2D fluctuations in a quasi-2D HTSC renormalizes the interplane tunneling $t_c(T)$ to such a degree that the dimensional crossover at T_c^0 occurs before the BKT transition. The fact that the values of T_c^0 for samples with different degrees of doping are close to the superconducting transition temperature $T_c(\delta_c) \sim 88$ K of an ideally doped sample allows us to assume that T_c^0 and the superconducting transition temperature in mean field theory with 3D fluctuations are quantities of the same order. For superconductors with a spin-fluctuation mechanism of pairing the temperature T_c^0 is determined by the interplane exchange interaction constant J_1 and is almost independent of the oxygen concentration. This definition of the temperature T_c^0 agrees with the results of $\rho_c(T)$ measurements: for samples with different degrees of doping the breakoff of the semiconductor trend of the resistivity is almost independent of the oxygen concentration and occurs at temperatures close to the superconducting transition temperature of an ideally doped sample, $T_c \sim 88$ K (Fig. 1).

4. DISCUSSION OF THE RESULTS

Nature of the superconducting fluctuations

Calculations have shown (Fig. 1) that in a large temperature interval $T_{cl} - T_{cm}$, which depends on the oxygen concentration, the $\rho_c(T)$ curves for Bi2212 single crystals[21] are satisfactorily described with allowance for 2D superconducting fluctuations [see expression (4)]. The size of the fluctuation interval depends on the dimensionality of the fluctuations—for a plane the transition to the superconducting state occurs at the temperature T_{BKT}, and the fluctuation interval for a ''striped'' plane would be determined by the difference $T_{c0} - T_{BKT}$, i.e., it would be much larger. In a quasi-2D HTSC, taking the 2D fluctuations into account renormalizes the interplane tunneling $t_c(T_c^0)$ to such a degree that the dimensional crossover occurs before the BKT transition.

In layered systems the probability $t_c(T_c^0)$ for the tunneling of charge along the $\hat{\mathbf{c}}$ axis determines the character of the superconducting transition:[23] at sufficiently small $t_c(T)$, when

$$T_c^0/\varepsilon_F \gg t_c(T_c^0), \tag{12}$$

the transition is 2D with 3D superconducting fluctuations for $T_c < T < T_c^0$ (Ref. 23). The ratio T_c^0/ε_F is limited from above by fluctuations of the phase of the order parameter and from below by fluctuations of the number of Cooper pairs:

$$\ln^{1/3} t_c(T_c^0) > T_c^0/\varepsilon_F > \ln^{-1} t_c(T_c^0). \tag{13}$$

Using expressions (12) and (13) and the above calculations, one can determine the dimensionality of the superconducting transition in a quasi-2D HTSC if, in addition to the results of the $\rho_c(T)$ measurements, the values of ε_F and ξ_c^2/ξ_{ab}^2 are known for the same samples. For four Bi2212 single crystals[21] with values $\delta < 0.26$ the superconducting transition occurs as two-dimensional, with a bounded interval $T_c - T_c^0$ of 3D superconducting fluctuations: condition (13) holds for $\varepsilon_F \sim 200$ K and $\xi_c^2/\xi_{ab}^2 < 0.01$.

Magnetic phase diagram

To illustrate how the behavior of the spins of the copper and holes in the CuO_2 plane of quasi-2D HTSCs depends on the oxygen concentration, a model of the magnetic phase diagram is shown in Fig. 2. Besides the previously observed[22] phases of ordering of the copper spins, such as the 3D AFM state at the Néel temperature $T_N(\delta)$ (*1*), the cluster spin glass states with strong magnetic correlations (*2*), and the superconducting state (*3*), two additional phases are noted in Fig. 2: a phase of 2D *XY* ordering of the copper spins in CuO_2 plane [regime *4*, $T_{2DXY}(\delta)$] and in the insulating stripes [regime *5*, $T_{BKT}(\delta)$]. The dependence of $T^*(\delta)$ gives an upper limit on the region of charge ordering of nonsuperconducting samples, the region of the normal state (regime *6*) of superconducting samples with a semiconductor behavior of $\rho_c(T)$, and, as will be discussed below, the regime *5+3* for $T < T_c$.

At low concentrations δ (regime *1*) the spins of the Cu^{2+} and the spins of the holes are ordered independently: the former orders in the 3D AFM state at the Néel temperature $T_N(\delta)$, while the hole spins ''freeze'' at $T_f(\delta)$. With increas-

ing δ, at intermediate doping, when there is neither long-range AFM order nor superconductivity, at δ_1, $T_N(\delta_1) = T_f(\delta_1) = T_g$, a transition occurs to a cluster spin glass state with strong magnetic correlations (regime *2*). The absence of long-range AFM order can be explained by the limited size $\sim \delta^{-1/2}$ of the AFM regions that arise upon charge ordering. Regime *2* with $\delta \geqslant \delta_2$ coexists with the superconducting state (regime *2+3*) up to the concentration δ_c at which $T_g(\delta_c) = 0$. In the case $\delta < \delta_1$ a region of 2D *XY* ordering of the copper spins in the CuO_2 plane,

$$T_{2DXY}(\delta) \leqslant T \leqslant T_N(\delta),$$

which has been well studied for anisotropic magnets (regime *4*), precedes the 3D AFM ordering. With increasing oxygen concentration, for $\delta > \delta_1$, a charge ordering of the nonsuperconducting regions occurs, and regime *4* goes over to regime *5*, a 2D *XY* ordering of the copper spins in the insulating stripes for $T_g(\delta) < T < T_{BKT}(\delta)$.

Regime *5* precedes the cluster spin glass state in nonsuperconducting samples with $\delta_1 < \delta < \delta_2$ (regime *2*), while for $\delta_2 < \delta < \delta_c$ it coexists with the superconducting state (*5+3*), and for $T > T_g$ it precedes the regime *2+3*. The existence region of regime *5+3* is bounded on the right by the line $T^*(\delta)$ all the way to the doping level δ_c at which charge ordering in the sample does not occur: $T_g(\delta_c) = 0$, $T^*(\delta_c) = 0$.

Here both the quantity $\log T_g(\delta)$, obtained in muon spin polarization measurements for $La_{2-\delta}Sr_\delta CuO_4$ and $Y_{1-\delta}Ca_\delta Ba_2Cu_3O_{6.02}$ (Ref. 22), and the quantity $\log T_{BKT}(\delta)$ which was found above [Eq. (10)] from measurements of the resistivity of Bi2212 single crystals,[21] depend linearly on the dopant concentration.

CONCLUSION

1. For quasi-2D HTSCs with semiconductor behavior of the $\hat{\mathbf{c}}$-axis resistivity $\rho_c(T)$, the features of the 2D spin and superconducting fluctuations in a CuO_2 plane with metallic and insulating stripes have been analyzed for $T_c < T < T^*$. It was shown that the 2D superconducting fluctuations lead to two channels of charge tunneling along the $\hat{\mathbf{c}}$ axis with a probability $t_c(T)$ that falls off with decreasing temperature. One of these channels, that at higher temperatures, is due to 2D fluctuations described by the Landau–Ginzburg theory, and the other is due to vortex fluctuations in the 2D *XY* model.

2. The temperature dependence of the resistivity $\rho_c(T)$ has been analyzed in detail. The relations obtained can be used with the results of $\rho_c(T)$ measurements to determine the temperature T_{BKT} of the 2D *XY* ordering of the copper spins in the insulating stripes. It was shown that the 2D fluctuations renormalize the interplane tunneling constant to such a degree that the dimensional crossover occurs before the BKT transition.

3. The temperature dependence of the tunneling probability $t_c(T)$ can be used to determine the dimensionality of the superconducting transition in a quasi-2D HTSC if, in addition to the results of $\rho_c(T)$ measurements, the value of the Fermi energy ε_F and the ratio of the correlation lengths ξ_c^2/ξ_{ab}^2 are known for the same samples. It was shown that for Bi2212 single crystals[21] the superconducting transition occurs as a 2D transition with a finite interval of 3D superconducting fluctuations.

4. The fluctuational temperature interval $T_{cl} - T_{cm}$, in which the temperature dependence $\rho_c(T)$ is satisfactorily described by 2D Landau–Ginzburg fluctuations, increases with decreasing oxygen concentration. It was conjectured that this is due to growth of the degree of anisotropy of the samples as δ decreases.

5. A model of the magnetic phase diagram was constructed as a function of the oxygen concentration in respect to the different regimes of behavior of the spins of the copper and holes of a quasi-2D HTSC (Fig. 2). Besides the previously observed[22] regimes, viz., a 3D AFM state at the Néel temperature $T_N(\delta)$, a cluster spin glass state with strong magnetic correlations, and a superconducting state, two additional regimes are noted: 2D *XY* ordering of the copper spins in the CuO_2 plane and in the insulating stripes.

*E-mail: gsergeeva@kipt.kharkov.ua

[1] T. Timusk and B. Statt, Rep. Prog. Phys. **62**, 61 (1999).
[2] J. P. Rice, J. Giapintzakis, D. M. Ginsberg, and J. M. Mochel, Phys. Rev. B **44**, 10158 (1991).
[3] M.-O. Mun, S. L. Lee, S.-H. Suck Salk, H. J. Shin, and M. K. Joo, Phys. Rev. B **48**, 6703 (1993).
[4] V. L. Berezinskiĭ, JETP Lett. **61**, 1144 (1971).
[5] J. M. Kosterlitz and D. J. Thouless, J. Phys. C **6**, 1181 (1983).
[6] J. M. Kosterlitz, J. Phys. C **7**, 1046 (1974).
[7] S. L. Cooper and K. E. Gray, in *Physical Properties of High Temperature Superconductors*, edited by D. M. Ginsberg, World Scientific, Singapore (1994), pp. 61–188.
[8] Y. Matsuda, S. Komiyama, T. Onogi, T. Tarashima, K. Shimura, and Y. Bando, Phys. Rev. B **58**, 10498 (1993); Y. Matsuda, S. Komiyama, T. Tarashima, K. Shimura, and Y. Bando, Phys. Rev. Lett. **69**, 3228 (1992).
[9] A. F. Ioffe and A. R. Regel, in *Progress in Superconductors*, Vol. 4, London (1960), p. 237; N. F. Mott, *Metal–Insulating Transition*, Taylor and Francis, New York (1974); Nauka, Moscow (1979), Ch. 1.
[10] V. M. Loktev, Fiz. Nizk. Temp. **22**, 3 (1996) [Low Temp. Phys. **22**, 1 (1996)]; V. P. Gusynin, V. M. Loktev, and S. G. Sharapov, Zh. Éksp. Teor. Fiz., **115**, 1243 (1999) [JETP **88**, 685 (1999)].
[11] V. Emery, S. A. Kivelson, and O. Zachar, Phys. Rev. B **56**, 6120 (1997).
[12] C. M. Varma, Phys. Rev. B **61**, R3804 (2000).
[13] G. Briceno, M. F. Crommie, and A. Zettle, Phys. Rev. Lett. **66**, 2164 (1991).
[14] P. W. Anderson, Science **268**, 1154 (1995).
[15] T. Ito, H. Takagi, S. Ishibashi, T. Ido, and S. Uchida, Nature (London) **350**, 596 (1991).
[16] N. Kumar and A. M. Jayanavar, Phys. Rev. B **45**, 5001 (1992); N. Nagaosa, J. Phys. Chem. Solids **53**, 1493 (1992).
[17] Y. Zha, S. L. Cooper, and D. Pines, Phys. Rev. B **53**, 8253 (1996).
[18] L. B. Ioffe, A. I. Larkin, A. A. Varlamov, and L. Yu, Phys. Rev. B **47**, 6037, 8936 (1993).
[19] G. G. Sergeeva, Fiz. Nizk. Temp. **26**, 453 (2000) [Low Temp. Phys. **26**, 331 (2000)], e-print: cond-mat/9902225, 0009212.
[20] T. Watanabe and A. Matsuda, Phys. Rev. B **54**, 6881 (1996).
[21] T. Watanabe, T. Fujii, and A. Matsuda, Phys. Rev. Lett. **79**, 2113 (1997).
[22] C. Nidermayer *et al.*, Phys. Rev. Lett. **80**, 3843 (1998).
[23] E. I. Kats, Zh. Éksp. Teor. Fiz. **56**, 1675 (1969) [Sov. Phys. JETP **29**, 897 (1969)].
[24] Z.-X. Shen and J. R. Schriffer, Phys. Rev. Lett. **78**, 1771 (1997).
[25] A. Millis, P. Montoux, and D. Pines, Phys. Rev. B **42**, 167 (1990).
[26] B. I. Halperin and D. Nelson, J. Low Temp. Phys. **36**, 599 (1979).
[27] T. Ito, K. Takeno, and S. Ushida, Phys. Rev. Lett. **70**, 3995 (1993).

Translated by Steve Torstveit

LOW-TEMPERATURE MAGNETISM

Influence of a large biquadratic interaction on the phase states of a non-Heisenberg biaxial ferromagnet

Yu. A. Fridman and O. A. Kosmachev

*V. I. Vernadskiĭ Tavricheskiĭ National University, ul. Yaltinskaya 4, 95007 Simferopol, Ukraine**

(Submitted November 7, 2000; revised December 25, 2000)
Fiz. Nizk. Temp. **27**, 642–648 (June 2001)

A study is made of the phase states of a biaxial non-Heisenberg ferromagnet with a large biquadratic interaction in an external magnetic field. It is shown that in such systems the formation of canted phases is energetically unfavorable but that the quadrupolar and ferromagnetic phases can exist in them. The phase transitions between these phases are studied, and it is shown that they are first-order transitions. The field of the first-order transition is found. The phase stability fields are determined from an analysis of the spectra of coupled magnetoelastic waves.
 [DOI: 10.1063/1.1382989]

1. INTRODUCTION

It is well known[1] that an adequate description of the exchange interaction of magnetically ordered systems with spin S greater than 1/2 requires taking into account not only the terms bilinear in the spin operators but also invariants of higher order. The simplest model that takes such invariants into account is that of a ferromagnet with a biquadratic interaction.[1–4] For example, taking the biquadratic interaction into account is important in studying the magnetic properties of the cubic intermetallides TmCd and TmZn.[5,6] The point is that the magnets mentioned, and a number of other systems as well (e.g., rare-earth pnyctides), can be found in a nonmagnetic state at $H=0$ (the so-called quadrupolar (QP) phases) and undergo a transition to a magnetic phase upon the imposition of a sufficiently high magnetic field.

The nature of this metamagnetic transition can vary. In some cases the singlet ground state of the magnet is due to a large value of the single-ion anisotropy (SA).[3,4,7] Another possible mechanism leading to a nonmagnetic phase at $H=0$ involves a biquadratic interaction.[1,2] In highly anisotropic non-Heisenberg magnets these two factors can act simultaneously, shaping the features of both the ground state and the spectral properties. It should also be noted that most often such systems are studied without taking into account the interaction of the magnetic subsystem with the crystal lattice, i.e., the magnetoelastic (ME) interaction.

Many papers have been devoted to the study of non-Heisenberg magnets (see, e.g., the review by Loktev and Ostrovskii[2]). Those papers have mainly investigated non-Heisenberg magnets with a weak biquadratic interaction. It is of interest to study the behavior of non-Heisenberg ferromagnets in the case when the biquadratic exchange is greater than the Heisenberg interaction.

2. PHASE STATES OF A BIAXIAL FERROMAGNET

As a model system we investigate a biaxial non-Heisenberg ferromagnet in an external field parallel to the $0X$ axis. The Hamiltonian for this model is written

$$\mathcal{H}=-H\sum_n S_n^x-\frac{1}{2}\sum_{n,n'}\{J(n-n')\mathbf{S}_n\cdot\mathbf{S}_{n'}+K(n-n')\times(\mathbf{S}_n\cdot\mathbf{S}_{n'})^2\}-B_2^0\sum_n\{3(S_n^z)^2-S(S+1)\}-B_2^2\sum_n\frac{1}{2}\{(S_n^+)^2+(S_n^-)^2\}+\nu\sum_{n,i,j}S_n^iS_n^ju_{ij}(n)+\int dr\left\{\frac{\lambda+\eta}{2}\sum_i u_{ii}^2+\eta\sum_{ij}u_{ij}^2+\lambda\sum_{i\neq j}u_{ii}u_{jj}\right\}, \tag{1}$$

where S_n^i is the spin operator at site n, $J(n-n')$ and $K(n-n')$ are the Heisenberg and biquadratic interaction constants, B_2^0 and B_2^2 are the SA constants, ν is the ME coupling constant, λ and η are elastic moduli, and $u_{ij}=1/2(\partial u_i/\partial x_j+\partial u_j/\partial x_i)$ is the symmetric part of the elastic strain tensor.

The system described by Hamiltonian (1) was studied in detail in Ref. 8. However, the case considered in Ref. 8 is that in which $B_2^2>0$ and the biquadratic interaction is small, i.e., $K_0<J_0$. In this paper we consider a different situation, when $B_2^2<0$ and the biquadratic interaction is greater than the Heisenberg exchange ($K_0>J_0$). As in Ref. 8, we assume that the magnetic ion has spin $S=1$. The SA and ME coupling effects are taken into account exactly by means of the Hubbard operator technique.[9] Many of the intermediate results of the present paper agree with the results of Ref. 8, and we shall therefore not give them in detail here.

Separating out in the exchange part of (1) the mean field associated with $\langle S^x\rangle$ and the additional fields q_2^p ($p=0,2$) due to the presence of the quadrupole moments, we obtain the one-site Hamiltonian, whose eigenvalues determine the energy levels of the magnetic ion:[8]

$$E_+=\frac{\tilde{B}_2^0-\tilde{B}_2^2}{2}+\nu\left(u_{xx}^{(0)}+\frac{u_{yy}^{(0)}+u_{zz}^{(0)}}{2}\right)-\frac{\chi}{2},$$

$$E_0=\frac{\tilde{B}_2^0-\tilde{B}_2^2}{2}+\nu\left(u_{xx}^{(0)}+\frac{u_{yy}^{(0)}+u_{zz}^{(0)}}{2}\right)+\frac{\chi}{2},$$

$$E_-=\tilde{B}_2^2-\tilde{B}_2^0+\nu(u_{yy}^{(0)}+u_{zz}^{(0)}),$$

$$\chi^2=4\overline{H}^2+[3\tilde{B}_{2n}^0+\tilde{B}_{2n}^2+\nu(u_{yy}^{(0)}-u_{zz}^{(0)})]^2. \qquad (2)$$

Here

$$\overline{H}=H+\left(J_0-\frac{K_0}{2}\right)\langle S^x\rangle;\quad \tilde{B}_{2n}^0=B_2^0+\frac{K_0}{6}q_{2n}^0;$$

$$\tilde{B}_{2n}^2=B_2^2+\frac{K_0}{2}q_{2n}^2;\quad q_{2n}^p=\langle O_{2n}^p\rangle;$$

$$O_{2n}^0=3(S_n^z)-2;\quad O_{2n}^2=\frac{1}{2}[(S_n^+)^2+(S_n^-)^2];$$

$$S_n^+=\frac{1}{2}(S_n^x\pm iS_n^y),$$

and $u_{ij}^{(0)}$ are the spontaneous strains, the explicit form of which is determined from the condition of minimum free energy density:

$$u_{xx}^{(0)}=-\frac{\nu(\lambda+\eta)}{\eta(\eta+3\lambda)};\quad u_{yy}^{(0)}=-\frac{\nu(\eta-\lambda)}{\eta(\eta+3\lambda)}\sin^2\theta;$$

$$u_{zz}^{(0)}=-\frac{\nu(\eta-\lambda)}{\eta(\eta+3\lambda)}\cos^2\theta,$$

$$\cos 2\theta=\frac{3\tilde{B}_{2n}^0+\tilde{B}_{2n}^2+\nu(u_{yy}^{(0)}-u_{zz}^{(0)})}{\chi},\quad \sin 2\theta=\frac{2\overline{H}}{\chi}.$$

The eigenfunctions of the one-site Hamiltonian[8] are used as a basis for constructing the Hubbard operators[9] $X_n^{M'M}\equiv|\Psi_n(M')\rangle\langle\Psi_n(M)|$, which describe the transition of the magnetic ion from state M to state M'. The spin operators are related to the Hubbard operators as

$$S_n^+=(H_n^+-H_n^0)\sin 2\theta+(X_n^{+0}+X_n^{0+})\cos 2\theta$$
$$+(X_n^{-+}-X_n^{+-})\sin\theta+(X_n^{-0}-X_n^{0-})\cos\theta,$$

$$S_n^-=(S_n^+)^+,$$

$$S_n^z=(X_n^{+-}+X_n^{-+})\cos\theta-(X_n^{0-}+X_n^{-0})\sin\theta. \qquad (3)$$

If the biquadratic exchange is greater than the Heisenberg interaction, then, as was shown in Refs. 3 and 4, for $H=0$ only the quadrupolar phases QP_1, QP_2, and QP_1' are realized in the system. The order parameters in these phases are

QP_1 KY_1: $\langle S\rangle=0,\quad q_2^0=q_2^2=1;$

QP_1' KY_1': $\langle S\rangle=0,\quad q_2^0=1,\quad q_2^2=-1;$

QP_2 KY_2: $\langle S\rangle=0,\quad q_2^0=-2,\quad q_2^2=0.$

The phase diagram for $H=0$ is given in Fig. 1 (see Refs. 3 and 4). The lines *1*, *2*, and *3* are lines of second-order phase transitions and are described by the equations $B_2^2=-3B_2^0$, $B_2^2=3B_2^0$, and $B_2^2=0$, respectively.

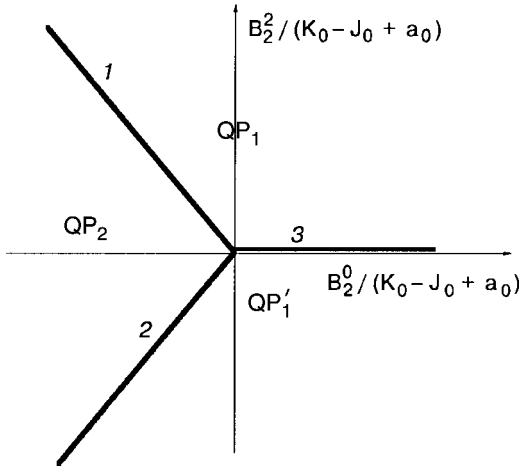

FIG. 1. Phase diagram of a biaxial non-Heisenberg ferromagnet with a large biquadratic interaction at $H=0$.

When an external magnetic field is turned on along the $0X$ axis a nonzero magnetic moment oriented along the $0X$ axis arises in the system, i.e., the phases QP_1 and QP_2 vanish, and in their place a ferromagnetic–quadrupolar (FM_x) phase is realized. In the parameter region $B_2^2<0$, $B_2^2<3B_2^0$ the QP_1' phase exists even for $H\neq 0$. For $K_0>J_0$ the formation of a canted ferromagnetic–quadrupolar phase becomes energetically unfavorable,[10] since in this case the ground state energy (E_+) in the ferromagnetic–canted phase becomes maximum. Thus two phases can be realized in the study under study: FM_x and QP_1'.

Let us investigate the phase states of the system in the two regions of material parameters $B_2^2>-3B_2^0$ and $B_2^2<-3B_2^0$, assuming that $B_2^2<0$. The parameter region $B_2^2=-3B_2^0$ corresponds to an easy-plane ferromagnet ($Z0Y$ is the basal plane), which was well studied in Ref. 11.

Let us first consider the case $B_2^2>-3B_2^0$. For $H\leqslant H_c$ the system is found in the phase QP_1'. At the point $H=H_c$ the system undergoes a transition to the FM_x phase. Here the order parameters change abruptly (the magnetization jumps from zero to $\langle S^x\rangle_c\sim 1$, and q_2^2 jumps from -1 to 0), and it can therefore be assumed that the FM_x–QP_1' phase transition is first-order. The value of $\langle S^x\rangle$ at $H=H_c$ and the value of the phase transition field H_c itself are determined from a system of two equations:

$$\langle S^x\rangle_c=\sin 2\theta_c=\left(\frac{2\overline{H}}{\chi}\right)_{H=H_c}, \qquad (4)$$

$$\frac{3}{2}(B_2^2-B_2^0)-\frac{1}{2}(K_0-J_0+a_0)\sin^2 2\theta_c+\frac{1}{2}|B_2^2+3B_2^0|$$
$$\times\cos 2\theta_c+H_c\sin 2\theta_c=[H_c-(K_0-J_0+a_0)\sin 2\theta_c]$$
$$\times\cos 2\theta_c-\frac{1}{2}|B_2^2+3B_2^0|\sin 2\theta_c. \qquad (5)$$

Here $a_0=\nu^2/2\eta$ is the ME interaction parameter. Equation (4) determines the value of the magnetization at the phase transition point, and Eq. (5) is the condition of equal free energy densities on the line of phase transitions.

In the parameter region $H \ll (B_2^2+3B_2^0)/2+K_0-J_0+a_0$ the field of the first-order phase transition of a biaxial non-Heisenberg ferromagnet is given by the expression

$$H_c=\sqrt{-2B_2^2[B_2^2+3B_2^0+2(K_0-J_0+a_0)]}, \tag{6}$$

and the jump in magnetization is small:

$$\langle S^x\rangle_c \approx 2\left[-\frac{2B_2^2}{B_2^2+3B_2^0+2(K_0-J_0+a_0)}\right]^{1/2}.$$

It follows from formula (6) that for $B_2^2=0$ the field $H_c=0$, which corresponds to the QP_1–QP_1' phase transition (see Fig. 1).

If the parameters of the system are related as $B_2^2+3B_2^0 \ll 2H-2(K_0-J_0+a_0)$, then the jump in magnetization is large (~ 1):

$$\langle S^x\rangle_c = 1-\frac{\Delta^2}{2},$$

where $\Delta = B_2^2+3B_2^0/2(H_c-K_0+J_0-a_0)$, and the field of the first-order phase transition is

$$H_c=\frac{3(B_2^0-B_2^2)+K_0-J_0+a_0}{2} + \frac{1}{4}\frac{(3B_2^0+B_2^2)^2}{3(B_2^2-B_2^0)+K_0-J_0+a_0}.$$

Let us investigate the behavior of the spectra in the vicinity of the field of the first-order phase transition. We assume that $H \geqslant H_c$, i.e., we are in the FM_x phase near the transition field. The wave vector $\mathbf{k}$ is in the direction of the external field, i.e., parallel to the $0X$ axis. In this geometry the nonzero components of the polarization unit vector of the quasiphonons are e_l^x, e_τ^y, and e_t^z, and the nonzero amplitudes of conversion of the magnons into phonons and back have the form

$$T^{-+}(k,t)=T^{+-}(k,t)=i\frac{\nu}{2}T_0(k,t)e_t^z k_x \sin\theta,$$

$$T^{-0}(k,t)=T^{0-}(k,t)=-i\frac{\nu}{2}T_0(k,t)e_t^z k_x \cos\theta,$$

$$T^{-+}(k,\tau)=-T^{+-}(k,\tau)=\frac{\nu}{2}T_0(k,\tau)e_\tau^y k_x \cos\theta,$$

$$T^{-0}(k,t)=-T^{0-}(k,\tau)=\frac{\nu}{2}T_0(k,\tau)e_\tau^y k_x \sin\theta,$$

$$T_0(k,\lambda)=\frac{\exp(i\mathbf{k}\cdot\mathbf{n})}{[2m\omega_\lambda(k)]^{1/2}},$$

where $\omega_\lambda(k)=c_\lambda k$ is the dispersion relation of the λ-polarized free phonon, and m is the mass of the magnetic ion.

The dispersion relation for coupled ME waves can be written in the form[8]

$$\det\|\delta_{ij}+x_{ij}\|=0, \tag{7}$$

where

$$x_{ij}=G_0^\sigma(\omega_n)b(\alpha)c_{ij}(\alpha)+B^0(k,\lambda,\lambda')T^{-\alpha}(k,\lambda) \times G_0^\alpha(\omega_n)b(\alpha)T^\beta(-k,\lambda')G_0^\beta(\omega_n)b(\beta)c_{ij}(\alpha,\beta);$$

$$B^0(k,\lambda,\lambda')=\frac{D_\lambda(k,\omega_n)}{1-Q_{\lambda\lambda'}D_\lambda(k,\omega_n)};$$

$$Q_{\lambda\lambda'}=T^\alpha(-k,\lambda)G_0^\alpha(\omega_n)T^{-\alpha}(k,\lambda');$$

$$c_{ij}(\alpha,\beta)=a_{ik}(\alpha,\beta)A_{kj};$$

$$a_{ik}=c_i(\alpha)c_k(-\beta), \quad b(\alpha)=\langle\alpha\cdot\mathbf{H}\rangle;$$

$$D_\lambda(k,\omega_n)=\frac{2\omega_\lambda(k)}{\omega_n^2-\omega_\lambda^2(k)}$$

is the Green's function of a free λ-polarized phonon, and $G_0^\alpha(\omega)=\{\omega+\boldsymbol{\alpha}\cdot\mathbf{E}\}^{-1}$ is the zeroth Green's function. The eight-dimensional vector $\mathbf{c}(\alpha)$ has the following components:

$$\mathbf{c}(\alpha)=\{\gamma_1^\parallel(\alpha),\ \gamma_1^\perp(\alpha),\ \gamma_1^{\perp *}(-\alpha),$$
$$\gamma_2^\parallel(\alpha),\ \gamma_2^\perp(\alpha),\ \gamma_2^{\perp *}(-\alpha),$$
$$\gamma_3^\perp(\alpha),\ \gamma_3^{\perp *}(-\alpha)\},$$

and the 8×8 matrix $\hat{A}_{nn'}$ decomposes into a direct sum of two matrices:

$$\hat{A}_{nn'}=\hat{A}^{(3)}_{nn'}\oplus\hat{A}^{(5)}_{nn'},$$

$$\hat{A}^{(3)}_{nn'}=\left\{J(n-n')-\frac{1}{2}K(n-n')\right\}\begin{pmatrix}1&0&0\\0&0&1/2\\0&1/2&0\end{pmatrix},$$

$$\hat{A}^{(5)}_{nn'}=\frac{K(n-n')}{2}\begin{pmatrix}1&0&0&0&0\\0&0&1/2&0&0\\0&1/2&0&0&0\\0&0&0&0&1/2\\0&0&0&1/2&0\end{pmatrix}.$$

The functions $\gamma_i^{\parallel(\perp)}(\alpha)$ are determined from the relation (3) between the spin operators and Hubbard operators. Equation (7) is valid at arbitrary temperatures and arbitrary relationships among the material constants.

Let us solve the dispersion relation (7) in the low-temperature region ($T \ll T_C$, where T_C is the Curie temperature), where all the main properties of the system can be seen unobscured by awkward mathematical manipulations.

The solution of equation (7) yields the spectrum of quasiphonons and quasimagnons. Here the first-order phase transition (at $H=H_c$) is not accompanied by the ''softening'' of any mode of collective excitations. A ''softening'' of the corresponding modes can be expected on the lines of phase stability.[12]

Let us investigate the behavior of the spectra of ME waves on the lines of stability. We first consider the same parameter region $B_2^2 > -3B_2^0$. Here it is assumed that the system is found in the FM_x phase. In this case the magnetic subsystem actively interacts with a τ-polarized quasiphonon mode having the spectrum

$$\omega^2(k)=\omega_\tau^2(k)\,\frac{\alpha k^2+H-H_{\rm st}}{\alpha k^2+H-H_{\rm st}+a_0}, \tag{8}$$

where $\alpha=J_0R_0^2$ (R_0 is the interaction radius), and $H_{\rm st}$ is the field of stability of the FM_x phase, which has the form

$$H_{\rm st}=\sqrt{-B_2^2[\xi+B_2^2+3B_2^0+2(K_0-J_0+a_0)]},$$
$$\xi=\sqrt{[3(B_2^2-B_2^0)-2(K_0-J_0+a_0)]^2+32B_2^2(K_0-J_0+a_0)}. \tag{9}$$

It follows from Eq. (9) that for $B_2^2=0$ the field $H_{\rm st}=0$, i.e., in the absence of external field the stability field (9) and the transition field (6) coincide on the line $B_2^2=0$ and correspond to the QP_1–QP_1' phase transition (see Fig. 1).

Thus for $H=H_{\rm st}$ the spectrum of quasiphonons "softens," and a gap appears in the quasimagnon spectrum; this gap is given by

$$\varepsilon^2(0)=a_0[a_0\sin^2 2\theta_c+2(K_0-J_0+a_0)\times\cos 2\theta_c(1+\cos 2\theta_c)],$$

where

$$\cos 2\theta_c=\frac{3(B_2^2-B_2^0)+2(K_0-J_0+a_0)+\xi}{4(K_0-J_0+a_0)}.$$

Let us now determine the field of stability of the QP_1' phase. The quasiphonon spectrum in this phase has the form

$$\omega^2(k)=\omega_\tau^2(k)\,\frac{\gamma k^2[3(B_2^0-B_2^2)+2(K_0-J_0+a_0)]+(H_{\rm st}')^2-H^2}{\gamma k^2[3(B_2^0-B_2^2)+2(K_0-J_0+a_0)]+(H_{\rm st}')^2-H^2+2a_0[3B_2^0-B_2^2+2(K_0-J_0+a_0)]},$$

where $\gamma=K_0\tilde R_0^2$, $\tilde R_0$ is the radius of the biquadratic exchange, and $H_{\rm st}'$ is the stability field of the QP_1' phase, which is given by

$$H_{\rm st}'=\sqrt{2B_2^2[B_2^2-3B_2^0-2(K_0-J_0+a_0)]}. \tag{10}$$

In the long-wavelength limit

$$\gamma k^2\ll 2a_0\frac{3B_2^0-B_2^2+2(K_0-J_0+a_0)}{3(B_2^0-B_2^2)+2(K_0-J_0+a_0)}$$

at $H=H_{\rm st}'$ the spectrum of τ-polarized quasiphonons "softens" and takes the form

$$\omega^2(k)=\omega_\tau^2(k)\,\frac{\gamma k^2}{2a_0}\left[\frac{3B_2^0-B_2^2+2(K_0-J_0+a_0)}{3(B_2^0-B_2^2)+2(K_0-J_0+a_0)}\right]^{-1},$$

and a ME gap appears in the quasimagnon spectrum.

It follows from expression (10) that the stability field of the QP_1' phase becomes equal to zero at $B_2^2=0$, which also corresponds to a line of phase transitions QP_1'–QP_1 for $H=0$. Thus the stability fields $H_{\rm st}$ and $H_{\rm st}'$ and the transition field H_c given by expression (6) coincide on the line $B_2^2=0$.

Let us now consider the case when the material parameters are related as $B_2^2<-3B_2^0$. As before, for $H\leqslant H_c$ the system is found in the QP_1' phase. At the point $H=H_c$ the system undergoes a transition to the FM_x phase. Here the order parameters change abruptly, i.e., the system undergoes a first-order phase transition. The transition field H_c and the jump in magnetization are also determined from Eqs. (4) and (5). In the parameter region $H\ll[2(K_0-J_0+a_0)-B_2^2-3B_2^2]/2$ the field of the first-order phase transition is given by

$$H_c=\sqrt{(B_2^2-3B_2^0)[B_2^2+3B_2^0-2(K_0-J_0+a_0)]}, \tag{11}$$

and the jump in magnetization is small and has the form

$$\langle S^x\rangle_c=\left[-\frac{B_2^2-3B_2^0}{B_2^2+3B_2^0-2(K_0-J_0+a_0)}\right]^{1/2}.$$

We note that on the line $B_2^2=3B_2^0$ the field H_c and the jump in magnetization go to zero. This situation corresponds to a QP_1'–QP_2 phase transition (at $H=0$).

In an analogous way one can obtain the value of the first-order phase transition field and the jump in magnetization in the parameter region $H\gg[2(K_0-J_0+a_0)-B_2^2-3B_2^0]/2$:

$$H_c=\frac{3(B_2^0-B_2^2)+K_0-J_0+a_0}{2}+\frac{1}{4}\,\frac{(3B_2^0+B_2^2)^2}{3(B_2^0-B_2^2)+K_0-J_0+a_0};$$

$$\langle S^x\rangle_c=1-\frac{\tilde\Delta^2}{2},\quad\text{where}\quad\tilde\Delta=\frac{B_2^2+3B_2^0}{2(K_0-J_0+a_0)-2H_c}.$$

Analysis of the dispersion relation (7) shows that the spectra of elementary excitations do not "soften" at the first-order phase transition point (H_c). Let us consider the behavior of the quasimagnon and quasiphonon spectra on the lines of stability of the FM_x and QP_1' phases in the parameter region $B_2^2<-3B_2^0$.

We begin by studying the line of stability of the FM_x phase, assuming that the geometry of the problem is the same as before. In the parameter region under study the magnetic subsystem actively interacts with a t-polarized quasiphonon mode having a spectrum of the form

$$\omega^2(k)=\omega_t^2(k)\,\frac{\alpha k^2+H-\tilde H_{\rm st}}{\alpha k^2+H-\tilde H_{\rm st}+a_0}, \tag{12}$$

where

$$\tilde{H}_{st}=\sqrt{1/2(3B_2^0-B_2^2)[\xi'-B_2^2-3B_2^0+2(K_0-J_0+a_0)]}$$

is the stability field of the FM_x phase, and

$$\xi'=\{[3(B_2^2-B_2^0)-2(K_0-J_0+a_0)]^2+16(B_2^2-3B_2^0)\times(K_0-J_0+a_0)\}^{1/2}.$$

In the long-wavelength limit (for $\alpha k^2 \ll a_0$) at the stability field ($H=\tilde{H}_{st}$) the spectrum of the t-polarized quasiphonons "softens," and a gap appears in the quasimagnon spectrum:

$$\varepsilon^2(0)=a_0[a_0\sin^2 2\theta_c'-2(K_0-J_0+a_0)\times\cos 2\theta_c'(1-\cos 2\theta_c')],$$

where $\cos 2\theta_c'=\dfrac{3(B_2^0-B_2^2)-2(K_0-J_0+a_0)-\xi'}{4(K_0-J_0+a_0)}$.

It should be noted that the stability field $\tilde{H}_{st}$ of the FM_x phase goes to zero on the line $B_2^2=3B_2^0$. This means that at zero field the system undergoes a phase transition QP_2–QP_1' (Fig. 1).

The behavior of the spectra of the coupled ME waves in the vicinity of the line of stability of the QP_1' phase can be studied in an analogous way. In that case the spectrum of t-polarized quasimagnons has the form

$$\omega^2(k)=\omega_t^2(k)\frac{\gamma k^2[3(B_2^0-B_2^2)+2(K_0-J_0+a_0)]+(\tilde{H}_{st}')^2-H^2}{\gamma k^2[3(B_2^0-B_2^2)+2(K_0-J_0+a_0)]+(\tilde{H}_{st}')^2-H^2+4a_0[-B_2^2+K_0-J_0+a_0]},$$

where $\tilde{H}_{st}'=\sqrt{2(B_2^2-3B_2^0)(B_2^2-K_0+J_0-a_0)}$ is the stability field of the QP_1' phase.

It follows from the quasiphonon spectrum that in the long-wavelength limit (for $\gamma k^2[3(B_2^0-B_2^2)+2(K_0-J_0+a_0)]\ll 4a_0[-B_2^2+K_0-J_0+a_0]$) at $H=\tilde{H}_{st}'$ the spectrum of the t-polarized quasiphonons "softens:"

$$\omega^2(k)=\omega_t^2(k)\frac{\gamma k^2}{4a_0}\left[\frac{-B_2^2+K_0-J_0+a_0}{3(B_2^0-B_2^2)+2(K_0-J_0+a_0)}\right]^{-1},$$

and a gap appears in the quasimagnon spectrum.

It must also be noted that on the line $B_2^2=3B_2^0$, which corresponds to a QP_1'–QP_2 phase transition, the stability field $\tilde{H}_{st}'=0$.

3. CONCLUSION

These studies have shown that a biquadratic interaction greater than the Heisenberg exchange will play a decisive role in the dynamics of the system. Its primary effect will be to change the type of phase transition in comparison with the case $K_0<J_0$ (Ref. 8). In addition, in the situation studied here the formation of a canted phase becomes impossible on account of the influence of the large biquadratic interaction.

An interesting feature of the study studied is that in the parameter region $B_2^2>-3B_2^0$ the magnetic subsystem actively interacts with a τ-polarized quasielastic branch of excitations and, as a consequence, a τ-polarized quasiphonon mode "softens" at the corresponding lines of stability. In the parameter region $B_2^2<-3B_2^0$ a t-polarized quasiphonon mode behaves in an analogous way. On a plane passing through the line $B_2^2=-3B_2^0$ and the H axis, the frequencies of the t- and τ-polarized quasiphonons coincide. This is obviously a consequence of the symmetry properties of the system.

*E-mail: MAN@expl.cris.crimea.ua

[1] É. L. Nagaev, *Magnets with Complicated Exchange Interactions* [in Russian], Nauka, Moscow (1988).
[2] V. M. Loktev and V. S. Ostrovskiĭ, Fiz. Nizk. Temp. **20**, 983 (1994) [Low Temp. Phys. **20**, 775 (1994)].
[3] V. V. Val'kov, G. N. Matsuleva, and S. G. Ovchinnikov, Fiz. Tverd. Tela (Leningrad) **31**, 60 (1989) [Sov. Phys. Solid State **31**, 948 (1989)].
[4] Yu. N. Mitsaĭ, Yu. A. Fridman, O. V. Kozhemyako, and O. A. Kosmachev, Fiz. Nizk. Temp. **25**, 690 (1999) [Low Temp. Phys. **25**, 513 (1999)].
[5] R. Aleonard and P. Morin, Phys. Rev. B **19**, 3868 (1979).
[6] P. Morin, J. Rouchy, and D. Schmitt, Phys. Rev. B **17**, 3684 (1978).
[7] Yu. N. Mitsay, Yu. A. Fridman, O. V. Kozhemyako, and M. S. Kochmanski, Acta Phys. Pol. A **96**, 363 (1999).
[8] Yu. A. Fridman, O. A. Kosmachev, and G. E. Bairamalieva, Fiz. Nizk. Temp. **26**, 1108 (2000) [Low Temp. Phys. **26**, 822 (2000)].
[9] R. O. Zaĭtsev, Zh. Éksp. Teor. Fiz. **68**, 207 (1975) [Sov. Phys. JETP **41**, 100 (1975)].
[10] V. V. Val'kov and G. N. Matsuleva, IF SO AN SSSR Preprint No. 645 F [in Russian], Institute of Physics, Siberian Branch of the Academy of Sciences of the USSR, Akademgorodok (1990).
[11] Yu. N. Mitsaĭ, A. N. Maĭorova, and Yu. A. Fridman, Fiz. Tverd. Tela (Leningrad) **34**, 66 (1992) [Sov. Phys. Solid State **34**, 34 (1992)].
[12] N. P. Grazhdanskina, Usp. Fiz. Nauk **2**, 291 (1968) [*sic*].

Translated by Steve Torstveit

Features of the magnetoelectric properties of $BiFeO_3$ in high magnetic fields

Yu. F. Popov,* A. M. Kadomtseva, S. S. Krotov, D. V. Belov, G. P. Vorob'ev, P. N. Makhov, and A. K. Zvezdin

M. V. Lomonosov State University, Vorob'evy Gory, 119899 Moscow, Russia
(Submitted November 7, 2000; revised January 21, 2001)
Fiz. Nizk. Temp. **27**, 649–651 (June 2001)

It is shown that the destruction of the cycloidal structure of the magnetic ferroelectric $BiFeO_3$ by a high magnetic field ($H_n \approx 200$ kOe) leads to the onset of a linear magnetoelectric effect and the appearance of a toroidal moment. The proof of the existence of a toroidal moment **T** in a high magnetic field ($H > H_n$) is based on the experimental observation that the off-diagonal components of the linear ME effect tensor are asymmetric ($\alpha_{12} = -\alpha_{21}$ for $\mathbf{L} \| \mathbf{c}$, where **L** is the antiferromagnetic vector), inasmuch as $T_z \sim \alpha_{12} - \alpha_{21}$. © *2001 American Institute of Physics.* [DOI: 10.1063/1.1382990]

Interest in the study of the magnetoelectric properties of the magnetic ferroelectric $BiFeO_3$ is largely motivated by the record high electric and magnetic ordering temperatures ($T_c = 1083$ K[1] and $T_N = 643$ K,[2,3] respectively). It is known that $BiFeO_3$ has the structure of a rhombohedrally distorted perovskite, which is described by the space group $R3c$.[4] The symmetry of these crystals admits the existence of a linear magnetoelectric (ME) effect and a toroidal moment, but so far only the quadratic ME effect has been observed[5,6] in $BiFeO_3$. This is because, according to the neutron-diffraction data, their magnetic structure is spatially modulated: the spins of the Fe^{3+} ions form a cycloidal structure with a large period (≈ 620 Å) in a plane passing through the c axis of the crystal and making an angle $\varphi = -60°$ with the a axis.[7] As a result of this, in the insufficiently high magnetic fields at which the measurements of Refs. 5 and 6 were made, the mean values of the projections of the antiferromagnetic vector remain equal to zero and, as a consequence, the ME effect and the related toroidal moment are effectively zeroed out. As was shown in Ref. 8, the cycloidal structure in $BiFeO_3$ is destroyed in a high magnetic field $H_n \approx 200$ kOe, which is accompanied by a jump of the electric polarization in connection with the onset of the linear ME effect.

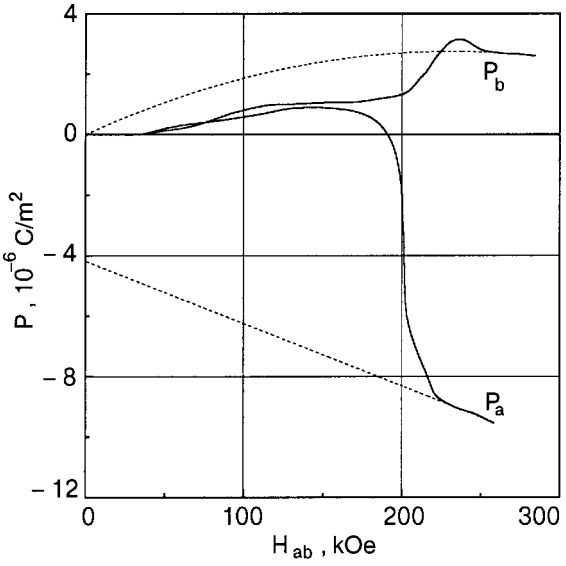

FIG. 1. Experimental curves of the components of the electric polarization of $BiFeO_3$ along the a and b axis (P_a and P_b) at a temperature of 20 K as functions of the magnetic field applied in the basal plane at a 45° angle to the a axis. The dashed lines show the straight line and parabola which approximate the experimental curves in the region $H > 250$ kOe according to formulas (5).

In this paper we establish that a toroidal moment appears in $BiFeO_3$ when the modulated structure is destroyed. As was shown in Ref. 9, the magnetic symmetry of the $BiFeO_3$ crystal in the homogeneous state admits the existence of the invariants $L_z T_z$ and $L_x T_x + L_y T_y$, where L_i and T_i are the components of the antiferromagnetic and toroidal-moment vectors.

To find the toroidal moment we investigated a quantity proportional to it, viz., the antisymmetric part of the components of the linear ME susceptibility tensor, in fields $H > H_n$ with the magnetic field oriented in the basal plane at a 45° angle to the a and b axes of the crystal. It is natural to assume that in this case for $H > H_n \approx 200$ kOe the spins of the Fe^{3+} ions are oriented along the c axis of the crystal. In this magnetic field direction we measured the field dependence of the components of the electric polarization along the a and b axis of the crystal, $P_a(H)$ and $P_b(H)$ (see Fig. 1), by the method described in Ref. 8. These curves, after the characteristic jump in polarization near the point $H_n \approx 200$ kOe, which is due to the onset of the linear ME effect after the destruction of the cycloid, have a gently sloping trend of the polarization. The electric polarization vector P_i, including the ME effects linear and quadratic in the field, is given by

$$P_i = \alpha_{ik} H_k + \beta_{ijk} H_j H_k . \tag{1}$$

As was shown in Ref. 8, in the general case the matrix $\hat{\alpha}$ in the homogeneous antiferromagnetic state of $BiFeO_3$ has the form

$$\hat{\alpha} = \begin{vmatrix} \lambda_1 L_y & \lambda_1 L_x - \lambda_2 L_z & -\lambda_4 L_y \\ \lambda_1 L_x + \lambda_2 L_z & -\lambda_1 L_y & \lambda_4 L_x \\ \lambda_3 L_y & -\lambda_3 L_x & 0 \end{vmatrix} . \tag{2}$$

For the field orientation indicated above, for $H > H_n$ one has

$\mathbf{L}\|\mathbf{c}$ ($L_x=L_y=0$), and the crystal belongs to the magnetic class $3m$, so that the only nonzero components are α_{12} and α_{21} (Ref. 10), with

$$\alpha_{12}=-\alpha_{21}. \tag{3}$$

The matrix β_{ijk} of the quadratic ME effect, according to Ref. 10, has a more awkward form; among the matrix elements which are important for our case, the nonzero ones are:

$$\beta_{111}=\gamma_1, \quad \beta_{122}=\beta_{212}=\beta_{221}=-\gamma_1. \tag{4}$$

Thus, since $H_a=H_b=H/\sqrt{2}$, we obtain

$$P_a=\frac{\alpha_{12}}{\sqrt{2}}H, \quad P_b=\frac{\alpha_{21}}{\sqrt{2}}H-\gamma_1 H^2. \tag{5}$$

From a processing of the ''tails'' of the experimental curves (Fig. 1) in the linear (for $P_a(H)$) and quadratic (for $P_b(H)$) approximations (the approximating straight line and parabola are shown by the dotted lines) we find

$$\alpha_{12}=-(0.029\pm 0.003)\times 10^{-6}\ \mathrm{C/(m^2kOe)},$$
$$\alpha_{21}=+(0.032\pm 0.003)\times 10^{-6}\ \mathrm{C/(m^2kOe)}, \tag{6}$$
$$\gamma_1=5\times 10^{-11}\ \mathrm{C/(m^2kOe^2)}.$$

Thus, in complete agreement with relation (3), the values obtained for the components α_{12} and α_{21} have different signs. The asymmetry of the off-diagonal components of the linear ME effect tensor attests to the onset of a toroidal moment $T_z\sim\alpha_{21}-\alpha_{12}$ when the cycloid is destroyed. We note that a toroidal moment induced by the magnetic field was first observed[11] in the magnetoelectric Cr_2O_3, in which, unlike the case of $BiFeO_3$, the toroidal moment is not parallel but perpendicular to the antiferromagnetic vector.

In this study we have also measured the dependence of the electric polarization along the a and b axes of the crystal on the value of the magnetic field applied along the c axis. As we see in Fig. 2, which shows the experimental curves of $P_a(H_c)$ and $P_b(H_c)$, after destruction of the cycloidal structure in a field $H_n\approx 200$ kOe the electric polarization increases with a jump, and for $H>250$ kOe it varies in a practically linear manner with the field. It is natural to suppose that here the spins of the Fe^{3+} ions, without leaving the plane of the cycloid, lie in the basal plane in such a way that $L_z=0$ and $L_y/L_x=\tan\varphi$, where $\varphi=-60°$ is the angle that the plane of the cycloid makes with the a axis of the crystal, according to the neutron diffraction measurements. Then in an approximation linear in the field, in accordance with Eq. (2), we obtain for the slope of the linear parts of the experimental curves (shown by the dotted lines in Fig. 2)

$$\frac{dP_a/dH}{dP_b/dH}=\frac{\alpha_{13}}{\alpha_{23}}=-\frac{L_y}{L_x}=-1.8, \tag{7}$$

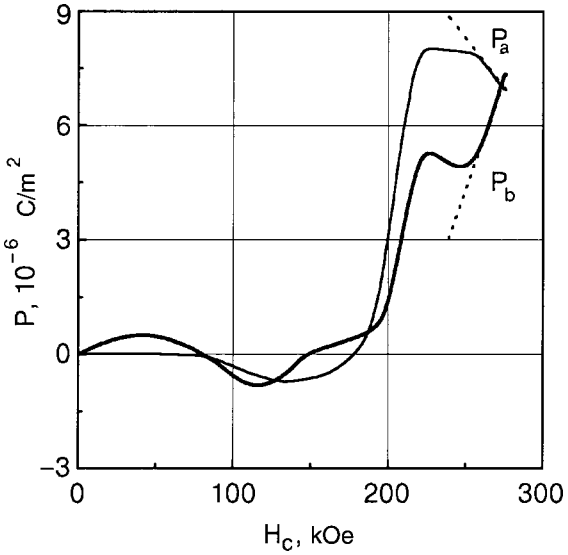

FIG. 2. Experimental curves of the electric polarization along the a and b axis of the crystal (P_a and P_b) as functions of the magnetic field $\mathbf{H}\|\mathbf{c}$ at a temperature of 18 K. The dashed lines show the slopes of the linear parts in the region $H>250$ kOe, which were used to calculate the derivatives dP_a/dH and dP_b/dH in formula (7).

which corresponds to an angle $\varphi=-61°$. The agreement of our results with the neutron diffraction data attests to the adequacy of our adopted model.

This study was done with the financial support of the Russian Foundation for Basic Research (00-15-96-695 and 01-02-16468) and the Ministry of Education (97-0-7.3-157).

*E-mail: popov@plms.phys.msu.su

[1] G. A. Smolenskiĭ, V. M. Yudin, E. S. Sher, and Yu. E. Stolypin, Zh. Éksp. Teor. Fiz. **43**, 877 (1962) [*sic*].
[2] C. Tabares-Munoz, J. P. Rivera, and H. Schmid, Ferroelectrics **55**, 235 (1984).
[3] P. Fischer, M. Polomska, I. Sosnowska, and M. Szimansky, J. Phys. C **13**, 1931 (1980).
[4] J. M. Moreau, C. Mickel, R. Gerson, and W. J. James, J. Phys. Chem. Solids **32**, 1315 (1971).
[5] C. Tabares-Múñoz, J. P. Rivera, A. Bezinges, A. Monnier, and H. Schmid, Jpn. J. Appl. Phys. **24**, 1051 (1984).
[6] V. A. Murashov, D. N. Rakov, I. S. Dubenko, A. K. Zvezdin, and V. M. Ionov, Kristallografiya **35**, 912 (1996).
[7] I. Sosnowska, T. Peterlin-Neumaier, and E. Steichele, J. Phys. C **115**, 4835 (1982).
[8] Yu. F. Popov, A. K. Zvezdin, G. P. Vorob'ev, A. M. Kadomtseva, V. A. Murashov, and D. N. Rakov, JETP Lett. **57**, 69 (1993).
[9] S. S. Krotov and V. V. Tugushev, Zh. Éksp. Teor. Fiz. **91**, 1708 (1986) [Sov. Phys. JETP **64**, 1010 (1986)].
[10] R. R. Birss, *Symmetry and Magnetism*, North-Holland, Amsterdam (1964).
[11] Yu. F. Popov, A. M. Kadomtseva, D. V. Belov, G. P. Vorob'ev, and A. K. Zvezdin, JETP Lett. **69**, 330 (1999).

Translated by Steve Torstveit

Magnetoelectric resonance of phonon and magnon polaritons in a ferrimagnet

I. E. Chupis* and A. A. Mishchenko

B. Verkin Institute for Low Temperature Physics and Engineering, National Academy of Sciences of Ukraine, pr. Lenina 47, 61103 Kharkov, Ukraine

(Submitted December 11, 2000)
Fiz. Nizk. Temp. **27**, 652–656 (June 2001)

The influence of the dynamic magnetoelectric interaction on the magnon (TE) and phonon (TM) polaritons in a ferrimagnet is studied in the IR region of the spectrum. The frequency dispersion of the dielectric permittivity and magnetic permeability is taken into account. It is shown that the spontaneous magnetic moment induces an additional radiative mode in the spectrum of TM polaritons. It is predicted that a resonant interaction and interconversion of the TM and TE polaritons can occur in a static electric field. © *2001 American Institute of Physics.* [DOI: 10.1063/1.1382991]

INTRODUCTION

An electromagnetic wave propagating in a medium interacts with the elementary excitations of the medium, and this affects the properties of the wave. The result is the formation of a polariton— an electromagnetic wave coupled with a given elementary excitation. Coupled waves of the electromagnetic field and the electric polarization are called phonon polaritons, and coupled photon–spin excitations are called magnon polaritons. The interaction of the electromagnetic wave with elementary excitations of a crystal is stronger near the eigenfrequencies of these excitations. Therefore, phonon polaritons are important in the IR and optical regions of the spectrum, and magnon polaritons are important in the microwave range. There is a vast literature on bulk and surface magnon polaritons (see, e.g., Refs. 1 and 2) and on the properties and methods of study of surface phonon polaritons.[3] In view of the considerable difference between the spin and optical-phonon frequencies, in the treatment of magnon polaritons one usually neglects the frequency dispersion of the dielectric permittivity (DP), and when studying phonon polaritons—that of the magnetic permeability (MP). Meanwhile, it is known that in many-sublattice magnets, in addition to the low-frequency spin branch, there exist high-frequency exchange excitations whose frequencies are close to the electric-dipole absorption bands of the phonons. For example, the frequencies of the exchange modes of hematite lie in the IR region of the spectrum,[4] and that is not an exceptional case. An increase in the magnetic resonance frequency is also promoted by a high magnetic field. For example, at the experimentally achievable magnetic fields of 10 T the spin frequency is of the order of $10^{12}\,\mathrm{s}^{-1}$. Furthermore, as was shown in Ref. 5, in magnetic compounds containing *d* ions the excitations of the orbital magnetic moment have energies of the order of the spin–orbit energy, i.e., frequencies of the order of $10^{13}\,\mathrm{s}^{-1}$. The interaction of the exchange spin modes with the electromagnetic waves has been investigated in a number of studies (see, e.g., Refs. 6 and 7). In Ref. 8 the frequency dispersion of the MP and DP of magnon polaritons was taken into account in the case when their resonance or antiresonance frequencies coincide, and it was shown that one of the branches of the polariton spectrum can exhibit anomalous dispersion.

In this paper we consider magnon (TE) and phonon (TM) polaritons in the IR region of the spectrum for different relations between the resonance and antiresonance frequencies of the DP and MP for the particular case of a ferrimagnet. We show that the dynamic magnetoelectric interaction[9] induces gyrotropy of the DP and an additional radiative mode in the spectrum of phonon polaritons. It is predicted that a resonance interaction and interconversion of phonon and magnon polaritons can occur in a static electric field.

ENERGY AND SUSCEPTIBILITY

As an example, let us consider a uniaxial ferrimagnet whose equilibrium moments $\mathbf{M}_{10}$ and $\mathbf{M}_{20}$ are antiparallel and in the absence of magnetic field are directed along the easy axis z, with $M_{10}>M_{20}$. The energy of the system consists of a magnetic energy, an electric-dipole energy, and an energy of interaction of the magnetic and phonon subsystems:

$$W=\int\left\{\Delta(\mathbf{M}_1\cdot\mathbf{M}_2)-\mathbf{h}\cdot(\mathbf{M}_1+\mathbf{M}_2)+\frac{C_1}{2}p_z^2+\frac{C_2}{2}(P_x^2+P_y^2)-\mathbf{P}\cdot(\mathbf{E}_0+\mathbf{e})+\frac{\Pi^2}{2\rho}+\frac{\mathbf{P}}{c\rho}\cdot[\mathbf{\Pi}\times\mathbf{B}]\right\}dV. \tag{1}$$

Here $\mathbf{M}_{1,2}$ and $\mathbf{\Pi}$ are the magnetic-moment and momentum densities, and $\mathbf{P}$ is the electric polarization vector. The first two terms in (1) are the magnetic energy in an alternating field $\mathbf{h}$ in the exchange approximation; $\Delta>0$ is the exchange constant. The electric-dipole energy includes the potential energy in the static $\mathbf{E}_0$ and alternating $\mathbf{e}$ electric fields and the kinetic energy $\Pi^2/2\rho$, where ρ is the density. In the IR region of the spectrum the main contribution to the polarization comes from the ions. The last term in the energy (1) is the dynamic magnetoelectric (ME) interaction,[9] i.e., the interaction of the electric polarization with the effective electric field $\mathbf{E}_{\mathrm{eff}}$ produced by the motion of an ion with charge e

at a velocity $\mathbf{v}$ in a medium with magnetic induction $\mathbf{B}$, i.e., $\mathbf{E}_{\text{eff}}=-(1/c)[\mathbf{v}\times\mathbf{B}]$, where $\mathbf{B}=\mathbf{h}+4\pi(\mathbf{M}_1+\mathbf{M}_2)$ and c is the speed of light. The energy expression (1) does not include the inhomogeneous terms, i.e., the spatial dispersion (we are assuming that $ak\ll 1$, where a is the lattice parameter and k is the wave vector), nor the damping. The static electric field is directed along the easy axis z. From the minimum of the energy (1) it follows that the electric polarization $P_0=E_0C_1^{-1}$.

Using the Lagrangian formalism, in the approximation linear in the small deviations of the moments from their equilibrium values, we easily obtain from (1) the following equations for the circular projections of the moments $a^+=a_x+ia_y$:

$$\begin{aligned}
&\dot{\pi}^+=\frac{e}{V_0}[-C_2p^++e^+]+igm_0\pi^+;\\
&\dot{m}_1^+=-ig_1\Delta M_{10}m_2^+-ig_1\Delta M_{20}m_1^+\\
&\qquad+ig_1M_{10}h^++g_1(\rho c)^{-1}M_{10}P_0\pi^+;\\
&\dot{m}_2^+=ig_2\Delta M_{20}m_1^++ig_2\Delta M_{10}m_2^+\\
&\qquad-ig_2M_{20}h^+-g_2(\rho c)^{-1}M_{20}P_0\pi^+;\\
&\dot{p}^+=\frac{e}{m}\pi^++ig[-4\pi P_0(m_1^++m_2^+)\\
&\qquad+4\pi m_0p^+-P_0h^+].
\end{aligned}\tag{2}$$

Here V_0 is the volume of the unit cell, $m=\rho V_0$; $g=e/mc$ is the gyromagnetic ratio for the ion, $g_{1,2}$ are the gyromagnetic ratios for the magnetic sublattices, and $m_0=M_{10}-M_{20}$ is the spontaneous magnetization. The equations for $a^-=a_x-ia_y$ are obtained from (2) by complex conjugation and the replacement of ω by $(-\omega)$.

We see from Eq. (2) that in the absence of the static magnetic field ($P_0=0$) the equations for the magnetic and electric subsystems are not coupled. In that case, assuming that a^+ is proportional to $\exp(-i\omega t)$, we obtain from (2) the following expressions for the nonzero components of the dielectric permittivity ε:

$$\begin{aligned}
&\varepsilon_{xx}=\varepsilon_{yy}=\varepsilon_1=\frac{(\omega^2-\Omega_1^2)(\omega^2-\Omega_2^2)}{(\omega^2-\omega_1^2)(\omega^2-\omega_2^2)};\\
&\omega_{1,2}=\omega_t\mp\omega_m,\quad \omega_m=4\pi g m_0;\\
&\omega_t^2=C_2\bar{\omega}_0^2,\quad \bar{\omega}_0^2=\frac{e^2}{mV_0},\\
&\varepsilon_{xy}=i\varepsilon'=-\frac{i8\pi\omega\omega_m\bar{\omega}_0^2}{(\omega^2-\omega_1^2)(\omega^2-\omega_2^2)};\\
&\varepsilon_{zz}=\varepsilon_2=\frac{\Omega_e^2-\omega^2}{\omega_e^2-\omega^2},\quad \Omega_e^2=\omega_e^2+4\pi\bar{\omega}_0^2,\quad \omega_e^2=C_1\bar{\omega}_0^2;\\
&\Omega_{1,2}^2=\omega_t^2+2\pi\bar{\omega}_0^2+\omega_m^2\mp2\sqrt{\pi^2\bar{\omega}_0^4+\omega_m^2(\omega_t^2+2\pi\bar{\omega}_0^2)}.
\end{aligned}\tag{3}$$

The frequency of the excitations of P_z is ω_e, and the frequency of the excitations of P_x and P_y is ω_t. The presence of spontaneous magnetization lifts the degeneracy in the spectrum of excitations of P_x and P_y. These excitations then have the character of left and right circular precessions about $\mathbf{m}_0$ with frequencies ω_1 and ω_2. We see from (3) that the spontaneous magnetization induces an electric gyrotropy $\varepsilon'\neq 0$ which, however, is very small, $\varepsilon'/\varepsilon_1\approx 4\pi\omega_m/\omega_t$. The expressions for the nonzero components of the magnetic permeability tensor in the IR region of the spectrum have the form

$$\begin{aligned}
&\mu_{xx}=\mu_{yy}=\mu=\frac{\Omega_0^2-\omega^2}{\omega_0^2-\omega^2};\\
&i\mu'=\mu_{xy}=\frac{i\omega_f(\Omega^2-\omega^2)}{\omega(\omega_0^2-\omega^2)},\quad \mu_{zz}=1;\\
&\Omega^2=4\pi\Delta g_1g_2\omega_0\omega_f^{-1}(M_{10}-M_{20})^2;\\
&\omega_f=4\pi(g_1M_{10}-g_2M_{20});\\
&\Omega_0^2=\omega_0^2+4\pi\Delta(g_1-g_2)^2M_{10}M_{20};\\
&\omega_0=\Delta(g_2M_{10}-g_1M_{20}).
\end{aligned}\tag{4}$$

In expressions (4) we assume that $\Delta\gg 1$, $g_2M_{10}>g_1M_{20}$, $g_1M_{10}>g_2M_{20}$.

In the case we are considering here, in which there is no static magnetic field and the magnetic anisotropy is ignored, the activational part of the lower branch of the magnon spectrum is equal to zero. The pole of the MP corresponds to the frequency ω_0 of exchange excitations, which lies in the infrared, where μ differs little from 1 and the magnetic gyrotropy is small. In fact, it follows from (4) that $|\mu'/\mu|$ is of the order of ω_f/ω_0, i.e., is of the order of $4\pi/\Delta$. The gyromagnetic ratio for an ion is significantly smaller than that for an electron ($g\ll g_{1,2}$), and therefore $\omega_m\ll\omega_f\ll\omega_0$. The values of the frequencies $\omega_{1,2}$ of the electric polarization differ little from $\omega_t\sim\omega_0$.

A static electric field E_0 couples the excitation of electric polarization and magnetic moments (see Eq. (2)). It induces nonzero components of the magnetoelectric susceptibility $\mathrm{X}_{xx}^{em}=\mathrm{X}_{yy}^{em}$, X_{xy}^{em}, the expressions for which, if one neglects the small corrections of order $(gE_0/\omega_0)^2$ and $(\omega_m/\omega_0)^2$, have the form

$$\begin{aligned}
&\mathrm{X}_{zz}^{em}=\frac{\partial P_x}{\partial h_x}\approx\frac{gP_0\omega_f(\Omega^2-\omega^2)}{(\omega^2-\omega_0^2)(\omega^2-\omega_t^2)};\\
&\mathrm{X}_{xy}^{em}=\frac{\partial P_x}{\partial h_y}\approx-\frac{igP_0\omega}{\omega_t^2-\omega^2}\left[1-\frac{4\pi\Delta M_{10}M_{20}(g_1-g_2)^2}{\omega_0^2-\omega^2}\right].
\end{aligned}\tag{5}$$

For frequencies not very close to ω_0, one has $|\mathrm{X}_{xx}^{em}/\mathrm{X}_{xy}^{em}|\approx(\omega_f/\omega_0)\ll 1$.

MAGNON (TE) AND PHONON (TM) POLARITONS

We obtain the polariton excitations in a ferrimagnet by solving Maxwell's equations for waves propagating along the x axis, using expressions (3) and (4) for the DP and MP. In the absence of a static electric field ($\mathrm{X}^{em}=0$) the TE and TM polaritons are independent.

The electric field of magnon polaritons propagating along the x axis is transversely directed (TE wave), and the nonzero field components are e_z, h_x, and h_y. The dispersion relation is

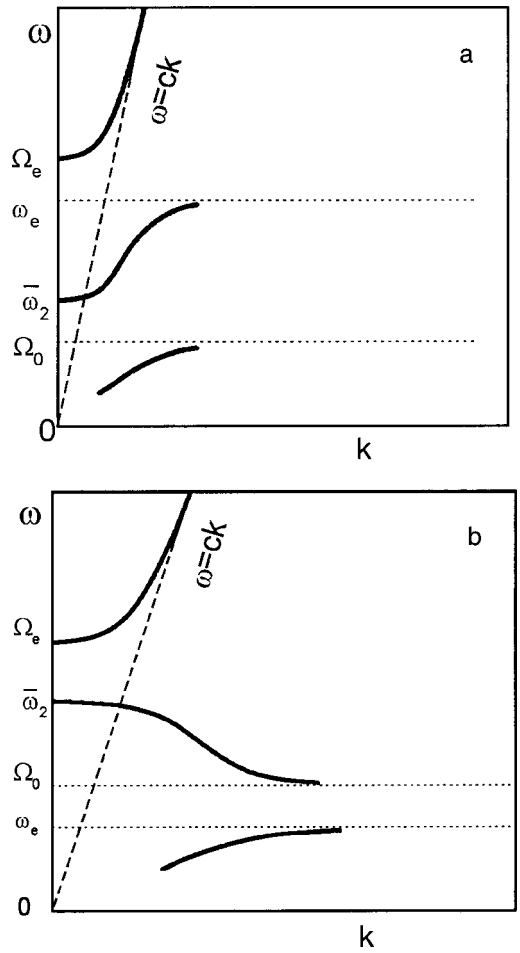

FIG. 1. Dispersion branches of TE polaritons in the IR region of the spectrum. For TM polaritons the lower branch starts from the value $\omega=0$ at $k=0$.

$$k^2=\frac{(\Omega_e^2-\omega^2)(\omega^2-\bar{\omega}_1^2)(\omega^2-\bar{\omega}_2^2)}{c^2(\omega_e^2-\omega^2)(\omega^2-\Omega_0^2)}, \tag{6}$$

where

$$\bar{\omega}_{1,2}=\frac{1}{2}[\sqrt{(\omega_0-\omega_f)^2+16\pi g_1 g_2\Delta(M_1-M_2)^2}\mp(\omega_0-\omega_f)].$$

A wave vector of zero corresponds to the frequencies Ω_e and $\bar{\omega}_2>\Omega_0$, where $\bar{\omega}_2-\Omega_0\sim\omega_f$. Near the frequencies Ω_0 and ω_e the wave vector tends to infinity.

The spectrum of TE polaritons consists of three modes. Figure 1a shows the spectrum of TE polaritons for the case when $\bar{\omega}_2<\omega_e$ or when the phonon antiresonance frequency Ω_e is greater than the magnon antiresonance frequency Ω_0. For $\Omega_e<\Omega_0$ the following substitutions should be made in Fig. 1a: $\Omega_0\to\omega_e$, $\bar{\omega}_2\to\Omega_e$, $\omega_e\to\Omega_0$, $\Omega_e\to\bar{\omega}_2$. If the frequencies Ω_0 and $\bar{\omega}_2$ are close to the phonon antiresonance frequency Ω_e ($\omega_e<\Omega_0<\Omega_e<\bar{\omega}_2$) or to the phonon resonance frequency ω_e ($\Omega_0<\omega_e<\bar{\omega}_2<\Omega_e$), or if they lie between the phonon resonance ω_e and antiresonance Ω_e frequencies, then the middle branch will have anomalous dispersion (Fig. 1b). However, this dispersion is very weak, since the frequency interval in which the middle branch exists is very small, $(\bar{\omega}_2-\Omega_0)\sim\omega_f$. The existence of anomalous dispersion in the spectrum of TE polaritons when the resonance (antiresonance) frequencies of the DP and MP coincide is predicted in Ref. 8.

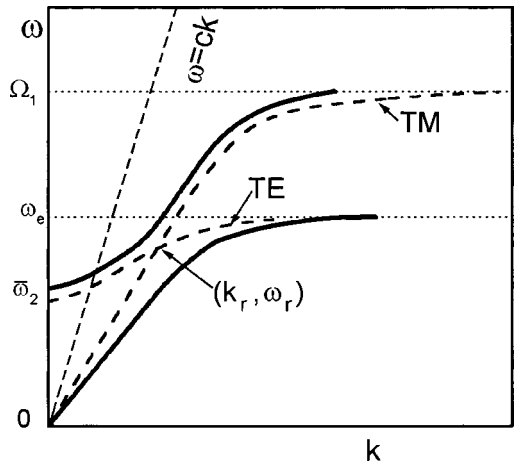

FIG. 2. Resonant interaction of TE and TM polaritons in an electric field.

We note that the middle branch of the TE polariton spectrum is radiative, since it crosses the light line $\omega=ck$, i.e., it can interact resonantly with an electromagnetic wave.

In a phonon polariton wave (TM wave) the nonzero field components are e_x, e_y, and h_z, and the spectral equation for it is

$$k^2=\frac{\omega^2(\omega^2-\tilde{\omega}_1^2)(\omega^2-\tilde{\omega}_2^2)}{c^2(\omega^2-\Omega_1^2)(\omega^2-\Omega_2^2)},$$

$$\tilde{\omega}_{1,2}=\Omega_t\mp\omega_m;\quad \Omega_t^2=\omega_t^2+4\pi\bar{\omega}_0^2. \tag{7}$$

The spectrum of TM polaritons is similar to the TE polariton spectrum presented in Fig. 1a, but with the following relabeling of the frequencies: $\Omega_0\to\Omega_1$, $\bar{\omega}_2\to\tilde{\omega}_1$, $\omega_e\to\Omega_2$, $\Omega_e\to\tilde{\omega}_2$. The frequencies $\tilde{\omega}_1$, $\tilde{\omega}_2$, and Ω_2 are close to one another, since $(\tilde{\omega}_2-\Omega_2)\sim(\Omega_2-\tilde{\omega}_1)\sim\omega_m$. In the absence of magnetization one has $\tilde{\omega}_2=\tilde{\omega}_1=\Omega_2$, and the spectrum contains only two modes. Thus the ME interaction adds a new mode. This mode has weak dispersion, lies near the bottom of the upper band, and is radiative, since it crosses the light line $\omega=ck$.

RESONANT INTERACTION OF TE AND TM POLARITONS IN AN ELECTRIC FIELD

The appearance of a new (middle) radiative branch in the polariton spectrum raises the possibility of a crossing of TE and TM modes, i.e., the probability of a ME resonance. Most often the exchange magnon frequency is lower than the optical phonon frequency ω_e, which, in turn, in a uniaxial crystal is lower than the excitation frequency ω_t of the transverse components of the electric polarization, i.e., $\Omega_0<\omega_e<\omega_1$. In this situation it is possible to have a crossover of the lower ($\omega<\Omega_1$) TM mode with the middle TE mode (see Fig. 1a). In the absence of a static electric field the TE and TM modes do not interact (the dotted lines in Fig. 2). In a static electric field a magnetoelectric interaction, described by the ME susceptibility (5), arises between the magnon and phonon polaritons. The electric displacement and magnetic induction are given by the following expressions:

$$d_i=\varepsilon_{ik}e_k+4\pi X_{ik}^{em}h_k;$$

$$b_i=\mu_{ik}h_k+4\pi X_{ik}^{me}e_k,$$

where $X_{ik}^{em}=\partial P_i/\partial h_k$; $X_{ik}^{me}=\partial m_i/\partial e_k$, and in the absence of damping $X_{ik}^{em}=(X_{ki}^{me})^*$. For frequencies that are not close to ω_0 we need consider only the off-diagonal components of the ME susceptibility, assuming that

$$\gamma=-4\pi i X_{xy}^{em}=\frac{4\pi g P_0\omega}{\omega^2-\omega_t^2}. \tag{8}$$

Maxwell's equations relate all of the electric and magnetic field components in the ferrimagnet:

$$\begin{aligned}
&\mu h_x+i\mu' h_y+i\gamma e_y=0;\\
&-i\mu' h_x+\mu h_y-i\gamma e_x+v e_z=0;\\
&i\gamma h_y+\varepsilon_1 e_x+i\varepsilon' e_y=0;\\
&i\gamma h_x+v h_z+i\varepsilon' e_x-\varepsilon_1 e_y=0;\\
&h_z=v e_y,\quad v h_y=-\varepsilon_2 e_z,\quad v=ck/\omega.
\end{aligned} \tag{9}$$

In a static electric field ($\gamma\neq 0$) the TE and TM waves are coupled by the ME interaction. Far from the ME resonance frequency ω_r the admixture of the ''external'' fields in the phonon (magnon) branch is small; it is proportional to the parameter γ characterizing the ME interaction. For example, the longitudinal electric field e_x arising in a ''quasi-TE'' wave is

$$e_x\cong\frac{i\gamma\varepsilon_2[\varepsilon'(\mu'\varepsilon_1+\mu\varepsilon')+\mu]}{\varepsilon_1\mu v[\varepsilon_1(\varepsilon_1-v^2)-\varepsilon'^2]}e_z, \tag{10}$$

and the longitudinal magnetic field in a ''quasi-TM'' wave is given by

$$h_x\cong-\frac{i\gamma[\mu'\varepsilon_2(\varepsilon_1-v^2)+\varepsilon'(\varepsilon_2\mu-v^2)]}{\varepsilon' v[\varepsilon_2(\mu^2-\mu'^2)-\mu v^2]}h_z. \tag{11}$$

The admixtures to the fields arise as the crossover point (k_r,ω_r) of the noninteracting branches is approached; there

$$\begin{aligned}
&\varepsilon_1\varepsilon_2(\mu^2-\mu'^2)=\mu(\varepsilon_1^2-\varepsilon'^2),\\
&k_r^2=\frac{\omega_r^2(\varepsilon_1^2-\varepsilon'^2)}{c^2\varepsilon_1}.
\end{aligned} \tag{12}$$

Near the point of the ME resonance (k_r,ω_r) all of the field components are of the same order, and a resonant interconversion of TE and TM waves occurs (Fig. 2).

Thus in a ferrimagnetic crystal in a static electric field a magnetoelectric resonance can arise in the IR region of the spectrum, accompanied by the interconversion of magnon and phonon polaritons. An analogous ME resonance in a static electric field in the IR region of the spectrum may also occur in other many-sublattice magnets.

*E-mail: chupis@ilt.kharkov.ua

[1] M. I. Kaganov, N. B. Pustyl'nik, and T. I. Shalaeva, Usp. Fiz. Nauk **167**, 191 (1997).
[2] A. G. Gurevich and G. A. Melkov, *Magnetic Oscillations and Waves* [in Russian], Nauka, Moscow (1994).
[3] V. M. Agranovich and D. L. Mills (Eds.), *Surface Polaritons* [North-Holland, Amsterdam (1982); Nauka, Moscow (1985)].
[4] E. I. Samuelsen and G. Shirane, Phys. Status Solidi **42**, 241 (1970).
[5] I. E. Chupis, Fiz. Tverd. Tela (St. Petersburg) **36**, 1910 (1994) [Phys. Solid State **36**, 1042 (1994)].
[6] V. V. Eremenko, A. I. Zvyagin, Yu. G. Pashkevich *et al.*, Preprint NITF-86-34R [in Russian], Institute of Theoretical Physics, Academy of Sciences of the UkrSSR, Kiev (1986).
[7] Yu. G. Pashkevich, V. L. Sobolev, and S. A. Fedorov, Fiz. Nizk. Temp. **12**, 411 (1986) [Low Temp. Phys. **12**, 237 (1986)].
[8] M. I. Kaganov and T. I. Shalaeva, Phys. Status Solidi B **162**, 469 (1990).
[9] I. E. Chupis, Fiz. Nizk. Temp. **23**, 290 (1997) [Low Temp. Phys. **23**, 213 (1997)].

Translated by Steve Torstveit

ELECTRONIC PROPERTIES OF METALS AND ALLOYS

Plastic-deformation-induced low-temperature anomalies of the resistivity of polycrystalline copper and aluminum

V. M. Dmitriev*

B. Verkin Institute for Low Temperature Physics and Engineering, National Academy of Sciences of Ukraine, pr. Lenina 47, 61103 Kharkov, Ukraine; International Laboratory of High Magnetic Fields and Low Temperatures, 95 Gajowicka St., 53-421 Wroclaw, Poland

I. L. Lebedeva

Kharkov State Economics University, pr. Lenina 9,a, 61091 Kharkov, Ukraine

N. N. Prentslau

B. Verkin Institute for Low Temperature Physics and Engineering, National Academy of Sciences of Ukraine, pr. Lenina 47, 61103 Kharkov, Ukraine

(Submitted November 1, 2000; revised January 30, 2001)
Fiz. Nizk. Temp. **27**, 657–667 (June 2001)

The temperature dependence of the electrical resistivity ρ of pure polycrystalline aluminum and copper after plastic deformation is investigated in the temperature interval 4.2–300 K. Using heat treatment as a tool for changing the crystallite size d and structural perfection of the sample, it is determined how ρ depends on the ratio of d to the electron mean free path l_e and on the degree of deformation of the Cu and Al. At temperatures below 10 K the $\rho(T)$ curves of the deformed samples of polycrystalline copper and aluminum exhibit minima and maxima. At higher temperatures a more complicated dependence of $\rho(d/l_e)$ is observed. It is found that in the region of the anomalous skin effect the experimentally determined and theoretically calculated values of the surface resistance R_s agree only in the case when the electron mean free path is smaller than the size of the crystallites. [DOI: 10.1063/1.1382992]

INTRODUCTION

Interest in the study of processes of charge carrier scattering in pure metals and in samples after deformation and with impurities introduced has not waned over the decades. The temperature dependence of the resistivity ρ of different metals at helium temperatures has been found[1–8] to have unusual minima, which are, as a rule, due to the Kondo effect,[6,9,10] i.e., to the scattering of conduction electrons on magnetic impurities in a spin-flip process. In a comparatively narrow temperature interval 20–50 K one observes an additional resistivity which increases sharply with increasing temperature and is due to the dislocation contribution.[11–15] The dislocation contribution to the temperature dependence $\rho(T)$ has still not found an unambiguous explanation. Nor has the minimum on $\rho(T)$ been conclusively explained. For example, why do diamagnetic impurities (germanium, lead, gold, bismuth, zinc) in copper also cause a minimum of the resistivity, or why do impurities of copper and silver produce the same effect in gold?[7,8] The influence of plastic deformation on $\rho(T)$ at low temperatures has not been adequately studied. After a significant plastic deformation, various anomalies can arise in connection with, for example, the crystallite size d in polycrystalline samples and the value of d relative to the electron mean free path l_e, grain boundaries, the complicated electronic structure of the dislocation cores and their surroundings, vibrations of dislocations,[16–21] the trapping of impurities by dislocations,[22] etc. It is also of interest to study the resistivity $\rho(T)$ and the active part of the impedance, $R_s(T)$, of a deformed metal in the temperature region of both the classical and anomalous skin effects.

There are various ways of introducing dislocations into a crystal. In Refs. 23 and 24 it was noted that dislocations introduced by bending have a larger scattering cross section than those obtained by other ways of deforming a metal, although this effect has not yet been conclusively explained.

It is known[25] that upon the recrystallization of a deformed metal the number, size, and shape of the crystallites change, as do the dislocation density, internal stresses, and other characteristics that affect the value of the resistivity. Therefore, if one uses recrystallization annealing as a method of altering the structural state of a sample, then by repeatedly annealing a sample at increasingly higher temperatures T_h and measuring $\rho(T)$ and the surface resistance $R_s(T)$ and also the parameters of the crystallites after each heating–cooling cycle, one can obtain information about the temperature dependence of the resistivity of the metal for various degrees of structural perfection. (Here and below T_h is the ratio of the annealing temperature to the melting temperature of the metal.)

In this paper we present the results of a comprehensive experimental study of the influence of the crystallite size and

the structural state of pure polycrystalline copper and aluminum on the temperature dependence of the resistivity ρ and the surface resistance R_s in the temperature interval 4.2–300 K. The deformation was done by bending at room temperature, and the structural state was changed by annealing. A total of 60 copper and 20 aluminum samples were studied.

SAMPLES AND MEASUREMENT PROCEDURE

Samples of M00 and M0b (electrotechnical) grades of copper and A999 and A996 aluminum were studied. The surface resistance was measured by a resonator method. For this the materials to be studied were made into helical resonators with the ends of the helices unclosed. The envelope of the resonators was mechanically finished. The internal conductors were obtained in the following way. From the initial blanks 70 mm in diameter we cut out blanks with a transverse cross section of 10×10 mm and length 12 mm, which were then drawn at 300 K through a system of dies until rods 2 mm in diameter and 400 mm long were obtained (relative elongation $\delta=32$). Several of the aluminum samples were drawn to $\delta=40$. These rods were twisted into helices 15 mm in diameter. Then the envelope of the resonators and the helices were repeatedly annealed in a vacuum of $\sim10^{-5}$ torr, with T_h increased in each cycle. To reduce the scatter of the experimental data on the $\rho(T)$ and $R_s(T)$ curves, all of the samples were annealed for four hours. After each annealing cycle the resistivity $\rho(T)$ of the copper and aluminum helices was measured by the four-contact method, and a metallographic analysis of the samples was carried out. After each anneal a sample 2–3 mm long for metallographic analysis was cut from the helical conductor and then polished and etched by the standard method.[26] The helical resonator was then assembled and its Q-factor $Q(T)$ was measured at a frequency of 400 MHz in the temperature interval 4.2–300 K. The value of $R_s(T)$ for the metals studied was obtained from the geometric factor. The temperature measurement and stabilization system permitted varying the temperature of the sample in the range 4.2–300 K with the aid of helium vapor and was capable of stabilizing the temperature to a precision of ±0.25 K in the temperature interval 30–300 K and ±0.1 K for $T<30$ K.[27] In the measurements of the resistive properties the error was 1% throughout the entire temperature interval. To reduce the measurement error the temperature dependence of the resistivity was measured several times and the values measured at the same temperature were averaged.

EXPERIMENTAL RESULTS

Characteristics of the structural state of copper

The characteristics of the structural state of a sample of M00 copper deformed by drawing through dies and then by bending into a helix and subsequently annealed at different temperatures T_h are presented in Figs. 1 and 2. Figure 1 shows histograms of the transverse dimensions d of the crystallites in the copper sample for different annealing temperatures T_h: 0.2 (i.e., without annealing after deformation) (a), 0.5 (b), and 0.75 (c). Metallographic studies established that for an annealing temperature $T_h=0.5$, twins appear at the center of the samples, and the transverse dimensions of these

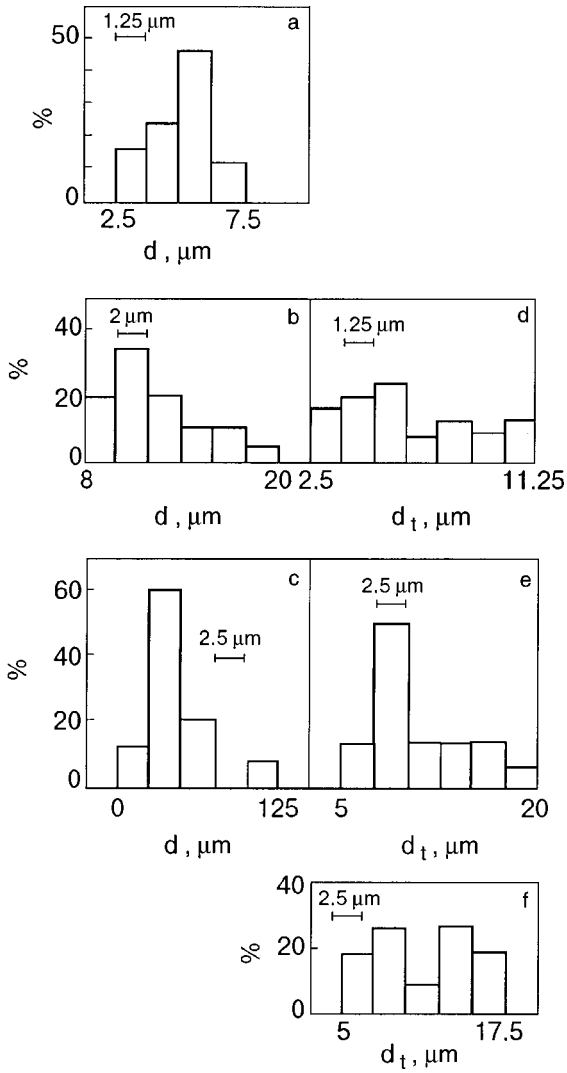

FIG. 1. Percent distribution of transverse sizes of the crystallites d (a–c) and twins d_t (d–f) in an M00 copper sample after annealing at different T_h: 0.2 (a), 0.5 (b,d), 0.75 (c,e), and 0.95 (f).

twins increases with increasing T_h. New twins are formed closer to the surface of the sample but are not observed in a layer of the order of 200 μm from the surface. Figure 1 also shows histograms of the transverse dimensions d_t of the twins in an M00 copper sample annealed at different temperatures T_h: 0.5 (d), 0.75 (e), and 0.95 (f). We note that after annealing at $T_h=0.95$ the mean transverse dimension of the copper crystallites is $d\sim200$ μm (not shown in Fig. 1). At places where large crystallites come together, small crystallites also form, possibly of a twinned orientation. Small crystallites also appear near the surface of the sample.

Figure 2 shows how the transverse dimensions d of the crystallites and the dimensions d_t of the twins in an M00 copper sample depend on T_h. Also shown are plots of the electron mean free paths l_e, calculated from the resistivity ρ at temperatures of 30 and 4.2 K, as functions of T_h.

TEMPERATURE DEPENDENCE OF ρ AND R_s IN THE INTERVAL 10–300 K

Figure 3 shows the curves of $\rho(T)$ measured in the temperature interval 10–70 K for the M00 copper sample an-

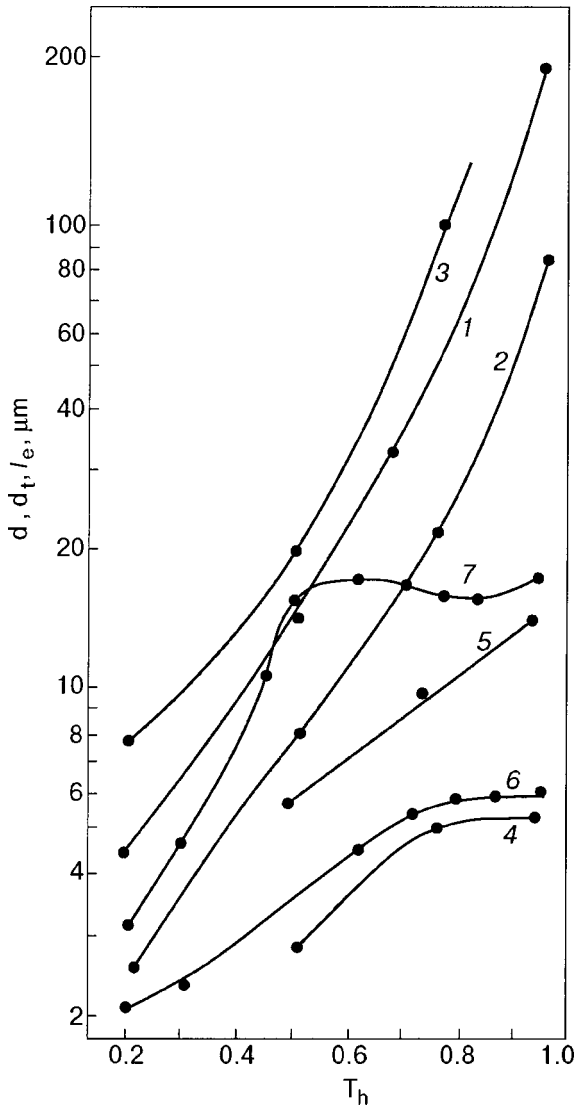

FIG. 2. Dependence on T_h of the transverse size d of the crystallites: mean (*1*), minimum (*2*), and maximum (*3*), and of the size d_t of the twins: minimum (*4*) and mean (*5*), for an M00 copper sample. The electron mean free path $l_e(T_h)$ at temperatures of 30 K (*6*) and 4.2 K (*7*).

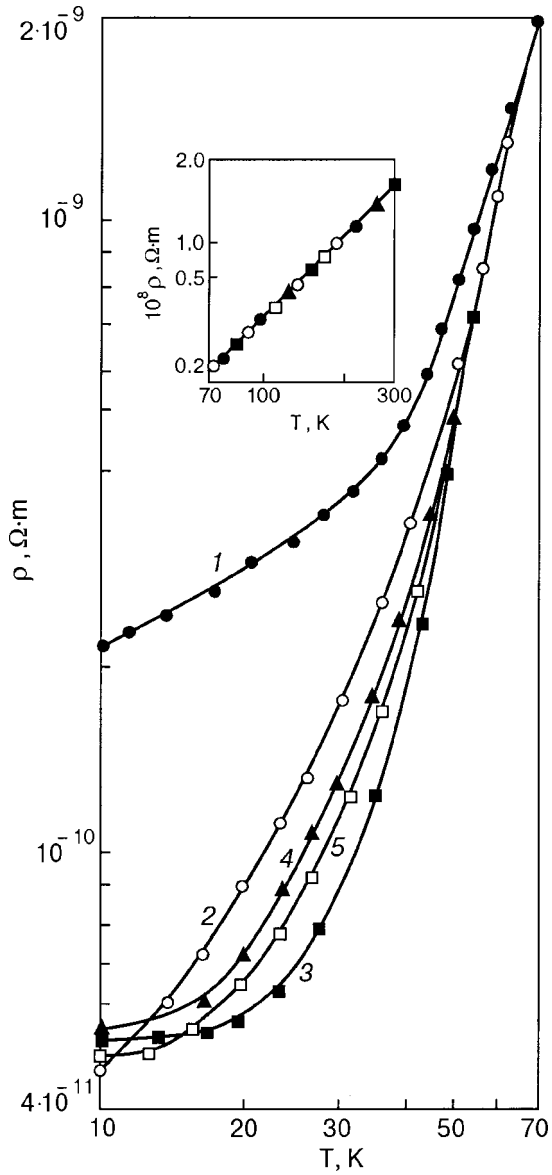

FIG. 3. Temperature dependence of ρ for an M00 copper sample annealed at different T_h: 0.2 (*1*), 0.5 (*2*), 0.75 (*3*), 0.84 (*4*), and 0.95 (*5*). The inset shows $\rho(T)$ for the M00 copper sample in the temperature interval 70–300 K after annealing at $T_h = 0.2$–0.95.

nealed at different temperatures T_h: 0.2 (*1*), 0.5 (*2*), 0.75 (*3*), 0.84 (*4*), and 0.95 (*5*), and the inset shows the same curves in the temperature interval 70–300 K.

Figure 4 shows the temperature dependence of ρ measured in the temperature interval 10–70 K for a sample of A999 aluminum deformed at $T_h = 0.32$ (*1*) and annealed at $T_h = 0.75$ (*2*); the relative elongation $\delta = 40$. (Here and below the values corresponding to the deformation temperature, i.e., 300 K, are $T_h = 0.2$ for copper and $T_h = 0.32$ for aluminum.)

Figure 5 shows the temperature dependence of the surface resistance R_s relative to $R_s(300)$ for the deformed samples of M00 copper (a) and A999 aluminum (b) after annealing at various temperatures T_h: 0.2 (*1*), 0.3 (*2*), 0.5 (*3*), 0.65 (*4*), 0.75 (*5*), and 0.95 (*6*) for the copper [Fig. 5a] and 0.41 (*1*), 0.75 (*2*), and 0.95 (*3*) for the aluminum [Fig. 5b].

Figure 6 shows the ratio $\rho(T^*)/\rho(300)$ as a function of T_h for samples of M00 copper at $T^* = 30$ K (*1*) and 10 K (*2*) and A999 aluminum at $T^* = 10$ K (*3*). Also shown are the curves of $R_s(T^*)/R_s(300)$ for the same copper and aluminum samples at $T^* = 10$ K (curves *4* and *5*, respectively), and the ratio of the surface resistance $R_s(e)$ obtained experimentally to the theoretical $R_s(t)$ calculated by the Chambers formula[28] from the measured values of ρ as a function of T_h for the samples of copper (curve *6*) and aluminum (curve *7*).

We see from Fig. 3 that in the temperature interval 70–300 K annealing has practically no effect on the value of ρ. In the temperature region 12–70 K the resistivity ρ decreases with increasing T_h, reaching a minimum value at $T_h = 0.75$. The resistivity of the Cu sample subjected to heat treatment at $T_h > 0.75$ is higher than that for the sample annealed at $T_h = 0.75$. For $T < 12$ K the lowest value of ρ is obtained for samples annealed at $T_h = 0.4$–0.5, while the resistivity of the samples heat treated at $T_h > 0.75$ increases. Thus the resistivity has a minimum value $\rho_{\min}$ at a certain annealing temperature T_h.

These features are not observed on the temperature de-

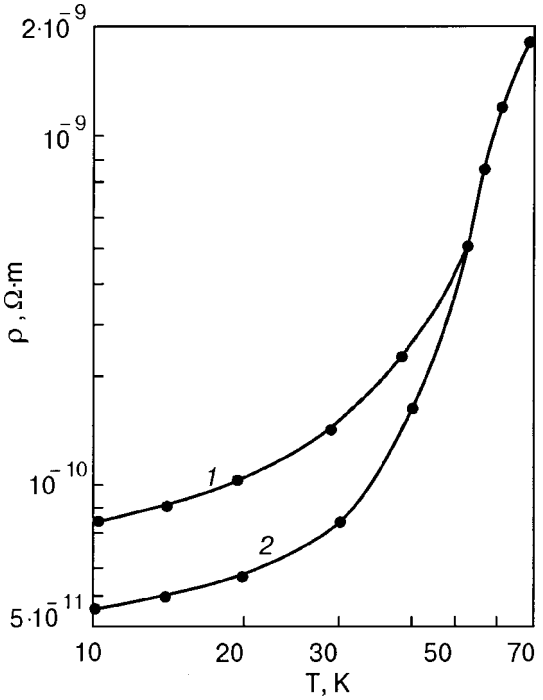

FIG. 4. Temperature dependence of ρ for a sample of A999 aluminum deformed at room temperature (*1*) and annealed at $T_h=0.75$ (*2*).

pendence of the surface resistance R_s of copper and aluminum. As can be seen in Fig. 5, the $R_s(T)$ curves measured after annealing at different T_h do not cross, unlike those of $\rho(T)$. With increasing T_h the resistance R_s decreases, reaches a minimum value at $T_h=0.75$, and again increases for samples annealed at $T_h>0.75$.

RESISTIVITY OF COPPER AND ALUMINUM AT TEMPERATURES BELOW 10 K

When the temperature is lowered below 10 K, the temperature dependence of ρ for different samples or for the same samples but differently annealed and deformed exhibit features in the form of a minimum, a minimum with a subsequent maximum, or a plateau. For approximately 80% of all the samples studied the $\rho(T)$ curves at $T<10$ K have a minimum or a minimum followed by a maximum. The remaining samples, deformed and annealed under the same conditions, have a plateau.

Figure 7 shows the temperature dependence of ρ for a sample of M00 copper measured in the temperature interval 4–16 K after annealing at the following temperatures T_h: 0.2 (unannealed sample) (*1*), 0.75 (*2*), 0.84 (*3*), and 0.95 (*4*). These curves were obtained on the same copper sample for which the $\rho(T)$ curves at $T>10$ K are shown in Fig. 3. It follows from the Fig. 7 that for this copper sample the temperature dependence of ρ has a minimum $\rho_{\min}$ at $T\approx 9.5$ K and a maximum $\rho_{\max}$ at $T\approx 6.5$ K. For aluminum the curves of the temperature dependence of ρ at $T<10$ K are analogous to those of copper. Figure 8 shows $\rho(T)$ for the same grade-A999 aluminum sample as in Fig. 4 ($T>10$ K) after it was annealed at different temperatures T_h: 0.32 (*1*), 0.37 (*2*), 0.75 (*3*), 0.84 (*4*), and 0.95 (*5*). We see that for the deformed Al sample the minimum on the $\rho(T)$ curve is observed at $T\approx 6.7$ K and the maximum at $T\approx 5.9$ K.

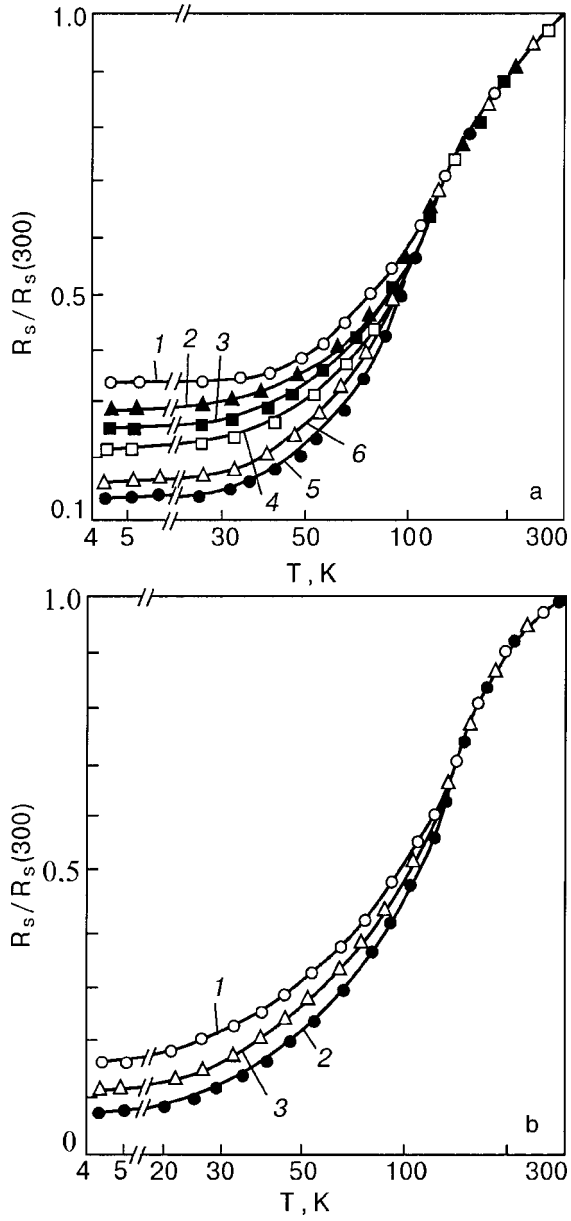

FIG. 5. Temperature dependence of the ratio $R_s/R_s(300)$ for samples of M00 copper (a) and A999 aluminum (b) annealed at different T_h: 0.2 (*1*), 0.3 (*2*), 0.5 (*3*), 0.65 (*4*), 0.75 (*5*), 0.95 (*6*) (a) and 0.41 (*1*), 0.75 (*2*), 0.95 (*3*) (b).

We note that annealing of metal samples has varying effects on the behavior of $\rho(T)$. In the majority of copper and aluminum samples the ratio $\rho_{\max}/\rho_{\min}$ decreases monotonically with increasing annealing temperature up to $T_h=0.75$. Figure 7 shows $\rho(T)$ for such a copper sample. For the more strongly deformed samples, however, the ratio $\rho_{\max}/\rho_{\min}$ increases with increasing T_h and then, after passing through a maximum at $T_h=0.4$–0.6, decreases. This sort of dependence is seen in Fig. 8 for an Al sample deformed by drawing to a relative elongation of 40.

One should note the group of deformed samples for which $\rho(T)$ at $T<10$ K has a plateau rather than a minimum and maximum, i.e., for which in a certain temperature interval the resistivity is practically independent of temperature. These samples were prepared and annealed under the same conditions as those for which the $\rho(T)$ curve has a minimum

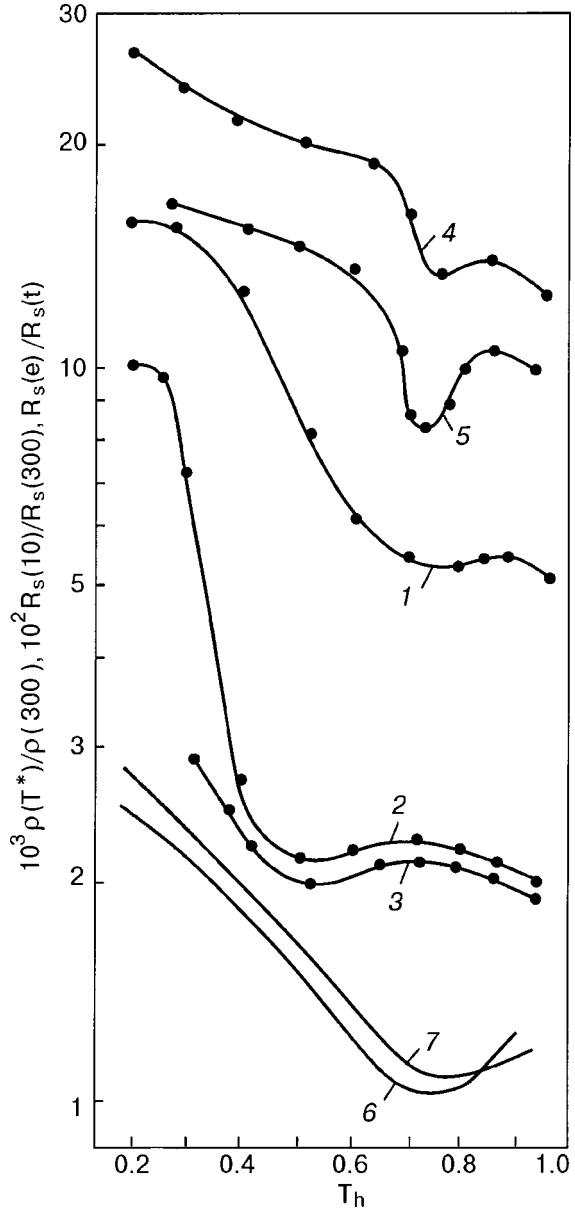

FIG. 6. The ratio $\rho(T^*)/\rho(300)$ versus T_h for an M00 Cu sample at $T^*=30$ K (*1*) and $T^*=10$ K (*2*) and an A999 Al sample at $T^*=10$ K (*3*); $R_s(10)/R_s(300)$ versus T_h for Cu (*4*) and Al (*5*); $R_s(e)/R_s(t)$ versus T_h for Cu (*6*) and Al (*7*) at $T=4.2$ K.

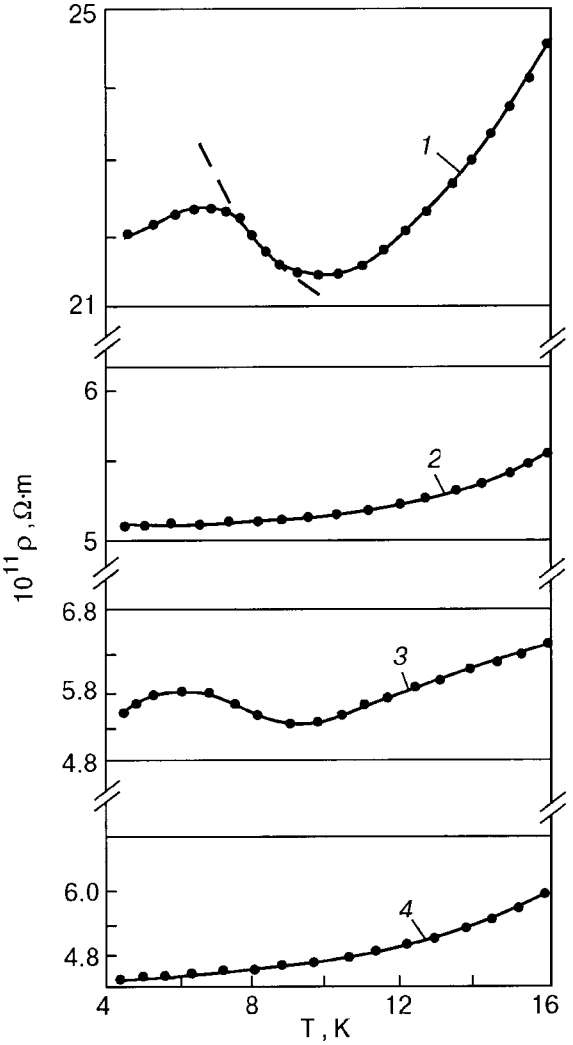

FIG. 7. Temperature dependence of ρ for an M00 copper sample deformed beforehand at $T=300$ K and then annealed at different temperatures T_h: 0.2 (*1*), 0.75 (*2*), 0.84 (*3*), and 0.95 (*4*). The dashed curve shows the function $\rho(T)\propto\ln(1/T)$.

and maximum. Figure 9 shows the temperature dependence of ρ for a sample of M0b copper, measured after annealing at the following temperatures T_h: 0.2 (*1*), 0.5 (*2*), 0.75 (*3*), and 0.84 (*4*). It is seen that the width of the plateau increases with increasing T_h, and for $T_h=0.75$ the $\rho(T)$ curve has a monotonic character. Thus for the same sample at different degrees of its structural perfection, the $\rho(T)$ curve can have a plateau or a minimum.

It follows from Figs. 7–9 that a general property of all the samples of the metals studied is that after annealing at $T_h=0.7-0.75$ their $\rho(T)$ curves do not exhibit any anomalies and acquire a monotonic character. After heat treatment of the samples at $T_h>0.75-0.85$ the anomalies reappear (curve *3* in Fig. 7, curve *4* in Fig. 8, and curve *4* in Fig. 9), and for these same samples annealed at $T_h>0.85$ they again vanish (curve *4* in Fig. 7 and curve *5* in Fig. 8).

If the deformed sample is annealed at the optimum temperature ($T_h=0.7-0.75$) and then again deformed by bending, the anomalies on $\rho(T)$ are restored. Figure 10 shows the $\rho(T)$ curve for an M00 copper sample annealed at $T_h=0.75$ (curve *1*) and twice straightened out from the helix and again twisted into a helix at room temperature (curve *2*). The repeat deformation of the copper sample by bending after it was annealed at $T_h=0.75$ leads to the appearance of a minimum on $\rho(T)$ independently of the type of anomaly prior to annealing. Figure 11 shows the temperature dependence of ρ for a grade-M0b copper sample. It is seen that the $\rho(T)$ curves for the deformed and unannealed sample and the sample annealed at $T_h=0.5$ does not exhibit an anomaly in the form of a plateau (curves *1* and *2*). For the sample annealed at $T_h=0.75$ (curve *3*) the curve has a monotonic character. A repeat deformation of the sample by bending after it was annealed at $T_h=0.75$ leads to the appearance of a minimum on the $\rho(T)$ curve (*4*).

DISCUSSION OF THE RESULTS

From Figs. 1–5 one can see how the temperature dependence of the resistivity ρ and surface resistance R_s of copper

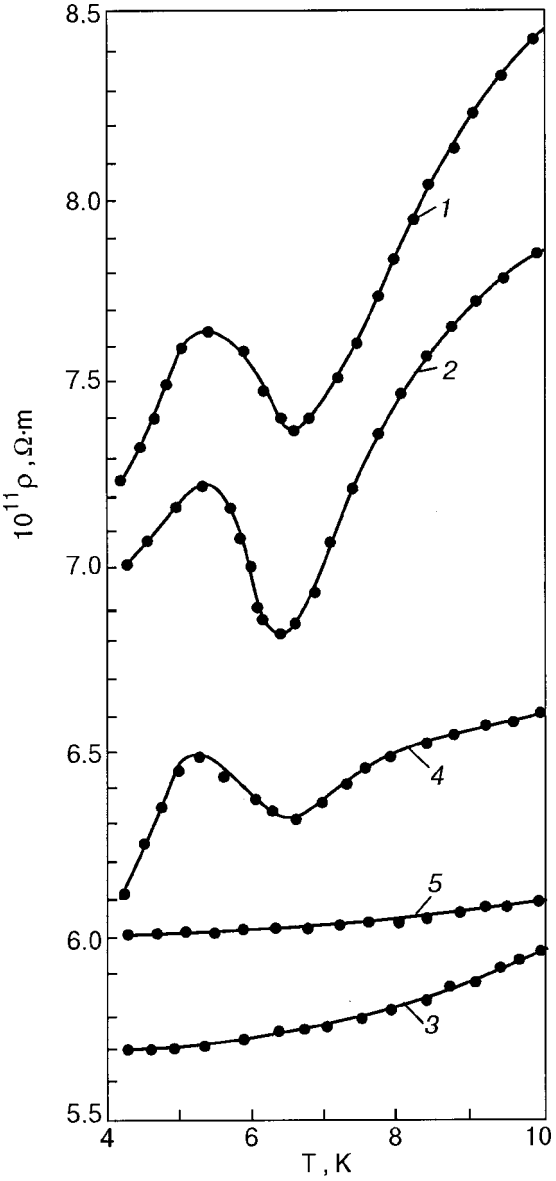

FIG. 8. Temperature dependence of ρ for a sample of A999 aluminum deformed beforehand at $T=300$ K and then annealed at different temperatures T_h: 0.32 (*1*), 0.37 (*2*), 0.75 (*3*), 0.84 (*4*), and 0.95 (*5*).

and aluminum samples with different annealing temperatures T_h change upon changes in the size of the crystallites d and the electron mean free path l_e.

It is seen in Fig. 2 that at temperatures above 30 K the mean free path l_e (curve *6*) is much smaller than the minimum transverse size of a crystallite (curve *2*) at all annealing temperatures T_h. This means that each crystallite is in essence a bulk conductor and, hence, its resistivity is mainly determined by the electron–phonon interaction. Therefore at temperatures $T/\Theta > 0.5$ one observes a linear trend of $\rho(T)$ (Θ is the Debye temperature, $\Theta_{Cu}=343$ K, $\Theta_{Al}=420$ K). At $T/\Theta=0.5$ the resistivity has a temperature dependence $\rho(T)\propto T^n$, where $\eta\leqslant 5$.[29] Since the size of the crystallites increases and the structural perfection of the metal improves with increasing T_h, in the samples studied the exponent n increases from 2.4 at $T_h=0.5$ to 3.5 at $T_h=0.75$, in good agreement with the results of Refs. 29–31.

At helium temperatures the resistivity ρ_{ph} caused by scattering on thermal vibrations of the lattice is small. Furthermore, upon annealing the interstitial atoms and vacancies of deformational origin are ''lost,'' as are some of the dislocations influencing the value of ρ. Therefore, in this temperature region ρ is governed by factors that are either independent of temperature or which depend weakly on temperature. The resistivity is influenced mainly by the number of impurities in the metal and its structural perfection.

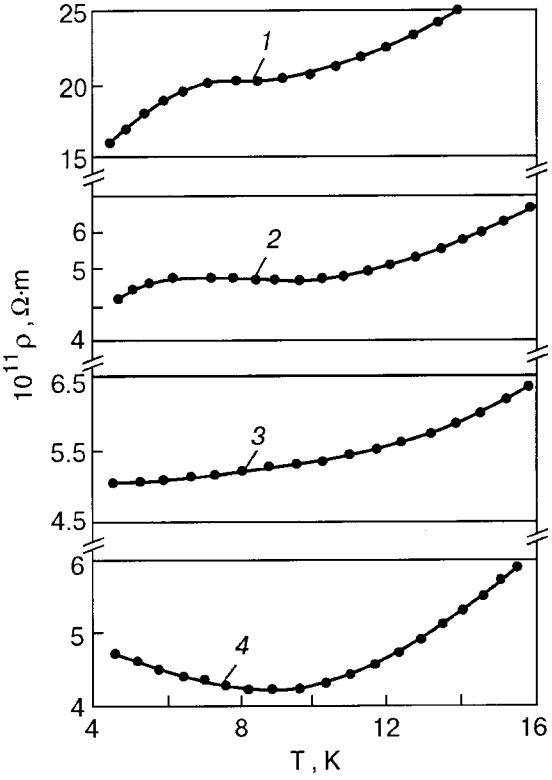

FIG. 9. Temperature dependence of ρ for an M0b copper sample after annealing at different T_h: 0.2 (*1*), 0.5 (*2*), 0.75 (*3*), and 0.84 (*4*).

Calculations show that at both room temperature and nitrogen temperatures the skin depth at 400 MHz is less than

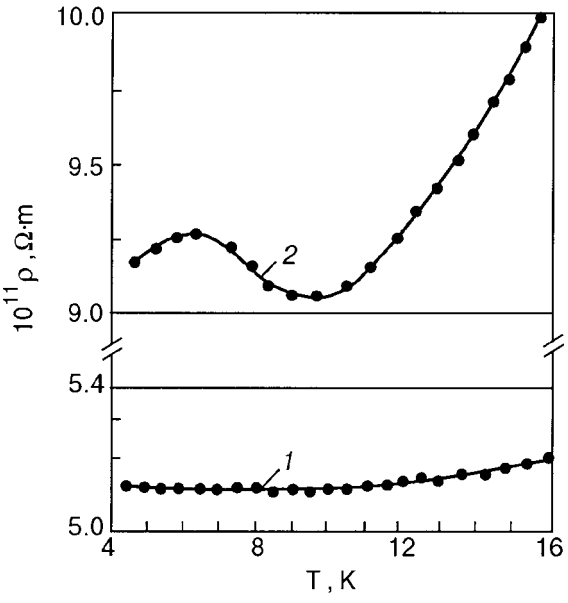

FIG. 10. Temperature dependence of ρ for an M00 copper sample after annealing at $T_h=0.75$ (*1*) and a subsequent deformation by bending (*2*).

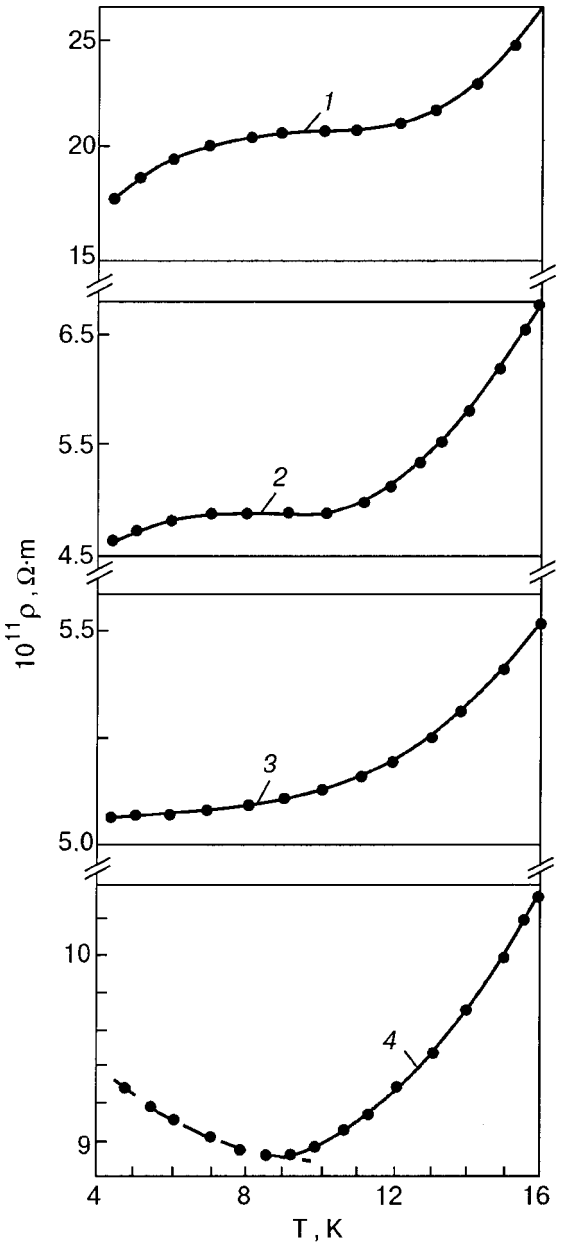

FIG. 11. Temperature dependence of ρ for a copper sample annealed at different T_h: 0.2 (*1*), 0.5 (*2*), and 0.75 (*3*) and also deformed by bending after annealing at $T_h=0.75$ (*4*). The dashed curve shows the function $\rho(T)\propto\ln(1/T)$.

the size of the crystallites of the samples annealed at $T_h<0.95$. Since this is the region of the classical skin effect, here the surface resistance $R_s(T)\propto\rho(T)^{0.5}$ and is independent of the dimensions of the sample. At temperatures below 130 K the anomalous skin effect begins to play a role; it is known[28] that in this effect R_s consists of two components, one of which is independent of ρ, while the other goes as ρ^l (l varies from 0.82 for specular reflection to 1.1 for diffuse reflection).

It is known[25] that in the plastic deformation of a metal the subsurface layer is the most deformed (the Beilby layer). In reality this means that the dc current density is nonuniform over the transverse cross section of the sample and is minimum in the subsurface layer. Therefore, the measured, integral value of the resistivity of a metallic sample differs from its value near the surface. If it is taken into account that a high-frequency current flows through the sample only within a skin layer (i.e., the most deformed layer of the metal), then the variation of ρ over the transverse cross section of the sample is a source of error in the value of R_s calculated from the measured ρ for a deformed sample. Heat treatment improves the structural state of the subsurface layer and thus decreases the error in the calculation of R_s from ρ, and annealing the Al and Cu samples at the optimum temperature T_h allows one to obtain close values for the calculated $R_s(t)$ and experimental $R_s(e)$ surface resistance (curves *6* and *7* in Fig. 6).

By analyzing the $\rho(T)$ curves for the copper (curves *1* and *3* in Fig. 3, curves *1* and *2* in Fig. 7) and aluminum (curves *1* and *3* in Figs. 4 and 8) samples, we can conclude that an appreciable deformation contribution to the resistivity is observed at $T>10$ K. This contribution may be caused by dislocations and interstitial atoms and vacancies arising on deformation. For example, Fig. 12a and 12b for the copper sample and Fig. 12c for the aluminum sample show the excess resistivity $\Delta\rho$ obtained as the difference of the values of ρ for a deformed and unannealed sample and a sample annealed at the optimum temperature $T_h=0.75$. Figure 12a shows the temperature dependence of $\Delta\rho$ that is widely discussed in the literature.[1,11–18,21,32] In the papers cited this dependence is explained by the dislocation contribution, since the contribution due to interstitial atoms and vacancies vanishes at low annealing temperatures, while the contribution due to dislocations persists up to the optimum annealing temperature. Figure 12b and 12c show $\Delta\rho(T)$ curves which reveal a large dislocation contribution to $\rho(T)$ at $T>10$ K and also reflect the features on the $\rho(T)$ curves in the form a minimum and maximum at $T<10$ K.

These features at $T>10$ K are less sensitive to the degree of deformation of the sample and are observed in some form or other for all of the samples subjected to plastic deformation.

The causes of the features in the form of minima, maxima, and a plateau on the $\rho(T)$ curve at $T<10$ K are not so obvious, although a number of mechanisms to explain them have been proposed in the literature. For example, it was predicted in Ref. 33 that, depending on the ratio of the transverse dimension d of the sample to the electron–phonon mean free path of the electron, a minimum or a plateau can appear on the $\rho(T)$ curve.

We note that the minimum of $\rho(T)$ due to the size effect[33] should be observed only for bulk samples. For thin samples the temperature dependence of ρ should have a plateau. However, we have observed a minimum on the $\rho(T)$ curve only for those Al and Cu samples which contained small crystallites. As a result of a high-temperature annealing the size of the crystallites increased, and the minimum on $\rho(T)$ gradually vanished. Therefore the features that we have observed on the $\rho(T)$ curve cannot be explained by the size effect.[33]

The temperature dependence of the resistivity of metals and alloys found in an amorphous state also has a minimum.[34–37]

We believe that the anomalies we observed on the $\rho(T)$ curve cannot be explained by an amorphous state of the Al and Cu samples, for at least two reasons. First, the $\rho(T)$

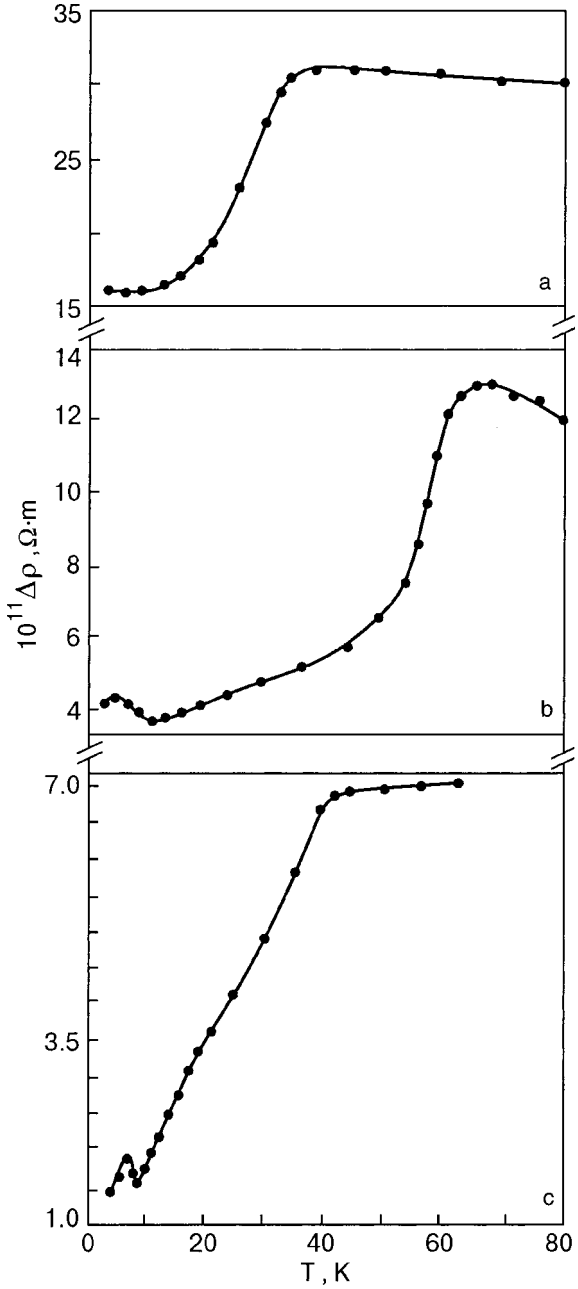

FIG. 12. Temperature dependence of the deformation contribution to the resistivity of samples of copper (a,b) and aluminum (c).

curve of amorphous materials exhibit only a minimum, although, as in the Kondo effect, $\rho(T)$ increases logarithmically with decreasing temperature after the minimum.[36,37] Second, we were studying polycrystalline samples of copper and aluminum. In the undeformed samples and in the samples annealed at $T_h = 0.75$ a minimum on the $\rho(T)$ curve was not observed. This agrees with the data of Ref. 29, where it was stated that for a pure single-crystal sample of aluminum there is no minimum on $\rho(T)$. According to Ref. 26, deformed metal samples have a fine-grained structure with crystallite dimensions down to submicron sizes. And, in spite of the fact that numerous defects arise upon deformation,[38] the metal retains its former crystalline structure. We did not observe any signs of amorphization of the Al and Cu samples as a result of their deformation or annealing.

It can be supposed that the observed features are a manifestation of the Kondo effect.[9,10] Moreover, with decreasing temperature after the minimum the resistivity increases by a logarithmic law $\rho \propto \ln(1/T)$ (curve *1* in Fig. 7 and curve *4* (dotted) in Fig. 11). However, our results contradict those of Ref. 6, in which it was shown that the minimum of $\rho(T)$ due to scattering on magnetic impurities in gold appeared precisely as a result of careful annealing, which lowered the residual resistivity. Upon plastic deformation of the samples the minimum on the $\rho(T)$ curve was not observed. In our experiments it is precisely for the deformed samples that the minimum is observed on $\rho(T)$ (see Figs. 7 and 11). This is particularly well demonstrated in Fig. 11, where it is seen that the minimum on the $\rho(T)$ curve (*4*) appears as a result of deformation by bending of the sample annealed at the optimum temperature (curve *3*).

It is known that deformation alters the properties of copper, and at a certain degree of plastic deformation a transition occurs from the diamagnetic to a paramagnetic state.[39] A subsequent annealing of the deformed copper sample restores it to the diamagnetic state. It is also known that some diamagnets can acquire paramagnetic properties when the crystallites are made very small.[39] In Ref. 40 it is noted that upon the transition to the paramagnetic state during plastic deformation the $3d$ shell of copper goes from being completely filled in the diamagnetic state[38] to partially filled, and so copper behaves as a transition metal.[40] Thus the necessary conditions for the onset of the Kondo effect can be created in the deformed copper sample. This may be the reason why impurity copper in gold, for example, leads to the appearance of a minimum on the $\rho(T)$ curve.[8] We note, however, that attempts to detect the dislocation magnetism of copper have so far been unsuccessful.[2,17] Since the behavioral features of $\rho(T)$ are observed for aluminum as well as copper, they cannot be explained by dislocation magnetism.

CONCLUSION

Let us summarize the main results. Plastic-deformation-induced anomalies are observed on the temperature dependence of the resistivity ρ in pure samples of copper and aluminum. In addition to the increase in resistivity observed previously by many authors, which is due to a dislocation contribution at $T > 10$ K, anomalies are also observed on $\rho(T)$ as the temperature is lowered: these are in the form a minimum, a plateau, or a minimum with a subsequent maximum. The features on the $\rho(T)$ curve for $T < 10$ K are more sensitive to the deformational state of the metals than is the increase in ρ due to the dislocation contribution at $T > 10$ K. None of the existing theoretical models that we know of predicts the anomalies on $\rho(T)$ due to plastic deformation at $T < 10$ K.

We have established that at low temperatures the resistivity ρ of highly deformed samples of copper and aluminum have a complicated dependence on the crystallite size d. The character of $\rho(d)$ is different in the temperature region where the resistivity is governed by the electron–phonon interaction and in the region of residual resistivity.

We have shown experimentally that the value of the surface resistance R_s calculated from the measured values of ρ and the value measured experimentally in the region of the

anomalous skin effect agree only in the case when the mean free path of the electrons is smaller than the crystallite size.

In closing we thank V. D. Natsik and S. V. Lubenets for helpful discussions of the results of this study.

This work was supported by the Ministry of Education and Science of Ukraine, Contract N2M/75-2000.

*E-mail: dmitriev@ilt.kharkov.ua

[1] W. J. De Haas, J. de Boer, and G. J. van der Berg, Physica **1**, 1115 (1934).
[2] T. H. Blewitt, R. R. J. Coltman, and J. K. Redman, Phys. Rev. **93**, 891 (1954).
[3] R. W. Schmitt and V. D. Fiske, Phys. Rev. **96**, 1145 (1954).
[4] R. W. Schmitt, Phys. Rev. **96**, 1446 (1954).
[5] N. E. Alekseevskiĭ and Yu. P. Gaĭdukov, Zh. Éksp. Teor. Fiz. **31**, 947 (1956) [Sov. Phys. JETP **4**, 807 (1957)].
[6] N. E. Alekseevskiĭ and Yu. P. Gaĭdukov, Zh. Éksp. Teor. Fiz. **35**, 804 (1958) [Sov. Phys. JETP **8**, 558 (1959)].
[7] A. I. Shal'nikov (Ed.), *Physics of Low Temperatures* [in Russian], IL, Moscow (1959).
[8] B. N. Aleksandrov, in *Physics of the Condensed State* [in Russian], FTINT AN UkrSSR, Kharkov, issue VI, 52 (1970).
[9] J. Kondo, Prog. Theor. Phys. **32**, 37 (1964).
[10] A. A. Abrikosov, *Fundamentals of the Theory of Metals* [in Russian], Nauka, Moscow (1987).
[11] Z. S. Basinski, J. S. Dugdale, and A. Howie, Philos. Mag. **8**, 1989 (1963).
[12] T. W. Barbee, R. A. Huggins, Jr., and W. A. Little, Philos. Mag. **14**, 255 (1966).
[13] Z. S. Basinski and S. Saimoto, Can. J. Phys. **45**, Part 3 1161 (1967).
[14] J. G. Rider and C. T. B. Foxon, Philos. Mag. **16**, 1133 (1967).
[15] V. F. Gantmakher and G. I. Kulesko, Zh. Éksp. Teor. Fiz. **67**, 2335 (1974) [Sov. Phys. JETP **40**, 1158 (1975)].
[16] R. A. Brown, Phys. Rev. **156**, 889 (1967).
[17] S. V. Bozhokin and N. V. Dushin, Fiz. Tverd. Tela (Leningrad) **19**, 1826 (1977) [Sov. Phys. Solid State **19**, 1066 (1977)].
[18] G. I. Kulesko, Zh. Éksp. Teor. Fiz. **75**, 171 (1978) [Sov. Phys. JETP **48**, 85 (1978)].
[19] V. D. Natsik and L. G. Potemina, Zh. Éksp. Teor. Fiz. **79**, 2398 (1980) [Sov. Phys. JETP **52**, 1215 (1980)].
[20] A. E. Koshelev, Fiz. Tverd. Tela (Leningrad) **26**, 3190 (1984) [Sov. Phys. Solid State **26**, 1920 (1984)].
[21] S. I. Mukhin, Zh. Éksp. Teor. Fiz. **91**, 140 (1986) [Sov. Phys. JETP **64**, 81 (1986)].
[22] A. Yu. Kasumov and V. N. Matveev, Fiz. Tverd. Tela (Leningrad) **18**, 3724 (1976) [Sov. Phys. Solid State **18**, 472 (1976)].
[23] A. Yu. Kasumov, Ch. V. Kopetskiĭ, L. S. Kokhanchuk, and V. N. Matveev, Fiz. Tverd. Tela (Leningrad) **23**, 271 (1981) [Sov. Phys. Solid State **23**, 151 (1981)].
[24] A. O. Fedotov, L. P. Mezhov-Deglin, and A. Yu. Kasumov, Fiz. Tverd. Tela (Leningrad) **23**, 31 (1981) [Sov. Phys. Solid State **23(2)**, 177 (1981)].
[25] S. S. Gorelik, *Recrystallization of Metals and Alloys* [in Russian], Metallurgiya, Moscow (1978).
[26] M. Beckert and H. Clemm, *Handbook of Metallographic Etching*, Metallurgiya, Moscow (1979).
[27] M. N. Ofitserov, N. N. Prentslau, N. A. Kucheryavenko, A. P. Beskorskyi, and N. M. Levchenko, "System of temperature regulation and stabilization with digital control" [in Russian], FTINT AN UkrSSR Preprint 47–88, B. Verkin Institute for Low Temperature Physics and Engineering, National Academy of Sciences of Ukraine, Kharkov, Ukraine (1988).
[28] R. G. Chambers, Proc. R. Soc. London, Ser. A **215**, 481 (1952).
[29] B. N. Aleksandrov and I. G. D'yakov, Zh. Éksp. Teor. Fiz. **43**, 852 (1962) [Sov. Phys. JETP **16**, 603 (1963)].
[30] I. F. Voloshin, V. V. Lavrova, L. M. Fisher, and V. A. Yudich, Tr. Vses. Elektrotekh. Inst. **86**, 3 (1976).
[31] I. F. Voloshin and L. M. Fisher, in *Cryogenic Electrodynamics and Energetics* [in Russian], Naukova Dumka, Kiev (1977), p. 50.
[32] D. B. Poker and C. E. Klabunde, Phys. Rev. B **26**, 7012 (1982).
[33] R. N. Gurzhi, Zh. Éksp. Teor. Fiz. **47**, 1415 (1964) [Sov. Phys. JETP **20**, 953 (1964)].
[34] I. V. Zolotukhin, *Physical Properties of Amorphous Metallic Materials* [in Russian], Metallurgiya, Moscow (1986).
[35] R. Harris and J. Ström-Olsen, in *Metallic Glasses*, edited by H. Beck and H. J. Güntherodt [Springer-Verlag, Berlin (1981); Mir, Moscow (1986)].
[36] R. W. Cochrane, R. Harris, I. O. Ström-Olson, and M. J. Zuckermann, Phys. Rev. Lett. **35**, 676 (1975).
[37] J.-E. Wegrowe, A. Comment, Y. Jaccard, and J.-Ph. Ansermet, Phys. Rev. B **61**, 12216 (2000).
[38] C. A. Wert and R. M. Thomson, *Physics of Solids* [McGraw-Hill, New York (1964); Mir, Moscow (1969)].
[39] B. G. Livshits, *Physical Principles of Metals and Alloys* [in Russian], Mashgiz, Moscow (1959).
[40] Ya. S. Umanskiĭ and Yu. A. Skakov, *Physics of Metals. Atomic Structure of Metals and Alloys* [in Russian], Atomizdat, Moscow (1978).

Translated by Steve Torstveit

Magnetic state in URu_2Si_2, UPd_2Al_3, and UNi_2Al_3 probed by point contacts

Yu. G. Naidyuk* and O. E. Kvitnitskaya

Grenoble High Magnetic Field Laboratory, Max-Planck-Institut für Festkörperforschung and Centre National de la Recherche Scientifique, Grenoble Cedex, 9, F-38042, France; B. Verkin Institute for Low Temperature Physics and Engineering of the National Academy of Sciences of Ukraine, Lenin Ave., 47, 61103 Kharkov, Ukraine

A. G. M. Jansen and P. Wyder

Grenoble High Magnetic Field Laboratory, Max-Planck-Institut für Festkörperforschung and Centre National de la Recherche Scientifique, Grenoble Cedex, 9, F-38042, France

C. Geibel

Max-Planck Institut für Chemische Physik Fester Stoffe, Dresden, D-01187, Germany

A. A. Menovsky

Van der Waals-Zeeman Laboratory, University of Amsterdam 1018 XE, The Netherlands
(Submitted January 18, 2001)
Fiz. Nizk. Temp. **27**, 668–673 (June 2001)

The antiferromagnetic (AFM) state is investigated in the three heavy-fermion compounds URu_2Si_2, UPd_2Al_3, and UNi_2Al_3 by measuring $dV/dI(V)$ curves of point contacts at different temperatures 1.5–20 K and magnetic fields 0–28 T. The zero-bias maximum in $dV/dI(V)$ for URu_2Si_2 points to a partially gapped Fermi surface related to the itinerant nature of the AFM state, contrary to the case of UPd_2Al_3, where analogous features have not been found. The AFM state in UNi_2Al_3 has more similarities with URu_2Si_2. For URu_2Si_2, the same critical field of about 40 T along the easy axis **c** is found for all features in $dV/dI(V)$, corresponding to the Néel temperature, the gap in the electronic density of states, and presumably the ordered moments.
 [DOI: 10.1063/1.1382993]

The U-based heavy-fermion (HF) systems URu_2Si_2, UPd_2Al_3, and UNi_2Al_3 exhibiting antiferromagnetic (AFM) order followed by a superconducting transition at lower temperatures attract much interest in view of the possible coupling between superconducting and magnetic order. The AFM ground state in the HF compounds mentioned while at first sight similar, reveals essential differences. While in URu_2Si_2 neutron-scattering experiments below the Néel temperature $T_N = 17.5$ K resolved an AFM ordered structure with a tiny ordered moment $(0.03 \pm 0.01)\mu_B$/U-atom along the **c** axis,[1] UPd_2Al_3 below $T_N = 14$ K has aligned U moments equal to $(0.85 \pm 0.03)\mu_B$ in the basal plane.[2] Although the latter compound has the largest moment among the HF superconductors, it has the highest superconducting critical temperature T_c of about 2 K, compared to the typical value of 1.4 K in URu_2Si_2. UNi_2Al_3 has been investigated much less than the other two compounds, probably because of certain difficulties in the preparation of good samples. This compound is isostructural and isoelectronic to UPd_2Al_3, but has a few times smaller magnetic moment of about $(0.24 \pm 0.10)\mu_B$ (Ref. 3) as well as lower critical (~1 K) and Néel (~5 K) temperatures.

Pronounced anomalies in the specific heat, magnetic susceptibility, resistivity, etc., for all three compounds indicate a phase transition to an AFM state. The resistivity has a well defined *N*-like structure at T_N in URu_2Si_2, which looks like a kink for UPd_2Al_3 and is even more shallow for UNi_2Al_3. For the interpretation of these anomalies a transition to a spin-density wave (SDW) state has been considered,[4] with a partial opening of a gap of about 10 mV at the Fermi surface.[4–6] Tunneling experiments which can determine the gap in the electronic density of states (DOS) and its anisotropy yield for all three compounds a gap in the range 10 to 20 mV in the basal plane.[7,8] However, far-infrared absorption[9] did not resolve any gap-like features for UPd_2Al_3, unlike in URu_2Si_2. For URu_2Si_2, the most investigated compound among this class of HF systems, it is still under discussion how the large anomalies in the transport and thermodynamic properties at T_N can be reconciled with the tiny ordered moments. Therefore, understanding the nature of the magnetic order parameter in the AFM state of URu_2Si_2 remains a challenge. Recent transport and neutron scattering measurements in a high magnetic field revealed different transition fields for the AFM order or T_N (~40 T; Ref. 10) and for the tiny staggered magnetic moments (~14 T; Ref. 11). This has led to a speculation about some additional ''hidden'' magnetic order parameter in URu_2Si_2.

To clarify some aspects of the aforementioned magnetic ordered state, we have performed a comparative point-contact study on these U-based HF compounds in strong magnetic fields. Of the three compounds the normal state properties have been investigated previously using point-contact spectroscopy only for URu_2Si_2 (Refs. 12–15), although not in applied magnetic fields. The $dV/dI(V)$ characteristics of point contacts with URu_2Si_2 show an *N*-type feature related to local contact heating above the Néel

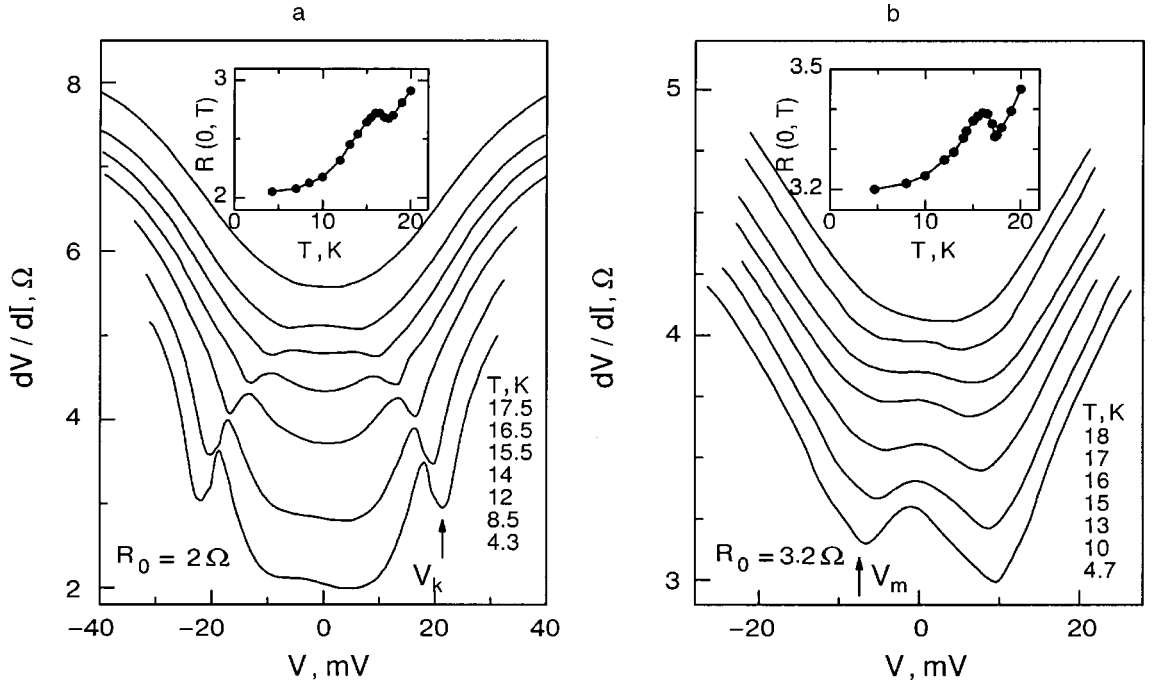

FIG. 1. Two types of behavior, (a) and (b), in the $dV/dI(V)$ curves for single crystal URu_2Si_2 homocontacts established in the basal plane at increasing temperature up to T_N. The curves are offset vertically for clarity. The insets show the temperature dependence of the zero-bias resistance, which mimics $\rho(T)$ for bulk samples.

temperature[15] and a zero-bias maximum which has been analyzed in terms of a partial suppression of the density of states related to an itinerant AFM ground state.[12,14,15] The present study allows one to follow these characteristics of the AFM ground state in a magnetic field with a complete temperature-dependent study of the phenomena.

We have investigated both homocontacts between the same HF compounds and heterocontacts between a HF compound and normal metals like Cu or Ag. The main difference was only in the degree of asymmetry of the $dV/dI(V)$ curves with respect to bias-voltage polarity, which is more pronounced for heterocontacts. The origin of the asymmetry is still under discussion.[15] Because this effect has no influence on the main conclusions of the present investigations, we will devote no more attention to it. In the case of the URu_2Si_2 single crystal, the heterocontacts were established in such a way that both the contact axis and magnetic field were parallel to the **c** axis or perpendicular to it. For the UPd_2Al_3 single crystal the contact axis and magnetic field were aligned along the easy basal plane direction, whereas we used UNi_2Al_3 samples of unknown orientation. The measurements were carried in magnetic fields up to 28 T at 4.2 K (but for UNi_2Al_3 up to 10 T at temperatures down to about 2 K).

The measured $dV/dI(V)$ curves of URu_2Si_2 contacts can be separated into three groups. In the first group the $dV/dI(V)$ curves mimic the behavior of bulk $\rho(T)$. The differential resistance increases with voltage and exhibits an *N*-type feature at about 20 mV (Fig. 1a) similar to $\rho(T)$ at T_N (Ref. 6). The second type of $dV/dI(V)$ curve exhibits a pronounced asymmetric zero-bias maximum (ZBM) with a width of about 10 mV in $dV/dI(V)$ (Fig. 1b), followed by gradually increasing signal at higher voltages. The third group contains simultaneously both kinds of structures in $dV/dI(V)$. We note that the temperature dependence of the contact resistance (Fig. 1, insets) corresponds in all cases to a $\rho(T)$ independent of the type of $dV/dI(V)$ behavior. This indicates that the material in the constriction reflects the bulk properties. The features mentioned, namely the *N*-type kink and ZBM, vanish at the Néel temperature (Fig. 1) and are therefore connected with the magnetic state.

The voltage position of the *N*-kink (marked by V_k in Fig. 1a) is determined by T_N and corresponds to the transition of the contact region from the AFM to the paramagnetic state, most likely due to bias-voltage heating in the constriction. The temperature dependence $\sqrt{1-(T/T_N)^2}$ of V_k shown in Fig. 2a is expected for such a local contact heating.[15] The ZBM is more pronounced for curves with shallow or unresolved kink anomalies. Moreover, the ZBM cannot be described in the thermal model, as can be seen directly upon comparing $dV/dI(V>0)$ with $dV/dI(V=0,T)=R(V=0,T)$ (see Fig. 1b). These observations point to the spectral nature of the ZBM. The latter has been related (see, e.g., Ref. 15) with the existence of a gap in the excitation spectrum of the electrons due to the formation of a SDW below T_N. The ZBM has a width which is comparable to the gap value estimated in Refs. 4 and 6–8. The intensity of the ZBM decreases gradually with increasing temperature,[12,15] analogously to the intensity of AFM Bragg peaks describing the behavior of the staggered magnetic moments or the order parameter.[16] Therefore, it is tempting to relate the ZBM also with the magnetic order parameter, although the microscopic nature of the tiny staggered magnetic moments in URu_2Si_2 and their influence on the measured dV/dI are still unknown. Because the intensity of the ZBM depends on the chosen criterion for subtraction of the increasing-with-voltage background, we suggest taking the voltage position of the minima

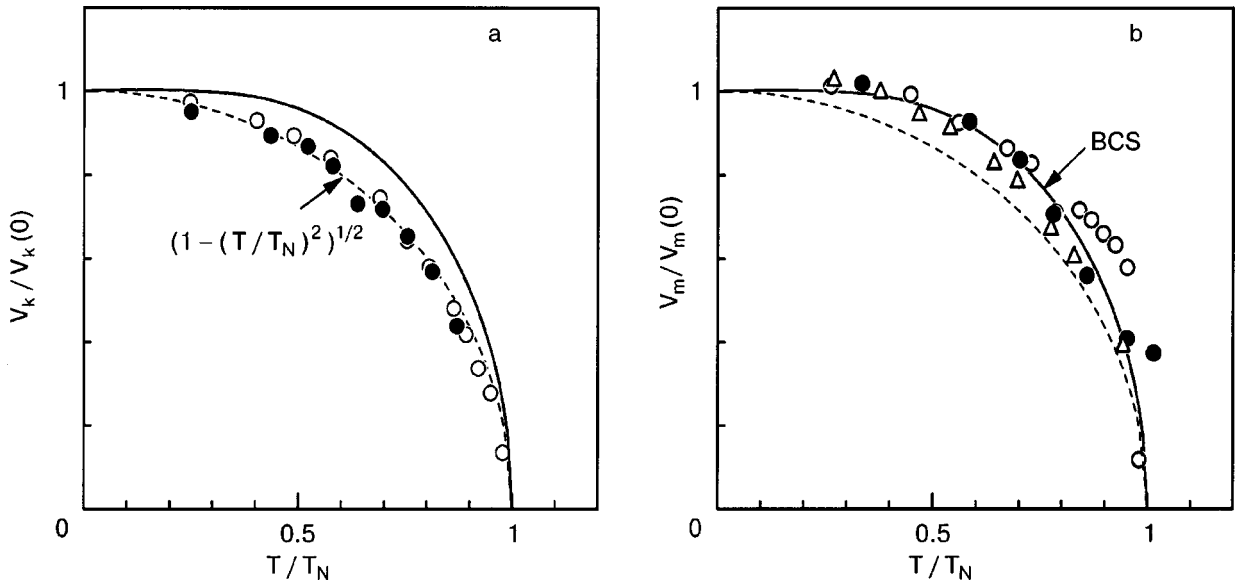

FIG. 2. Temperature dependence of the reduced voltage positions V_k (a) and V_m (b) (for definition see Fig. 1) for a few URu_2Si_2 homocontacts established in the basal plane. The solid circles for both figures correspond to the same homocontact. The solid line in both figures is the mean-field BCS dependence, while the dashed curve describes the thermal regime behavior.[15]

V_m (see Fig. 1b) as an additional measure of the magnetic order parameter, as supported by the mean-field (BCS-like) $V_m(T)$ dependence in Fig. 2b, which was also found in Refs. 13 and 14.

The point-contact data presented in Fig. 3a for magnetic fields parallel to the easy axis **c** exhibit both types of features discussed above, i.e., ZBM and *N*-kink. The integrated intensity of the ZBM (after subtraction of a polynomial voltage-dependent background) is close to a $\sqrt{1-(B/B_c)^{3/2}}$ behavior, like that for magnetic moments.[11] As is shown in Fig. 3b, the same dependence is found for V_m as well. On the other hand, V_k follows a magnetic field dependence $(1-(B/B_c)^2)$ like that for T_N (Ref. 10; shown in Fig. 3b). The latter dependence is found also for the width of the ZBM (not shown), which is related to the SDW gap. Thus the abovementioned features in $dV/dI(V)-V_k$, the ZBM width, and the ZBM intensity or V_m measured on the same contact —are described by the magnetic field dependencies characteristic for the behavior of the transition temperature T_N, magnetic gap width,[10] and magnetic order parameter,[11] respectively. Moreover, as can be seen in Fig. 3b, independent of the type of behavior, in all cases the critical field is estimated to be about 40 T, which coincides with the B_c values measured by magnetoresistance.[17] Therefore, unlike in Refs. 10 and 11, where for the ordered magnetic moments the critical field is estimated to be about 14 T, our data show the presence of

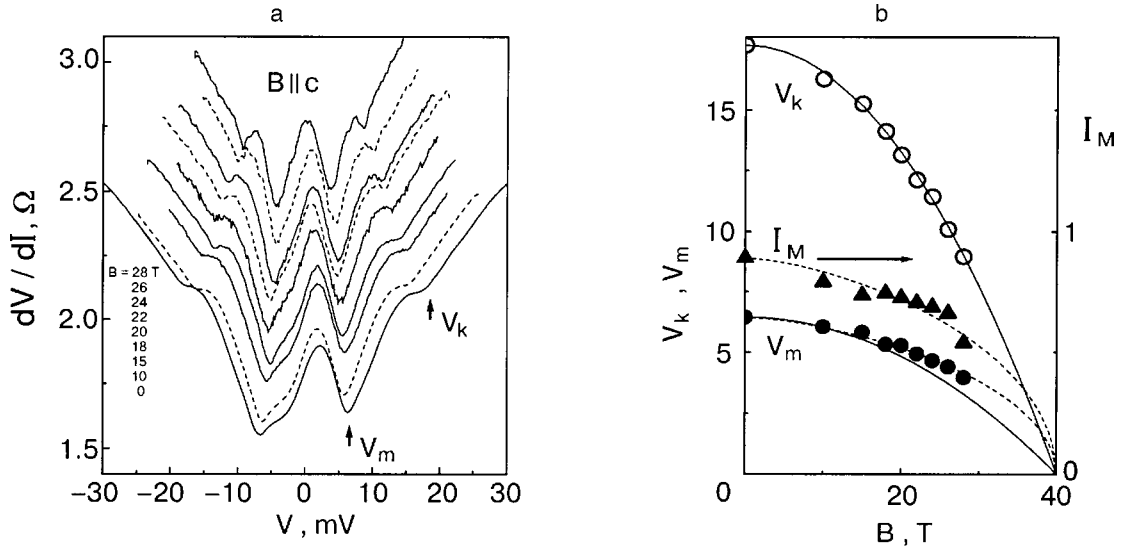

FIG. 3. $dV/dI(V)$ curves for a URu_2Si_2–Cu heterocontact in magnetic fields along the easy axis **c** at $T=4.2$ K. The solid curves correspond to the field sweep up, while the dashed curve is for the field sweep down. The arrows indicate the kink V_k and minimum V_m positions. The curves are offset vertically for clarity (a). Dependence of V_k, V_m and ZBM integrated intensity I_M versus magnetic field. Note, that the position of V_k, V_m, and ZBM intensity was taken after symmetrizing of the $dV/dI(V)$ curves. The solid lines represent the dependence $(1-(B/B_c)^2)$ characteristic for $T_N(B)$ and the spin-wave gap $\Delta(B)$,[10] while the dashed line $\sqrt{1-(B/B_c)^{3/2}}$ is taken from Ref. 11 for staggered magnetic moments (b).

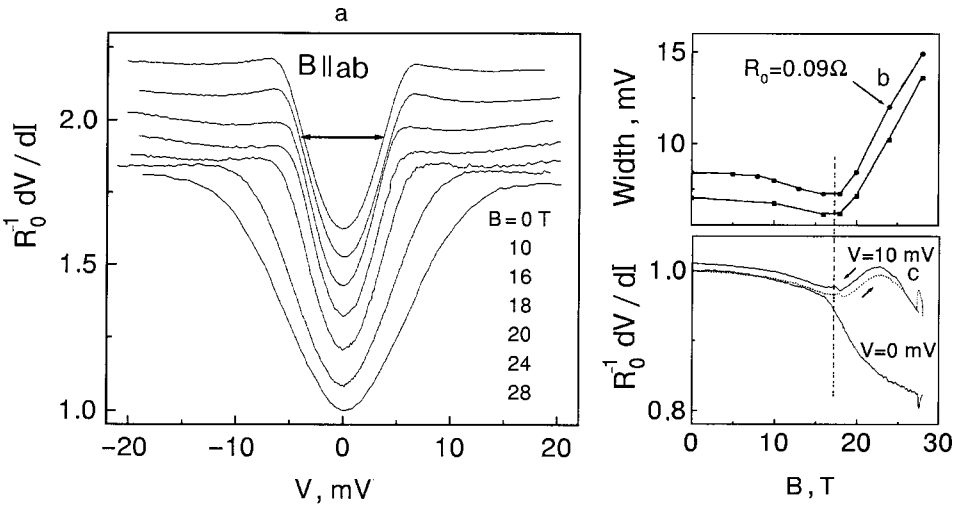

FIG. 4. $dV/dI(V)$ curves for a UPd_2Al_3–Cu heterocontact with $R_0 = 4.3\,\Omega$ at different magnetic fields along the basal plane and $T = 4.2$ K. The horizontal line with arrows indicates the width of the minimum. The curves are offset vertically for clarity (a). Width of the minimum versus magnetic field for the previous contact and for another contact with $R_0 = 0.09\,\Omega$ (b). Magnetoresistance of the contact with $R_0 = 4.3\,\Omega$ at zero bias and at 10 mV. The vertical dashed line marks the position of the metamagnetic transition at 18 T (c).

one order parameter, which vanishes at $T_N = 17.5$ K and $B_c \simeq 40$ T. This is in line with the recent observation of van Dijk *et al.*[16] that the ordered moments remain coupled to the energy gap in the magnetic excitation spectrum in fields up to at least 12 T. We should emphasize that in measuring URu_2Si_2 contacts in a field perpendicular to the direction of the easy axis **c** we did not find any noticeable influence of magnetic field on $dV/dI(V)$, testifying that the point contact data really reflect the bulk properties.

Let us turn to the other compounds. The $dV/dI(V)$ curve of UPd_2Al_3 contacts (see Fig. 4) show a minimum at $V = 0$, with edge maxima or shoulders which are connected with the AFM transition due to the heating effect,[18] analogously to the *N*-type feature in the case of URu_2Si_2. However, for UPd_2Al_3 contacts we have never seen even a shallow ZBM neither for homo- nor for heterocontacts after a study of more than 20 contacts both below and above the Néel temperature. Therefore no evidence of the partially gapping of the Fermi surface is observed for UPd_2Al_3, unlike in URu_2Si_2, a finding which points to a quite different magnetic ground state as well as to a different nature of the ordered moments for the two compounds.

A magnetic field along the easy basal plane modifies the $dV/dI(V)$ curves of UPd_2Al_3, as can be seen from Fig. 4a. The maxima shift slightly ($\approx$15%) to lower energies and broaden with increasing magnetic field up to 18 T, and then vanish in higher fields. The width of the $dV/dI(V)$ minimum at $V = 0$ has a minimum at 18 T, while the contact resistance has a kink at this field both at zero bias and finite bias voltage (see Fig. 4b,c). Hence the metamagnetic transition at 18 T[19] is clearly resolved in the point-contact measurements, while no other phase boundary was observed both at lower and higher fields up to 28 T. From measurements of the dc susceptibility, dc magnetization, transverse magnetoresistivity, and magnetostriction, Grauel *et al.*[20] have also found a phase boundary in UPd_2Al_3 at a critical field of about 4 T along the basal plane. However, the influence of this low-field transition on the resistivity is at least one order of magnitude smaller than for the transition at 18 T. Moreover, the fact that de Visser *et al.*[19] did not find a transition at 4 T in their magnetoresistance data indicates that a reorientation of the AFM domains could play a role in this phenomenon.

The $dV/dI(V)$ curves of UNi_2Al_3 usually represent a smooth, broad, almost symmetric minimum around zero bias. However, often a shallow ZBM can be observed around $V = 0$ (Fig. 5). The distance between the minima in $dV/dI(V)$ with a ZBM is a few mV (often up to 10 mV), and the ZBM disappears at about 5 K (between 10–15 K for wider maxima). For a ZBM with a critical temperature of about 5 K the critical field was about 10 T. From this point of view UNi_2Al_3 behaves similarly to URu_2Si_2, hinting at the development of a magnetic state with a partial gapping of the Fermi surface in this compound, too. It should be noted that for UNi_2Al_3 we did not resolve any feature in $dV/dI(V)$ (Fig. 5) connected with T_N, like that in URu_2Si_2 (Fig. 1a) and UPd_2Al_3 (Fig. 5). This transition at T_N is also very shallow in the $\rho(T)$ dependence of UNi_2Al_3. Probably a better quality of the UNi_2Al_3 samples is required to register the AFM transition and to study the temperature behavior of the ZBM in $dV/dI(V)$.

Summarizing, the point-contact measurements for the investigated U-based heavy-fermion compounds yield information on the differences in the AFM ground state of these systems. The ZBM structure in $dV/dI(V)$ for the URu_2Si_2 contacts points to a partially gapped Fermi surface in the

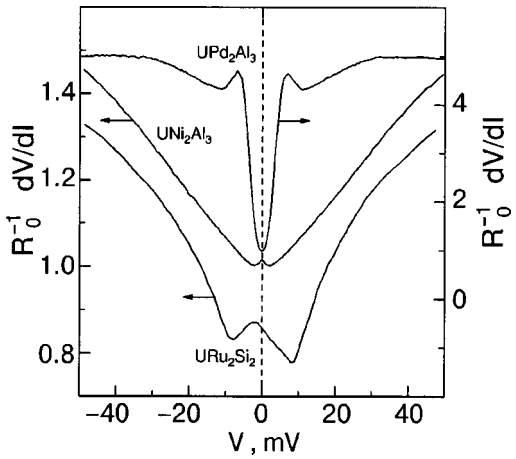

FIG. 5. Comparison of the $dV/dI(V)$ curves for homocontacts with the three HF compounds studied: UPd_2Al_3 ($R_0 = 0.61\,\Omega$, $T = 4.2$ K), UNi_2Al_3 ($R_0 = 1.5\,\Omega$, $T = 2.3$ K), and URu_2Si_2 ($R_0 = 3.2\,\Omega$, $T = 4.2$ K). A ZBM is only resolved for the latter two compounds. The curve for URu_2Si_2 is shifted down by 0.15.

magnetically ordered state, but no evidence of an analogous structure has been found in the case of UPd_2Al_3, unlike for UNi_2Al_3, where it is possible to resolve a shallow ZBM. The results for URu_2Si_2 in the $H-V$, T diagram yield only one critical Néel temperature of 17 K and one critical field of about 40 T along the easy axis **c** for all features in $dV/dI(V)$, testifying that they result from the same order parameter in the magnetic state.

*E-mail: naidyuk@itl.kharkov.ua

[1] C. Broholm, J. K. Kjems, W. J. L. Buyers, P. Matthews, T. T. M. Palstra, A. A. Menovsky, and J. A. Mydosh, Phys. Rev. Lett. **58**, 1477 (1987).
[2] A. Krimmel, P. Fischer, B. Roessli, H. Maletta, C. Geibel, C. Schank, A. Grauel, A. Loidl, and F. Steglich, Z. Phys. B: Condens. Matter **86**, 161 (1992).
[3] A. Schröder, J. G. Lussier, B. D. Gaulin, J. D. Garrett, W. J. L. Buyers, L. Rebelsky, and S. M. Shapiro, Phys. Rev. Lett. **72**, 136 (1994).
[4] M. B. Maple, J. W. Chen, Y. Dalichaouch, T. Kohara, C. Rossel, M. S. Torikachvili, M. W. McElfrech, and J. D. Thompson, Phys. Rev. Lett. **56**, 185 (1986).
[5] T. T. M. Palstra, A. A. Menovsky, J. van der Berg, A. J. Dirkmaat, P. H. Kes, G. J. Nieuwenhuys, and J. A. Mydosh, Phys. Rev. Lett. **55**, 2727 (1985).
[6] J. A. Mydosh, Phys. Scr. T **19**, 260 (1987).
[7] F. G. Aliev, V. Kovachik, V. V. Moshchalkov, V. V. Pryadun, N. E. Alekseevskii, A. V. Mitin, N. Agrait, S. Viera, and R. Villar, J. Low Temp. Phys. **85**, 359 (1991).
[8] J. Aarts, A. P. Volodin, A. A. Menovsky, G. J. Nieuwenhuys, and J. A. Mydosh, Europhys. Lett. **26**, 203 (1994).
[9] L. Degiorgi, S. Thieme, H. R. Ott, M. Dressel, G. Grüner, Y. Dalichaouch, M. B. Maple, Z. Fisk, C. Geibel, and F. Steglich, Z. Phys. B: Condens. Matter **102**, 367 (1997).
[10] S. A. M. Mentink, T. E. Mason, S. Süllow, G. J. Nieuwenhuys, A. A. Menovsky, J. A. Mydosh, and J. A. A. J. Perenboom, Phys. Rev. B **53**, 6014 (1996).
[11] T. E. Mason, W. J. L. Buyers, T. Petersen, A. A. Menovsky, and J. D. Garrett, J. Phys.: Condens. Matter **7**, 5089 (1995).
[12] K. Hasselbach, J. R. Kirtley, and P. Lejay, Phys. Rev. B **46**, 5826 (1992).
[13] R. Escudero, F. Morales, and P. Lejay, Phys. Rev. B **49**, 15271 (1994).
[14] St. Thieme, P. Steiner, L. Degiorgi, P. Wachter, Y. Dalichaouch, and M. B. Maple, Europhys. Lett. **32**, 367 (1995).
[15] Yu. G. Naidyuk and I. K. Yanson, J. Phys.: Condens. Matter **10**, 8905 (1998).
[16] N. H. van Dijk, F. Bourdarot, B. Fåk, F. Lapierre, L. P. Regnault, P. Burlet, J. Bossy, N. Pyka, and A. A. Menovsky, Physica B **234–236**, 693 (1997).
[17] K. Sugiyama, H. Fuke, K. Kindo, K. Shimohata, A. A. Menovsky, J. A. Mydosh, and M. Date, J. Phys. Soc. Jpn. **59**, 3331 (1990).
[18] O. E. Kvitnitskaya, Yu. G. Naidyuk, A. Nowack, K. Gloos, C. Geibel, A. G. M. Jansen, and P. Wyder, Physica B **259–261**, 638 (1999).
[19] A. de Visser, K. Bakker, L. T. Tai, A. A. Menovsky, S. A. M. Mentink, G. J. Nieuwenhuys, and J. A. Mydosh, Physica B **186–188**, 291 (1993).
[20] A. Grauel, A. Böhm, H. Fischer, C. Geibel, R. Köhler, R. Modler, C. Schank, F. Steglich, G. Weber, T. Komatsubara, and N. Sato, Phys. Rev. B **46**, 5818 (1992).

This article was published in English in the original Russian journal. Reproduced here with stylistic changes by AIP.

QUANTUM EFFECTS IN SEMICONDUCTORS AND DIELECTRICS

Quantum biexcitonic liquid in monoclinic ZnP_2 crystals

I. S. Gorban,† O. A. Yeshchenko,* I. M. Dmitruk, and M. M. Biliy

Physics Faculty Kyiv, Taras Shevchenko University, Akad. Glushkov pr., 6, 03127 Kyiv, Ukraine
(Submitted December 18, 2000; revised February 5, 2001)
Fiz. Nizk. Temp. **27**, 674–682 (June 2001)

A phonon–roton dispersion relation is proposed for the elementary excitations of a quantum biexcitonic liquid in semiconductors. The proposed dispersion relation is used as a starting point for a calculation of the photoluminescence spectrum of the liquid and an analysis of its behavior under variation of temperature and density of the biexcitonic liquid. The parameters of the dispersion curve of elementary excitations of the quantum biexcitonic liquid are evaluated by fitting the calculated photoluminescence spectrum to the experimental spectrum of the biexcitonic liquid of semiconducting β-ZnP_2 crystals. Experimental studies of how the photoluminescence spectrum of a biexcitonic liquid in β-ZnP_2 depends on the temperature and the intensity of the laser excitation confirm the initial theoretical model. The dependence of the temperature of the crystals on the excitation intensity is measured, and for some of the samples an anomalous dependence is found: the temperature of the crystal decreases as the excitation intensity increases. This effect is probably a consequence of the giant thermal conductivity of the superfluid biexcitonic liquid in β-ZnP_2 crystals.
[DOI: 10.1063/1.1382994]

INTRODUCTION

For a long time the phenomenon of superfluidity was observed exclusively in liquid ^{4}He at temperatures below 2.17 K. It is well known that the dispersion relation for elementary excitations in superfluid He II is characterized by a so-called roton gap. A dispersion relation of this sort was first proposed by Landau[1] and later investigated theoretically by Feynman,[2] and it was subsequently confirmed in neutron scattering experiments.[3] Among the Bose liquids, ^{4}He is unique in that it remains liquid at atmospheric pressure down to the lowest temperatures. Other Bose liquids crystallize at temperatures above those at which superfluidity can arise. Crystallization sets in because the energy of the intermolecular interaction is greater than the vibrational energy at temperatures above the temperature of the onset of superfluidity. Since the vibrational energy goes as $\hbar\omega_{\text{vibr}} \propto m^{-1/2}$ (m is the mass of the molecule), superfluidity is more likely to arise in liquid molecular hydrogen than in other liquids. However, even in the case of liquid H_2 the energy of the intermolecular interaction is too large, and crystallization sets in before superfluidity as the temperature is lowered.

The analogy between Wannier–Mott excitons in semiconductors and atomic hydrogen is well known. This analogy extends to excitonic molecules (EMs or biexcitons) and to the hydrogen molecule. The problem of Bose condensation and superfluidity in a system of excitons has been very popular in semiconductor physics for the past 20–25 years (see, e.g., Refs. 4–6). The possibility of superfluidity of excitons in a strong magnetic field was pointed out in Ref. 5. An unusual ballistic solitonlike regime of exciton motion in Cu_2O crystals was observed in Ref. 6. This effect was interpreted as evidence of superfluidity of Bose-condensed excitons.

Guided by the analogy between excitonic molecules and hydrogen molecules, one can analyze the possibility for superfluidity to arise in such a biexcitonic (molecular) liquid. The existence of a biexcitonic liquid in semiconductors was first considered in Ref. 7. As we have said, superfluidity is not observed in liquid hydrogen because of the earlier onset of crystallization. However, the effective mass of excitonic molecules is 2–3 orders of magnitude smaller than that of the H_2 molecule, and crystallization of a biexcitonic liquid probably should not occur at all. Therefore, at sufficiently low temperatures a biexcitonic liquid can go into a superfluid state. However, as it turns out, the formation of a biexcitonic liquid itself is extremely problematical. Keldysh[8] and later Brinkman and Rice[9] pointed out two important differences between H_2 molecules and EMs in typical semiconductors. First, since the effective masses of the electron and hole are often of the same order, the binding energy of the excitonic molecule, measured in units of the binding energy of the exciton (atom), should be much less than 0.35 for the hydrogen molecule. Second, the contribution of the energy of zero-point motion is considerably larger in a system of biexcitons because of the small mass of a biexciton. For these two reasons, as experiments have shown, in typical semiconductors (Si, Ge, and a number of others) at high excitation intensities an electron–hole Fermi liquid is formed. One therefore expects that the formation of a biexcitonic Bose liquid can occur only in crystals in which the effective masses of the electron and hole are sufficiently different. Furthermore, the mass of the EM should be sufficiently large that the contribution of the zero-point motion is sufficiently small and it

becomes possible for a molecular liquid to form. At the same time, the mass of the EM must be small enough that ''early'' crystallization cannot occur.

Crystals of monoclinic zinc diphosphide (β-ZnP_2) meet the stated requirements. This crystal is characterized by an appreciable difference of the electron and hole effective masses ($\sigma = m_e/m_h = 0.06$), a rather large value of the translational mass of the biexciton $m_{bex} = 3m_0$ (m_0 is the free electron mass), and a very strong anisotropy of the effective masses of the carriers. For example, the anisotropy parameter $\gamma = \mu_\parallel/\mu_\perp$ is equal to 0.19 ($\mu_\parallel$ and $\mu_\perp$ are the values of the reduced masses of an exciton in the directions parallel to and perpendicular to the Z (c) axis of the crystal). As we know, the anisotropy leads to an increase in the binding energy of free electron–hole complexes, i.e., excitons, biexcitons, and their condensates. Therefore, the excitonic molecule in β-ZnP_2 has a rather high binding energy $E^b_{bex} = 6.7\,\text{meV} = 0.15E^b_{ex}$.

The excitonic state with the lowest energy in this crystal is the dipole-forbidden $1S$ state of the orthoexciton.[10] This makes it rather easy to create an appreciable concentration of excitons and, hence, biexcitons under laser excitation. Studies by the authors have shown that the condensation of biexcitons in β-ZnP_2 crystals occurs via a hydrogenlike scenario, i.e., unlike the case of typical semiconductors, a liquid of the molecular (insulator) type forms in them. In the photoluminescence (PL) spectrum of these crystals one observes the so-called C line, which is due to two-photon annihilation of biexcitions[1)] condensed into a molecular (insulator) liquid.[11–13] In Refs. 12 and 13 the phase diagram of a biexcitonic liquid was measured and its critical parameters were determined: $T_C = 4.9\,\text{K}$, $n_{bex,C} = 4.1\times10^{18}\,\text{cm}^{-3}$ ($r_{bex,C} \approx 63\,\text{Å} = 4.2a_{ex}$, where a_{ex} is the excitonic Bohr radius).

In this paper we propose a model for the quantum biexcitonic Bose liquid and calculate its emission spectrum. In the framework of this model we analyze the experimentally observed features of the fine structure of the emission line of a biexcitonic liquid in β-ZnP_2 (the C line) as the temperature and the intensity of the laser excitation of the crystal are varied.

DISPERSION RELATION FOR ELEMENTARY EXCITATIONS OF A QUANTUM BIEXCITONIC LIQUID

Thus we assume that the biexcitonic liquid does not crystallize down to the temperatures at which quantum effects become important. What sorts of elementary excitations can exist in a quantum biexcitonic Bose liquid? It is logical to assume that, first, there are acoustic phonons. Their dispersion relation is given as

$$E(k) = \hbar u k, \tag{1}$$

where u is the sound velocity, and k is the wave vector. Second, we assume that owing to the intermolecular interaction in the liquid a collectivization of the intramolecular excitations can occur in it. Since the lowest-energy excited state of an excitonic molecule is a rotational state,[15] these collectivized molecular excitations can be rotational excitations of the molecules. Here, following Landau,[1] these collectivized excitations/quasiparticles will be called rotons. Rotons in a biexcitonic (molecular) liquid can be regarded as molecular Frenkel excitons. The excitation energy of the molecule in the presence of phase correlation between the molecules in the liquid can be written as

$$\Delta E = \Delta E_0 + D + 2M\cos[(k - k_0')a], \tag{2}$$

where ΔE_0 is the excitation energy of a free molecule, D is the change of the interaction energy of a given molecule with its neighbors upon its excitation, M is the matrix element for the transfer of the energy of excitation from the excited molecule to a neighbor in the ground state, a is the average distance between these molecules, and k is the wave vector of a Frenkel exciton, i.e., in our case the roton. The last term in Eq. (2) describes the dispersion relation of rotons and is physically meaningful for $|\Delta k| = |k - k_0'| \leqslant \pi/2a$. Thus the photon–roton dispersion relation for elementary excitations of a biexcitonic liquid can be written as

$$\begin{aligned} &E(k) = \hbar u k \quad \text{for} \quad 0 \leqslant k < k_0' - \pi/2a \\ &\text{and} \quad k > k_0' + \pi/2a; \quad E(k) = \hbar u k - \gamma\cos[(k - k_0')a] \\ &\text{for} \quad k_0' - \pi/2a \leqslant k \leqslant k_0' + \pi/2a, \end{aligned} \tag{3}$$

where $\gamma = -2M$. For small $|\Delta k|$ the second relation of system (3) can be written in the form

$$E_r(k) = \Delta + \frac{\hbar^2(k - k_0)^2}{2m_r}. \tag{4}$$

Equation (4) is exactly the same as the equation proposed by Landau[1] for describing the dispersion relation of rotons in superfluid He II. Thus our choice of the term ''roton'' is not arbitrary but is based on the similarity of the dispersion relations of rotons in helium and the collectivized molecular excitations of a biexcitonic liquid. In Eq. (4) we have introduced the following notation: $m_r = -\hbar^2/2Ma^2$ is the roton effective mass, $k_0 = k_0' - m_r u/\hbar$ is the wave vector corresponding to the roton minimum of the dispersion relation, and $\Delta = \hbar u k_0 + 2M + m_r u^2/2$ is the energy gap in the spectrum of elementary excitations of the biexcitonic liquid.

Starting from the dispersion relation (3) for a quantum biexcitonic liquid, let us calculate the PL spectrum for such a liquid. The spectrum we are looking for can be obtained by convolution of the slit function and the function $I(E) = I_0\rho(E)f(E)$, where $I_0 = \text{const}$, $\rho(E) = \rho_0 k^2(E) \times (dk(E)/dE)$ is the density of states of the liquid, which is determined from the dispersion relation for the elementary excitations ($\rho_0 = \text{const}$); $f(E) = 1/[\exp(E/k_BT) - 1]$ is the distribution function for the excitations/quasiparticles of the liquid (the Bose–Einstein distribution function). The zero of energy E is taken as the value corresponding to the radiative transition from the state with $k = 0$. For the parameters of the dispersion curve we used the values obtained from a best fit of the calculated luminescence spectrum to the experimental PL spectrum of a biexcitonic liquid, recorded for a β-ZnP_2 crystal of high purity. Figures 1–4 show the calculated PL spectra of a quantum biexcitonic liquid of various densities at different temperatures and also the characteristics of these spectra as functions of temperature T and the square of the excitation intensity I^2_{exc} (the density of the biexcitonic liquid

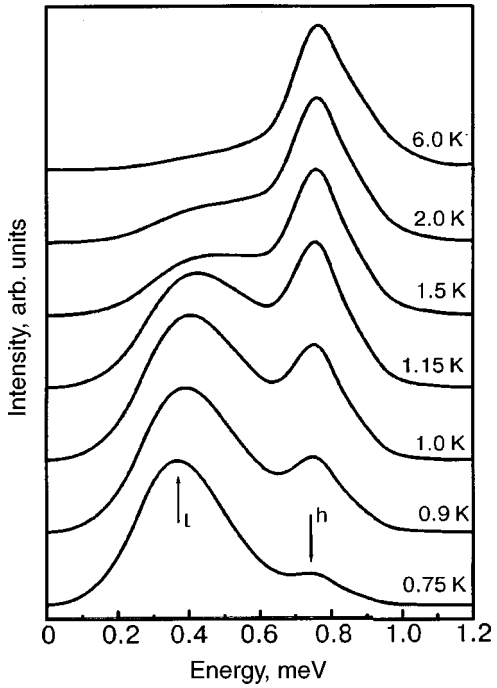

FIG. 1. Evolution with temperature of the calculated photoluminescence spectrum of a quantum biexcitonic liquid with a phonon–roton dispersion relation for the elementary excitations. The arrow labeled l indicates the low-energy (l) component of the spectrum, and the arrow h the high-energy (h) component.

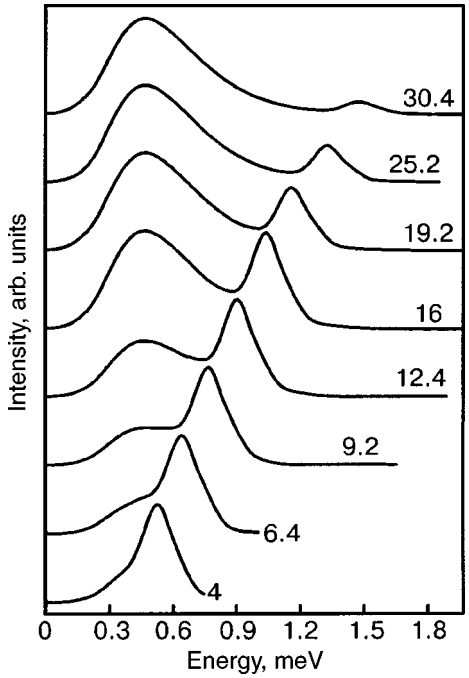

FIG. 3. Evolution of the theoretical PL spectrum of a quantum biexcitonic liquid under variation of the square of the excitation intensity (density of the liquid): $n \propto I_{\mathrm{ex}}^2$. The curves are labeled with the value of I_{exc}^2 in arbitrary units.

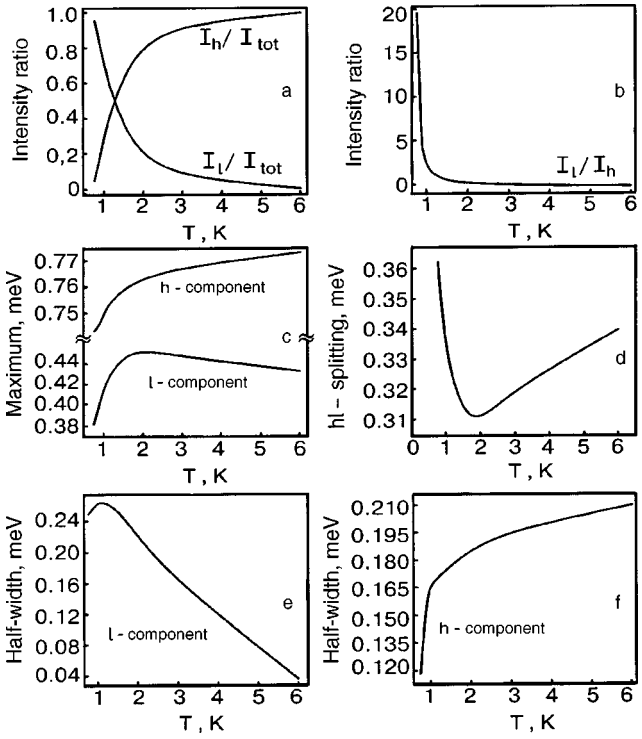

FIG. 2. Temperature dependence of the characteristics of the theoretical PL spectrum of a quantum biexcitonic liquid: I_l / I_{tot} is the ratio of the intensity of the l component to the total intensity of the C spectrum, I_h / I_{tot} is the same for the h component (a); I_l / I_h is the ratio of the intensities of the l and h components (b); the positions of the maxima of the components (c); the spectral distance (splitting) between the maxima of the components (d); the half-widths of the components (e) and (f).

is proportional to I_{exc}^2). It is seen that the PL spectrum of a biexcitonic liquid should have a two-component structure. In the proposed model it is assumed that the shape and parameters of the dispersion curve are independent of temperature

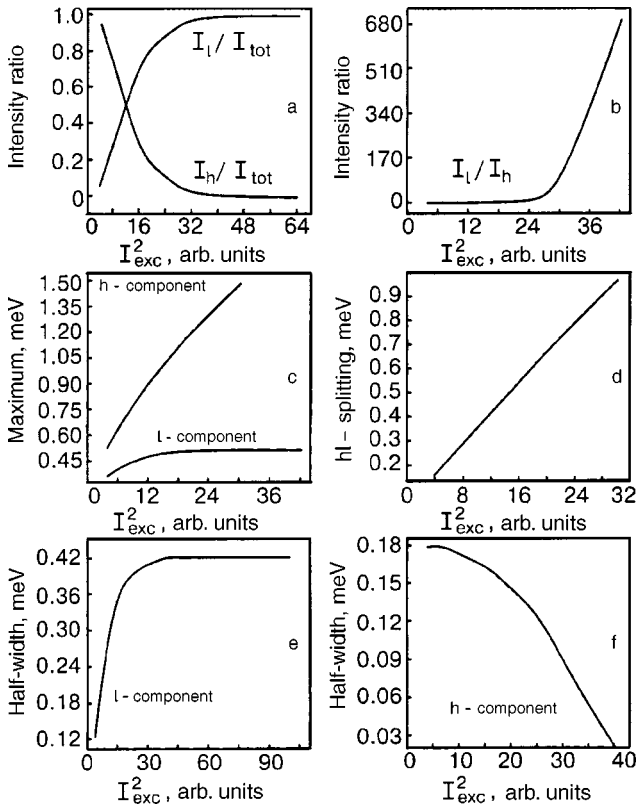

FIG. 4. Characteristics of the theoretical PL spectrum of a quantum biexcitonic liquid as functions of the square of the excitation intensity (density of the liquid). The notation is the same as in Fig. 2.

and depend only on the density of the liquid. The density of the liquid influences the shape of the dispersion curve and, through it, the shape of the PL spectrum. We used the following proportionalities relating the parameters of the dispersion curve and the density of the liquid (which is proportional to the square of the excitation intensity): average intermolecular distance $a \propto n^{-1/3} \propto I_{\mathrm{exc}}^{-2/3}$, sound velocity $u \propto n^{1/2} \propto I_{\mathrm{exc}}$, $k_0' a = \mathrm{const}$, and the modulus of the matrix element for the excitation transfer between molecules of the liquid $|M| \propto a^{-3} \propto I_{\mathrm{exc}}^2$.

In concluding this Section we must mention the following. A pronounced short-range order should be established in the system of biexcitons due to the substantial interaction between them; however, there is apparently no long-range order. The presence of short-range order ensures that relation (2) will apply at least in a qualitative way. On the other hand, because of the absence of long-range order in the case of a strong interaction between excitonic molecules, quasimomentum should not be conserved in optical transitions. This allows us to ignore the quasimomentum conservation law in the expression for the luminescence spectrum and to assume that the spectrum is completely determined by the shape of the dispersion curve.

EXPERIMENTAL DETAILS

We studied semiconducting single crystals of monoclinic zinc diphosphide of high purity, grown from the gas phase. The technology of the synthesis and growth of these crystals is described in Ref. 16. For excitation of the luminescence we used a cw Ar^+ laser (emission line 5145 Å).

During laser excitation the temperature of the crystal at the point of excitation differs substantially from the temperature of the external environment, i.e., of the helium bath surrounding the sample and the unilluminated region of the sample. This makes it impossible to use a thermosensor for precision temperature measurements, as one would get some averaged temperature. It was therefore necessary to use an internal temperature standard (ITS) that would make it possible to determine the temperature of the crystal at the point of excitation. For this standard we used the temperature dependence of the spectral position of the narrow, intense B line of the PL spectrum (the emission line of the free forbidden orthoexciton). Because of the variation of the energy gap E_g with changing temperature, the B line changes its spectral position (shifts to lower energy with increasing temperature). Since the shift of the B line with temperature is small $(dT/d\lambda_B = 3.625 K/\text{Å})$, for correct measurement we recorded a reference line of neon in the investigated spectral region simultaneously with the PL spectrum. This technique made it possible to determine the temperature of the sample at the point of excitation to an accuracy of 0.05 K.

BIEXCITONIC LIQUID IN β-ZnP_2 CRYSTALS. EXPERIMENTAL RESULTS AND DISCUSSION

At excitation intensities above 1 kW/cm^2 and temperatures below 5 K the PL spectrum of β-ZnP_2 crystals, as we have said, contains an emission line of the biexcitonic liquid (the C line, henceforth called the C spectrum). As we see from Figs. 5–9 the C spectrum has a two-component form,

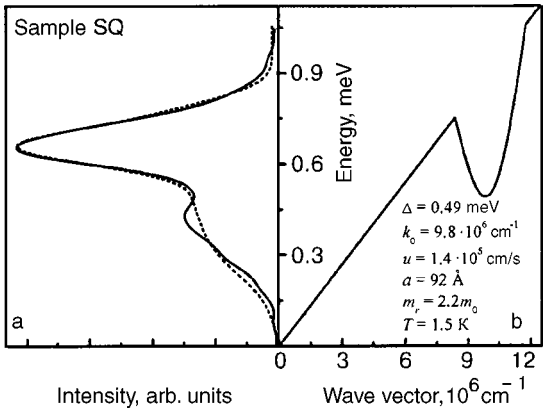

FIG. 5. Experimental PL spectrum of a biexcitonic liquid in a β-ZnP_2 crystal (solid curve) and its approximation by the theoretical spectrum (dashed curve) (a); the dispersion curve for the elementary excitations of the quantum biexcitonic liquid with the parameters obtained by fitting the theoretical PL spectrum to the experimental spectrum (b). Excitation intensity 3 kW/cm^2.

as was predicted by the model set forth above. Using the dispersion relation of elementary excitations of a biexcitonic liquid (3), we fit the experimental PL spectrum of the biexcitonic liquid (Fig. 5), which was obtained for a sample of high purity (excitation energy 3 kW/cm^2). This made it possible to determine the parameters of the dispersion curve of the elementary excitations: $\Delta = 0.49$ meV, $k_0 = 9.8 \times 10^6$ cm^{-1}, $u = 1.4 \times 10^5$ cm/s, and $m_r = 2.2 m_0$ (m_0 is the free electron mass), and also the value of the intermolecular distance in the liquid $a = 92\,\text{Å} = 6.1 a_{\mathrm{ex}}$ and the temperature of the crystal at the point of excitation, $T = 1.5$ K. The values obtained are physically reasonable, a fact which, in our view,

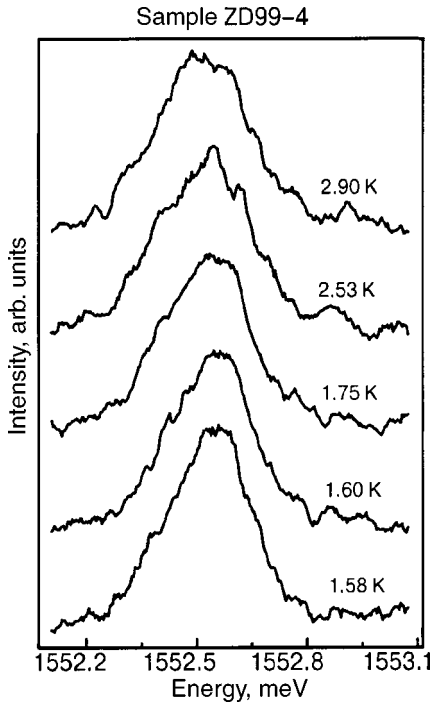

FIG. 6. Evolution of the experimental PL spectrum of a biexcitonic liquid in a β-ZnP_2 crystal under variation of the temperature of the sample at the point of excitation. Excitation intensity 4.8 kW/cm^2.

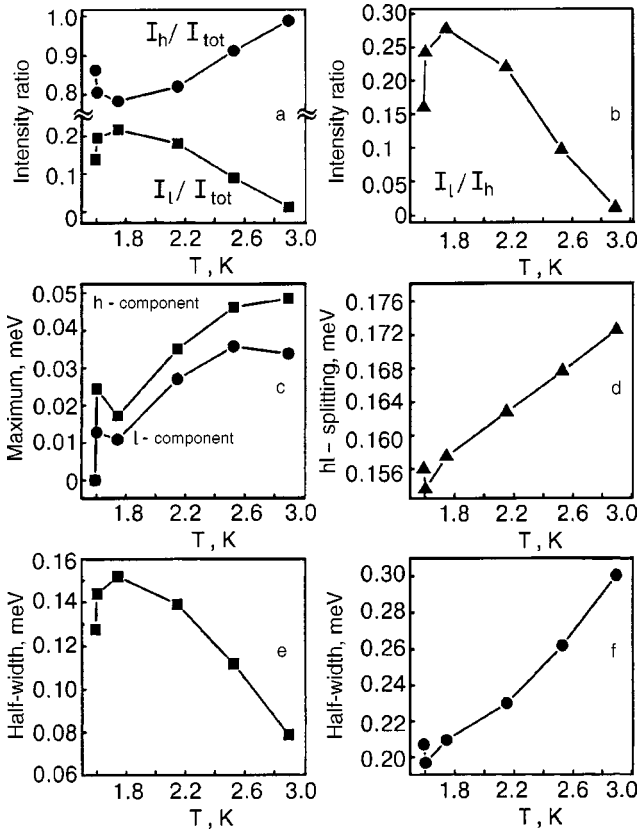

FIG. 7. Temperature dependence of the characteristics of the experimental PL spectrum of a biexcitonic liquid in a β-ZnP_2 crystal. The notation is the same as in Figs. 2 and 4. Plotted along the vertical axis in part Fig. 7c is the difference $[E_m(T)-E_b(T)]-[E_m(T_0)-E_b(T_0)]$, where E_m is the position of the maximum of the l or h component, and E_b is the position of the maximum of the narrow line of the forbidden free orthoexciton (B line), which was used to determine the temperature of the crystal at the point of excitation, and T_0 is the minimum temperature reached in the experiment.

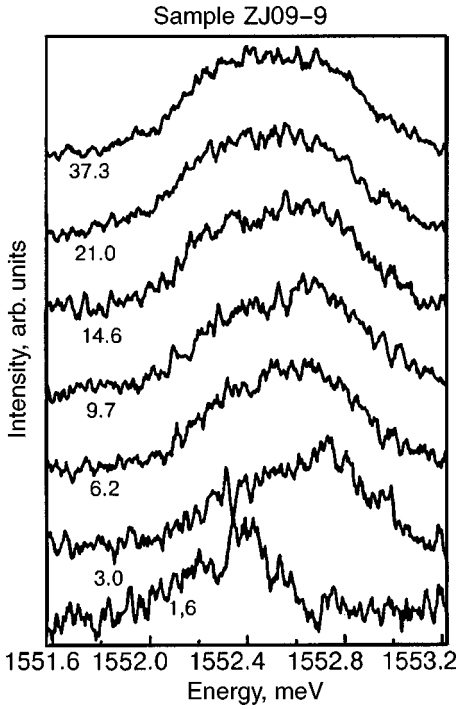

FIG. 8. Evolution of the experimental PL spectrum of a biexcitonic liquid in a β-ZnP_2 crystal under variation of the square of the excitation intensity. The curves are labeled by the value of I_{exc}^2 in $(kW/cm^2)^2$.

tends to confirm that the proposed theoretical model is correct. Further evidence of this is the good agreement of the experimental and theoretical spectra, in view of the approximate, model character of the dispersion curve given by Eqs. (3).

The evolution of the shape of the C spectrum and the behavior of its characteristics under variation of the temperature and the square of the excitation intensity are shown in Figs. 6–9. The behavior of the experimental spectrum under variation of the temperature (Figs. 6 and 7) is similar to that of the theoretical spectrum (Figs. 1 and 2). Analysis of the C spectrum under variation of the excitation intensity is made difficult by the fact that simultaneously with the variation of the excitation intensity there is also a change in temperature, which has a definite effect on the shape of the spectrum. In comparing Figs. 2, 4, and 9 we can conclude that the change in the C spectrum at moderate levels of excitation is probably due mainly to the influence of temperature (the rise in temperature with increasing I_{exc}), while at higher excitation intensities the evolution of the shape of the C spectrum occurs mainly on account of the increase in the density of the liquid with increasing I_{exc}. What we have said agrees with the intensity dependence of the temperature of the crystal at the point of excitation, shown in Fig. 10. Thus the experiment is described by the theory in a completely satisfactory way. The shape of the C spectrum can differ substantially for different samples. This is due to the fact that at the same values of the excitation intensity and crystal temperature, a liquid of higher density should arise in purer samples than in less pure samples. Consequently, the shape of the PL spectrum of the liquid varies with its density.

The results presented above suggest that a quantum biexcitonic liquid characterized by a phonon–roton dispersion relation for the elementary excitations can form in β-ZnP_2 crystals under certain conditions. This sort of dispersion relation, as we know, is evidence that superfluidity can arise in a Bose liquid, in particular, in liquid ^{4}He. Is it possible that superfluidity can arise in a biexcitonic liquid in a β-ZnP_2 crystal? To answer this question we performed the following experiments. For some of the samples (Fig. 10) we studied the temperature of the crystal at the point of excitation as a function of the intensity of the excitation. The normal situation is for the temperature of the crystal to increasing with increasing excitation intensity. Besides the normal monotonically increases behavior of $T(I_{exc}^2)$ (curve *1*), for several samples we obtained anomalous $T(I_{exc}^2)$ curves: decreasing (curve *2*) or nonmonotonic (curve *3*). We think that the anomalous $T(I_{exc}^2)$ curves can be explained by an anomalously large (giant) thermal conductivity, which accompanies the appearance of the superfluid (s) component in a quantum liquid below the superfluid transition. Such an effect is well known for superfluid He II. We propose the following explanation for the anomalous behaviors observed. At a certain excitation intensity the density of the liquid reaches values sufficient for a transition of the liquid to the superfluid state. Upon further increase in I_{exc} the density of the liquid increases, with the result that the temperature of the superfluid transition increases and, with it, the s-component fraction.

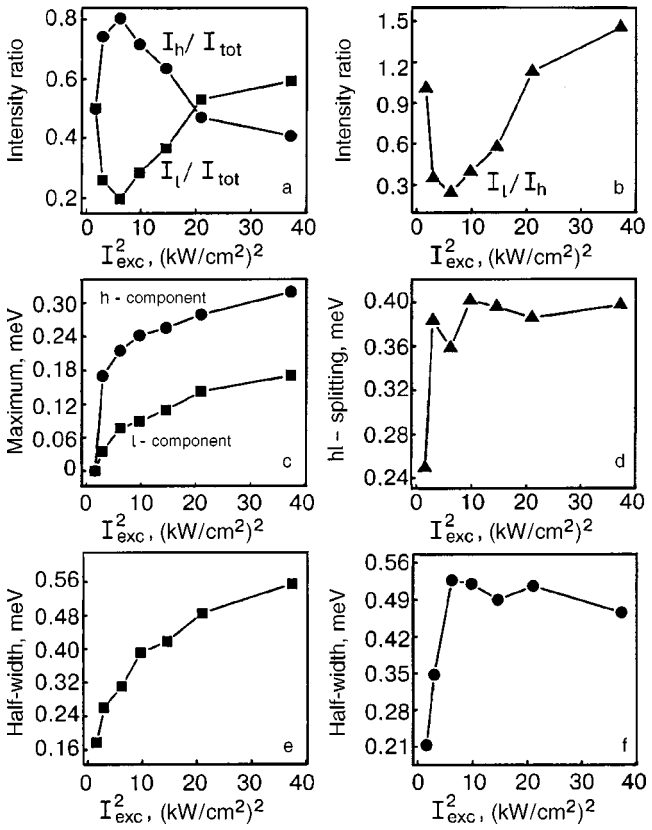

FIG. 9. Characteristics of the experimental PL spectrum of a biexcitonic liquid in a β-ZnP_2 crystal upon changes in the square of the excitation intensity. The notation is the same as in Figs. 2 and 4 and 7. Plotted along the vertical axis in Fig. 9c is the difference $[E_m(I^2_{exc})-E_b(I^2_{exc})]-[E_m(I^2_0)-E_b(I^2_0)]$, where E_m is the position of the maximum of the *l* or *h* component, E_b is the position of the maximum of the *B* line, and I_0 is the lowest excitation intensity used in the experiment.

This can increase the thermal conductivity, i.e., the thermal energy should be removed more efficiently from the excitation region of the crystal, and so the temperature of the crystal should decrease with increasing excitation intensity. Apparently those crystals with a monotonically decreasing $T(I^2_{exc})$ curve (curve *2* in Fig. 10) are the purest and most perfect: they have a low concentration of lattice defects, and therefore a biexcitonic liquid is formed in them with a sufficiently high density for the onset of superfluidity and the corresponding giant thermal conductivity. Those crystals with a nonmonotonic $T(I^2_{exc})$ curve (curve *3* in Fig. 10) would be less pure. The liquid formed in them is of a lower density but is nevertheless sufficient for the appearance of the *s* component. However, this component represents a smaller fraction than in the perfect crystals, and the giant thermal conductivity provides a sufficiently effective heat removal only up to certain values of the incoming laser power. When the power is increased further, the temperature of the crystal begins to grow. In those crystals with a monotonically increasing $T(I^2_{exc})$ curve (curve *1* in Fig. 10) the concentration of defects is rather high, and therefore the density of the liquid in them does not reach the values necessary for a transition to the superfluid state and the resulting onset of giant thermal conductivity. As a result, the temperature of the crystal at the point of excitation increases with increasing excitation intensity.

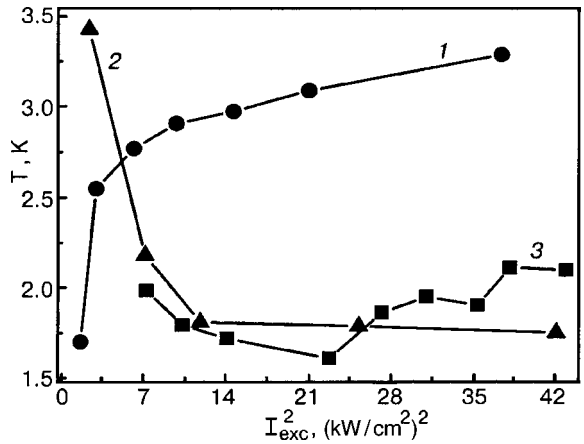

FIG. 10. Temperature of the crystal versus the square of the excitation energy for different samples: ZJ09-9 (*1*), ZJ09-14 (*2*), and ZD99-1 (*3*).

This study was supported in part by the Foundation for Basic Research of the Ministry of Scientific and Technological Affairs of Ukraine (Project No. 2.4/311).

†Deceased
*E-mail: yes@mail.univ.kiev.ua

[1)] In two-photon annihilation there is no recoil particle that could take an appreciable part of the momentum of the annihilating EM. For this reason, since the photon momentum is very small, momentum conservation allows two-photon decay only for an EM with $k \approx 0$, i.e., the two-photon PL line should be very narrow.[14] In two-electron (one-photon) transitions, in which only one exciton of a molecule annihilates, the second, surviving exciton can take an arbitrary quasimomentum, i.e., the one-photon PL lines are rather wide. This makes it possible to distinguish the two-photon PL lines of free biexcitons and of a biexcitonic liquid, unlike the case of the one-photon PL lines.

[1] L. D. Landau, Zh. Éksp. Teor. Fiz. **11**, 592 (1941).
[2] D. P. Feynman, Phys. Rev. **94**, 262 (1954).
[3] J. L. Yarnel, G. P. Arnold, P. J. Bandt, and E. C. Kerr, Phys. Rev. **113**, 1379 (1959).
[4] N. Peyghambarian, L. L. Chase, and A. Mysyrowicz, Phys. Rev. B **27**, 2325 (1983).
[5] A. V. Korolev and M. A. Liberman, Phys. Rev. Lett. **72**, 270 (1994).
[6] A. Mysyrowicz, E. Fortin, E. Benson, S. Fafard, and E. Hanamura, Solid State Commun. **92**, 957 (1994).
[7] P. H. Handel and C. Kittel, Proc. Natl. Acad. Sci. U.S.A. **68**, 3120 (1971).
[8] L. V. Keldysh, in *Proceedings of the 9th International Conference on the Physics of Semiconductors*, Moscow 1968, p. 1384.
[9] W. F. Brinkman and T. M. Rice, Phys. Rev. B **7**, 1508 (1973).
[10] I. S. Gorban, M. M. Biliy, I. M. Dmitruk, and O. A. Yeshchenko, Phys. Status Solidi B **207**, 171 (1998).
[11] I. S. Gorban, M. M. Biliy, I. M. Dmitruk, and O. A. Yeshchenko, Phys. Status Solidi B **191**, 337 (1995).
[12] I. S. Gorban, M. M. Biliy, I. M. Dmitruk, and O. A. Yeshchenko, Solid State Commun. **98**, 489 (1996).
[13] I. S. Gorban, M. M. Biliy, I. N. Dmitruk, and O. A. Yeshchenko, Ukr. Fiz. Zh. (Russ. Ed.) **41**, 840 (1996).
[14] I. S. Gorban, I. M. Dmitruk, and O. A. Yeshchenko, Solid State Commun. **98**, 941 (1996).
[15] I. Dmitruk, T. Goto, A. Kasuya, and Z. Yanchuk, submitted to Phys. Rev. B.
[16] I. S. Gorban', A. P. Krokhmal', and Z. A. Yanchuk, Fiz. Tverd. Tela (St. Petersburg) **41**, 193 (1999) [Phys. Solid State **41**, 170 (1999)].

Translated by Steve Torstveit

PHYSICAL PROPERTIES OF CRYOCRYSTALS

Phonon scattering by structural defects in solid p-H_2 and in p-H_2–o-D_2 solutions

O. A. Korolyuk,* B. Ya. Gorodilov, A. I. Krivchikov, and A. V. Raenko

B. Verkin Institute for Low Temperature Physics and Engineering, National Academy of Sciences of Ukraine, pr. Lenina 47, 61103 Kharkov, Ukraine

A. Jeżowski

W. Trzebiatowski Institute of Low Temperature and Structure Research, Polish Academy of Sciences, P.O. Box 937, 50-950 Wroclaw, Poland

(Submitted February 8, 2001)
Fiz. Nizk. Temp. **27**, 683–689 (June 2001)

A study is made of the influence of structural defects on the thermal conductivity in parahydrogen crystals and in parahydrogen–orthodeuterium solutions. The defects in the crystals are generated by means of a thermal shock. The temperature dependence of the thermal conductivity is analyzed in the framework of the Callaway relaxation model in the Debye approximation for the phonon spectrum with allowance for phonon–phonon scattering processes and Rayleigh scattering on isotopic defects and structural defects such as dislocations and low-angle boundaries. The effect produced in the sample by the thermal shock is found to depend on the deuterium concentration. In pure parahydrogen an increase in the dislocation density is observed, and in parahydrogen–orthodeuterium solutions an increase in the density of low-angle boundaries. The change in the density of low-angle boundaries in the solutions after the thermal shock depends linearly on the concentration of o-D_2. [DOI: 10.1063/1.1382995]

INTRODUCTION

Structural defects have a strong influence on the properties of simple molecular crystals having a van der Waals type of interaction (cryocrystals). There is published research on the plastic deformation of solidified inert gases and crystalline hydrogen[1,2] and on the influence of structural defects on the thermal conductivity of cryocrystals.[3–5] At present there is still an open question as to the factors that influence the formation of the dislocation structure in a crystal.

The presence of stacking faults in a lattice can be assessed from the character of the temperature dependence of the thermal conductivity of the crystal. The behavior of the thermal conductivity is governed by the frequency dependence of the relaxation time of the phonons participating in scattering processes on structural defects. Depending on the density of dislocations in the crystal, they can be treated either as individual simple scattering centers that do not interact with one another or as dislocation walls (low-angle boundaries), which divide the crystal into subgrains.[6–8] The frequency dependence of the phonon relaxation time will be different in each case.

In this paper we present the results of a study of how structural defects formed as a result of thermal stresses affect the thermal conductivity of crystalline samples of pure parahydrogen and of parahydrogen–orthodeuterium solutions.

EXPERIMENT

Measurements of the thermal conductivity at temperatures ranging from 1.5 K to the melting temperature of the sample were carried out by a modified thermal potentiometer method.[9]

A sample of parahydrogen (7.0 mm in diameter and 75 mm long) was investigated the measurement cell described in Ref. 10 in the temperature interval from 1.5 to 12 K. Samples of a p-H_2-o-D_2 solid solution with o-D_2 concentrations $c=0.001$, 0.05, 0.1, and 0.2 were investigated at temperatures from 1.8 K to the melting temperature in a new measurement cell. A diagram of the low-temperature cell is shown in Fig. 1. The ampoule for growth of the crystal and for measurement of its thermal conductivity is a stainless-steel tube *1* with an inner diameter of 4.6 mm. Thermometers *2* and *3* (TSU-2, made by the All-Russia Scientific-Research Institute of Physicotechnical and Radio Engineering Measurements, Moscow) were placed on the outer surface of the tube, 20 mm apart. The upper part of the tube contains a heater *4* for producing a heat flux along the sample. The lower part of the tube is mounted to a cooled copper block *5* with a heater and a temperature sensor *6*. The cooling of the copper block *5* was done with a Wheatley chamber combined with a heat exchanger *7*. In the interval range 5–300 K helium vapor from a helium bath *8* enters the chamber *7* along a tube *9* with a diameter of 1 mm. The flow of helium vapor into the heat exchanger is regulated by a low-temperature valve *10*. To obtain temperatures below 5 K the

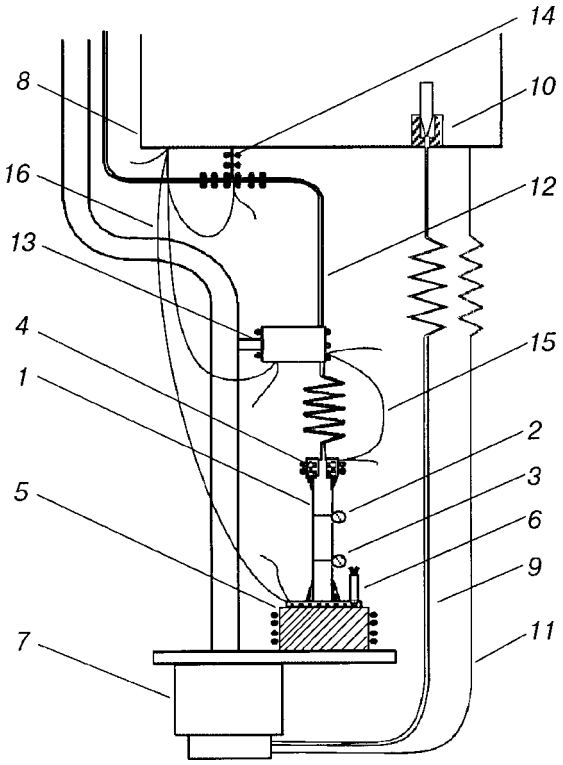

FIG. 1. Diagram of the low-temperature measurement cell: *1*—ampoule for growing the sample; *2,3*—TSU-2 thermometers; *4*—gradient sample heater; *5*—heat sink; *6*—temperature sensor; *7*—Wheatley chamber combined with a heat exchanger; *8*—helium bath; *9*—capillary; *10*—low-temperature valve; *11*—throttle; *12* inlet capillary for the gas under study; *13*—copper block; *14*—capillary heater; *15*—(Au+Fe)–Cu differential thermocouple; *16*—Manganin–Constantan thermocouples.

valve *10* was closed off, and helium from the helium bath entered through a throttle *11*. The filling of the cell by the substance to be studied was done with the use of a capillary inlet *12* connected to the upper part of the ampoule *1* for growing the sample. The temperature of the capillary inlet was monitored both during the growth of the crystal and during measurement of the thermal conductivity of the sample with the use of a copper block *13* and a capillary heater. The temperature of the capillary was monitored by an (Au+Fe)–Cu differential thermocouple (*15*) and Manganin–Constantan thermocouples *16*. In the thermal conductivity measurements, in order to eliminate the leakage of heat from the sample heater through the inlet capillary and the conducting leads of the heater and thermocouple, the temperature of the copper block *13* was set equal to the temperature of the gradient heater *4*. The low-temperature cell was surrounded by a radiation shield.

The growth of a crystalline sample and measurement of its thermal conductivity was a completely automated process. The measurement process was controlled by a personal computer.

The hydrogen for the experiment was cleaned with a palladium filter. The concentration of chemical impurities in the cleaned hydrogen was not above 1×10^{-7}, and the concentration of isotopic impurity was at the natural level of around 1×10^{-4}. The initial deuterium gas had a chemical purity of 99.67%. Parahydrogen containing 0.21% orthohydrogen and orthodeuterium containing 2% paradeuterium were obtained by catalytic conversion of $Fe(OH)_3$ at a temperature near 20 K.[9]

Solid solutions with a low concentration of structural defects were grown, annealed, and cooled by a technique which made it possible to obtain reproducible results on samples of good quality.[10] The crystals were grown directly from the gas phase at a temperature slightly below the melting temperature.

The thermal deformation procedure (thermal shock) was as follows. At 4–5 K the temperature of the upper part of the crystal was sharply raised almost to the melting temperature by means of the gradient heater. This produced a gradient of 2–3 K/cm along the sample. Then the gradient heater was turned off, and the temperature along the crystal rapidly equalized to its original value (4–5 K). This whole procedure took 5–6 min. Structural defects were produced on account of the plastic deformation of the sample under the influence of the thermal stresses and to the deformation arising because of the difference in the coefficients of thermal expansion of the sample and the cell in which it was located.

The relative random error for the thermal conductivity measurement was not over 2% in the entire temperature interval investigated except for temperatures below 2 K, where it was around 5% as a result of the lower temperature gradient produced. The combined error in the thermal conductivity measurements was not over 10% and was mainly due the error in the determination of the geometric parameter of the measurement cell. The error in the determination of the concentration was less than 15% of the indicated value of the concentration.

RESULTS

Figure 2 shows the temperature dependence of the thermal conductivity $K(T)$ for a sample of pure p-H_2 before and after the thermal shock. Before the thermal shock the thermal conductivity displayed the typical behavior for a perfect insulator crystal, with a distinct maximum at $T=3.0$ K and a temperature dependence $K(T)\propto T^3$ below the maximum. After the thermal shock the value of the thermal conductivity at the maximum decreased by a factor of 3, and its temperature

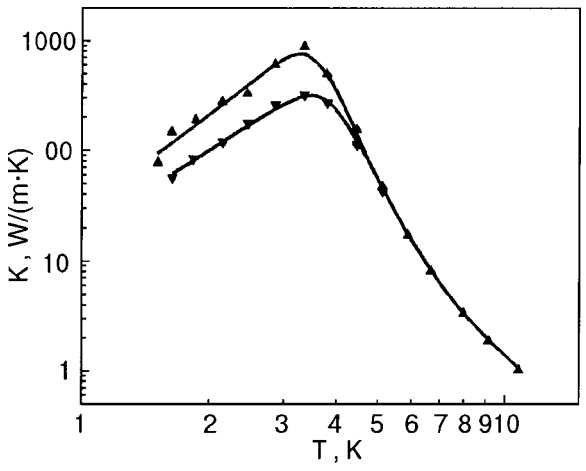

FIG. 2. Temperature dependence of the thermal conductivity K of pure parahydrogen before (▲) and after (▼) the thermal shock; the solid curves show the result of a fitting by the Callaway formula.

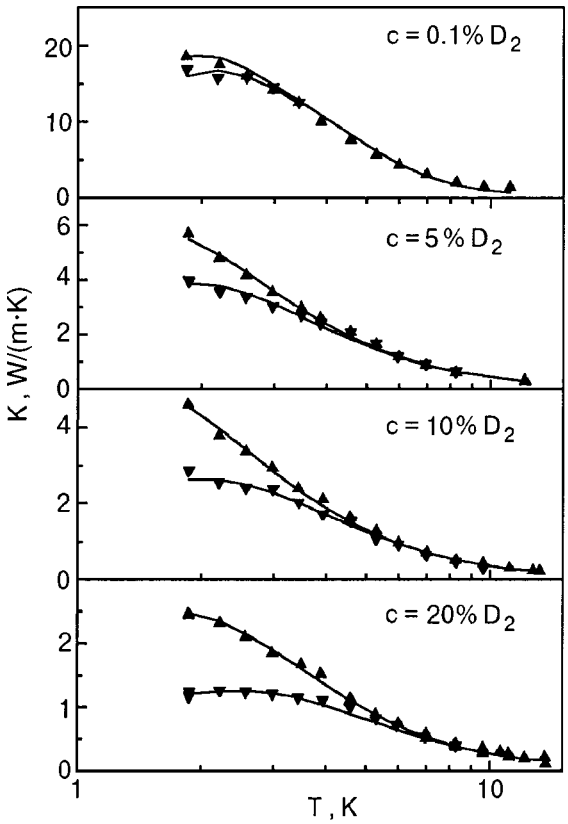

FIG. 3. Temperature dependence of the thermal conductivity of a p-H_2–o-D_2 solution for o-D_2 concentrations $c=0.001$; 0.05, 0.1, and 0.2: ▲—immediately after growth of the sample (growth from the gas for 300 min, annealing, and slow cooling); ▼—the same sample after a thermal shock; the solid lines show the calculated curves.

dependence to the left of the maximum became weaker than T^3. At temperatures in the region where phonon–phonon scattering processes are dominant, the curves of the thermal conductivity obtained before and after the thermal shock are the same.

For the p-H_2–o-D_2 solutions the temperature dependence of the thermal conductivity prior to the thermal shock was governed mainly by impurity scattering of phonons. After the thermal shock the thermal conductivity of the solutions at 1.8 K decreased by a factor of 1.5–2. The difference between the thermal conductivity curves before and after the thermal shock became smaller as the temperature was raised, and above a certain temperature these curves practically coincide. This means that the thermal shock does not destroy the continuity of the samples, in contrast to the data of Ref. 3, where the thermal conductivity of a ^{4}He crystal after a thermal shock decreased in the entire temperature interval investigated. The results of the measurements of the thermal conductivity of the solutions before and after the thermal shock are presented in Fig. 3.

ANALYSIS AND DISCUSSION

The analysis of the experimental data was done in the framework of the Callaway model with allowance for the normal phonon–phonon scattering processes (N processes).[11] The inverse relaxation time of the N processes were described by the expression[12]

$$\tau_N^{-1}(x,T)=A_N x^2 T^5,$$

where $x=\hbar\omega/kT$ and ω is the phonon frequency.

The relaxation rates of the following resistive processes were taken into account:

—phonon–phonon scattering (U processes):

$$\tau_U^{-1}(x,T)=A_U x^2 T^3 e^{(-E/T)};$$

—Rayleigh scattering of phonons on impurities (D_2 molecules):

$$\tau_{\text{imp}}^{-1}=\frac{\Gamma V}{4\pi s^3}\omega^4;$$

—scattering of phonons on the boundaries of the crystalline grains:

$$\tau_b^{-1}=s/L,$$

where V is the volume of the unit cell of the crystal lattice, Γ is a parameter characterizing the properties of the impurity scattering center (it takes into account the relative change of the mass at the impurity site, the lattice distortion, and the change in the interaction constants),[10] s is the speed of sound, and L is the mean grain size.

The values of the parameters A_U and E for phonon–phonon U processes in pure parahydrogen agreed with the values obtained in Ref. 10: $A_U=5.69\times10^7\ \text{s}^{-1}\text{K}^{-3}$, $E=36.57$ K. The values of the parameter A_N that determines the intensity of the normal scattering processes for pure parahydrogen was taken from Ref. 9 ($A_N=6.7\times10^4\ \text{s}^{-1}\text{K}^{-5}$). For the solutions the intensity of the normal scattering processes (A_N) was calculated from the expression[12]

$$A_N\approx 991.6\frac{\hbar\gamma^2 N_A^{5/3}}{\mu V^{2/3}\Theta^5},$$

where μ is the molar mass, γ is the Grüneisen constant, N_A is Avogadro's number, and Θ is the Debye temperature. It was taken into account that Θ and V are functions of the concentration c. The Debye temperature for the solution was calculated according to the procedure proposed in Ref. 13:

$$\Theta(c)=\Theta(0)\left(\frac{V(0)}{\overline{V}}\right)^{\gamma}\left(\frac{M(0)}{\overline{M}}\right)^{1/2},$$

where $\overline{V}$ and $\overline{M}$ are the mean molar volume and mass of the solution, which depend on the deuterium concentration:

$$\overline{V}=cV_{D_2}+(1-c)V_{H_2},$$

$$\overline{M}=cM_{D_2}+(1-c)M_{H_2}.$$

The average speed of sound in the solutions was calculated from the Debye temperature. For pure parahydrogen the following characteristic parameters were used: $\Theta=118.5$ K, $s=1340$ m/s, $V=23.06\ \text{cm}^3$/mole, and $\gamma=2$.

The relaxation of the phonons on account of structural defects depends on the type and number of defects and their spatial configuration. The rate of relaxation of the phonons due to the stress fields of individual dislocations is usually calculated from the expression[14]

TABLE I. The parameters found as a result of a fitting of the calculated curves to the experimental data. The first row for each concentration corresponds to the thermal conductivity of the sample before the thermal shock, the second row (sh) to after. The values of N_D were calculated from Eq. (2) on the assumption that $d=50b$. The column labeled $\tau_{b,\mathrm{sh}}^{-1}-\tau_b^{-1}$ gives the rate of relaxation on individual dislocations at 2 K for pure p-H_2 after the thermal shock.

$c_{o\text{-}D_2}$	τ_b^{-1}, $10^6\ \mathrm{s}^{-1}$	L, mm	$\tau_{b,\mathrm{sh}}^{-1}-\tau_b^{-1}$, s^{-1}	N_{disl}, $10^8\ \mathrm{cm}^{-2}$	N_D, $10^{11}\ \mathrm{s}^{-2}$	Γ
0	1.14	1.18	–	–	–	0
0(sh)	1.14	1.18	4.27×10^5	2.9	–	0
0.001	3.1	0.433	–	–	–	0.0018
0.001(sh)	4.59	0.292	1.49×10^6	–	4.11	0.0018
0.05	1.11	1.187	–	–	–	0.0828
0.05(sh)	4.93	0.269	3.82×10^6	–	4.46	0.0828
0.1	0.642	2.042	–	–	–	0.1737
0.1(sh)	4.48	0.293	3.838×10^6	–	4.10	0.1737
0.2	0.993	1.294	–	–	–	0.4682
0.2(sh)	10.5	0.122	9.507×10^6	–	9.82	0.4682

$$\tau_D^{-1}(\omega)=N_{\mathrm{disl}}(\gamma b)^2\omega, \tag{1}$$

where N_{disl} is the density of dislocations and b is the Burgers vector; for hydrogen $b=3.75\times10^{-10}$ m.

The adjustable parameters used to fit the calculated curves were the phonon mean free path L for scattering on boundaries, the Rayleigh scattering parameter Γ for each concentration of o-D_2, and the density of dislocations N_{disl}. The thermal conductivity of a sample of pure parahydrogen not subjected to thermal shock was described using two resistive scattering processes (scattering on boundaries and phonon–phonon scattering). For a description of the thermal conductivity after the thermal shock it was necessary to take into account the scattering of phonons by dislocations (formula (1)). After the thermal shock the dislocation density obtained from the fitting procedure was $N_{\mathrm{disl}}=2.9\times10^8\ \mathrm{cm}^{-2}$.

In the analysis of the data for the solid solutions prior to thermal shock the Rayleigh scattering on impurity molecules was taken into account in addition to the boundary and phonon–phonon scattering. The parameter Γ characterizing the intensity of this scattering was determined for all the samples not subjected to thermal shock. Its values remained the same for the samples after thermal shock. The experimental curves of the thermal conductivity of the solutions subjected the thermal shock could not be described by expression (1) as they could in the case of pure parahydrogen. These curves can be explained by a growth of the contribution from the frequency-independent scattering of phonons (scattering on boundaries). The results of a fitting are shown by the solid curves in Figs. 2 and 3. The best-fit parameters L, Γ, and N_{disl} before and after the thermal shock are presented in Table I. For a given concentration, the first line gives the thermal conductivity of the sample before the thermal shock, and the second line the value after the thermal shock.

It follows from the above analysis that the main cause of the difference in the thermal conductivity curves of the p-H_2–o-D_2 solutions before and after thermal shock is due to a scattering mechanism whose contribution is proportional to T^3. Good agreement (see Fig. 3) is obtained between the calculated curves and the experimental data. It follows from the calculation that after the thermal shock the intensity of phonon scattering on boundaries in the impure samples is increased severalfold (see Table I). In the general case the sources of such phonon scattering can be both the outer boundaries of the sample and grain boundaries, and dislocations bunched into regular rows that interact with one another (low-angle boundaries).[8] Deuterium impurity molecules are pinning centers for dislocations and thereby stimulate the generation of dislocations in the crystal when it is deformed. The increase in the intensity of scattering on boundaries upon the thermal shocking of impure samples can be interpreted as the formation of new dislocation walls, which divide the crystal into a large number of subgrains. The formation of low-angle boundaries is characteristic for an impure crystal during its polygonization (microcrystallization). If the distance d between dislocations in a dislocation wall is much shorter than the phonon wavelength, then the rate of relaxation of phonons at such a defect is independent of frequency and will be described by the expression[14]

$$\tau_\varepsilon^{-1}=\frac{N_D s(\gamma b)^2}{36d}, \tag{2}$$

where d is the distance between dislocations in the dislocation wall, and N_D is the effective density of dislocations. If the wavelength becomes small compared to the distance d, the dislocations will scatter the phonons independently, and expression (2) goes over to (1) if s is replaced by ωd. For the crystals studied the condition that the phonon wavelength be sufficiently large holds throughout the entire existence region. Therefore, such a phonon scattering mechanism is entirely probable, as is confirmed by the results of the above analysis of the experimental data.

Table I gives the values of N_D calculated on the assumpiton that $d=50b$ (the value usually used for analysis in similar situations[3,8,15]). The values of N_D are quite large and correspond to crystals that have been subjected to plastic deformation. It should be kept in mind that the N_D are certain effective densities of dislocations in the sample which are determined from the fitting of the experimental data and which are related to the numerical coefficients determined in Ref. 16 for the case of phonon scattering by the stress field around an isolated dislocation. At the same time, they are in complete agreement with the values of the dislocation densities obtained in experiments on the plastic deformation of

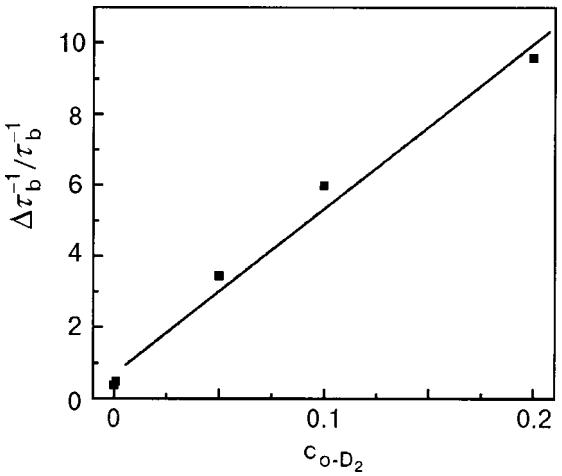

FIG. 4. Concentration dependence of the relative change in intensity of scattering on boundaries as a result of a thermal shock for p-H_2–o-D_2 solutions.

normal hydrogen.[2] Unfortunately, the only study that we know of on the scattering of phonons by a dislocation wall[17] does not give the expression that may have been used for the phonon relaxation times in the analysis of the experimental results on the thermal conductivity.

In the case of pure parahydrogen, which is a highly plastic crystal, the thermal deformation leads to the formation of isolated dislocations with a density of the order of 10^8 cm^{-2}. Since the impurity molecules are pinning centers for dislocations, the dislocation structure of the sample depends on the concentration of deuterium molecules. In the case of the solution of hydrogen with deuterium the crystal becomes stiffer and the formation of low-angle boundaries occurs. Figure 4 shows how the change in intensity of the boundary scattering before and after the thermal shock depends on the concentration of the orthodeuterium impurity. The data correspond completely to a linear dependence. Probably the density of low-angle boundaries is directly proportional to the concentration of impurity orthodeuterium.

We note one more difference between crystals with and without impurities. The density of dislocations for the pure crystal after thermal shock corresponds to the case of its elastic straining. At the same time, for samples containing impurities the density of dislocations attests to a plastic deformation regime, and so the impurity makes the crystal stiffer.

Thus the result of the action of thermal stresses on a sample depends on the concentration of deuterium impurity molecules. In the case of a sample with the minimum possible deuterium content (pure p-H_2) the result of the action of the stresses is the generation of a large number of individual dislocations, while in the case of the H_2–D_2 solutions it is an increase in the density of low-angle boundaries.

This study was supported in part by the Ukrainian Ministry of Education and Science (Project No. 2M/74-2000 in the framework of a Ukrainian–Polish cooperation).

The authors thank Prof. V. G. Manzhelii, Academician of the National Academy of Sciences of Ukraine, for his steady interest and support of this study. We also thank Prof. R. Pohl, Prof. H. Meyer, and Dr. K. A. Chishko for a helpful discussion.

*E-mail: korolyuk@ilt.kharkov.ua

[1] Yu. E. Stetsenko, D. N. Bol'shutkin, L. A. Indan, and A. A. Khudoteplaya, Fiz. Tverd. Tela (Leningrad) **14**, 187 (1972) [Sov. Phys. Solid State **14**, 149 (1972)].
[2] D. N. Bol'shutkin, Yu. E. Stetsenko, and L. A. Alekseeva, Fiz. Tverd. Tela (Leningrad) **12**, 151 (1970) [Sov. Phys. Solid State **12**, 119 (1970)].
[3] A. A. Levchenko and L. P. Mezhov-Deglin, Zh. Éksp. Teor. Fiz. **82**, 278 (1982) [Sov. Phys. JETP **55**, 166 (1982)].
[4] A. A. Golub and S. V. Svatko, Fiz. Nizk. Temp. **7**, 413 (1981) [Sov. J. Low Temp. Phys. **7**, 203 (1981)].
[5] R. M. Kimber and S. J. Rogers, J. Phys. C **6**, 2279 (1973).
[6] A. H. Cottrel, *Theory of Dislocations* [Gordon and Breach, New York (1964); Mir, Moscow (1969)].
[7] M. Omini and A. Sparavigna, Phys. Rev. B **61**, 6677 (2000).
[8] V. A. Osipov and S. E. Krasavin, J. Phys.: Condens. Matter **10**, L639 (1998).
[9] T. N. Antsygina, B. Ya. Gorodilov, N. N. Zholonko, A. I. Krivchikov, V. G. Manzhelii, and V. A. Slyusarev, Fiz. Nizk. Temp. **18**, 417 (1992) [Sov. J. Low Temp. Phys. **18**, 283 (1992)].
[10] B. Ya. Gorodilov, O. A. Korolyuk, A. I. Krivchikov, and V. G. Manzhelii, J. Low Temp. Phys. **119**, 497 (2000).
[11] J. Callaway, Phys. Rev. **122**, 787 (1961).
[12] O. A. Korolyuk, B. Ya. Gorodilov, A. I. Krivchikov, and V. V. Dudkin, Fiz. Nizk. Temp. **26**, 323 (2000) [Low Temp. Phys. **26**, 235 (2000)].
[13] M. I. Bagatskii, I. Ya. Minchina, V. G. Manzhelii, P. I. Muromtsev, A. I. Krivchikov, and V. S. Parbuzin, Fiz. Nizk. Temp. **16**, 1009 (1990) [Sov. J. Low Temp. Phys. **16**, 589 (1990)].
[14] B. M. Mogilevskiĭ and A. F. Chudnovskiĭ, *Thermal Conductivity of Semiconductors* [in Russian], Nauka, Moscow (1972).
[15] D. Hull, *Introduction to Dislocations* [Pergamon Press, Oxford–New York (1965); Atomizdat, Moscow (1968)].
[16] P. G. Klemens, Proc. Phys. Soc., London, Sect. A **68**, 1113 (1955).
[17] K. A. Chishko, Metallofizika (Kiev) **7**, 12 (1985).

Translated by Steve Torstveit

SUPERLOW TEMPERATURES TECHNIQUES

The influence of small impurities of ^{4}He on the melting curve of ^{3}He

A. N. Ganshin, V. N. Grigor'ev, V. A. Maĭdanov, A. A. Penzev, E. Ya. Rudavskiĭ,*
A. S. Rybalko, and E. V. Syrnikov

B. Verkin Institute for Low Temperature Physics and Engineering, National Academy of Sciences of Ukraine, pr. Lenina 47, 61103 Kharkov, Ukraine
(Submitted February 9, 2001)
Fiz. Nizk. Temp. **27**, 690–692 (June 2001)

The melting curve of ^{3}He containing a small ^{4}He impurity is measured in the temperature range 20–600 mK. It is found that the coordinates of the minimum of the melting curve are shifted, that hysteresis appears, and that the slope of the melting curve at low temperatures is changed. The data obtained agree with a calculation that takes into account the change in the coordinates of the minimum due to the entropy of mixing of the ^{3}He–^{4}He solution. The results of the experiment are used to estimate the error arising when the melting curve of ^{3}He is used to determine the temperature. © *2001 American Institute of Physics.*
[DOI: 10.1063/1.1382996]

Thermometers based on measurement of the melting curve of ^{3}He are now widely used in the physics laboratory for temperatures in the millikelvin range. The idea of using the melting curve of ^{3}He as a sensitive thermometer for ultralow temperatures belongs to Scribner and Adams,[1] who noticed that the relation between the pressure and temperature at melting of ^{3}He is universal and can be measured to high accuracy. Straty and Adams[2] developed a technique of precise measurement of the pressure at low temperatures by means of a capacitive membrane pickup, refined modifications of which are widely used for thermometry based on the melting curve of ^{3}He.

An important advantage of thermometers based on measurement of the melting curve of ^{3}He (crystallization thermometers) is the presence of three reliable reference points on the melting curve: a clear minimum, a point of transition of normal ^{3}He the superfluid *A* phase, and a point of transition of solid ^{3}He to a magnetically ordered state. By now all of the singular points on the melting curve of ^{3}He have been well determined, reconciled with one another, and constitute a practical temperature standard in the range from 1 mK to 1 K.[3,4]

In spite of the widespread application of crystallization thermometers, there has remained an unanswered question as to the possible influence of ^{4}He impurities on the melting curve of ^{3}He. This question is especially topical because ^{3}He of ''commercial purity'' usually contains 0.2–0.6% ^{4}He. In Ref. 5 an estimate was made of the effect of ^{4}He impurities on the coordinates of the minimum of the melting curve of ^{3}He. It was assumed that the main role in the shift of the position of the minimum, which is known to arise where the entropies of the liquid and crystal are equal, is played by the entropy of mixing of the solution. However, these estimates could not be checked because of a lack of experimental data. The solidification curves of ^{3}He–^{4}He solutions have been well studied only at large ^{4}He concentrations (10–100%) and in the region of high temperatures up to 0.3 K.[6–8]

At impurity concentrations in the range 1–2% there should be noticeable effects at millikelvin temperatures, since, on the one hand, separation of both the solid and liquid solutions should occur, and, on the other hand, the solidification pressure and the melting pressure for solid solutions do not coincide. Therefore, it is advisable to check the degree to which small impurities of ^{4}He deform the melting curve of ^{3}He in the millikelvin temperature range.

In the experiment we used two crystallization thermometers placed on the same copper slab of a dissolution chamber. In one of the thermometers pure (99.99%) ^{3}He was used as the working substance, and in the other, ^{3}He containing $\sim$2.1% ^{4}He in the gas phase.

The low-temperature part of the experimental apparatus used in this study is described in detail in Ref. 6. The pressure was changed by means of a General Radio 1615-A capacitive bridge, and the temperature was determined from the melting of the pure ^{3}He with the use of the polynomial proposed in Ref. 3. Also placed on the slab of the dissolution chamber were several resistance thermometers which had been calibrated with the crystallization thermometer. The temperature range investigated was 20–700 mK.

After blocking off the capillaries of the crystallization thermometers containing pure ^{3}He and a solution with 2.1% ^{4}He, the temperature was lowered in small steps, the temperature-stabilizing system was turned on, and the equilibrium pressure in each pickup was measured. The hold time at each temperature step was 40–60 min. Measurements were made both on cooling and heating. The results are presented in Fig. 1.

It can be clearly seen that the melting–solidification curve of ^{3}He containing ^{4}He impurities has a number of important differences from the melting curve of pure ^{3}He:

—The results of the pressure measurements made on cooling differ appreciably from the data obtained on heating

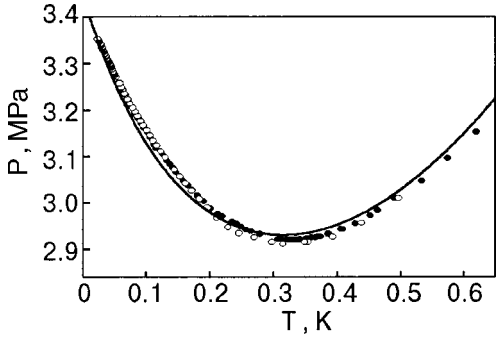

FIG. 1. Melting curve of a ^{3}He–^{4}He solution containing 2.1% ^{4}He: ○ — cooling, ● — heating. The solid line is the melting curve of pure ^{3}He (Ref. 3).

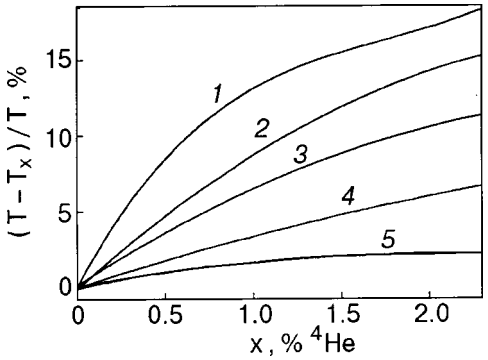

FIG. 3. Relative error in measurement of the temperature using the melting curve of ^{3}He containing ^{4}He with concentration x at $T=60$ (*1*), 100 (*2*), 200 (*3*), 300 (*4*), and 400 (*5*) mK.

in the range 180–480 mK; the maximum disparity is observed in the region of the minimum—around 0.1 atm. This is because, as we have said, the melting pressure in a solution does not coincide with the solidification pressure.

—The pressure at which the minimum is observed on the melting–solidification curves is much lower than for pure ^{3}He.

—The position of the minimum is shifted appreciably to higher temperatures.

—At low temperatures the slope of the melting curve of the solution begins to differ noticeably from that for pure ^{3}He.

For a more precise determination of the position of the minimum, Fig. 2 shows the results of the measurements for pure ^{3}He and for the isotopic solution on an expanded scale for the region near the minimum. The minimum on the melting curve of the solution is observed at $T=333$ mK, which is substantially higher than for pure ^{3}He (315 mK), i.e., the temperature of the minimum for the solution under study is shifted by 18 mK to higher temperatures, while the pressure at the point of the minimum is shifted lower by $\sim 10^4$ Pa as compared to $P_{\min}$ for pure ^{3}He. These results can be compared with the estimates of the influence of ^{4}He impurities on the position of the minimum of the melting curve of ^{3}He which were made in Ref. 5, where the shift of the minimum of the pressure due to the change in the entropy of mixing is given as

$$\Delta P_{\min} = \alpha\, x T. \tag{1}$$

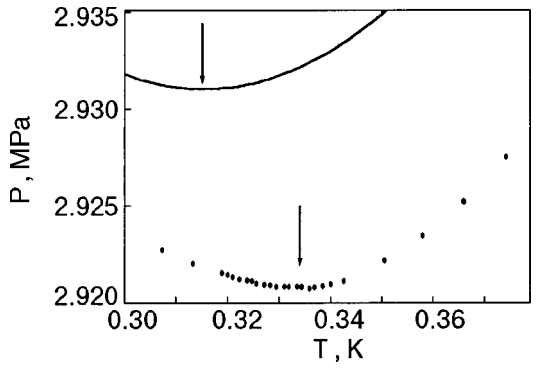

FIG. 2. Melting curve in the region of the minimum; the points were obtained on heating of a solution containing 2.1% ^{4}He, the curve is for pure ^{3}He.

Here x is the ^{4}He concentration, $\alpha = 7\times 10^6$ Pa/K, and T is the temperature, and the corresponding change in the temperature of the minimum is

$$T'_{\min} = T_{\min} + \alpha x/2b, \tag{2}$$

where $b = 3.8\times 10^6$ Pa/K^2. Estimates according to formulas (1) and (2) for the solution investigated here give $\Delta P_{\min} = 4\times 10^4$ Pa and $\Delta T_{\min} = 18$ mK, in agreement with our experimental data.

Thus the presence of ^{4}He impurities (with concentration x) in ^{3}He will cause the measured temperature T_x to differ from the real temperature T by an amount $\Delta = T - T_x$. The resulting relative error in the determination of the temperature is presented in Fig. 3. Here it was assumed that, in accordance with formulas (1) and (2), the shifts of the coordinates of the minimum $\Delta P_{\min}$ and $\Delta T_{\min}$ for the solution relative to pure ^{3}He are proportional to the ^{4}He concentration. The deviation of the melting curve of the solution from the melting curve of pure ^{3}He was also taken into account over the entire temperature interval. Figure 3 may be used to estimate the error of a temperature determination by means of a crystallization thermometer if the working substance contains a ^{4}He impurity.

*E-mail: rudavskii@ilt.kharkov.ua

[1] A. A. Scribner and E. D. Adams, Rev. Sci. Instrum. **41**, 287 (1970).
[2] G. C. Straty and E. D. Adams, Rev. Sci. Instrum. **40**, 1393 (1969).
[3] G. Shuster, A. Hoffmann, and D. Hechtfisher, in *Comite Consultatif de Thermometrie, Toward an International Temperature Scale from 0.65 K to 1 mK*, Leiden (1998), p. 27.
[4] J. S. Xia, E. D. Adams, and W. Ni, in *Comite Consultatif de Thermometrie, Toward an International Temperature Scale from 0.65 K to 1 mK*, Leiden (1998), p. 21.
[5] J. Bremer, *Noise Thermometry and the* ^{3}He *Melting Curve Below 1 K*, Ph.D. Thesis, Leiden (1992).
[6] K. N. Zinov'eva, Zh. Éksp. Teor. Fiz. **44**, 1837 (1963) [Sov. Phys. JETP **17**, 991 (1963)].
[7] C. Le Pair, K. W. Taconis, R. De Bryun Ouboter, P. Das, and E. Delong, Physica (Utrecht) **31**, 764 (1965).
[8] P. H. Tedrow and D. H. Lee, Phys. Rev. **181**, 399 (1969).
[9] A. N. Gan'shin, V. N. Grigor'ev, V. A. Maĭdanov, N. F. Omelaenko, A. A. Penzev, E. Ya. Rudavskiĭ, A. S. Rybalko, and Yu. A. Tokar, Fiz. Nizk. Temp. **25**, 796 (1999) [Low Temp. Phys. **25**, 592 (1999); Erratum **25**, 928 (1999)].

Translated by Steve Torstveit

SHORT NOTES

Phonon echo in hydrogen-containing metals

L. L. Chotorlishvili,* I. A. Tutberidze, and G. R. Kakabadze

I. Dzhavakhishvili Tbilisi State University, pr. Chavchavadze 3, 380028 Tbilisi, Georgia
(Submitted August 8, 2000; revised January 16, 2001)
Fiz. Nizk. Temp. **27**, 693–695 (June 2001)

The phonon echo due to the tunneling of the hydrogen atom between two equilibrium positions in hydrogen-containing niobium NbO_xH_y is investigated. The time dependence of the intensity and shape of the two-pulse echo signal is obtained. [DOI: 10.1063/1.1382997]

Amorphous systems characterized by the presence of two-level tunneling systems (TTSs) have been well studied.[1] The TTS model has been applied to hydrogen-containing metals such as NbO_xH_y and NbO_xD_y $(0.005 \leqslant x,y \leqslant 0.02)$.[2,3]

According to Refs. 2 and 3, around an oxygen impurity atom there are 16 tetrahedral interstitial positions in which hydrogen atoms can be trapped. These 16 positions are grouped in pairs, forming 8 tunneling systems. As compared to the standard model of TTSs, the model used for hydrogen-containing metals has a number of specific features, including the absence of dependence of the distribution function on the tunneling energy Δ_0 (in view of its constancy). It is this circumstance that leads to distinctive temperature and frequency behavior of the various physical quantities.

The goal of the present study was to investigate the two-pulse phonon echo in NbO_xH_y due to the tunneling of the hydrogen atoms. As we shall show below, by studying the phonon echo one can determine the structure and low-temperature properties of hydrogen-containing metals.

We write the Hamiltonian of the system as

$$H = ES^Z + \frac{\gamma}{2}\left[\frac{\Delta_0}{E}(S^+ + S^-) + \frac{2(E^2-\Delta_0^2)^{1/2}}{E}S^Z\right] \times \cos\omega t + H_{SS} + H_{\text{int}}, \tag{1}$$

where S^Z is the pseudospin operator of the TTS, E is the energy splitting of the TTS, γ is the coupling constant of ultrasound with the TTS, H_{SS} is the dipole–dipole interaction Hamiltonian of the TTS, and H_{int} is the interaction Hamiltonian of the TTS with the conduction electrons, which has the form

$$H_{\text{int}} = \frac{1}{N}\sum_{k,p}\left[V_{\parallel}(q)S^Z + V_{\perp}(q)S^x\right]C_k^+ C_{k+q}, \tag{2}$$

where C_k^+ and C_k are the creation an annihilation operators for electrons in states with wave vector $\mathbf{k}$, and $V_{\parallel}$ and $V_{\perp}$ are interaction constants whose explicit form is given in Ref. 4. In the case when the Nb is found in the normal (nonsuperconducting) state, the longitudinal T_1 and transverse T_2 relaxation times of the TTSs are determined by the interaction of the TTSs with the conduction electrons (Korringa relaxation),[4] and so in order of magnitude $T_1 \sim T_2$.

The dominance of the Korringa relaxation in the formation of the time T_1 is due to the high density of states of conduction electrons.[5] The Korringa relaxation will also be the governing influence in the formation of T_2, since the dipole–dipole interaction between two-level systems, even at their maximum concentration,[6] is less efficient than the interaction with nonlocalized conduction electrons, with an extraordinarily high density of states at the Fermi level.[7] Without going into the simple calculations, we shall state that by using the Kubo method[8] one can obtain for the relaxation rates of the TTS

$$\frac{1}{T_2} \sim \frac{1}{T_1} = \frac{\pi}{4\hbar}(\tilde{\rho}V_{\perp})^2 E \coth\frac{E}{2T}, \tag{3}$$

where $\tilde{\rho} = N(\varepsilon_p)/\Omega$ is the density of electron states at the Fermi level.

Substituting into (3) the standard values $T = 1$ K, $E/\hbar \approx 1$ GHz, $V_{\perp} \approx 0.1$ eV, and $\tilde{\rho} \approx 1\ \text{eV}^{-1}$, we obtain $T_2 \sim T_1 \sim 10^{-9}$ s.

Such small values of the times T_2 and T_1 in comparison with the values of T_2 and T_1 associated with the spin–lattice and dipole–dipole interactions are due to the high electron density of states at the Fermi level ε_F.

We obtain expressions for the time dependence of the intensity and shape of the echo signal by the method described in Ref. 9. That paper[9] reports a study of the rotational echo in spin glasses due to oscillations of the macroscopic electric polarization at the effective Rabi frequency. Later an analogous technique was used to study the rotational echo in amorphous ferromagnets.[10] The echo signal contains contributions from tunneling systems with different effective Rabi frequencies (owing to the different energy splitting of the TTSs). The peculiarity of the formation of the phonon echo lies only in acoustic action on two-level systems. The expression for the shape of the echo signal is

$$A(t) = \int_{\Delta_0}^{E_{\max}} p(E,\Delta_0)\frac{\Delta_0}{E}\frac{\gamma\cos\omega t}{|\cos\omega t|}\left[\frac{\Omega_R}{\Omega}\right]^3 \times \exp(-\beta(t-2t_p)^2)\sin[\Omega(t-2t_p)]dE, \tag{4}$$

where $p(E,\Delta_0)$ is the distribution function for TTSs over the

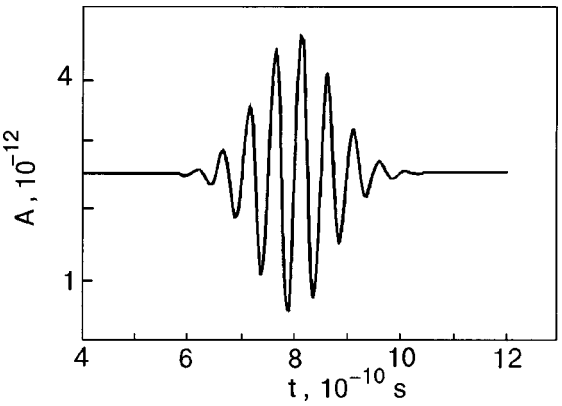

FIG. 1. Time dependence of the shape of the two-pulse echo signal.

energy splitting E for hydrogen-containing metals, $\Omega_R = 1/\hbar(\Delta_0/E)\gamma$ is the Rabi frequency, $\Omega = \sqrt{\Omega_R^2 + \omega_a^2}$,

$$\omega_a = \omega - \frac{E}{\hbar}; \quad \beta = \frac{1}{\Omega}\left(\frac{\omega_a^2}{T_2} + \frac{\Omega_R^2}{2T_1} + \frac{\Omega_R^2}{2T_2}\right),$$

and t_p is the time interval between pulses.

Using numerical methods for the standard parameter values $\Delta_0 \sim 0.01\,\mathrm{K}$, $E_{\max} \sim 10\,\mathrm{K}$, $\omega \sim 10\,\mathrm{GHz}$, $T \sim 1\,\mathrm{K}$, $t_p \sim 10^{-10}\,\mathrm{s}$, we calculated the time dependence of the shape and intensity of the two-pulse echo signal (Figs. 1 and 2).

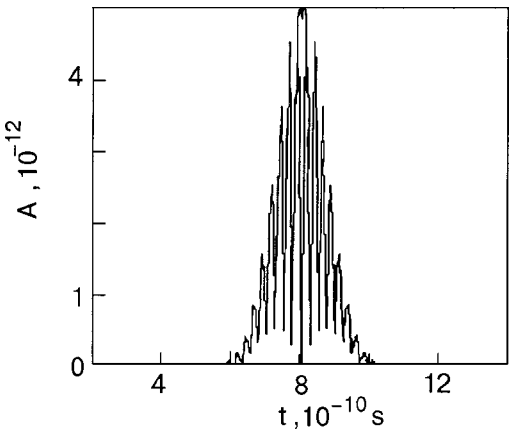

FIG. 2. Time dependence of the intensity of the two-pulse echo signal.

The results can be used to determine experimentally the longitudinal and transverse relaxation times T_1 and T_2, respectively.

For experimental determination of the relaxation times T_1 and T_2 we deemed it advisable to use the technique described in Ref. 11. Ordinarily the determination of T_1 requires a three-pulse echo, but since in our case $T_1 \sim T_2$, the two-pulse echo investigated here is entirely satisfactory. According to Ref. 11, we have for T_2 (formula (4.1.2) of Ref. 11)

$$T_2 = -4\frac{t_p - t_p'}{\ln I(t_p)/\ln I(t_p')},$$

where $I(t_p) = (A^2(t_p))^{1/2}$ is the intensity of the echo signal. Using the two-pulse echo signal for different time intervals t_p between pulses, one can determine $T_2 \sim T_1$, which, in turn, gives an idea of the value of the interaction constant of the TTSs with the conduction electrons in hydrogen-containing niobium. Moreover, as we have said, the distribution function $p(E, \Delta_0)$ of the TTSs, which was used to average the results obtained in Ref. 9, has in the case of hydrogen-containing metals a number of specific features[2,3] that distinguish it from the standard model.[1] In particular, the distribution function of the TTSs does not depend on the tunneling parameter Δ_0. Because of this, as can be seen from Eq. (4), one can determine Δ_0 by varying $|A(t)|$, i.e., one can obtain information about the structure of the TTSs, and that may prove useful in the study of hydrogen-containing metals.

*E-mail: Lchotor@usa.net

[1] P. W. Anderson, B. J. Halperin, and C. M. Varma, Philos. Mag. **25**, 1 (1972).
[2] H. Wipf and K. Neimaier, Phys. Rev. Lett. **52**, 1308 (1984).
[3] H. Wipf, Phys. Rev. Lett. **46**, 947 (1991).
[4] J. Korringa, Physica (Utrecht) **16**, 601 (1950).
[5] H. J. Güntherodt and H. Beck (Eds.), *Glassy Metals* [Springer-Verlag, Berlin (1981); Mir, Moscow (1983)].
[6] R. C. Zeller, Phys. Rev. B **4**, 2029 (1971).
[7] J. Winter, *Magnetic Resonance in Metals* [Clarendon Press, Oxford (1971); Mir, Moscow (1976)].
[8] I. V. Aleksandrov, *Theory of Magnetic Relaxation* [in Russian], Nauka, Moscow (1975).
[9] S. Hunkliger, Czech. J. Phys. **46**, Suppl. 6, 3284 (1996).
[10] G. R. Kakabadze and L. L. Chotorlishvili, Fiz. Nizk. Temp. **26**, 84 (2000) [Low Temp. Phys. **26**, 62 (2000)].
[11] E. A. Manykin and V. V. Samartsev, *Optical Echo Spectroscopy* [in Russian], Nauka, Moscow (1984).

Translated by Steve Torstveit